Synthesis, properties and applications of itaconate based engineering elastomers

Xinxin Zhou

En co-tutelle avec
l'Université des
Technologies Chimiques de
Pékin

Ecole Doctorale :
Ressources Procédés
Produits Environnement
(RP2E)

Ecole Nationale
Supérieure des Industries
Chimiques
(ENSIC)

Laboratoire Réactions
et Génie des Procedes
(LRGP-CNRS)

Procédé de synthèse, propriétés et applications d'élastomères techniques à base d'itaconates

T H È S E

Présentée en vue de l'obtention du grade de

DOCTEUR DE L'UNIVERSITE DE LORRAINE

Spécialité: Génie des Procédés et des Produits

par

Xinxin ZHOU

Thèse soutenue publiquement le 7 février 2018

Composition du Jury:

François LEQUEUX (DR)	ESPCI Paristech (France)	Rapporteur
Dean SHI (Prof.)	Université de Hubei (Chine)	Rapporteur
Isabelle ROYAUD (Prof.)	Université de Lorraine (France)	Examinateur
Meizhen YIN (Prof.)	Université des Technologies Chimiques de Pékin (Chine)	Examinateur
Guo-Hua HU (Prof.)	Université de Lorraine (France)	Directeur de thèse
Liqun ZHANG (Prof.)	Université des Technologies Chimiques de Pékin (Chine)	Directeur de thèse

En co-tutelle avec
l'Université des
Technologies Chimiques de
Pékin

Ecole Doctorale :
Ressources Procédés
Produits Environnement
(RP2E)

Ecole Nationale
Supérieure des Industries
Chimiques
(ENSIC)

Laboratoire Réactions
et Génie des Procedes
(LRGP-CNRS)

Synthesis, Properties and Applications of Itaconate Based Engineering Elastomers

T H E S I S

In Fulfillment of the Requirements for the Degree of

Doctor

of the University of Lorraine

Specialty: Process and Product Engineering

Defended by

Xinxin ZHOU

Defended on the 7th February, 2018

Jury:

François LEQUEUX (DR)	ESPCI Paristech (France)	Reviewer
Dean SHI (Prof.)	Hubei University (China)	Reviewer
Isabelle ROYAUD (Prof.)	University of Lorraine (France)	Examiner
Meizhen YIN (Prof.)	Beijing University of Chemical Technology (China)	Examiner
Guo-Hua HU (Prof.)	University of Lorraine (France)	Supervisor
Liqun ZHANG (Prof.)	Beijing University of Chemical Technology (China)	Supervisor

Acknowledgements

This thesis presented here is mainly completed at the Center of Advanced Elastomer Materials (CAEM), Beijign University of Chemical Technology, Beijing, China, and the Laboratoire Réactions et Génie des Procédés (LRGP), CNRS UMR 7274, Université de Lorraine, ENSIC, Nancy, France. I would extend my sincere gratitude to all the members for their kind help.

First and foremost, I am grateful to my supervisors Prof. Liqun ZHANG and Prof. Guo-hua HU for their guidance and suggestions on this research work, and for their support and help on my daily life. I would also give my sincere thanks to Prof. Baochun Guo and Dr. Runguo WANG for his inspiring advices and discussions. It is a great pleasure and honor to work with them.

I am profoundly indebted to all the staffs and students of LRGP and CAEM who offered great help to my study and daily life and their research experiences with me. Special thanks to my friends. My words are not sufficient to express how much I love you all. Especially, my friends in Nancy, France, Zhengkun Jiang, Chang He, Xiaofeng jiang, Yujing liu, Liang Zhang, Jingjing Liao, Daniela Florez, Thays Cristina, Ana Clara, etc. gave me great help in the past two years.

I would like to sincerely appreciate all the jury members Prof. François LEQUEUX, Prof. Dean SHI, Prof. Isabelle ROYAUD, Prof. Meizhen YIN and my supervisors for taking time out of their busy schedules to review my dissertation and achieve my PhD defense.

I would like to extend my sincere gratitude to my endlessly loving family. They all kept me going. Without their support and understanding, it would have been impossible for me to make it through.

At last, I gratefully acknowledge financial support from the National 973 Basic Research Program of China (2015CB654700), National Natural Science Foundation of China (50933001, 51503010 and 51673065), and the China-France Cooperation Program of PHC CAI YUANPEI (CHINA SCHOLARSHIP COUNCIL, No. 201504490120). I would also express my gratitude to the Linglong Tire Co. Ltd. and the Jilin Petrochemical Research Institute in China for technological supports.

31 October, 2017

Nancy, France

Abstract

This thesis deals with the preparation and application of itaconate based engineering elastomers and their nanocomposites. The following elastomers or nanocomposites were prepared: (1) nanocomposites based on 3,9-bis[1,1-dim ethyl-2-{b-(3-tertbutyl-4-hydroxy-5-methylphenyl)propionyloxy}ethyl]-2,4,8,10-tetraoxaspiro-[5,5]-undecane (AO-80) and poly(diisoamyl itaconate-*co*-isoprene) (PDII), (2) a bio-based carboxylic elastomer, poly(dibutyl itaconate-*co*-isoprene-*co*-methacrylic acid) (PDIM), and nanocomposites based on it and silica or halloysite nanotubes, (3) a novel bio-based elastomer, poly(dibutyl itaconate-*co*-butadiene) (PDIB), and nanocomposites based on it and silica. Bio-based green tires were manufactured by using PDIB/silica nanocomposite in a tire tread formulation. In addition to the preparation of the above bio-based elastomers and their nanocomposites, this thesis also gives a review on the progresses on bio-inspired sacrificial bonds in polymeric materials. This review will serve as a guide to engineer sacrificial bonds into itaconate based elastomers with high strength and toughness.

Keywords: Bio-based engineering elastomers; Preparation processes; Properties; Applications.

Résumé

Cette thèse traite la préparation et l'application d'élastomères bio-sourcés et leurs nanocomposites qui sont les suivants : (1) des nanocomposites basés sur le 3,9 - bis [ethyl-2-à 1,1 terne {b-(3-tertbutyle-4-hydroxy-5-méthylephényle) propionyloxy} éthyle]-2,4,8,10-tetraoxaspiro-[5,5]-undécane (AO-80) et le poly(itaconate de diisoamyle-*co*-isoprène) (PDII), (2) le poly(itaconate de dibutyle-*co*-isoprène-co-acide méthacrylique) (PDIM), un élastomère carboxylique bio-sourcé, et des nanocomposites basés sur cet élastomère et la silice ou les nanotubes de halloysite, (3) le poly(itaconate de dibutyle-*co*-butadiène) (PDIB), un nouvel élastomère bio-sourcé, et des nanocomposites basés sur cet élastomère et la silice. Des pneus verts bio ont été fabriqués en utilisant les nanocomposites PDIB/silice dans une formulation de bande de roulement de pneu. En plus de la préparation de ces dits élastomères bio et leurs nanocomposites, cette thèse donne aussi une revue sur les travaux sur des liaisons sacrificielles bio-inspirées qui sont introduites dans des matériaux polymères. Cette revue servira d'un guide pour incorporer des liaisons sacrificielles dans des élastomères à base d'itaconate ayant une grande rigidité et résistance.

Mots-clés : Bio-élastomères techniques; Procédés de synthèse; Propriétés; Applications.

Contents

Résumé étendu en français

I. Introduction

Actuellement, l'industrie pétrochimique doit faire face à la diminution des ressources fossiles et à l'alerte des pollutions environnementales. D'un côté, la formation des ressources fossiles nécessite un très long âge géologique. En raison de notre exploitation excessive des ressources fossiles, une crise énergétique sans précédent approche. D'un autre côté, l'exploitation et l'utilisation excessives des ressources fossiles entraînent de graves menaces pour le climat, l'environnement, les ressources et les bénéfices sociétaux. Ces crises et menaces ont suscité une préoccupation et une réflexion mondiales. Une voix qui demande le remplacement des ressources fossiles par des ressources durables se répand partout dans le monde.

En raison de leur grande résilience, les élastomères, connus comme matériau stratégique important, ont été largement utilisés dans les industries minières, les transports, l'agriculture, la foresterie et la conservation de l'eau, la défense nationale militaire, les secteurs médicaux et sanitaires, les communications électriques, etc. Jusqu'à aujourd'hui, la quasi-totalité de nos produits élastomères dépendent encore du caoutchouc naturel et des caoutchoucs synthétiques d'origine fossile. Actuellement, le caoutchouc naturel est récolté principalement sous la forme de latex à partir des hévéas. Cependant, la croissance des hévéas naturels est influencée par plusieurs facteurs tels que la situation géographique et les conditions climatiques. Les hévéas naturels poussent bien uniquement à proximité de l'équateur entre 10^{o} de latitude sud et 15^{o} de latitude nord. Le développement des caoutchoucs synthétiques compense la sous-production du caoutchouc naturel, mais la dépendance fossile des caoutchoucs synthétiques ne pourra pas assdurern le développement durable de l'industrie du caoutchouc. L'utilisation de ressources renouvelables au lieu de ressources fossiles est d'une grande importance pour le développement durable de l'économie mondiale.

De nos jours, des polymères dérivés de produits chimiques biosourcés ont été développés par des chercheurs en matériaux et en chimie. Les produits chimiques biosourcés peuvent être obtenus à partir de la biomasse. Ces produits chimiques biosourcés comprennent (1) des

monomères fermentaires tels que des acides, des alcools et des alcènes de la biomasse et (2) des monomères extractifs tels que l'amidon, la lignine, la cellulose et l'huile végétale. Les élastomères biosourcés sont des matériaux élastomères synthétisés à partir des produits chimiques biosourcés. Selon différentes applications, les élastomères biosourcés peuvent être classés en tant qu'élastomères biosourcés pour des applications médicales et en élastomères biosourcés pour des applications techniques. Les matériaux biosourcés pour des applications médicales, caractérisés par leur biocompatibilité et leur biodégradabilité, peuvent être utilisés dans l'ingénierie tissulaire, l'administration de médicaments, la suture chirurgicale, *etc*. Les élastomères biosourcés techniques, caractérisés par leur résistance mécanique, leur coût de production et leur stabilité environnementale, peuvent être utilisés dans le transport, les vibrations, l'étanchéité et d'autres applications techniques traditionnelles.

Dans l'industrie du caoutchouc, il n'y a pas encore d'étude sur les applications des élastomères biosourcés. Deux raisons principales devraient en être responsables: d'une part, la recherche sur les élastomères techniques biosourcés est encore au stade initial, et de nombreux produits chimiques biosourcés ne sont pas encore utilisés; d'autre part, les performances des élastomères biosourcés demeurent insuffisantes. Il existe un vaste espace de développement pour modifier et renforcer les élastomères techniques biosourcés. Dans nos études précédentes, un élastomère de poly(itaconate de diisoamyle-*co*-isoprène) (PDII) a été préparé par polymérisation en émulsion amorcée par oxydoréduction à base d'acide itaconique biosourcé, d'isoamylol et d'isoprène. C'est une voie importante pour modifier et renforcer l'élastomère PDII pour des applications techniques.

II. Objectifs de la thèse

L'un des objectifs de cette thèse est d'explorer la faisabilité des élastomères à base d'itaconate en tant que matériaux d'amortissement potentiels en développant et en évaluant des nanocomposites à base de PDII et AO-80. Nous supposons que les groupements ester dans les élastomères à base d'itaconate peuvent former une forte interaction intermoléculaire (éventuellement des liaisons hydrogène) avec les groupements hydroxyles phénoliques dans les molécules organiques AO-80 (Figure 1). L'interaction intermoléculaire pourrait améliorer la friction intermoléculaire et entraîner une grande dissipation d'énergie. Ainsi, les nanocomposites PDII/AO-80 présenteraient d'excellentes performances d'amortissement et constitueraient un matériau d'amortissement biosourcé potentiel.

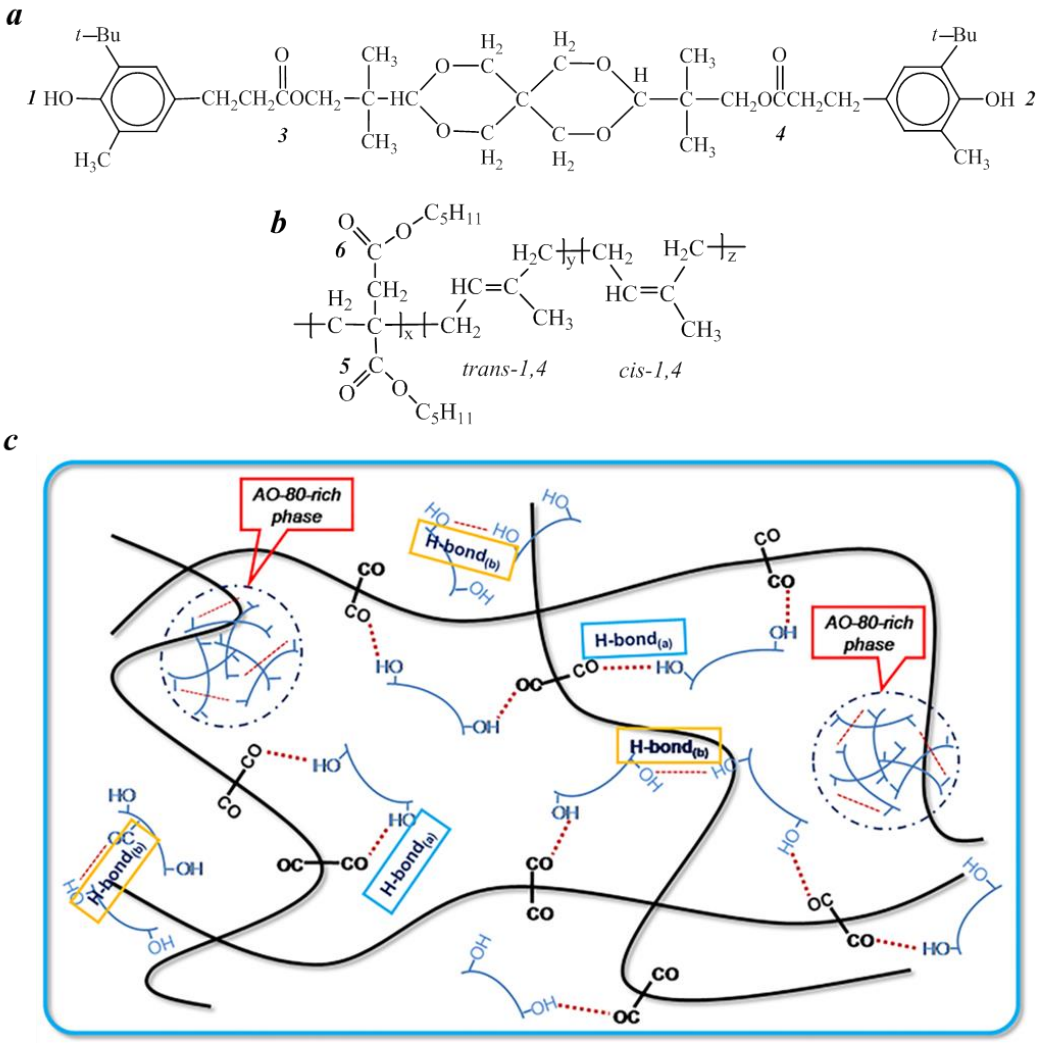

Figure II-1. Structures moléculaires de (a) AO-80 et (b) PDII. (c) Liaison hydrogène éventuelle (a) et liaison hydrogène (b) dans les hybrides, avec des lignes épaisses noires, des lignes courtes bleues et des lignes pointillées rouges désignant les molécules PDII, les petites molécules AO-80 et les liaisons hydrogène, respectivement.

Notre objectif principal ici est de préparer des pneus verts biosourcés. Pour atteindre cet objectif, un élastomère biosourcé doit d'abord être conçu et synthétisé à partir d'un itaconate biosourcé. Un matériau de bande de roulement de pneu vert devrait avoir une bonne performance. Normalement, la contrainte de traction doit être supérieure à 15 MPa, tan δ à 60^{o}C doit être inférieure à 0,1 pour une faible résistance au roulement, et tan δ à 0^{o}C doit être supérieure à 0,2 pour une bonne adhérence sur sol mouillé. Pour répondre à ces exigences, l'élastomère biosourcé doit avoir une faible T_g (normalement inférieure à -30^{o}C), être réticulable (normalement possédant des doubles liaisons), et avoir une masse molaire élevée (normalement supérieure à 200000 g/mol). Les élastomères sans charges (renforts) ne peuvent

pas être utilisés comme matériau de bande de roulement même s'ils ont une masse molaire élevée. Par conséquent, afin de répondre aux exigences de la bande de roulement du pneu vert, les élastomères à base d'itaconate doivent être renforcés par des charges. Une forte interaction interfaciale élastomère-charge et une dispersion homogène des charges sont les conditions préalables à de bonnes performances. Le cadre du travail principal est illustré dans la Fig. 2.

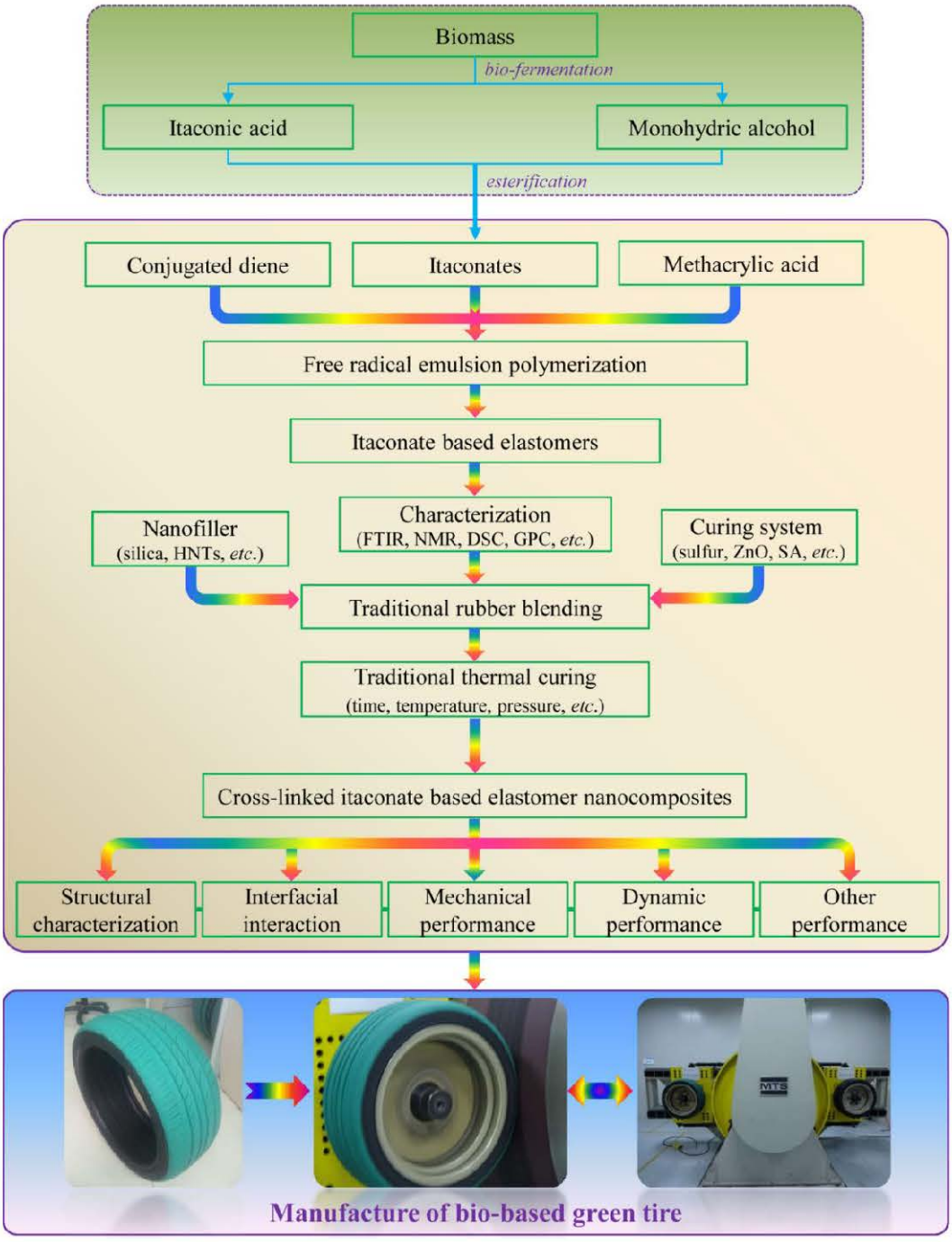

Figure II-2. Cadre du travail de thèse.

III. Contenu de la recherche et principaux résultats de cette thèse

Comme l'élastomère PDII a été synthétisé avec succès, la question clé à traiter était la recherche d'une application concrète de cet élastomère technique à base d'itaconate. En raison de nombreux groupements d'esters dans l'élastomère PDII, on s'attendait à ce qu'il soit un matériau d'amortissement. Dans cette recherche, une molécule organique polaire et rigide AO-80 a été introduite dans la matrice PDII pour préparer les nanocomposites PDII/AO-80 par un procédé à l'état fondu au-dessus de la température de fusion de AO-80. Le cisaillement intense associé au procédé de malaxage mécanique à haute température pourrait favoriser de manière significative le mélange au niveau moléculaire entre le PDII à l'état caoutchoutique et l'AO-80 à l'état liquide. Une partie des molécules AO-80 formaient une phase riche en AO-80, mais la plupart d'entre elles se dissolvaient dans le PDII pour former une dispersion à l'échelle moléculaire sous forme amorphe. Les résultats de FTIR et DSC ont indiqué qu'une forte interaction intermoléculaire était formée entre les molécules PDII et AO-80. Chaque nanocomposite PDII/AO-80 présentait une transition unique avec une température de transition vitreuse plus élevée et une valeur de tangente de perte (tanδ) significativement plus élevée que le PDII seul en raison de l'interaction intermoléculaire entre les molécules PDII et AO-80. Par exemple, tanδ de PDII/AO-80 contenant 100 parts de AO-80 atteint 2,6 fois celle du PDII seul.

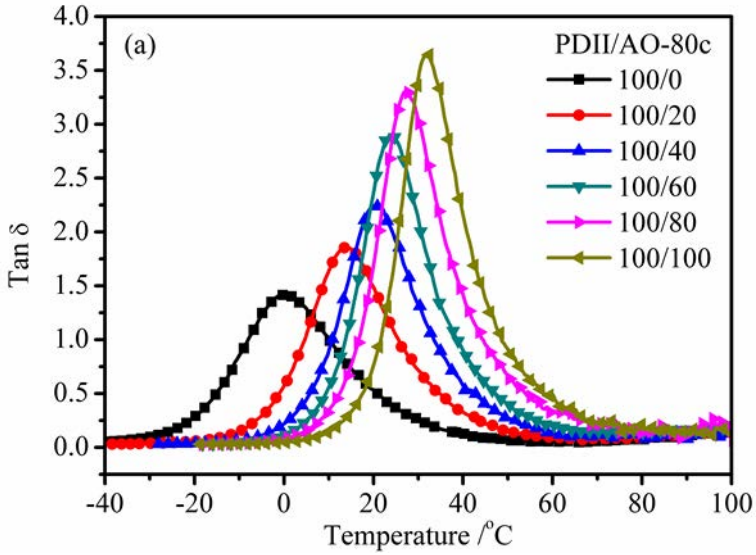

Figure III-1. Dépendance en température de la tangente de perte (tanδ) pour les hybrides PDII/AO-80 avec différents rapports massiques PDII/AO-80.

Rappelons que notre objectif principal est de préparer une bande de roulement de pneu biosourcé. Pour atteindre cet objectif, nous avons d'abord préparé deux élastomères à base d'itaconate de masse molaire élevée, de faible T_g et de pouvoir de réticulation (Figure III-2).

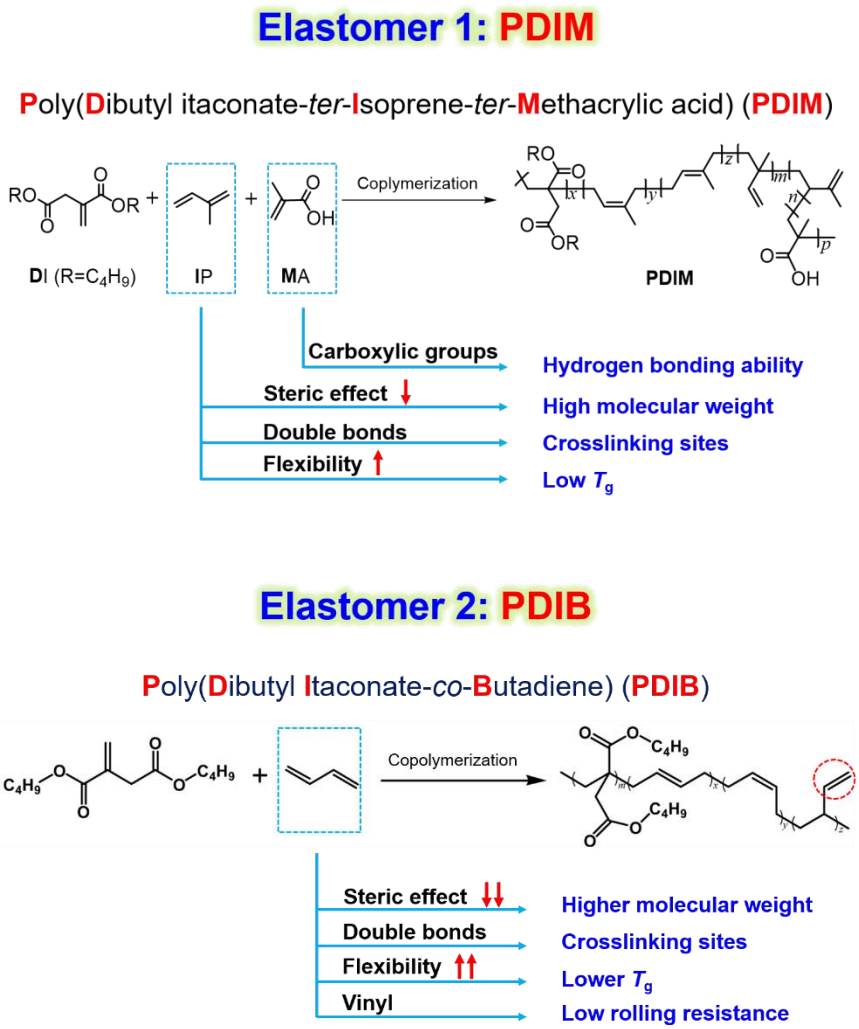

Figure III-2. Deux élastomères à base d'itaconate (PDIM et PDIB) pour les pneus verts biosourcés.

Les élastomères seuls sans charges (renforts) ne peuvent pas être utilisés comme matériau de bande de roulement même s'ils ont une masse molaire élevée. Par conséquent, afin de répondre aux exigences (haute résistance, faible tan δ à 60°C et haute tan δ à 0°C) de la bande de roulement du pneu vert, les élastomères à base d'itaconate doivent être renforcés par des charges. Une forte interaction interfaciale élastomère-charge et une dispersion homogène des charges sont les conditions préalables à de bonnes performances. Nous avons donc utilisé deux principes pour améliorer l'interaction interfaciale et la dispersion des charges. L'un

consiste à construire une interface de liaison hydrogène et l'autre une interface de liaison covalente dans les nanocomposites élastomères. Basé sur le principe interfacial de la liaison hydrogène, nous avons préparé deux nanocomposites (Figure III-3). Dans les deux nanocomposites, une interaction de liaison hydrogène s'est formée entre carboxyle et siloxy. Basé sur le principe interfacial de liaison covalente, nous avons préparé un troisième nanocomposite à base de PDIB et de silice. L'interaction de liaison covalente a été formée par la réaction en deux étapes (Figure III-4). Enfin, le PDIB a été lié de manière covalente à la silice par des agents de couplage.

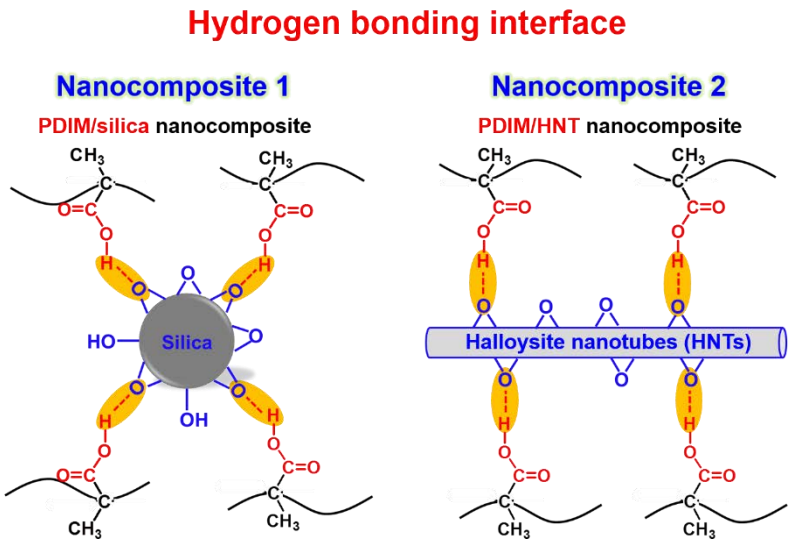

Figure III-3. Principe de l'interface de liaison hydrogène dans les nanocomposites à base de PDIM et de charges.

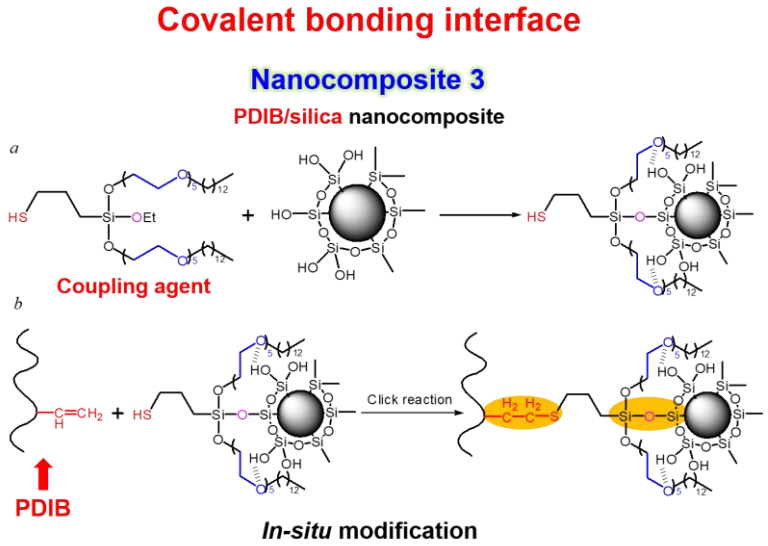

Figure III-4. Principe de l'interface de liaison covalente dans un nanocomposite à base de PDIB et de silice.

Élastomères à base d'itaconate

Des élastomères poly(itaconate de diisoamyle-ter-isoprène-ter-acide méthacrylique) (PDIM) à haute masse molaire ont été synthétisés par polymérisation en émulsion initiée par redox à base d'itaconate de dibutyle (DI), d'isoprène (IP) et d'acide méthacrylique (MA). De petites quantités d'acide méthacrylique (1-5% en poids) ont été utilisées pour introduire les groupements carboxyliques dans les chaînes macromoléculaires PDIM pour leur conférer la capacité de former la liaison hydrogène. Pour toutes les synthèses, les rendements de PDIM étaient supérieurs à 70% après 12 heures de polymérisation. Les élastomères PDIM avaient une masse molaire moyenne en nombre élevée (> 250 000 g/mol) et de basses températures de transition vitreuse (<-30°C). Les teneurs en carboxyle dans les élastomères PDIM ont été déterminées par titrage à la butanone, comme indiquées dans le tableau III-1.

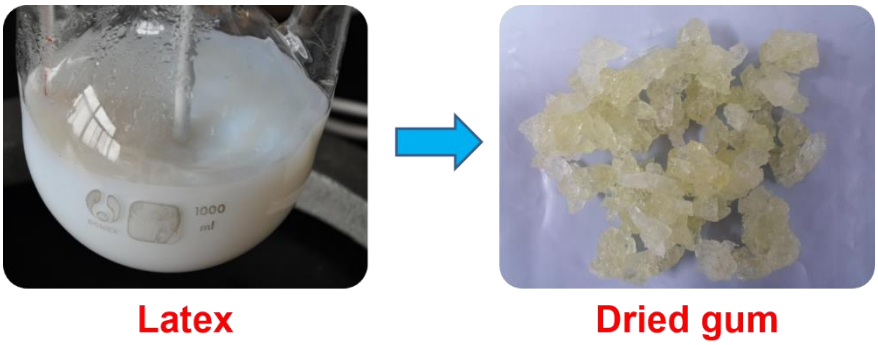

Figure III-5. Latex PDIM et gomme PDIM.

Table III-1. Synthèse d'élastomères PDIM par polymérisation en émulsion initiée par redox.

PDIM	Copolymerization feeds			PDIM elastomers				
	DI (g)	IP (g)	MA (g)	Yield (%)	M_n (g/mol)	M_w/M_n	T (°C)	MA content
PDIM0	70.0	30.0	0	77	251 000	2.72	-40	0
PDIM1	70.0	30.0	1.0	74	297 000	3.82	-38	0.58
PDIM3	70.0	30.0	3.0	78	289 000	4.17	-34	2.62
PDIM5	70.0	30.0	5.0	75	279 000	3.63	-32	4.12

Le deuxième élastomère à base d'itaconate, le poly (itaconate de dibutyle-co-butadiène) (PDIB), a été synthétisé par polymérisation en émulsion initiée par rédox de l'itaconate de dibutyle avec du butadiène (Bd). L'élastomère PDIB a une masse molaire plus élevée et une

Tg inférieure à celle de l'élastomère PDIM, comme le montre le tableau III-2. La microstructure de l'élastomère PDIB a été confirmée par FTIR et RMN. Les copolymères résultants avaient principalement du trans- et du vinyl-polybutadiène dans leurs chaînes (figure III-6). Les rapports de réactivité de l'itaconate de dibutyle et du butadiène ont été déterminés par les méthodes classiques de Fineman-Ross et de Kelen-Tüdös (tableau III-3). La distribution de la séquence des monomères a indiqué que le butadiène pouvait subir une auto-propagation pour former de longs segments flexibles, tandis que l'itaconate de dibutyle préférait former de courtes séquences avec des segments isolés, des diades ou des triades. Les propriétés mécaniques du PDIB pourraient concurrencer ou même surpasser celles des caoutchoucs synthétiques traditionnels.

Table III-2. Synthèse d'élastomères PDIM par polymérisation en émulsion initiée par redox.

Sample	DI /g	Bd /g	M_n /10^4	M_w/M_n	T_g /°C	Gel /%	Yield /%
PDIB0	100	0	9.3	2.65	-4	0	–
PDIB10	90	10	23.6	2,97	-42	2	60.5
PDIB20	80	20	31.4	3.23	-44	2	76.2
PDIB30	70	30	36.8	3.76	-48	3	80.7
PDIB40	60	40	39.2	3.81	-52	5	86.3
PDIB50	50	50	35.3	4.12	-55	6	84.7
PDIB60	40	60	33.7	3.96	-58	8	80.2
PDIB70	30	70	34.5	4.32	-63	11	70.8
PDIB80	20	80	32.6	4.29	-68	15	56.3
PDIB90	10	90	–	–	-72	21	45.4
PDIB100	0	100	–	–	-75	24	19.8

Table III-3. Rapports de réactivité de l'itaconate de dibutyle (r_1) et du butadiène (r_2).

Méthode	r_1	r_2	$r_1 \times r_2$	Point azéotropique point
Fineman-Ross	0.137	0.466	0.064	0.382
Kelen-Tüdös	0.141	0.466	0.066	0.383
Valeur moyenne	0.139	0.466	0.065	0.383

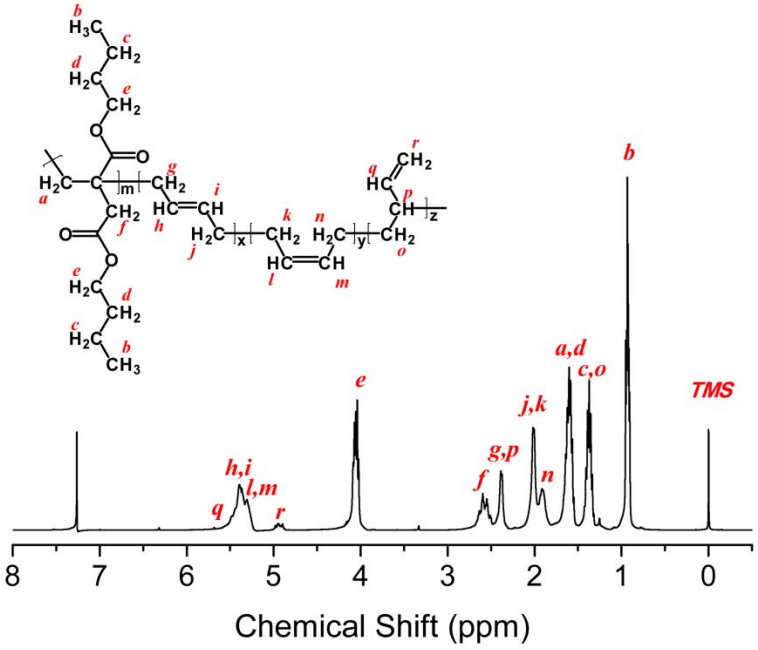

Figure III-6. Spectre ^{1}H NMR du PDIB40 (dans $CDCl_3$).

Nanocomposites élastomères à base d'itaconate

Trois types de nanocomposites ont été évalués en termes de propriétés mécaniques, tan δ à 60^{o}C et tan δ à 0^{o}C. Celui qui peut répondre aux exigences de la bande de roulement du pneu vert sera utilisé pour préparer un pneu vert.

Le premier type de nanocomposite à base de PDIM et silice a été préparé selon le principe d'interface de liaison hydrogène. L'interaction de liaison hydrogène entre le PDIM et la silice a été confirmée par les spectres FTIR. En raison de l'interface de liaison hydrogène, une dispersion de silice homogène a été observée (voir images TEM dans la figure III-7). Cependant, les performances mécaniques et dynamique des nanocomposites à base de PDIM et silice ont indiqué qu'elles ne convenaient pas à une bande de roulement à faible résistance au roulement.

Le deuxième type de nanocomposite à base de PDIM et HNTs, a été développé par co-coagulation de la suspension aqueuse de latex PDIM et de nanotube de halloysite (HNT) (figure III-8), suivie d'un malaxage mécanique avec d'autres additifs de caoutchouc. L'interaction de liaison hydrogène a été confirmée entre carboxyle et siloxy dans les nanocomposites, comme le montre la figure III-9. Avec l'incorporation de HNT dans le PDIM, la contrainte de traction et l'énergie de fracture ont toutes les deux augmenté, ce qui indique que les nanocomposites PDIM/HNT ont une contrainte élevée et une bonne ductilité.

Cependant, la contrainte à la traction la plus élevée est inférieure à 15 MPa, ce qui n'est pas suffisante pour un matériau de bande de roulement de pneu.

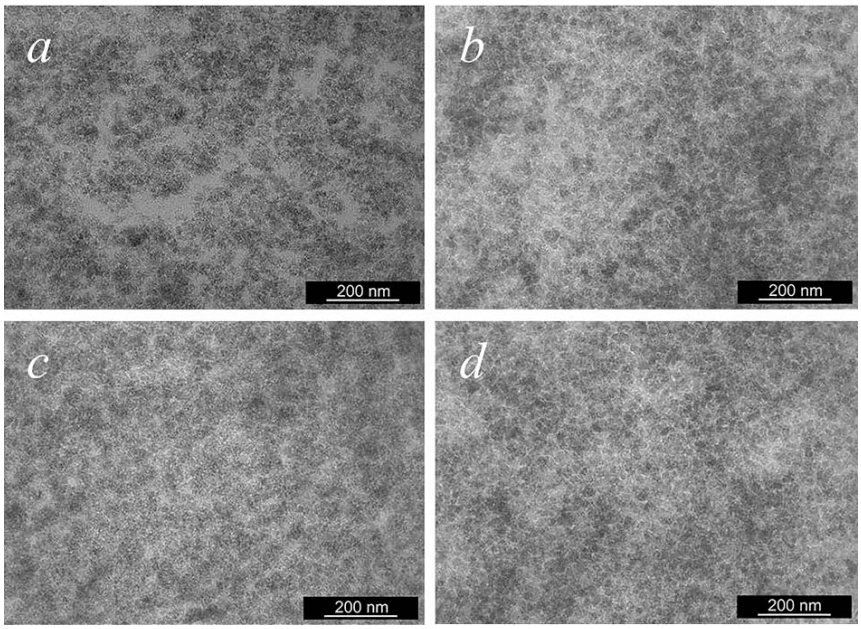

Figure III-7. Images TEM des nanocomposites (a) PDIM0/silice, (b) PDIM1/silice, (c) PDIM3/silice, et (d) PDIM5/silice.

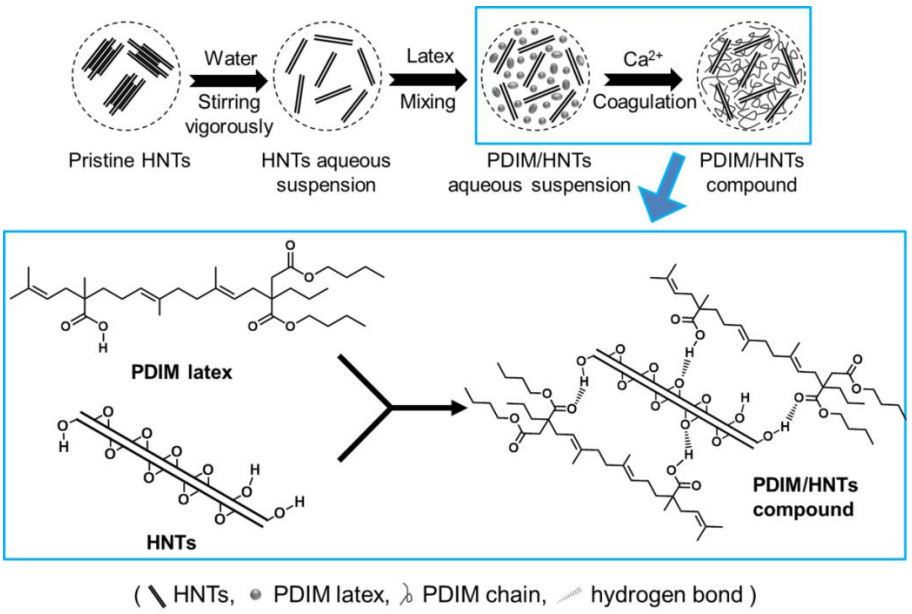

Figure III-8. Schéma de co-coagulation dans la preparation des nanocomposites PDIM/HNTs.

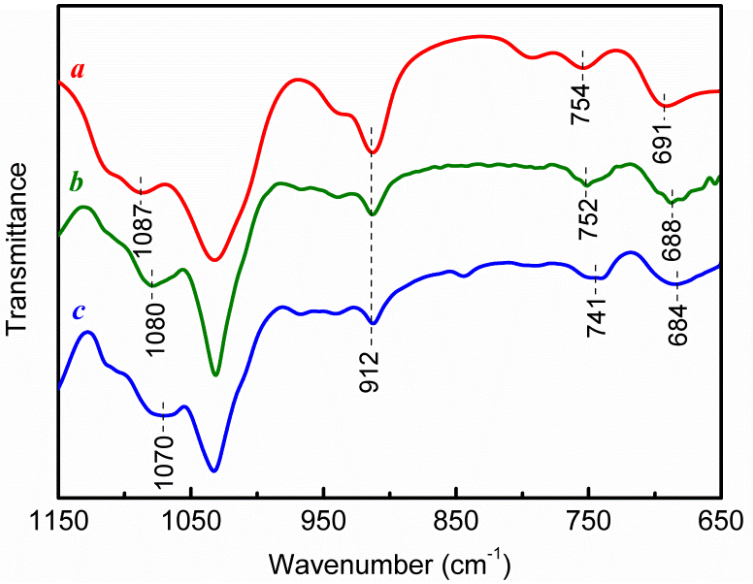

Figure III-9. Spectres FTIR de (a) HNTs, (b) nanocomposite poly (itaconate de dibutyle-co-isoprène)/HNTs nanocomposite, et (c) nanocomposite PDIM/HNTs.

La discussion ci-dessus permet de conclure que le PDIM n'est pas un élastomère approprié pour préparer une bande de roulement de pneu. La structure chimique du PDIM devrait en être la cause. Par conséquent, nous avons préparé un troisième type de nanocomposite à base de PDIB et silice selon le principe de l'interface de liaison covalente en utilisant une modification in-situ. Le procédé de modification in situ permet aux groupements vinyliques du PDIB de se lier de manière covalente au silanol sur silice par l'intermédiaire d'un agent de couplage. Ainsi, une interface de liaison covalente est formée dans les nanocomposites PDIB/silice. La silice s'est dispersée de manière homogène dans la matrice PDIB (figure III-10).

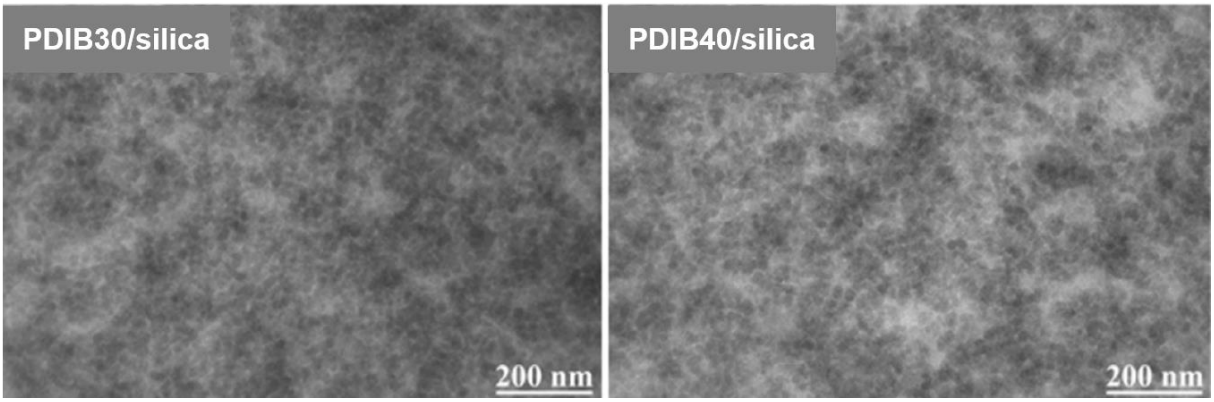

Figure III-10. Images TEM images des nanocomposites PDIB/silice.

Les propriétés mécaniques et tan δ à 60°C et 0°C de nanocomposites PDIB/silice sont montrées dans le tableau III-4 et le tableau III-5, respectivement. Sur la base d'une contrainte élevée, une tan δ à 60°C faible (une faible résistance au roulement), et une tan δ à 0°C haute (une bonne adhérence sur sol mouillé), le nanocomposite PDIB40/silice avait les propriétés les mieux équilibrées et était apparu comme un matériau élastomère potentiel de hautes performances pour fabriquer des bandes de roulement de pneus verts.

Table III-4. Propriétés mécaniques des nanocomposites PDIB/silice

Sample	Tensile strength (MPa)	Elongation at break (%)	300% Tensile stress (MPa)	Permanent set (%)
PDIB20/silica	12.7 ± 0.6	492 ± 38	7.5 ± 0.2	40 ± 4
PDIB30/silica	17.4 ± 1.3	509 ± 42	8.8 ± 0.3	32 ± 4
PDIB40/silica	**18.6** ± 0.9	**590** ± 43	6.1 ± 0.2	**16** ± 2
PDIB50/silica	**21.2** ± 1.1	**640** ± 36	6.4 ± 0.1	**16** ± 3
PDIB60/silica	**23.6** ± 1.5	**643** ± 27	6.5 ± 0.5	**16** ± 2
PDIB70/silica	**25.0** ± 1.4	**774** ± 51	4.3 ± 0.3	**16** ± 2
PDIB80/silica	**24.8** ± 0.8	**545** ± 46	9.3 ± 1.2	**10** ± 1
PDIB90/silica	20.6 ± 2.2	263 ± 23	N/A	2 ± 1
PDIB100/silica	17.6 ± 2.6	255 ± 29	N/A	2 ± 1

Table III-5. Tan δ at 60°C and 0°C pour les nanocomposites PDIB/silice.

Sample	T_g (°C)	**Tan δ**		
		0°C	**60°C**	**Max**
PDIB20/silica	-34.6	0.282	0.125	0.652
PDIB30/silica	-30.2	0.284	0.125	0.667
PDIB40/silica	**-33.4**	**0.280**	**0.119**	0.754
PDIB50/silica	-38.3	0.227	0.121	0.686
PDIB60/silica	-41.0	0.196	0.113	0.676
PDIB70/silica	-50.0	0.149	0.102	0.633
PDIB80/silica	-53.2	0.116	0.078	0.661
PDIB90/silica	-54.5	0.113	0.090	0.574
PDIB100/silica	-58.8	0.104	0.077	0.551

Pour réduire davantage la tan δ à 60°C, le PDIB40 a été mélangé avec le BR. La contrainte maxiale à la traction, l'allongement à la rupture et la contrainte à 100% d'allongement pour le nanocomposite PDIB40-BR /silice sont respectivement de 15,6 MPa, 368% et 2,5 MPa. Les tan δ à 60°C et 0°C du nanocomposite PDIB-BR/silice sont respectivement de 0,09 et 0,21, ce qui indique une faible résistance au roulement et une bonne adhérence sur sol mouillé pour un pneu.

Le pneu vert biosourcé basé sur le nanocomposite PDIB40/BR/silice a été fabriqué et testé à l'aide d'un système de mesure de résistance au roulement MTS (figure III-11) de LingLong Tire Co. Ltd. Le coefficient de résistance au roulement était de 7,7 kg/tonne, ce qui classait le pneu dans la classe « B » selon le règlement européen sur l'étiquetage des pneumatiques 1222/2009, ce qui est un niveau élevé puisque la classe « A » est peu présente sur le marché des pneus.

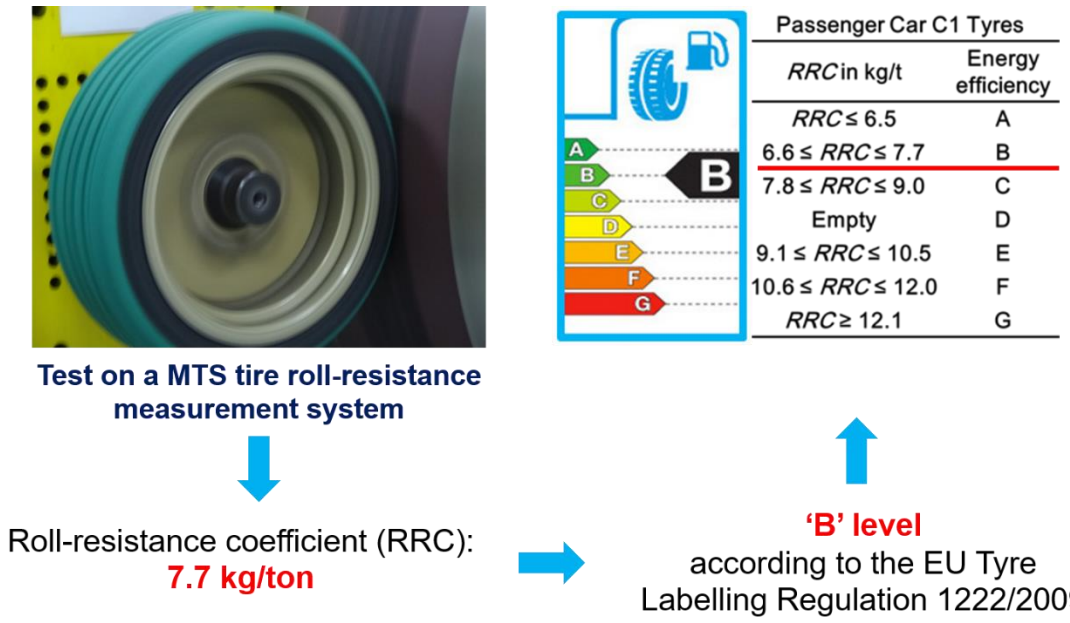

Figure III-11. Essai de résistance au roulement pour le pneu vert biosourcé.

Chapter1 General introduction

1.1 Overview

Currently, the petrochemical industry has to confront the diminution of fossil resources and the alarm of environmental pollutions. On the one hand, the formation of fossil resources needs a very long geological age. Due to our excessive exploitation of fossil resources, an unprecedented energy crisis is approaching. On the other hand, the excessive exploitation and use of fossil resources result in serious threats to climate, environment, resource, and societal benefits. These crisis and threats have aroused global concern and reflection. A voice to replace fossil resources with sustainable resources is spreading all over the world.

Due to unique high resilience, elastomers, known as an important strategical material, have been widely applied in industrial mines, transportation, agriculture, forestry and water conservancy, national defense military, medical and health, electrical communications, and educational fields. Until today, almost all of our elastomer products are still dependent on natural rubber and fossil-based synthetic rubbers. Currently, natural rubber is harvested mainly in the form of the latex from the rubber trees (*Hevea brasiliensis*). However, the growth of the natural rubber trees is affected by several factors such as geographical location and climatic conditions. The natural rubber trees only grow well nearby equator from 10^{o} south latitude to 15^{o} north latitude. The development of synthetic rubbers offsets the underproduction of natural rubber, but the fossil dependence of synthetic rubbers will not keep the sustainable development of rubber industry. Use of renewable resources instead of fossil resources is of great significance to the sustainable development of the global economy.

Nowadays, polymers derived from bio-based chemicals have been developed by material and chemical scientists. Bio-based chemicals can be obtained from biomass. These bio-based chemicals include (1) fermentative monomers such as acids, alcohols, and alkene from biomass and (2) extractive monomers such as starch, lignin, cellulose, and plant oil from natural plants. Bio-based elastomers are synthetic elastomeric materials based on bio-based chemicals. According to different applications, bio-based elastomers can be categorized as

bio-based medical elastomers and bio-based engineering elastomers. Bio-based medical materials, emphasized by their biocompatibility and biodegradability, can be applied in tissue engineering, drug delivery, surgical suture and so on. Bio-based engineering elastomers, emphasized by their mechanical strength, production cost, and environmental stability, can be applied in transportation, vibration, sealing and other traditional engineering applications.

In the rubber industry, there is no report on the applications of bio-based engineering elastomers yet. Two main reasons should be responsible for this: on the one hand, the research on bio-based engineering elastomers is still at the initial stage, and many bio-based chemicals are not still used; on the other hand, the performance of bio-based engineering elastomers has yet to be improved. There is a broad development space to modify and reinforce the bio-based engineering elastomers. In our previous studies, a poly(diisoamyl itaconate-co-isoprene) (PDII) elastomer was prepared by redox-initiated emulsion polymerization based on bio-based itaconic acid, isoamylol, and isoprene. It is important direction to modify and reinforce the PDII elastomer for engineering applications.

Filler modification is an effective technology for improvement of elastomer performance. Modified with reinforcing or functional filler, elastomer can exhibit improved mechanical or functional performance. Hindered phenol is a kind of organic molecules containing multiple phenolic hydroxyl groups, which can form hydrogen bonding networks with polar groups in polymers. Polar polymers modified with hindered phenol can dissipate amounts of mechanical energy by sacrificing the hydrogen bonding networks, and thus exhibit improved damping property. Following our previous works, 3,9-bis[1,1-dim ethyl-2-{b-(3-tertbutyl-4-hydroxy-5-methylphenyl)propionyloxy}ethyl]-2,4,8,10-tetraoxaspiro-[5,5]-undecane (AO-80), a hindered phenol, was introduced into PDII matrix to prepare a bio-based elastomer nanocomposite that exhibited excellent damping properties.

With the international calls for environmental protection and energy conservation and emission reduction, the EU Tyre Labelling Regulation introduced higher labelling requirements with regard to the display of information on the rolling resistance, wet grip and external rolling noise of tires. As one of the main components of tires, elastomeric material is the only part that directly touches the ground. Therefore, the performance of elastomeric materials plays a decisive role for low rolling resistance and good wet grip resistance of tires. It has been reported that introduction of carboxyl groups into elastomer chains can effectively improve the interfacial interaction between elastomer and non-petroleum based silica to

obtain good dispersion of silica, which is expected to improve the rolling resistance and the wet grip resistance of rubber/silica nanocomposite-based tires. With introduction of third monomer in PDII polymerization system, a bio-based carboxylic elastomer poly(dibutyl itaconate-*co*-isoprene-*co*-methacrylic acid) (PDIM) was synthesized and developed. Silica and halloysite nanotubes (HNTs), two non-petroleum based fillers, were introduced into the PDIM elastomer to study the interfacial interaction between filler and PDIM elastomer and seek the application of the PDIM elastomer on non-petroleum based "green tires". The results showed the PDIB elastomer was not suitable as a tire tread material although it could form strong interfacial interaction with silica or HNTs.

The diene structure is another important factor for viscoelastic energy dissipation of PDII and PDIM elastomers. Therefore, we used butadiene instead of isoprene as a comonomer to polymerize with dibutyl itaconate and prepared a new bio-based engineering elastomer poly(dibutyl itaconate-co-butadiene) (PDIB). The performance of PDIB elastomer could be tuned according to the microstructure of PDIB macromolecules. The mechanical properties of silica-filled PDIB elastomeric nanocomposites were comparable with those of silica-filled conventional rubber nanocomposites and could meet the most requirements of engineering applications. Especially, PDIB/silica nanocomposite-based tire was manufactured and exhibited 7.7 kg/ton of rolling resistance coefficient which rated as class 'B' according to the European Tyre Labelling Regulation 1222/2009, which is a high level since class 'A' is few in the tire market.

1.2 Research objectives of this thesis

Our objectives here are to develop bio-based engineering elastomers based on itaconic acid, to further explore applications of these bio-based elastomers in engineering fields, and to provide a theoretical basis for sustainable development of rubber industry.

One of the main objectives of this thesis is to explore the feasibility of itaconate based elastomers as potential damping materials by developing and evaluating PDII/AO-80 nanocomposites. We supposed that the ester groups in the itaconate based elastomers can form strong intermolecular interaction (possibly hydrogen bonds) with the phenolic hydroxyl groups in the AO-80 organic molecules. The intermolecular interaction might be enhance the intermolecular friction and result in large energy dissipation. Thus, the PDII/AO-80

nanocomposites would exhibit excellent damping performance and be a potential bio-based damping material.

Another objective of this thesis is to introduce carboxylic groups into itaconate based elastomers to prepare a bio-based carboxylic elastomer (PDIM), aiming to further improve interfacial interaction with non-petroleum based fillers such as silica and HNTs. Generally, good interfacial interaction between polymer matrix and fillers implies good mechanical performance of the polymer composites. Especially, the bio-based carboxylic elastomer reinforced by silica was expected to show a good interfacial interaction and to be a tire tread material. Inspired by sacrificial bonding theory, HNTs was selected to fill the PDIM, where hydrogen bonds and macromolecular coils might be formed at interface of PDIM/HNTs nanocomposites. The application of sacrificial bonding theory in itaconate based elastomers would be first explored.

Also, the current thesis aims to develop a new itaconate based elastomer (PDIB) from dibutyl itaconate and butadiene for tire tread. The change of chemical structure might result in a change of performance. The PDIB would be evaluated on chemical structure, performance, and potential applications. Silica would be used to reinforce PDIB for feasibility of PDIB/silica nanocomposites as tire tread materials.

1.3 Research contents and main results of this thesis

This PhD thesis focuses on the development of itaconate based engineering elastomers and their nanocomposites and on the application of these nanocomposites. The framework of this thesis work is shown in Fig. 1-1.

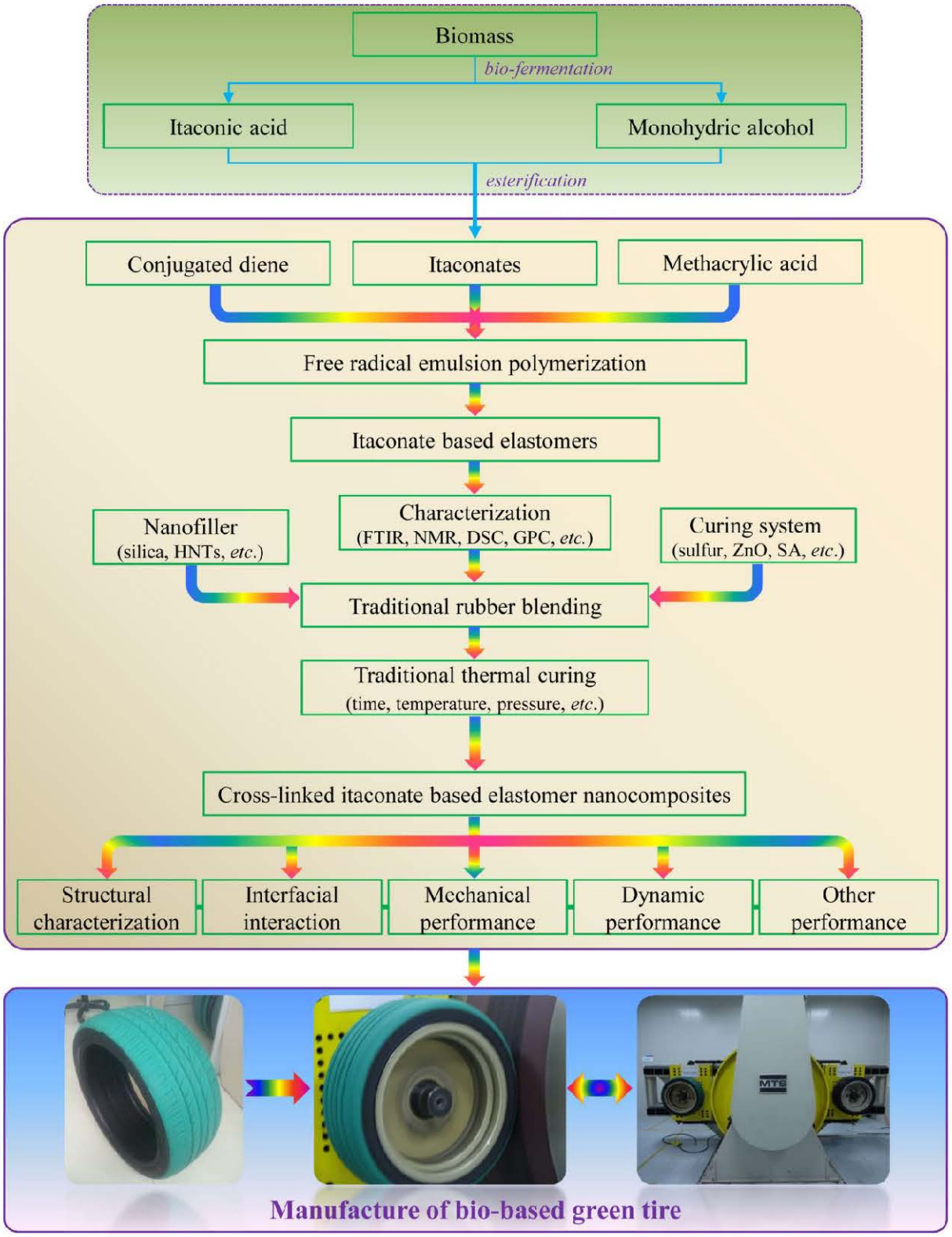

Figure 1-1. Framework of this thesis work.

Since the PDII elastomer was successfully synthesized, the key issue to be addressed was seeking practical application of this itaconate based engineering elastomer. Due to numerous ester groups in the PDII elastomer, it was expected to be a damping material. In this research, a polar and rigid organic molecule AO-80 was introduced into the PDII matrix to prepare PDII/AO-80 nanocomposites. In order to obtain molecular-level dispersion of AO-80, the PDII/AO-80 nanocomposites were prepared by melt blending technique above the melting temperature of AO-80. The extensive shearing associated with the high temperature mechanical kneading process could significantly promote the molecular-level mixing of the rubbery-state PDII molecules and the liquid-state AO-80 molecules. Part of the AO-80 molecules formed an AO-80-rich phase, but most of them dissolved in the PDII to form a molecular-level dispersion in amorphous form. The results of FTIR and DSC indicated that strong intermolecular interaction was formed between the PDII and the AO-80 molecules. Each PDII/AO-80 nanocomposite showed a single transition with a higher glass transition temperature and significantly higher loss tangent (tanδ) value than the neat PDII because of intermolecular interaction between the PDII and the AO-80 molecules. For instance, tanδ of PDII/AO-80 consisting of 100 phr AO-80 achieved 2.6 times as neat PDII.

A poly(diisoamyl itaconate-*co*-isoprene-*co*-methacrylic acid) (PDIM) elastomer with high molecular weight was synthesized by redox-initiated emulsion polymerization based on dibutyl itaconate, isoprene, and methacrylic acid, as shown in Fig. 1-2. Small quantities of methacrylic acid (1-5 wt.%) was used to introduce the carboxyl groups into the macromolecular chains. The yields of PDIM were over 70% after 12 hours in all runs. The PDIM elastomers had high number average molecular weight (>250 000 g/mol) and low glass transition temperatures (<-30^{o}C). The carboxyl contents in the PDIM elastomers were determined by butanone titration. With the increase of carboxyl content in the PDIM elastomers, the T_g was increased, with improved the physical properties and strong interfacial interaction between PDIM and silica. This resulted in a good dispersion of silica in the PDIM matrix, which might play a crucial role in reducing the rolling resistance. However, the dynamic performance of the PDIM/silica nanocomposite indicated that they were not suitable for low rolling resistance tire tread.

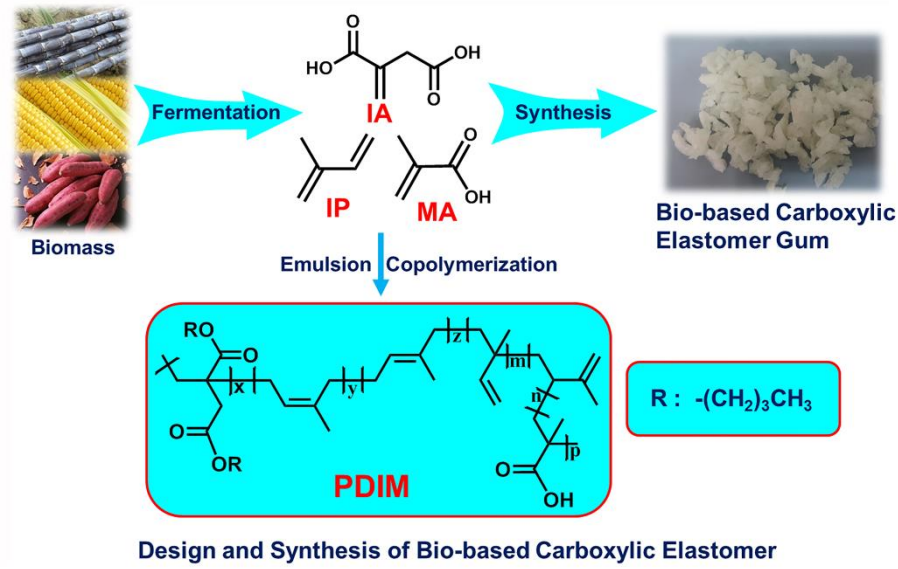

Figure 1-2. Design strategy for bio-based carboxylic elastomer.

Recently, it has been revealed that the energy dissipating mechanisms via sacrificial bonds are among the important factors which account for strong and tough attributes of natural materials. Inspired by the sacrificial bonding mechanisms, we developed PDIM/HNTs nanocomposites by co-coagulation of PDIM latex and HNTs aqueous suspension, followed by mechanical kneading with other rubber additives. The hydrogen bonds were confirmed at interface in the nanocomposites, as shown in Fig. 1-3. The hydrogen bonds played a sacrificial bonding role in the PDIM/HNTs nanocomposites. The investigation of the tensile fracture surface of the PDIM/HNTs nanocomposite revealed a mechanism responsible for improvement in mechanical properties which is composed of four steps: (1) alignment of the PDIM chains further orients the HNTs along the loading direction during the uniaxial stretching; (2) dissociation of the hydrogen bonds dissipates energy; (3) Coils of PDIM from the applied force by the hydrogen bonds are stretched to sustain a large deformation and dissipate energy; (4) finally, the HNTs are pulled out from or rupture at the tensile fracture surface of the PDIM/HNTs nanocomposites. Consequently, the strength and ductility of the nanocomposites are simultaneously improved without sacrificing the extensibility.

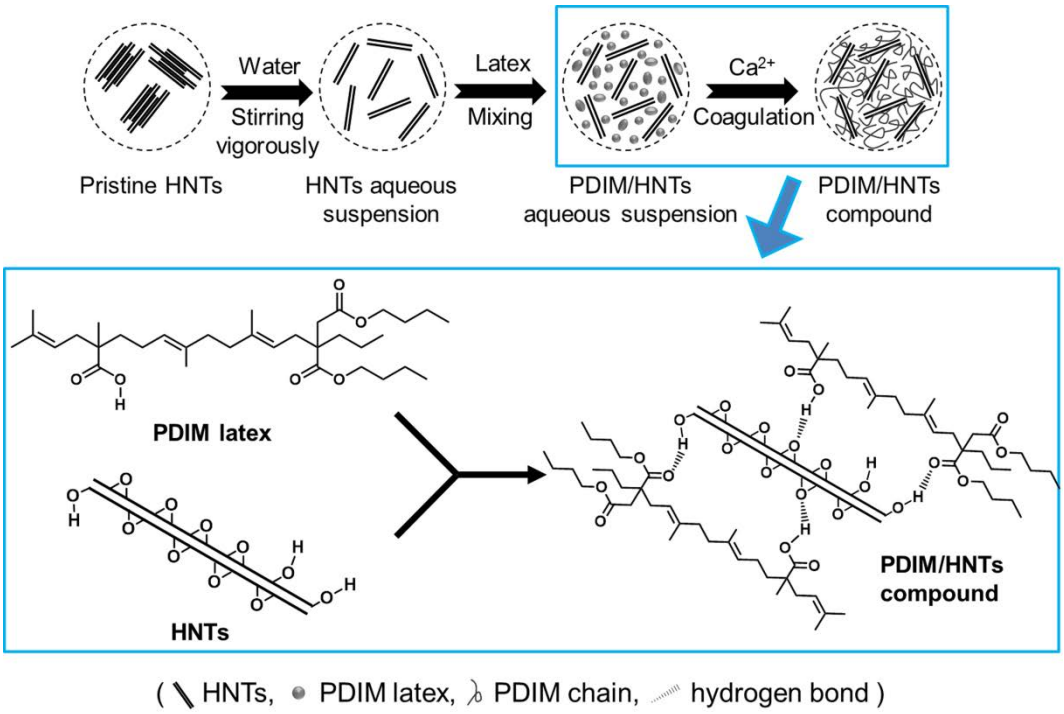

Figure 1-3. Illustration of the co-coagulation in the preparation of PDIM/HNTs compounds.

In order to obtain an ideal itaconate based elastomer for green tire tread, we synthesized PDIB elastomer by redox-initiated emulsion polymerization of dibutyl itaconate with butadiene. The microstructure of PDIB elastomer was confirmed by FTIR and NMR. The resultant copolymers had predominately *trans*- and *vinyl*-polybutadiene in their chains, a molecular weight from 236, 000 to 392, 000 g/mol, and a glass transition temperature from -42 to -72^{o}C, depending on the feed weight percentage of butadiene. The reactivity ratios of dibutyl itaconate and butadiene determined by the classical Fineman-Ross method and Kelen-Tüdös one indicated a non-ideal copolymerization behavior with an azeotropic point at 0.383. The monomer sequence distribution indicated that butadiene could undergo self-propagation to form long flexible segments while dibutyl itaconate preferred to form short sequences with isolated, diad or triad moieties. The mechanical properties of PDIB could compete with or even surpass those of traditional synthetic rubbers. By combining a molecular structural design with non-petroleum based silica and *in-situ* modification technique to tune the viscoelastic properties of the PDIB elastomer nanocomposites, we have successfully manufactured low roll-resistance green tires based on PDIB/silica nanocomposites. The tire based on PDIB/silica nanocomposite was tested using a MTS tire rolling resistance

measurement system. The rolling resistance coefficient was 7.7 kg/ton and rated as a class "B" according to the EU Tire Labelling Regulation 1222/2009.

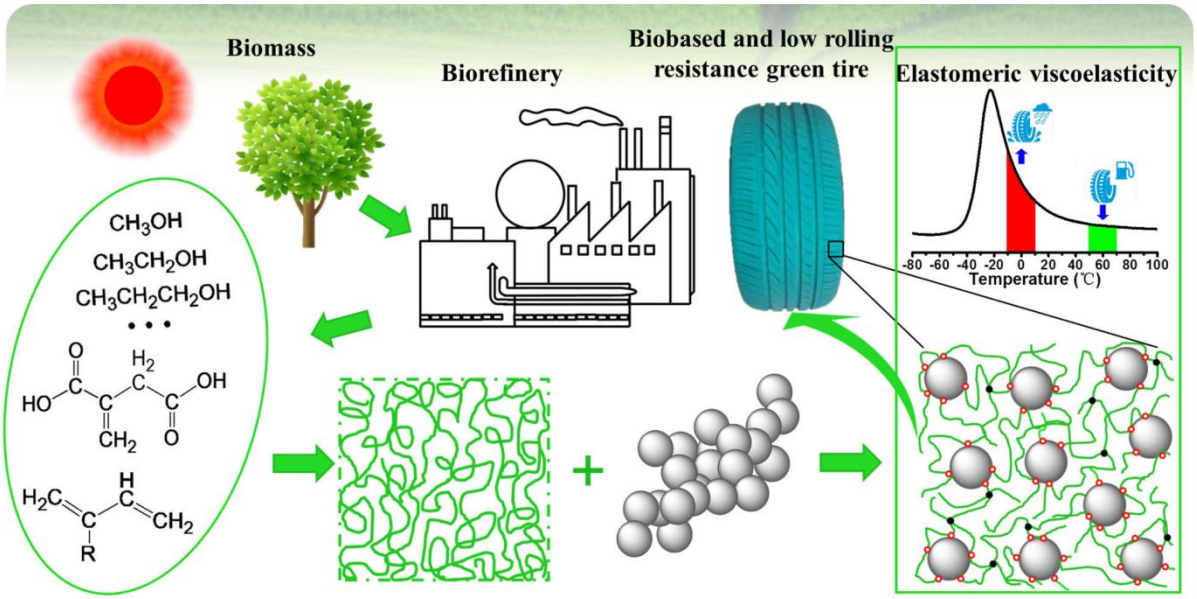

Figure 1-4. The integrated biomass-based chemicals with chemosynthesis-bio-based low rolling resistance elastomer pathway for sustainable resources and environmental protection.

1.4 Thesis organization

The chapters of this thesis are organized as follows.

Chapter 1 includes general introduction, research objectives of this thesis, research contents and main results of this thesis, and thesis organization.

Chapter 2 is a brief overview of bio-based chemicals and bio-based elastomers.

Chapter 3 is a published article about the preparation and evaluation of PDII/AO-80 nanocomposites.

Chapter 4 are two published articles about the preparation and performance of PDIM elastomer and its nanocomposites. The first article focuses on the synthesis of PDIM elastomer and the interfacial interaction between PDIM and silica, and the second one focuses on the preparation and properties of PDIM/HNTs nanocomposites, in which hydrogen bonds paly a sacrificial bonding role.

Chapter 5 includes two parts about the preparation and performance of PDIB elastomer and its nanocomposites. The first part focuses on the synthesis and chemical structure of PDIB elastomer, and the second one on the performance of PDIB/silica nanocomposites and the manufacture of bio-based green tire.

Chapter 6 gives a critical review on the progress on bio-inspired sacrificial bonds in polymeric materials. This review will serve as a guide to engineer sacrificial bonds into itaconate based elastomers with high strength and toughness.

Chapter 7 provides conclusions about the thesis work that could be useful for sustainable development of rubber industry all over the world, on the one hand, and perspectives for future work, on the other hand.

Chapter 2 State of the art

The state of the art intends to give the reader an overview covering the areas of interest to our research, divided in three parts. In the first part, we present the development of bio-based chemicals which are potential to replace today‘s petroleum-based chemicals. Especially, bio-based itaconic acid and bio-based monohydric alcohols are described briefly. In the second part, we present the progress in bio-based elastomers which are prepared from bio-based chemicals. In the third part, we summarize the development of bio-based elastomers.

2.1 Bio-based chemicals

Chemicals are used in numerous applications ranging from materials to pharmaceuticals, and are still often made from fossil resources. We have a wonderful opportunity to learn from the mistakes, as well as the successes, of close to a century of fossil exploitation, two centuries of industrialization and many more centuries of living off the land. These must all come together and work together in a sustainable manner if our standards of living in modern society are to be maintained. It is critical for us to balance the growing need of chemical products mainly based on diminishing fossil resources and the alarming level of pollution to land, sea and air inexorably created by our exploitation of those resources. Driven especially by the rapid depletion and limited supplies of non-sustainable fossil resources and by the concerns over oil price, climate change, and environmental impact, a growing demand to make chemical production more sustainable and green is widespread, thus calling for an integration between energy, resources, sustainable development, environmental and societal benefits, and technological and economic issues. [1-3] The use of renewable feedstocks, *e.g.* biomass, is one of the guiding principles of sustainable and green chemistry, introduced in the early 1990s by the US Environmental Protection Agency (http://www.epa.gov/), in order to promote chemical technologies that reduce or eliminate the generation of hazardous substances in the design, manufacture and use of chemical products.

Biomass refer to abundant carbon-neutral recyclable or renewable organic substances with the potential to replace fossil feedstocks as a carbon source, such as crops, trees, other plants or residues, and animal waste. Cycle carbon system based on biomass resources is more sustainable and greener than that based on fossil resources. [4] According to a review on conversion of biomass into chemicals, [6] the most common production scheme of bio-based chemicals is the conversion of carbohydrates into platform molecules via depolymerization and/or bio-fermentation processes. These platform molecules are then converted into target bio-based chemicals, which are used as building blocks for the synthesis of polymers. The conversion process flow of bio-based chemicals is schematically shown in Fig 2-1. [6] Bio-based chemicals offer a sustainable alternative to fossil-based chemicals. Technically, almost all organic materials prepared from fossil-based chemicals could be substituted by their bio-based counterparts. However, bio-based chemicals represent only a minor market share at the moment, mainly due to still high production cost. The global market share of bio-based chemicals is estimated to increase from 3-4 wt.% in 2010 to 30 wt.% in 2050. [5] By then, a considerable amount of fossil-based chemicals will be replaced by bio-based ones to produce sustainable chemical products.

The progress in bio-based chemicals has been given through several authoritative reviews. [6-9] Considering the vast range of bio-based chemicals, industrial production and scientific research are currently focusing on high value-added and low volume bio-based chemicals. The US Department of Energy reported a first group of high value-added bio-based chemicals in 2004, known as ―top 12" platform chemicals, including succinic, fumaric and malic acids, 2,5-furan dicarboxylic acid, 3-hydroxypropionic acid, aspartic acid, glucaric acid, glutamic acid, itaconic acid, levulinic acid, 3-hydroxybutyrolactone, glycerol, sorbitol, and xylitol/arabinitol. [10] In 2010, the ―top 12" platform chemicals was updated to ―top 10" platform chemicals which are ethanol, furans, glycerol and derivatives, biohydrocarbons, lactic acid, succinic acid, hydroxypropionic acid/aldehyde, levulinic acid, sorbitol, and xylitol. [11] These promising bio-based platform chemicals included in the ―top 12" and the ―top 10" collections can transform into a series of derivatives by using enzymes, cells, or inorganic catalysts, such as alcohols, carboxylic acids, esters, and alkenes. Recently, a growing interest in synthesis of polymers from these bio-based chemicals and their derivatives increased rapidly within academia and industrial companies. In this study, bio-based elastomers were prepared through emulsion polymerization of dibutyl itaconate with conjugated dienes. The dibutyl itaconate, a derivative of itaconic acid, is obtained through esterification of bio-based

itaconic acid with bio-based *n*-butanol, while the conjugated dienes such as isoprene and butadiene are potentially obtained from biomass feedstocks.

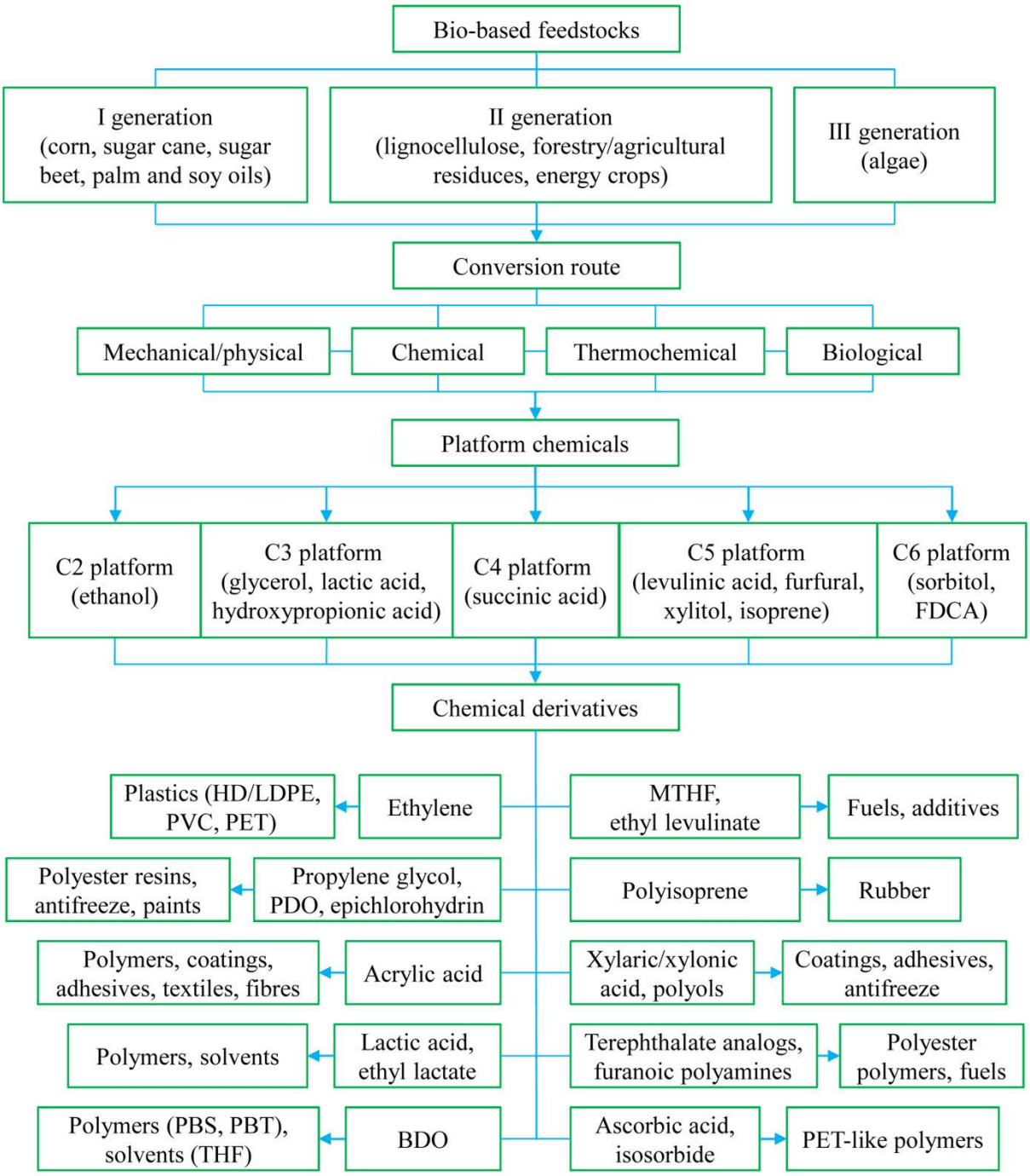

Figure 2-1. Schematic process flow of bio-based chemicals (FDCA, 2,5-furandicarboxylic acid; HDPE, high density polyethylene; LDPE, low density polyethylene; PVC, polyvinylchloride; PET, polyethylene terephthalate; PDO, 1,3-propandiol; BDO, 1,4-butanediol; PBS, polybutylene succinate; PBT, polybutylene terephthalate; THF, tetrahydrofuran; MTHF, methytetrahydrofuran). [6]

Itaconic acid

Itaconic acid, or methylene succinic acid, is one of the most promising bio-based chemicals. Itaconic acid was first reported in 1836 as a product of citric acid distillation. [12] The first method for production of itaconic acid is chemical synthesis routes. However, none of the chemical synthesis routes can compete with biosynthesis routes, *e.g.* bio-fermentations by various microbial strains. Therefore, none of the chemical synthesis routes were practiced in industry. The first bio-fermentation by fungi based on carbohydrates was reported in 1932, [13] where itaconic acid was isolated from the growth medium of *Aspergillus itaconicus*. Later studies showed the *Aspergillus terreus* strains are more suitable for biosynthesis of itaconic acid. More information about biosynthesis of itaconic acid can be found in several reviews [14-16]. Itaconic acid was listed as one of the ~~"t~~op 12" most promising bio-based platform chemicals in 2004 by the US Department of Energy. Although itaconic acid was removed from the updated ~~"t~~op 10" list in 2010, [11] it has been shown a scientific spotlight all over the world. A report by Global Industry Analysts Inc. in 2011 forecasted the global market of itaconic acid will reach over US$398.3 million by the year 2017. [17] The producers of the itaconic acid are mainly in several countries such as US, Russia, Japan, and China. Globally, at least 80,000 tons of itaconic acid will be produced annually. The price per kilogram for itaconic acid decreased from US$4 in 2001 [14] to US$2 in 2009 [15], and is current stable in the region of US$1.5 to US$2.5.[16] The growing market of itaconic acid and its derivatives will facilitate further increase of its production capacity and decrease of its price.

Itaconic acid belongs to C5 bio-based platform chemicals. As an unsaturated dicarboxylic organic acid, itaconic acid is capable of transforming into various derivatives, shown in Fig. 2-2. [10] Itaconic acid and its derivatives such as dialkyl itaconates are expected to replace acrylic or methacrylic monomer to synthesize polymers. The functional carboxylic groups allow itaconic acid to undergo polycondensation with diols and diamines to prepare polyesters and polyamides, respectively. By using double carbon bonds, itaconic acid can undergo free radical polymerization to prepare poly(itaconic acid). More commonly, dialkyl itaconate is used as substitute of itaconic acid to homopolymerize or copolymerize with other unsaturated monomer.

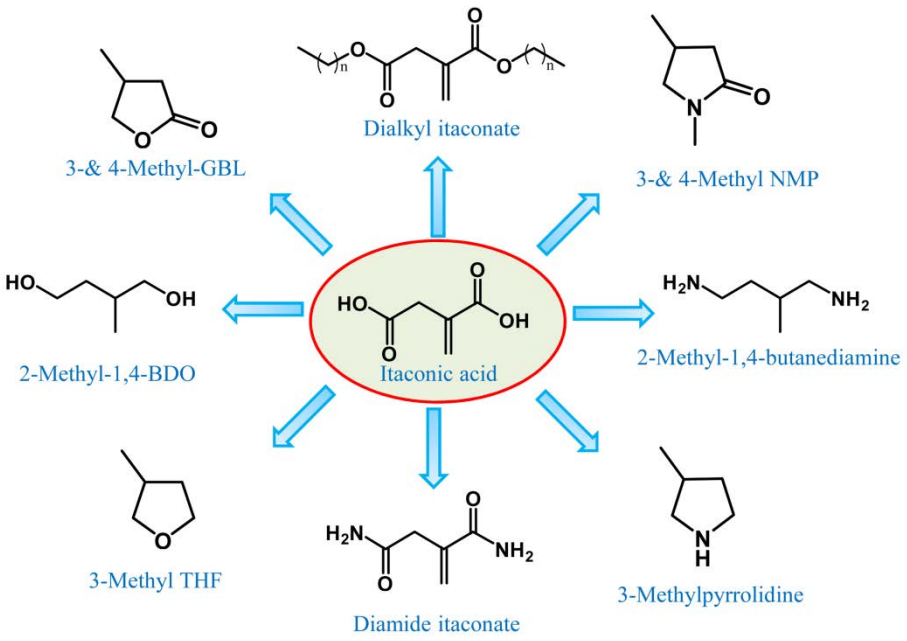

Figure 2-2. Itaconic acid chemistry to derivatives. [10]

Bio-based monohydric alcohols

Bio-based dialkyl itaconate is synthesized by esterification of bio-based itaconic acid and bio-based monohydric alcohols. Bio-based monohydric alcohols prepared by bio-fermentation include methanol, ethanol, *n*-propanol, *n*-butanol, isoamylol and so on. As the simplest saturated alcohol, methanol is an important organic chemical and raw material for the production of biodiesel. Bio-based methanol, known as wood alcohol, can derive from wood and lignin by destructive distillation. Ethanol fermentation, developed since ancient times, is still the most fermentation process in today‘s industry. Currently, ethanol is used in beverages and as solvent, fuel, and chemical intermediate. The bio-based ethanol can be derived from food carbohydrates such as glucose via pyruvate in an anaerobic fermentation process. The current researches of ethanol fermentation were focused on deriving from nonfood carbohydrates [18,19] and bio-based syngas [20,21]. There are two routes for the biosynthesis of *n*-propanol. One route is to convert 2-oxobutylrate into *n*-propanol via propyl aldehyde. [22, 23] 2-Oxobutylrate is a metabolite of biomolecules such as threonine and citramalate. [8] Another route is to dehydrate 1,2-propanediol into *n*-propanol via propyl aldehyde. 1,2-Propanediol can be produced by an anaerobic batch fermentation. [24] Bio-based *n*-butanol was discovered in the early 1860s by a so-called ABE (acetone-butanol-ethanol) anaerobic fermentation using glucose resource. [25] In the beginning of the 20th century, industrial ABE fermentation technology was developed to produce bio-based *n*-butanol and bio-based

acetone. Nowadays, commercial fermentative *n*-butanol with an annual production capacity of about 500,000 tons possesses a large market share. [26] In addition, bio-based 2-butanol [27,28] and bio-based isobutanol [22,29] can also be produced by bio-fermentation technology. Bio-based isoamylol can be extracted from the fusel oil, a byproduct of ethanol fermentation. It has been found more than 50% (v/v) of the fusel oil is isoamylol. [30-32] In the past, fusel oil only was used as fuel and solvent. In recent years, with the increase of bio-based ethanol production, many important fine chemicals have been derived from the fusel oil. Among these fine chemicals, isamylol is the most used with the largest output.

2.2 Bio-based elastomers

2.2.1 Bio-based elastomers for medical applications

Due to analogous mechanical performance and network structure between elastomers and human elastic tissues, elastomers have potential applications on biomedical fields. Recently, biomedical elastomers have been developed and reported all over the world. Wang *et al.* reported a tough biocompatible poly(glycerol sebacate) (PGS) elastomer synthesized by melt polycondensation of glycerol and sebacic acid. [33] This PGS elastomer exhibited excellent biocompatibility and biodegradability, and performed as well as poly(lactide-*co*-glycolide) which is widely applied in tissue engineering. [34] The PGS elastomer was expected to be applied in tissue engineering, drug delivery, and *in vivo* sensing. However, the inferior mechanical strength (0.5 MPa) and modulus (0.28 MPa) restricted its application as biomedical materials. Nijst *et al.* prepared photocurable elastomers by chemical modification of PGS with acrylate moieties (designated as PGSA). [35] The PGSA still exhibited inferior mechanical strength (0.05-0.5 MPa) and modulus (0.05-1.38 MPa). Yang *et al.* reported a polyester network poly(1,8-octane-diol-*co*-citric acid) (POC) with a controllable number of crosslinks for tissue engineering. [36] The mechanical strength of the POC elastomer reached up to 6 MPa. Cartilage tissue was successfully regenerated by chondrocyte implantation on a porous POC scaffold. [37] The POC elastomer exhibited good biocompatibility with various cells such as osteoblasts, myoblasts, and endothelial cells. [38-41] Furthermore, the blend film of POC with chitosan exhibited simultaneous improved mechanical and biological performance. [42] Ding *et al.* reported a groups of biodegradable poly(PEG-*co*-CA) (PEC) elastomers with various crosslinking degrees by polycondensation of poly(ethylene glycol)

(PEG) and citric acid (CA). [43] The mechanical strength and the modulus of the PEC elastomers ranged from 1.5 to 2.5 MPa and from 0.25 to 0.91 MPa, respectively.

It can be seen that the objective of these studies was to obtain biodegradable and biocompatible elastomers, which generally had inferior mechanical strength (typically below several MPa), high water absorption, and fast degradation. Moreover, the building blocks for these biomedical elastomers do not must be derived from bio-based chemicals, and degradation products of them must be nontoxic to human body.

2.2.2 Bio-based elastomers for engineering applications

In the past few years, more and more studies have been focused on bio-based elastomers for engineering applications in traditional rubber fields such as tire industry. Zhang‘s group defined the bio-based elastomers for engineering applications as bio-based engineering elastomers which should meet the following criteria: [44] (i) monomers should be obtained primarily from readily available and inexpensive renewable biomass feedstock; (ii) the chemical synthesized or biosynthesized elastomers should possess excellent environmental stability, a comparatively low swelling ratio in water and a particularly slow degradation rate; (iii) they should be compatible with traditional rubber processing, such as mixing, molding and curing; (iv) the prepared elastomers (reinforced or non-reinforced) should exhibit desirable mechanical properties, which are suitable for various engineering applications.

Bio-based polyester elastomers

Bio-based polyester elastomers for engineering applications refer to unsaturated polyesters which were synthesized by polycondensation of bio-based diacids and diols. Typically, this polyester elastomers were obtained from five bio-based chemicals including 1,3-propanediol, 1,4-butanediol, itaconic acid, sebacic acid, and succinic acid, which are produced based on biomass in large-scale. [44] The use of the five bio-based chemicals decreased the regularity of the polyester chains and therefore suppressed crystallization of the resultant polyesters. The sebacic acid was used to increase the flexibility of the polyester chains and decrease the density of the ester groups, resulting in low glass transition temperature (T_g) and good environmental stability. Itaconic acid provided pendent vinyl groups for subsequent crosslinking. The synthetic strategy of the bio-based polyester elastomers is shown in Scheme 2-1.

By controlling the synthesis conditions such as monomer molar ratio, catalyst amount, and reaction temperature, Wei *et al.* prepared the polyester elastomer with excellent comprehensive performance. [44] The number-average molecular weight (M_n) and the polydispersity index (PDI) of the polyester elastomer were 33,000 and 3.68, respectively, while the T_g of the polyester elastomer was -54^oC, lower than that of many conventional synthetic rubbers. The linear polyester chains could be transformed into a network structure by further crosslinking, which made up the defect of the relatively low M_n. This linear polyester elastomer was compatible well with traditional rubber processing. Besides, the bio-based polyester elastomer could be produced in large-scale using conventional polyester synthetic instruments and processing route. A pilot-scale product line with an annual production capacity of 100 tons has been built in Beijing University of Chemical Technology.

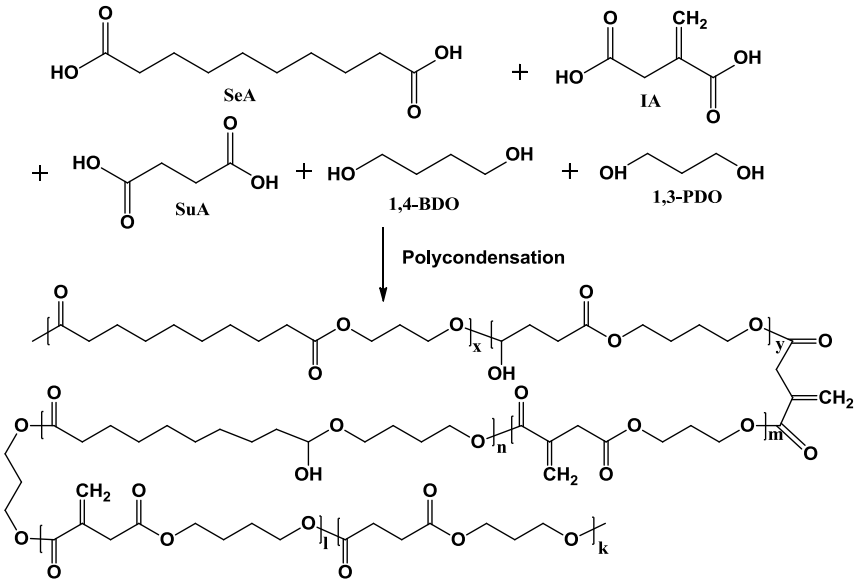

Scheme 2-1. Synthetic strategy for bio-based polyester elastomers.

Bio-based Elastomers from vegetable oils

As a natural and renewable resource, soybean oil is one of vegetable oil with large output. The use of soybean oil to prepare polymers is a hot topic of current researches. However, there are very few studies on elastomers based on soybean oil, mainly due to the fact that soybean oil is of triglyceride structures and therefore the polymers based on soybean oil is essentially thermosets and cannot be further processed. Wang *et al*. reported a bio-based elastomer poly(epoxidized soybean oil-*co*-decamethylene diamine) (PESD) by ring-opening polymerization of epoxidized soybean oil (ESO) with decamethylene diamine (DDA). [45] On the one hand, DDA underwent ring-opening reaction with epoxy groups of ESO to form

polymer chains. On the other hand, DDA underwent ammonolysis reaction with ester groups of ESO to break glycerol center, resulting in linear and processable soybean-oil-based elastomers. The synthetic strategy is shown in Scheme 2-2. The T_g of PESD ranged from -17 to -30^{o}C by adjusting the molar ratio of ESO to DDA. With the 1:2 molar ratio of ESO to DDA, the resultant PESD had a weigh-average molecular weight of 130,000 g/mol and a gel content of 6 wt.%, indicating good processibility. The PESD was cross-linked by succinic anhydride according to conventional rubber processing technique and had a mechanical strength of 8.5 MPa and an elongation at break of 200% without reinforcement. The PESD showed potential candidate for an engineering rubber. Recently, Wang *et al.* reported a sustainable thermoplastic elastomer derived from soybean oil monomers through atom transfer radical polymerization followed by chain extension. [46] This thermoplastic elastomer was cross-linked by ―click-coupling" the soft middle blacks using triazolinedione chemistry. The ―click-coupled" thermoplastic elastomer exhibited improved mechanical strength without sacrificing elongation at break and excellent elastic recovery property.

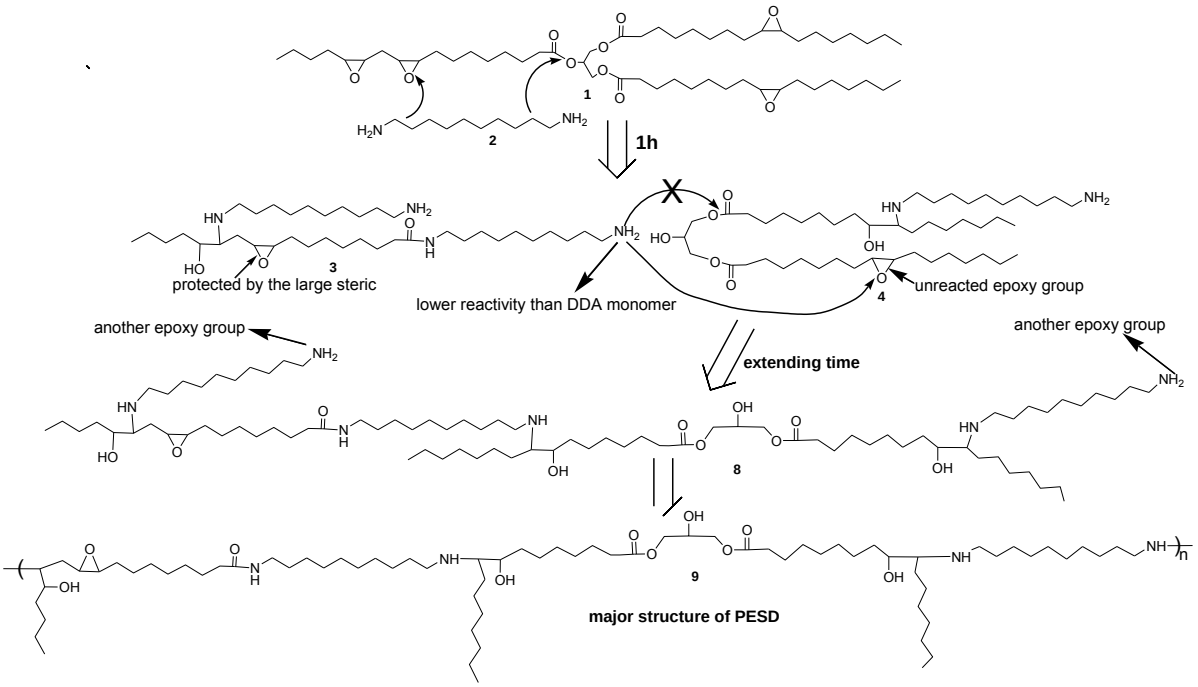

Scheme 2-1. Synthetic strategy for poly(epoxidized soybean oil-*co*-decamethylene diamine).

Bio-based elastomers form itaconic acid

Itaconic acid is widely used in preparation of polymers, for instance, it can used as a co-monomer to effectively improve the performance of the resultant polymers. It had been found

that the addition of a small amount of itaconic acid during the preparation of polyacrylonitrile (PAN) can reduce activation energy of the reaction and promote cyclization and crosslinking. [47] The melting temperature of PAN modified with itaconic acid (158^{o}C) was lower than that of unmodified PAN (186^{o}C) and that of PAN modified with methacrylic acid (164^{o}C). [48] According to the structure of itaconic acid, it can be used as a co-monomer to participate in the polycondensation to prepare polyesters. [49] Another approach for ~~"u~~se of itaconic acid" is radical homopolymerization or copolymerization of dialkyl itaconates with other unsaturated monomers.

Our previous study reported a cross-linkable, high molecular weight poly(diisoamyl itaconate-*co*-isoprene) (PDII) elastomer by redox-initiated free polymerization of diisoamyl itaconate with isoprene. [50] The diisoamyl itaconate was firstly prepared by esterification of bio-based itaconic acid and isoamyl alcohol, and then copolymerized with isoprene to synthesize the PDII elastomer, as shown in Scheme 2-3. The introduction of isoprene units in the PDII macromolecules not only increased the flexibility of the PDII chains and decreased the T_g of the PDII, but also provided double bonds for the further crosslinking. The reactivity ratios of diisoamyl itaconate and isoprene indicated that the two monomers tended to undergo copolymerization rather than homopolymerization. The number-average molecular weight of the PDII reached up to 352,000 g/mol with the PDI as 3.41 and the T_g of the PDII was -39^{o}C when the feed mass ratio of diisoamyl itaconate to isoprene was 4/1. The high molecular weight promised good mechanical properties while the low T_g allowed PDII as a elastomer in room temperature. The PDII was cross-linked by sulfur under conventional rubber processing technique and effectively reinforced by silica and carbon black. Recently, a bio-based poly(myrcene-co-dibuty itaconate) elastomer was developed by emulsion polymerization of bio-based β-myrcene with dibutyl itaconate. [51] However, the low molecular weight of this bio-based elastomer might limit its application for engineering fields.

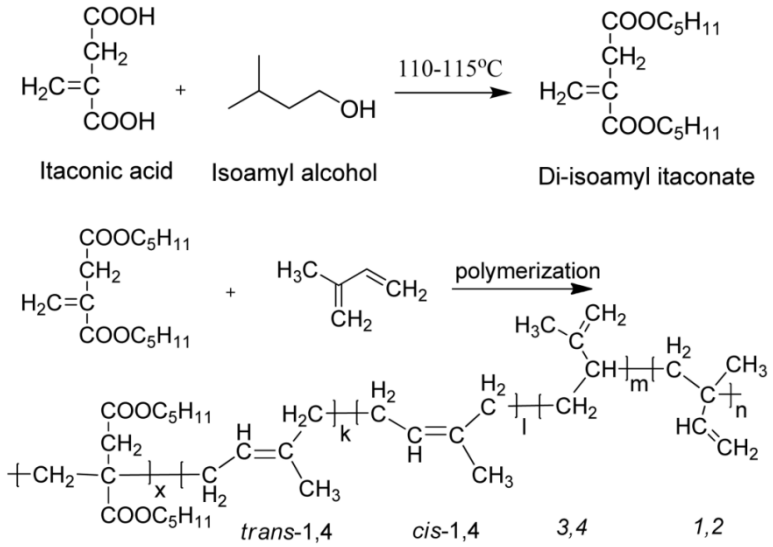

Scheme 2-3. Synthetic strategy for poly(diisoamyl itaconate-*co*-isoprene).

Conventional elastomers from bio-based chemicals

At present, some international companies such as Genencor, Amyris, Lanxess, Goodyear, and Michelin have developed bio-fermentation technologies for bio-based chemicals including alkenyl pyrophosphate, ethanol, propanol, butanol, and butanediol. These bio-based chemicals were further transformed into conventional building blocks for polymers, such as isoprene, butadiene, ethylene, and propylene. Conventional elastomers such as polyisoprene, polybutadiene, and ethylene-propylene elastomer could be derived from these bio-based building blocks.

Polyisoprene elastomer refers to solution-polymerized *cis*-1,4-polyisoprene, which is a substitute of natural rubber. Generally, isoprene is derived from petroleum-based resources. Besides, isoprene is widely found in nature and mainly refers to volatile C5 terpenoids discharged into atmosphere by some trees and herbs. However, it is very difficult to collect this terpenoids in the atmosphere as sustainable raw materials. Bio-based isoprene could be obtained by catalyzing dimethylallyl diphosphate (DMAPP) with isoprene synthase, where pyrophosphoric acid is released. The intermediate DMAPP could be obtained through two biosynthetic routes, namely, mevalonate (MVA) route in eukaryotic and prokaryotic cells [52] and 5-methylerythritol phosphate (MEP) route in prokaryotes and plants [53]. With the rapid development of biocatalysis, it is a feasible technology to prepare isoprene by bio-fermentation. Bio-fermentation is based on sugar as carbon resource and produce bio-based

isoprene through MVA or MEP routes under the help of microorganisms, [54,55] shown in Scheme 2-4.

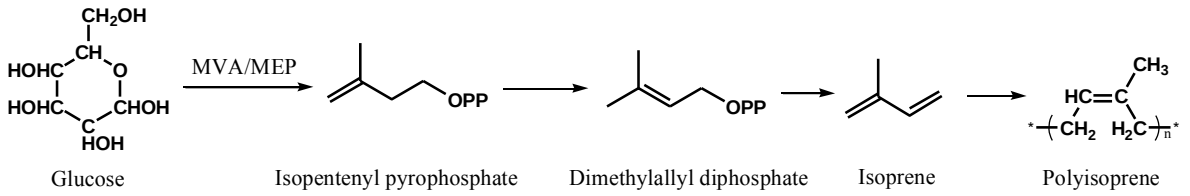

Scheme 2-4. Synthetic strategy for bio-based polyisoprene elastomer.

Genencor and Goodyear announced the formation of a consortium in 2010 to develop an integrated bio-fermentation, recovery and purification system for the production of bio-based isoprene from carbohydrates and further synthesize polyisoprene. Amyris and Michelin also have signed an agreement in 2011 to develop bio-based isoprene. Amyris has commercialized farnesene by mature technology, which can also be used to convert carbohydrates into isoprene.

Bio-based ethylene-propylene elastomer (EPDM) can be prepared by copolymerization of bio-based ethylene with propylene. Bio-based ethylene was produced by catalytic dehydration of bio-based ethanol. The catalysts for dehydration of ethanol included alumina, zeolite, heteropoly acid and molecular sieve. [56] Currently, bio-based ethanol was mainly prepared by bio-fermentation of sugar (sugar cane, beets, *etc.*) or by hydrolysis of starch (corn, potatoes, cassava, *etc*.). Bio-based propene was produced by catalytic dehydration of isopropanol which derived from bio-based acetone. [57,58] The bio-based EPDM was synthesized from bio-based ethylene and propene, as shown in Scheme 2-5.

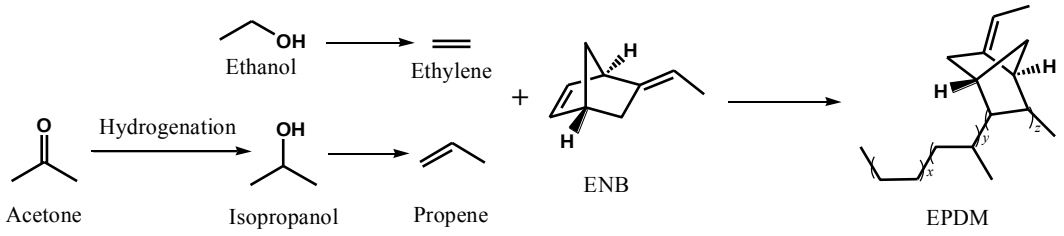

Scheme 2-5. Synthetic strategy for bio-based EPDM.

Lanxess Company is conducting an industrialized attempt to produce bio-based EPDM from bio-based ethylene at the EPDM plant in Triunfo, Brazil. The first batch of bio-based EPDM production is expected to reach up to hundreds of tons annually. In addition, Lanxess

Company has announced that bio-based isobutylene has been successfully produced in pilot-scale and has synthesized butyl rubber from the bio-based isobutylene. [59] In this way, Lanxess's butyl rubber production can significantly reduce carbon emission and the carbon emission by 2025 is expected to be reduced 25% compared with that in 2002.

The key for preparation of bio-based *cis*-polybutadiene elastomer is how to obtain bio-based butadiene. Bio-based butadiene can be derived from bio-based ethanol or bio-based 2,3-butanediol. [60] In recent years, the production of 2,3-butanediol by bio-fermentation based on glucose has become a new spotlight in bio-energy field. [61] The bio-based 2,3-butanediol can be further transformed into butadiene. The synthetic strategy for bio-based polybutadiene is shown in Scheme 2-6.

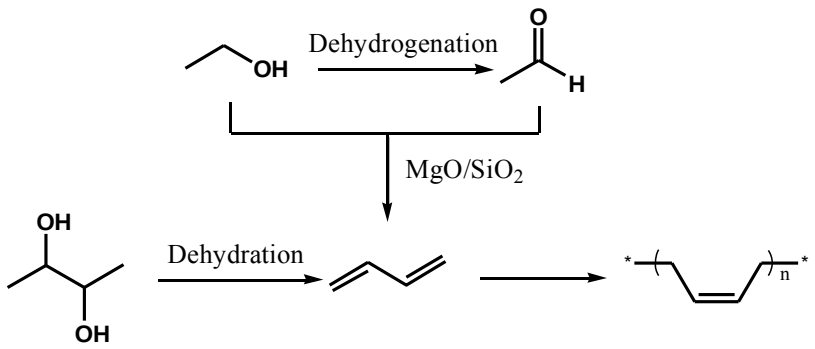

Scheme 2-6. Synthetic strategy for bio-based *cis*-polybutadiene.

Bio-based polyurethane elastomers for engineering applications

Polyurethane (PU) elastomer is widely used in biomedical engineering, industrial products, defensing products and so on because of its excellent mechanical properties, abrasion resistance, high elasticity, biocompatibility, oil resistance and chemical resistance. With the development of bio-based chemicals and biotechnology, scientists focused on the preparation of bio-based PU elastomers from plant oils such as soybean oil and castor oil. Vegetable oil is a renewable resource with low price. The preparation of PU elastomers from vegetable oil not only meets the environmental requirement, but also has good chemical and physical properties. The plant oils were incorporated into PU elastomers as a soft segment. Sonnenschein et al. reported a high-performance bio-based PU elastomer in which a blend of conventional polyester polyols with seed-oil based polyester polyols was used as soft segments. [62] Recently, jatropha oil based polyol was used to react with dipheylmethane-4,4'-diisocyanate (MDI) and toluene-2,4-diisocyanate (TDI) to prepare bio-based PU

elastomer, which exhibited comparable mechanical properties to those of polycaprolactone-based PU elastomer. [63] Lee et al. reported a synthesis route to non-isocyanate PU elastomer from lignin and soybean oil. [64] The synthetic strategy is shown in Scheme 2-7. The tensile strength of the non-isocyanate PU elastomer increased with the lignin content and reached up to 1.4 MPa.

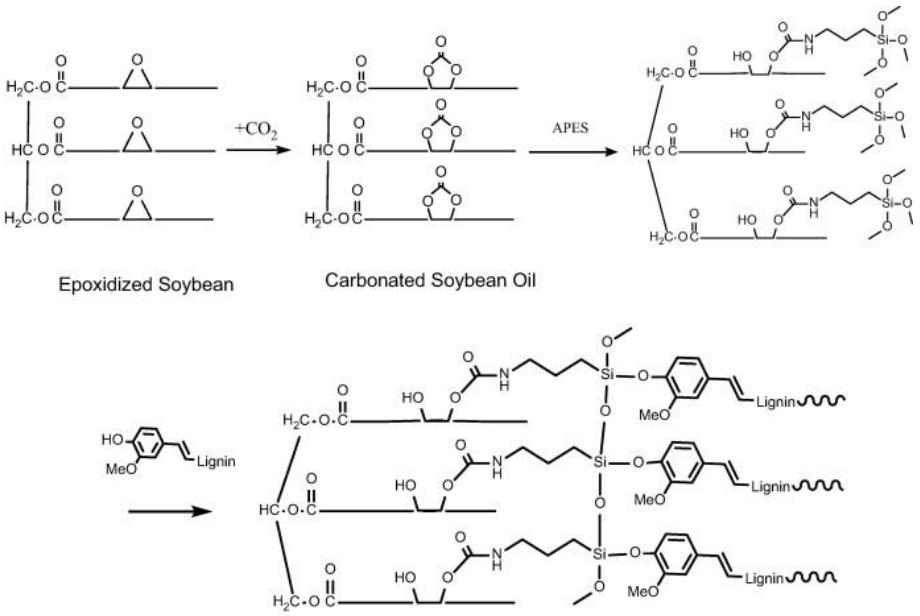

Scheme 2-7. Synthetic strategy for non-isocyanate polyurethane elastomer. [64]

2.3 Conclusions and perspectives

To meet the concepts of green chemistry and sustainable development, more and more material scientists designed and synthesized polymers from biomass resources. As an important renewable resource, biomass can be covert into biofuel and bio-based chemicals by biosynthetic technology. Several reviews have given in-depth overview on conversion of biomass into bio-based chemicals. [6-9] Bio-based elastomers have been developed from these bio-based chemicals in the past decades. The research on bio-based medical elastomers has made significant progress. The bio-based medical elastomers were focused on their synthesis process and their functional properties such as biodegradable property, surface property, and cytotoxicity. The application of the bio-based medical elastomers requires in-depth cooperation of researchers from material and medical fields. Therefore, in-depth cooperation of the researchers has become the key to further development of bio-based medical elastomers. As the next generation of engineering elastomer, bio-based elastomers have been developed all over the world. Bio-based elastomers with new structures, such as

polyester bio-based elastomer, itaconic acid-based elastomer, and soybean oil-based elastomer, have been successfully synthesized using low-cost bio-based chemicals which can produced by mature bio-fermentation technology. The difficulties of the research on these bio-based engineering elastomers are improvement of their properties and development of their applications. Some bio-based conventional elastomers have also been developed from fermentative ethylene, propylene, butadiene, and isoprene. The bio-based conventional elastomers exhibited identical performance as that of the conventional elastomers and could directly replace the conventional elastomers. However, the high cost and the low productivity of these fermentative monomers limit the development of bio-based conventional elastomers. Bio-based medical elastomers and bio-based engineering elastomers have a bright future, which are worthy of further in-depth research and investment.

Chapter 3 Feasibility of itaconate based elastomers as damping materials

Itaconate based elastomers might have excellent damping performance due to numerous polar ester groups in their chains. In order to explore the feasibility of itaconate based elastomers as damping materials, we developed and evaluated crosslinked hybrids (or nanocomposites) of polu(diisoamyl itaconate-*co*-isoprene) (PDII) and 3,9-bis[1,1-dimethyl-2{β-(3-tert-butyl-4-hydroxy-5-methylphenyl)propionyloxy}ethyl]-2,4,8,10-tetraoxaspiro[5,5]-undecane (AO-80). In order to achieve molecular-level dispersion of AO-80 in PDII matrix, melt blending technique was used to prepare the PDII/AO-80 hybrids. The interfacial interaction between PDII and AO-80 was investigated by FT-IR, DSC, XRD, and SEM. The damping performance of PDII/AO-80 hybrids was evaluated by studying DMTA results. The mechanical properties of PDII/AO-80 hybrids were also given in this chapter.

Preparation and intermolecular interaction of bio-based elastomer/hindered phenol hybrid with tunable damping properties

Abstract: In this research, crosslinked hybrids of a newly invented bio-based elastomer poly(di-isoamyl itaconate-*co*-isoprene) (PDII) and 3,9-bis[1,1-dimethyl-2{β-(3-tert-butyl-4-hydroxy-5-methylphenyl)propionyloxy}ethyl]-2,4,8,10-tetraoxaspiro[5,5]-undecane (AO-80) were designed and prepared by the mechanical kneading of the PDII/AO-80 hybrids at a temperature higher than the melting point of AO-80, followed by the crosslinking of PDII during the subsequent hot-pressing/vulcanization process. The microstructure, morphology, and mechanical properties of the hybrids were systematically investigated in each preparation stage by using DSC, FTIR, XRD, SEM, DMTA, and tensile testing. Part of the AO-80 molecules formed an AO-80-rich phase, but most of them dissolved in the PDII to form a very fine dispersion in amorphous form. The results of FTIR and DSC indicated that strong intermolecular interactions were formed between the PDII and the AO-80 molecules. Each PDII/AO-80 crosslinked hybrid showed a single transition with a higher glass transition temperature and significantly higher loss value (tanδ) than the neat PDII because of intermolecular interactions between the PDII and the AO-80 molecules. For instance, tanδ of PDII/AO-80 consisting of 100 phr AO-80 achieved 2.6 times as neat PDII. The PDII/AO-80 crosslinked hybrids with applicability at room temperature are potential bio-based damping materials for the future.

Keywords: bio-based material; elastomer; hybrid; damping properties

1 Introduction

Vibration and noise often lead to undesirable consequences such as unpleasant noise, fatigue and failure of structures, decreased reliability, and degraded performance [65]. Rubber is commonly used in controlling noise and vibration because of its high damping property. The viscoelastic properties of rubbers make them ideally suited for use as effective damping materials because of their ability to dissipate mechanical energy [66, 67]. Based on the damping theory [68-70], the damping properties can be determined by dynamic mechanical testing. The loss tangent (tanδ) and the loss modulus (G″) are measures of damping, which requires the transformation of mechanical energy into heat. Thus, the damping characteristics of rubbers are dependent upon the intensity and breadth of the tanδ or the G″ peaks at the applicable temperature. The damping properties of rubbers are dominated by the glass transition. Typically, the temperature range for efficient damping of known rubbers is about 20-30^{o}C around the glass transition temperature. The glass transition can be broadened or shifted by the use of plasticizers or fillers, blending, grafting, copolymerization, crosslinking, or the formation of interpenetrating polymer networks (IPNs) [71-78]. But it is hard to obtain a damping material with a high tanδ value and a wide temperature range for damping properties at the same time.

Hybrid materials are a type of multiphase materials in which the dimension of at least one phase is on the nano or even molecular scale. The nanophase interacts with other phases through various nanoscale chemical bonding and physical absorption phenomena [79]. The hindered phenol 3,9-bis[1,1-dim ethyl-2-{b-(3-tertbutyl-4-hydroxy-5-methylphenyl)propionyloxy}ethyl]-2,4,8,10-tetraoxaspiro-[5,5]-undecane (AO-80) was introduced into various polymeric matrices to prepare hybrids that exhibited damping properties. Figure 3-1 shows the chemical structure of AO-80, which includes many hydroxyl and ester groups. Compared with neat chlorinated polyethylene (CPE), the CPE/AO-80 hybrid exhibited a much higher dynamic mechanical loss [80, 81]. Furthermore, AO-80 also can be used to improve the damping properties of rubbers. The binary hybrid damping materials of acrylic rubber (ACM) and nitrile butadiene rubber (NBR) with AO-80 were prepared by Wu et al. [82] and Zhao et al. [83], respectively. The ACM/AO-80 hybrid showed only one relaxation peak, which is larger than that of pure ACM [82]. Interestingly, the damping properties and the static mechanical performance of pure NBR were both improved by blending NBR with AO-80 because of the strong intermolecular interactions between the AO-80 and the NBR molecules [83].

In recent years, many researchers focused on the transformation of biomass into chemicals [84-87] and the synthesis of bio-based monomers into polymers [88-93]. Monomers that come from biomass directly and indirectly, such as vegetable oils, lactic acid, and itaconic acid, have been used to synthesize various polymers. These polymers are commonly known as bio-based materials and are expected to replace polymers based exclusively on petrochemical feedstock. Recently, we have reported on a series of new bio-based engineering elastomers (BEE) based on bio-based monomers [44,45,50,94-98]. Four primary criteria for BEE have been introduced first by our group [44]. According to the criteria, large-scaled bio-based monomers, such as sebacic acid, itaconic acid, succinate acid, 1,3-propanediol, 1,4-butanediol, and vegetable oils, were chosen to generate polyester-typed BEE (PE-BEE) [44], poly(di-alkyl itaconate-*co*-isoprene)-typed BEE (PDII) [50], and poly(epoxidized soybean oil-*co*-decamethylene diamine)-typed BEE (PESD) [45], all of which are linear and noncrystalline elastomers with low glass transition temperatures (T_g) and crosslinkable groups. These new elastomers exhibit physical and mechanical properties that are comparable with those of commercially available elastomers, and may replace petroleum-based rubbers in many applications.

In our previous studies, a novel crosslinkable, high molecular weight poly(diisoamyl itaconate-*co*-isoprene) (PDII) elastomer was prepared from itaconic acid, isoamyl alcohol, and isoprene by redox emulsion polymerization [50]. Carbon black (CB) and silica were used as fillers to reinforce the elastomer, and the dispersion of silica in the silica/PDII composites was more homogenous than that of CB in the PDII/CB composites because of the formation of hydrogen bonds between the silica silanols and ester groups attached to the PDII backbone [96]. The ester groups directly attached to the polymer backbone have already been found to make a significant contribution to the high damping of these polymeric materials [99]. Thus, the PDII elastomers with appropriate compositions are expected to exhibit good damping abilities.

The aim of this study was to prepare, characterize, and evaluate PDII/AO-80 crosslinked hybrids with expected damping performance. We supposed that the ester groups in the PDII chains can form intermolecular interactions (possibly hydrogen bonds) with the phenolic hydroxyl groups in the AO-80 molecules. In addition, we believed that sporadic AO-80-rich phases exist in the PDII/AO-80 crosslinked hybrids because of the intermolecular interactions of AO-80 with itself. Figure 3-1(*c*) shows two kinds of potential H-bonds and the AO-80-rich phases in the PDII/AO-80 cross-linked hybrids. The first kind refers to the H-bonds$_{(a)}$ between

the phenolic hydroxyl groups -OH of AO-80 (denoted by 1 and 2 in Fig. 3-1(*a*)) and the carbonyl groups -C=O of PDII (denoted by 5 and 6 in Fig. 3-1(*b*)). The second kind refers to the H-bonds$_{(b)}$ between the phenolic hydroxyl groups -OH of AO-80 (denoted by 1 and 2 in Fig. 3-1(*a*)) and the carbonyl groups -C=O of AO-80 (denoted by 3 and 4 in Fig. 3-1(*a*)). These two kinds of H-bonds formed a network, as shown in Fig. 3-1(*c*). The intermolecular interactions will enhance the intermolecular friction and result in large energy consumption during dynamic deformations. Thus, the PDII/AO-80 crosslinked hybrids will exhibit excellent damping performance. Four stages were adopted in the preparation of the NBR/AO-80 crosslinked hybrids [83]. We improved the second stage of the preparation by blending the PDII/AO-80 uncross-linked hybrids in a Haake mixer at 135^{o}C instead of kneading the hybrids on a two-roll mill at 135^{o}C. The PDII/AO-80 uncross-linked hybrids become viscous fluids at 135^{o}C and cannot be effectively kneaded on the two-roll mill. However, the PDII/AO-80 uncross-linked hybrids, even in the state of viscous fluid, can be kneaded in the sealed chamber of the Haake mixer. During the kneading of PDII/AO-80 uncross-linked hybrids at 135^{o}C, the AO-80 molecules were not only melted but also dispersed well in the PDII. The structure and morphology of the PDII/AO-80 hybrids in each preparation stage were systematically investigated, and the static and dynamic mechanical properties of the crosslinked hybrids were evaluated. The results indicated that PDII/AO-80 crosslinked hybrids were successfully prepared and exhibited high dynamic mechanical loss values. The PDII/AO-80 crosslinked hybrids with applicability at room temperature are potential bio-based damping materials for the future and are expected to replace the petroleum-based damping materials.

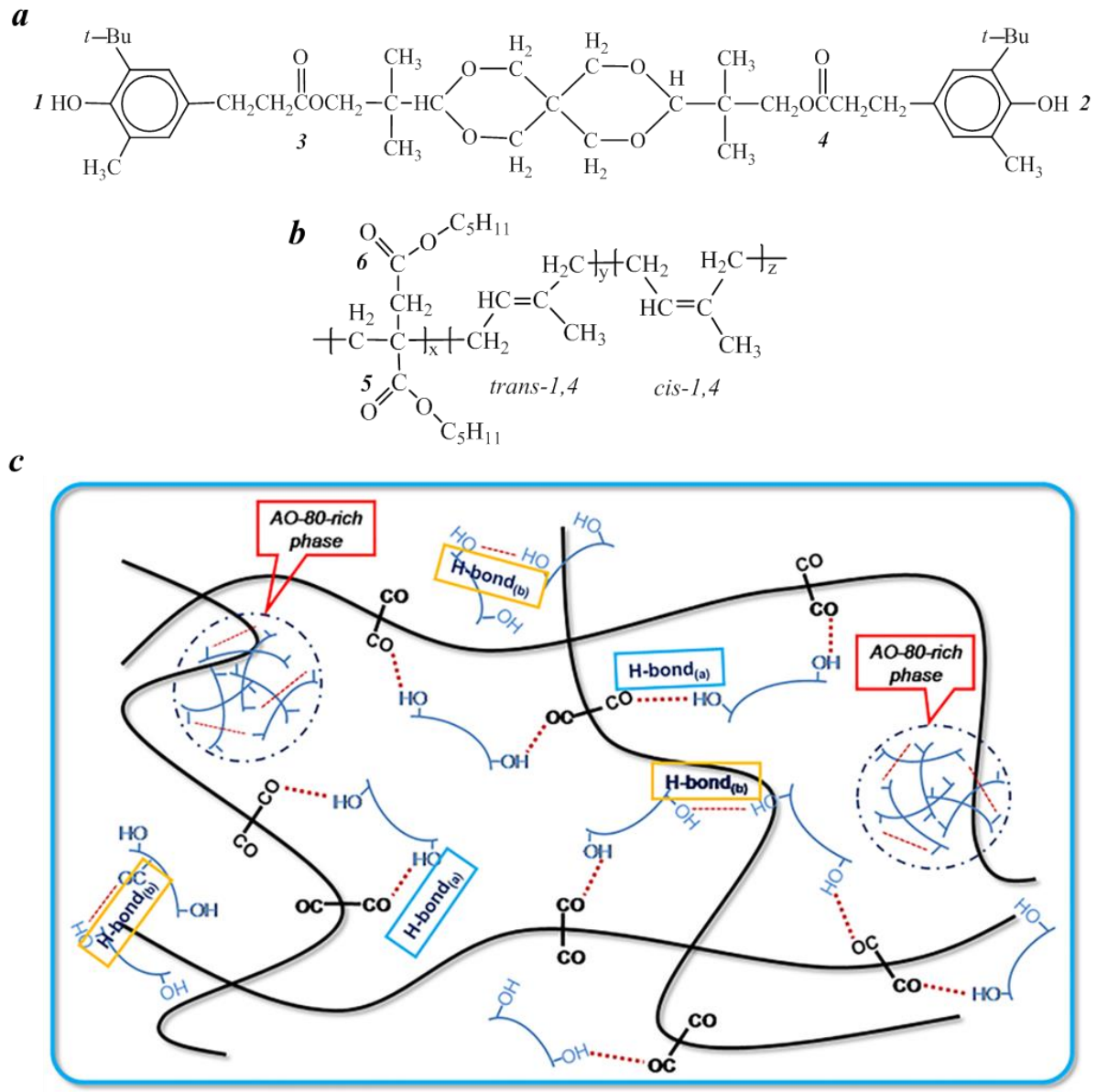

Figure 3-1. Molecular structures of (*a*) AO-80 and (*b*) PDII. (*c*) Possible H-bond$_{(a)}$ and H-bond$_{(b)}$ in hybrids, with black thick lines, blue short lines, and red dashed lines denoting PDII molecules, AO-80 small molecules, and H-bonds, respectively.

2 Experimental

2.1 Materials

The bio-based PDII elastomer, which was synthesized by redox emulsion copolymerization in our lab, consisted of 80 wt.% di-isoamyl itaconate and 20 wt.% isoprene [50]. AO-80 (ADK-ATAB-AO-80) in the form of crystalline powder was provided by Asahi Denka Co. Ltd.

(Tokyo, Japan) and was used without further purification. All other chemicals and ingredients were commercially available and were used without further purification.

2.2 Preparation of PDII/AO-80 hybrids

PDII/AO-80 crosslinked hybrids were prepared according to the following procedure: (1) After the prepared PDII was kneaded on a 6-inch two-roll mill at room temperature for 2 min, AO-80 (crystalline powder) was added in the PDII/AO-80 mass ratios of 100/0, 100/20, 100/40, 100/60, 100/80, and 100/100. Each of these mixtures was kneaded at room temperature for 5 min to form the first-stage PDII/AO-80a hybrids. (2) The PDII/AO-80a hybrids were then kneaded in a Haake mixer (Rheomix 600p, Thermal Electron Corp., USA) at 50 rpm for 5 min at 135^{o}C and then gradually cooled to room temperature to form the PDII/AO-80b hybrids. (3) The PDII/AO-80b hybrids were then blended with compounding and crosslinking additives, including 5.0 phr of ZnO, 2.0 phr of stearic acid, 0.2 phr of tetramethylthiuram disulfide, 0.5 phr of diphenyl guanidine, 0.5 phr of dibenzothiazole disulfide, and 1.0 phr of sulfur. The hybrids were then kneaded on the two-roll mill at room temperature for 10 min. (4) Finally, the hybrids were hot-pressed and vulcanized at 150^{o}C under the pressure of 15 MPa for various periods of time, and then naturally cooled down to room temperature to form the PDII/AO-80 crosslinked hybrids (PDII/AO-80c hybrids). The optimum vulcanization time for each crosslinked hybrid was determined by using a disc rheometer (P355C2, Huanfeng Chemical Technology and Experimental Machine Co., Beijing, China).

2.3 Measurements and characterization

Infrared (IR) measurements were conducted on a Bruker Tensor 27 spectrometer. The FTIR spectra were acquired by scanning the specimens in the wavenumber range 400 cm^{-1} to 4000 cm^{-1} for 128 times with a resolution of 2 cm^{-1}. The FTIR spectra of AO-80 (both as-received and quenched AO-80) were acquired from ultra-thin disk specimens pressed from AO-80 and KBr. The FTIR spectra of PDII/AO-80 hybrids were acquired from film specimens (prepared by hot-pressing and crosslinking) with a thickness of approximately 1 mm by using the Attenuated Total Reflection (ATR) technique. Differential scanning calorimetry (DSC) analysis was performed on a DSC 204F1 calorimeter (Netzsch Co., Germany). The DSC curves were recorded from -80^{o}C to 200^{o}C at a heating rate of 10^{o}C/min and under a nitrogen purge of 50 cm^{3}/min. X-ray diffraction (XRD) measurements were performed on a Rigaku

D/Max 2500 VBZt/PC X-ray diffractometer (Rigaku Co., Japan). The XRD data were recorded in the scattering angle range 3^o to 90^o. The surface morphologies of the PDII/AO-80 hybrids were observed under a Hitachi S-4800 scanning electron microscope (SEM) (Hitachi, Ltd., Japan). The SEM specimens were prepared by fracturing the hybrids in liquid nitrogen. Dynamic viscoelasticity measurements were performed on a VA3000 dynamic mechanical thermal analyzer (DMTA) (01 dB-Metravib Co., France). The DMTA specimens were 10 mm long, 10 mm wide, and 1 mm thick, and were prepared by hot-pressing and crosslinking. The temperature dependence of the dynamic tensile modulus was measured in the range -40^{o}C to 100^{o}C at a frequency of 10 Hz and a heating rate of 3^{o}C/min. Tensile tests of the PDII/AO-80 hybrids were conducted according to ASTM standard (D412: dumbbell-shaped), and the specimens were tested on an LRX Plus Tensile Tester (Lloyd Instruments, Ltd., UK).

3 Results and discussion

3.1 Thermal behavior and crystallization of PDII/AO-80 hybrids

We chose the PDII/AO-80 (100/60) hybrids to investigate the structures and the intermolecular interactions in PDII/AO-80 hybrids. The DSC curves for AO-80, neat PDII, and the PDII/AO-80 (100/60) hybrids are shown in Fig. 3-2(a). As shown in Fig. 3-2(a), the as-received AO-80 powder is crystalline and has a melting temperature at around 123^{o}C. After the as-received AO-80 was heated to 200^{o}C and quickly quenched to room temperature, amorphous AO-80 with a T_g at around 45^{o}C is obtained. It also can be seen that the neat PDII is amorphous, with a T_g at around -21^{o}C, and no crystallization melting peaks are found. Additionally, the DSC curve of the PDII/AO-80a (100/60) hybrid shows both the T_g of PDII and the melting temperature of AO-80. The PDII and the AO-80 molecules were weak in the PDII/AO-80a (100/60) hybrid, and a phase separation occurred, consistent with the SEM results (Fig. 3-3). Furthermore, the early start of melting and the blunting of the melting peak of AO-80 in the PDII/AO-80a (100/60) hybrid suggest that the crystal structure of AO-80 is destroyed because of the heat and the shear force in the blending process.

The DSC curve of the PDII/AO-80b (100/60) hybrid shows neither the T_g nor the melting temperature of AO-80, and the T_g of PDII is shifted from -21.3^{o}C to -6.5^{o}C, as shown in Fig 3-2(a). The AO-80 in the PDII/AO-80b hybrid might exist mainly as tiny nanoparticles or even as molecules after the PDII/AO-80a hybrid was mechanically kneaded above the melting temperature of AO-80. The extensive shearing associated with the high temperature

mechanical kneading process could significantly promote the molecular-level mixing of the rubbery-state PDII molecules and the liquid-state AO-80 molecules. Interestingly, the subsequent cooling did not cause any evident phase separation, probably because of the strong intermolecular interactions between the PDII and the AO-80 molecules. The strong intermolecular interactions act as physical crosslinking points and remarkably restrict the mobility of the PDII macromolecules. The restriction greatly increases the glass transition temperature of PDII. Therefore, the PDII/AO-80b hybrids could be considered as molecular composites. This conclusion is further supported by the FTIR, XRD, SEM, and DMA results.

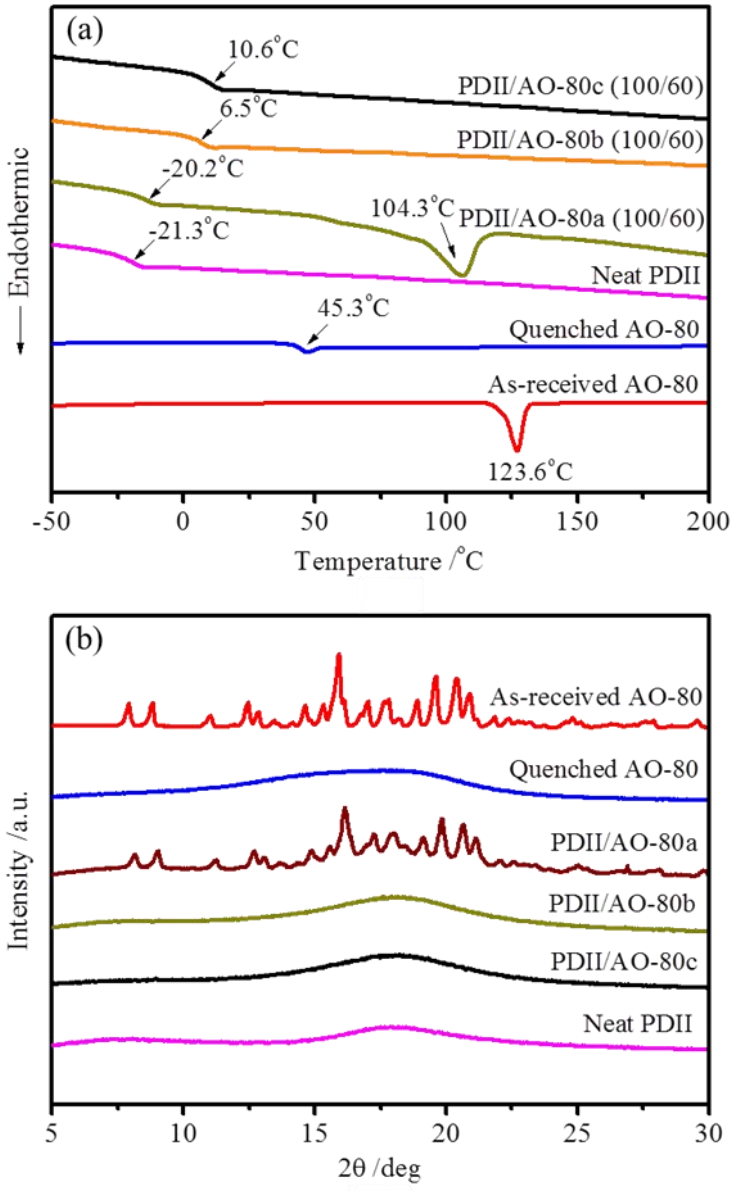

Figure 3-2. (a) DSC curves and (b) XRD traces of AO-80 (as-received and quenched), neat PDII, and PDII/AO-80 (100/60) hybrids in different preparation stages.

The DSC curve of the PDII/AO-80c (100/60) hybrid shows little difference from the PDII/AO-80b (100/60) hybrid, except that the T_g of PDII was further increased by 4°C because of the chemical crosslinking. The AO-80 molecules in PDII/AO-80c (100/60) as well as in PDII/AO-80b (100/60) could not reaggregate and crystallize during the subsequent cooling, mainly because of the strong intermolecular interactions and the fast cooling rate. As a result, the AO-80 melting peak disappear.

Figure 3-2(b) shows the X-ray diffraction (XRD) traces of AO-80 (both as-received and quenched), neat PDII, and the PDII/AO-80 (100/60) hybrid in different preparation stages. As shown in Fig. 3-2(b), the as-received and the quenched AO-80 demonstrate crystalline and amorphous characteristics, respectively. The XRD trace of the PDII/AO-80a (100/60) hybrid is similar to that of the as-received AO-80, indicating that the AO-80 in the hybrid is crystalline. However, the position (2θ) of the crystallization peak of the AO-80 in PDII/AO-80a (100/60) is larger than that of the as-received AO-80, indicating that the thickness of the AO-80 crystals in PDII/AO-80a (100/60) is smaller than that of the as-received AO-80, based on the Bragg equation, because the crystal structure of AO-80 may be destroyed by the heat and the shear force in the blending process, consistent with the DSC results. The XRD traces of the PDII/AO-80b (100/60) and PDII/AO-80c (100/60) hybrids, however, indicate that AO-80 molecules in these hybrids are amorphous, consistent with the DSC results.

3.2 Morphology of PDII/AO-80 hybrids

Phase morphology studies can provide the relationship between the microstructure and mechanical properties. Therefore, representative fracture surfaces of the prepared PDII/AO-80 (100/60) hybrids were studied by SEM. In Fig. 3-3(a), a rough surface with large particles is observed, indicating that the normal mechanical blending of PDII and AO-80 at room temperature will lead to a poor dispersion of AO-80 in the PDII. Besides, the interfacial adhesion between AO-80 and the PDII was very weak, as indicated by the numerous holes left behind by the removal of AO-80 particles from the fracture surface.

Figure 3-3(b) and (c) show the microstructure of the PDII/AO-80b (100/60) hybrid. The representative fracture surface of the PDII/AO-80b (100/60) hybrid is uneven and distorted, mainly because the PDII/AO-80b (100/60) hybrid was not hot-pressed and crosslinked. But AO-80 particles cannot be clearly observed and very few voids can be identified by the microscope. These results suggest that the mechanical kneading of the PDII/AO-80a (100/60)

hybrid above the melting temperature of AO-80 improves the dispersion of AO-80 and intermolecular interactions between then PDII and the AO-80 in the hybrid. Additionally, the subsequent cooling did not cause any obvious phase separation, probably because of the strong intermolecular interactions between PDII and the AO-80 molecules. The SEM results are in accordance with the DSC results.

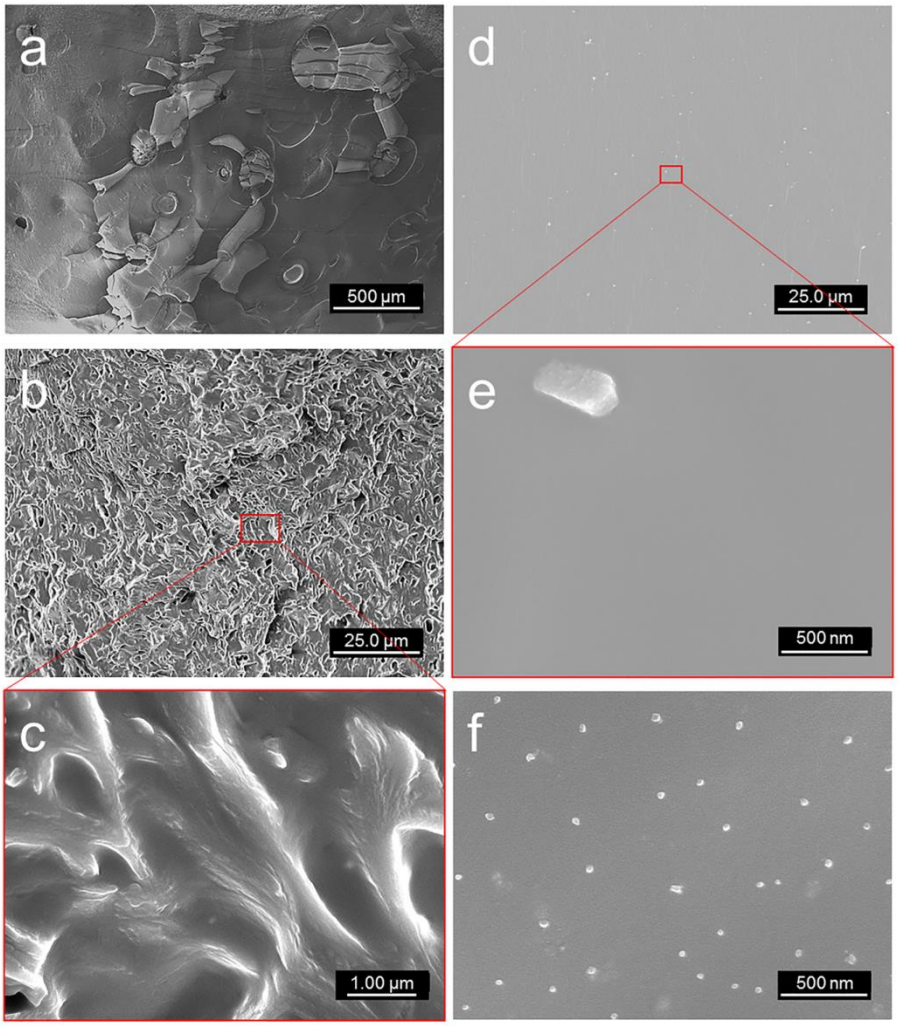

Figure 3-3. SEM images of representative fracture surfaces: (a) PDII/AO-80a (100/60), (b and c) PDII/AO-80b (100/60), (d and e) PDII/AO-80c (100/60) hybrids, and (f) AO-80-rich phase.

Representative fracture surface of the PDII/AO-80c (100/60) hybrid are shown in Fig. 3-3(d) and (e). The fracture surface of the hybrid is very smooth, and no AO-80 particles are observed on the surface. The particles in Fig. 3-3(d) and (e) were confirmed to be ZnO by using the energy dispersive spectrometer (EDS) attached to the SEM (Fig. 3-4). In addition, sporadic aggregations of AO-80 molecules are observed in the PDII/AO-80c (100/60) hybrid, as shown in Fig. 3-3(f). The excess AO-80 molecules readily come into contact with one

another to form aggregates because of the intermolecular interactions (H-bonds$_{(b)}$) between the AO-80 molecules. Thus, the AO-80-rich phases that were supposed in Fig. 3-1 are demonstrated by the sporadic aggregations of AO-80 molecules in Fig. 3-3(f). However, crosslinked PDII network was developed during the hot-pressing and vulcanization process, and the three-dimensional rubbery network could block the AO-80 molecules and effectively prevent them from aggregating into large particles. Even more important, the intermolecular interactions between the PDII and the AO-80 molecules restrict the free movement of the AO-80 and the PDII. Thus, the PDII/AO-80c hybrid is indeed a molecular composite.

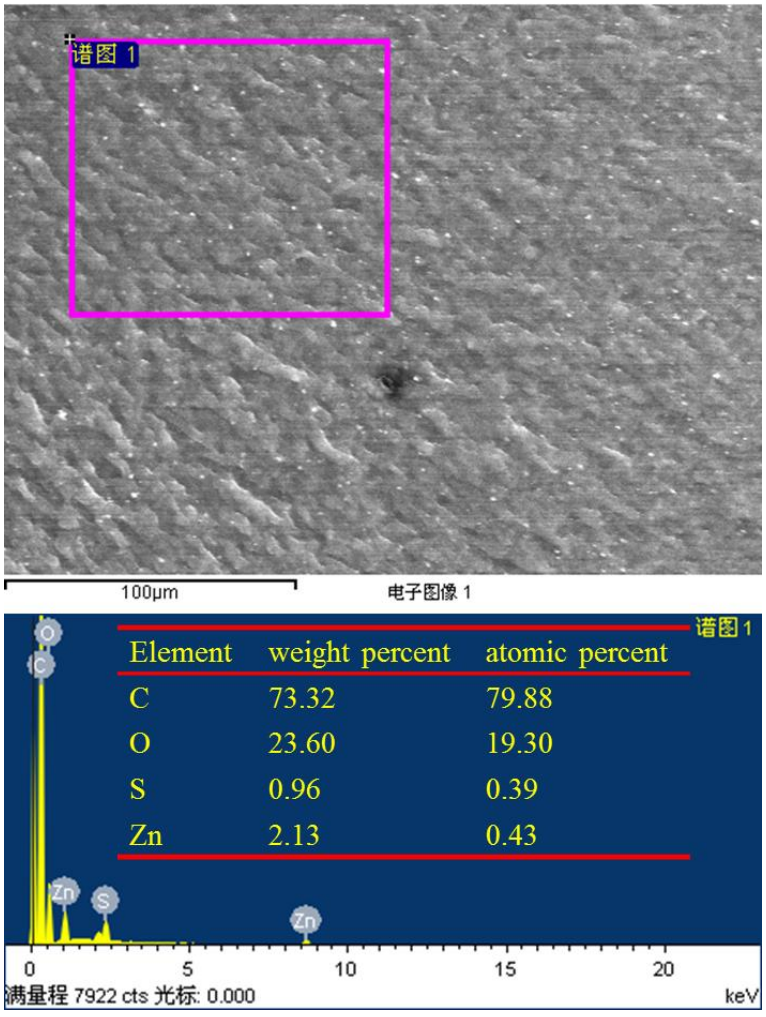

Figure 3-4. EDS spectrum of PDII/AO-80c (100/60) nanocomposite.

3.3 FTIR spectra of AO-80 and PDII/AO-80 hybrids

Figure 3-5 shows the FTIR spectra of AO-80 and the PDII/AO-80 hybrids. The telescopic vibration of -OH is absorbed usually in the range 3125-3704 cm^{-1}. In Fig. 3-5(a), there is an absorption peak near 3552 cm^{-1} associated with free hydroxyl groups and another absorption

peak near 3467 cm^{-1} associated with the hydroxyl groups with hydrogen bonds in the AO-80 crystals. After the crystalline AO-80 powder was melted and then quenched to room temperature, amorphous AO-80 with hydrogen bonds was obtained, as indicated by the single infrared absorption peak near 3494 cm^{-1} in Fig. 3-5(a). After the crystalline AO-80 was added into the PDII, the same change of AO-80 was observed, as shown in Fig. 3-5(b). Furthermore, the infrared absorption peak near 3502 cm^{-1} in Fig. 3-5(b) suggests that there are molecular interactions (H-$bonds_{(a)}$) between the PDII and the AO-80 molecules in the PDII/AO-80 hybrids.

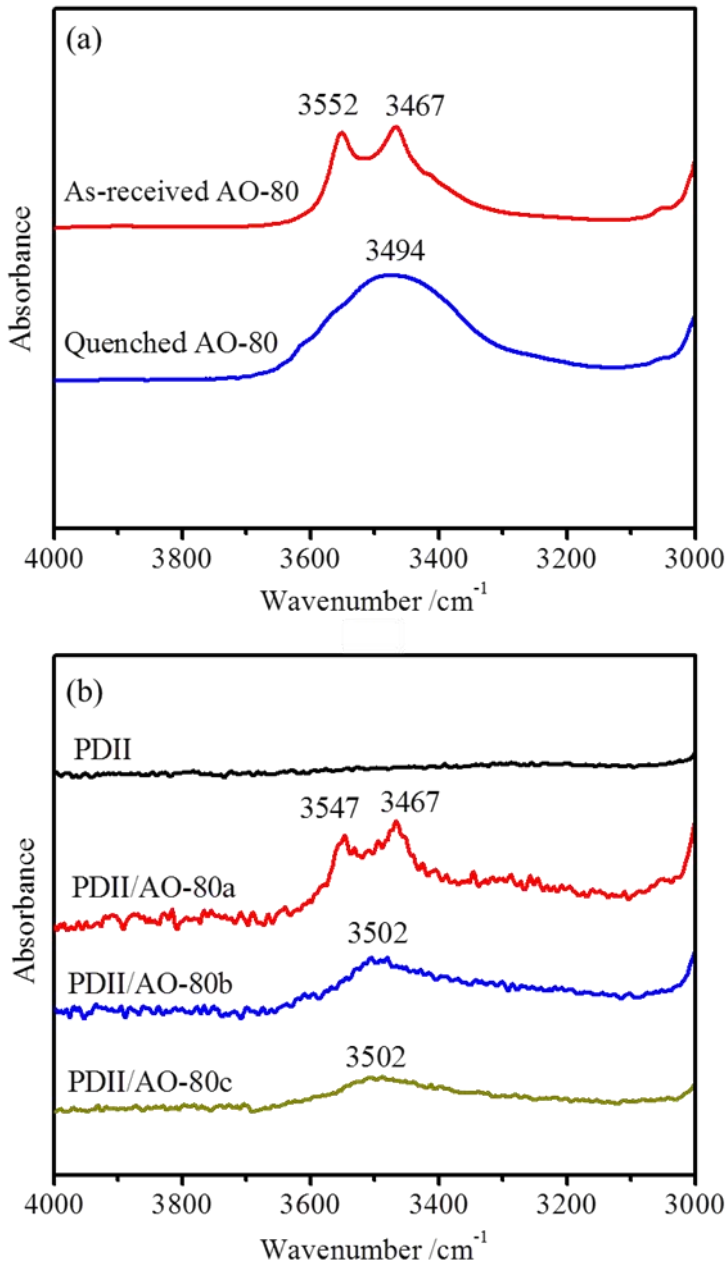

Figure 3-5. FTIR spectra of (a) AO-80 (as-received and quenched) and (b) PDII/AO-80 hybrids in different preparation stages.

3.4 Dynamic mechanical properties of PDII/AO-80c hybrids

Of the DMTA results, the loss factor tanδ reflects the internal and the external friction and expresses the ratio of energy dispersed in one deformation cycle to energy accumulated during the deformation cycle. A high value of tanδ means good damping performance of the material.

Figure 3-6(a) shows the temperature dependence of the tanδ values of the prepared PDII/AO-80c hybrids with various mass ratios of PDII to AO-80. Every PDII/AO-80c hybrid has only one tanδ peak, as shown in Fig. 3-6(a), indicating that the AO-80 molecules have a good compatibility with the PDII molecules. The H-bonds$_{(a)}$ formed between the PDII and the AO-80 molecules also improve the compatibility. Specifically, as the AO-80 content in the PDII/AO-80c hybrids increases from 0 to 100 phr, the tanδ value increases from 1.42 to 3.66. Such an uncommon but favorable increase in the tanδ value is very remarkable. Different from other materials, a polymeric material gives the damping performance mainly by its viscoelastic behavior in the transitional region between the rubbery and the glassy state (near the glass transition temperature). In this region, macromolecular chain segments, but not entire macromolecules, essentially transform from the "frozen" state to the "free" state and tend to vibrate in phase with an external vibration. However, the molecular conformational changes usually cannot keep up with the imposed vibration, resulting in internal friction and energy dissipation. The stronger the internal friction, the higher the tanδ value and the better the damping performance of the material will be. Generally speaking, the introduction of inorganic fillers (such as carbon black, silica, and metal oxide/hydroxide) and organic molecules (such as plasticizers) into a polymer typically leads to a decrease of the tanδ value because the interactions between the fillers and the matrix are often weak. For the PDII/AO-80c hybrids, however, the increase in tanδ value can be attributed to the strong intermolecular interactions between the finely dispersed AO-80 molecules and the PDII molecules, which effectively restrict the motion of PDII molecules and increase the intermolecular friction during dynamic deformation. The high energy dissipation of intermolecular interaction under dynamic deformation is responsible for the remarkable increase of tanδ. A high tanδ in the glass transition region suggests that the PDII/AO-80c hybrids can be a good damping material in the corresponding working temperature range.

Figure 3-6(b) shows the temperature dependence of the storage moduli (G') of the prepared PDII/AO-80c hybrids. Every storage modulus curve displays only one transition, and the

curve gradually moves toward high temperatures with increasing amount of AO-80. Previous studies [100-103] showed that the G' values of rubber nanocomposites increased with increasing amount of inorganic filler. For the PDII/AO-80c hybrids, the G' values in the glassy region do not vary significantly, but those in the rubbery region significantly decrease as the AO-80 content increases. Because the stiffness of the amorphous AO-80 particles is similar to that of the crosslinked matrix, the AO-80 particles have little effect on the G' value of the matrix in the glassy state. However, the AO-80 particles become soft at temperatures higher than the glass transition temperature of AO-80 (45.3°C), leading to the decrease of G' in the rubber region of the PDII/AO-80c hybrids.

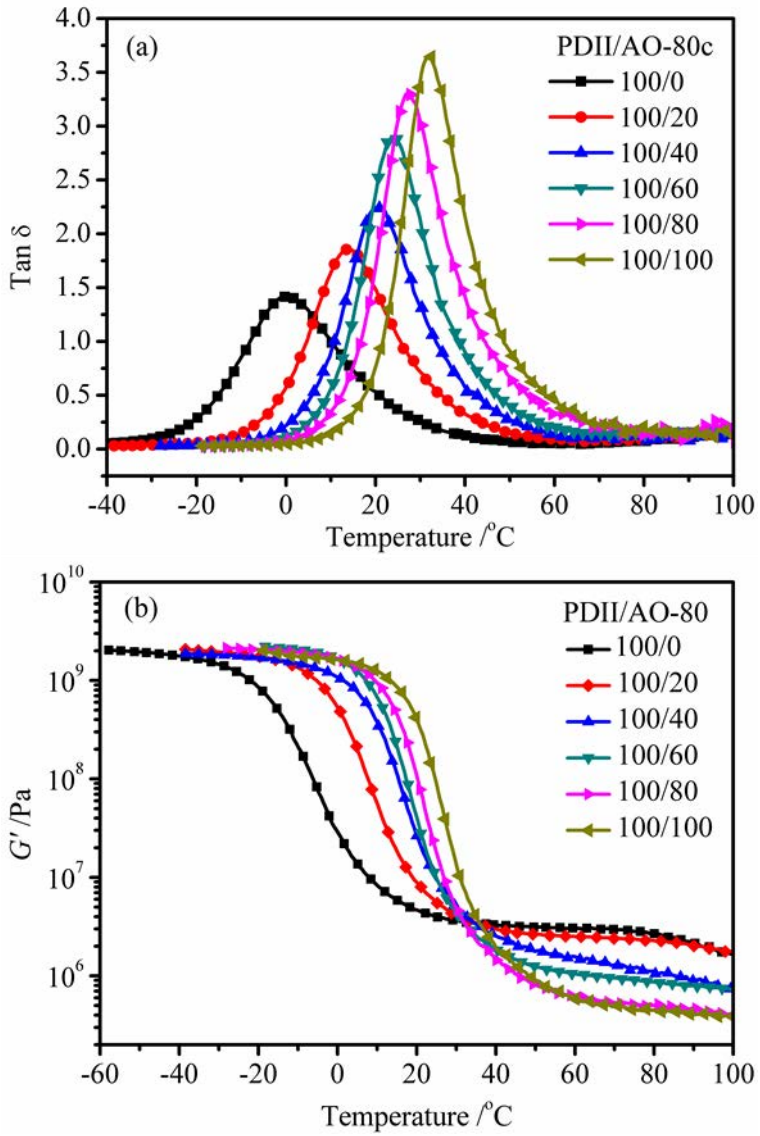

Figure 3-6. Temperature dependence of (a) loss tangent (tanδ) and (b) storage modulus (G') for PDII and PDII/AO-80c hybrids with various mass ratios of PDII to AO-80.

Crosslink density can also affect the strength of tanδ and the G' at high temperature. The crosslink densities of the PDII/AO-80c hybrids were measured by swelling in toluene using the Flory-Rehner theory [104,105]. The Flory-Huggins interaction parameter χ was calculated in previous study, and the value is 0.12 [50]. The crosslink densities of the PDII/AO-80c hybrids are listed in Table 3-1. As expected, crosslink density of PDII/AO-80c hybrids decreased with the increase of AO-80 content. The decrease of the crosslink density helps partly to increase the tanδ values and decrease the G' values at high temperature.

Table3-1 Crosslink density of PDII/AO-80c hybrids

Loadings of AO-80	0	20	40	60	80	100
Crosslink density (10^{-4} mol cm^{-3})	4.2	3.6	2.8	1.9	1.5	1.2

3.5 Static mechanical properties of PDII/AO-80 hybrids

Figure 3-7 shows the characteristic curing curves of neat PDII and the PDII/AO-80 hybrids with various mass ratios of PDII to AO-80 at 150°C. The torque of the vulcanizates decreases with the increase of AO-80 content, an indication that the AO-80 acted as a plasticizer in the PDII/AO-80 hybrids at 150°C. Actually, the AO-80 molecules melted in the PDII/AO-80 hybrids at a temperature (150°C) higher than the melting point of AO-80 (123.6°C). The liquid AO-80 plasticized the PDII and decreased the torque of the hybrids. Table 3-2 shows the static mechanical properties of the PDII/AO-80c hybrids with various mass ratios of PDII to AO-80.

Unexpectedly, the PDII/AO-80c hybrids are not reinforced by the organic filler AO-80, although it is well dispersed in the PDII matrix and the interfacial bonding is strong. As the AO-80 content increases, the elongation at break of PDII/AO-80c increases from 199% to 278%, but the tensile strength decreases from 5.64 to 3.70 MPa. The decrease of the PDII/AO-80c hybrid crosslink density is responsible for the increase of the elongation at break and the decrease of the tensile strength. These results indicate that the PDII/AO-80c hybrids are more suitable to be used as functional damping materials rather than engineering materials. Table 3-2 also shows that the hybrids have very small permanent residual deformations, which are important for damping applications.

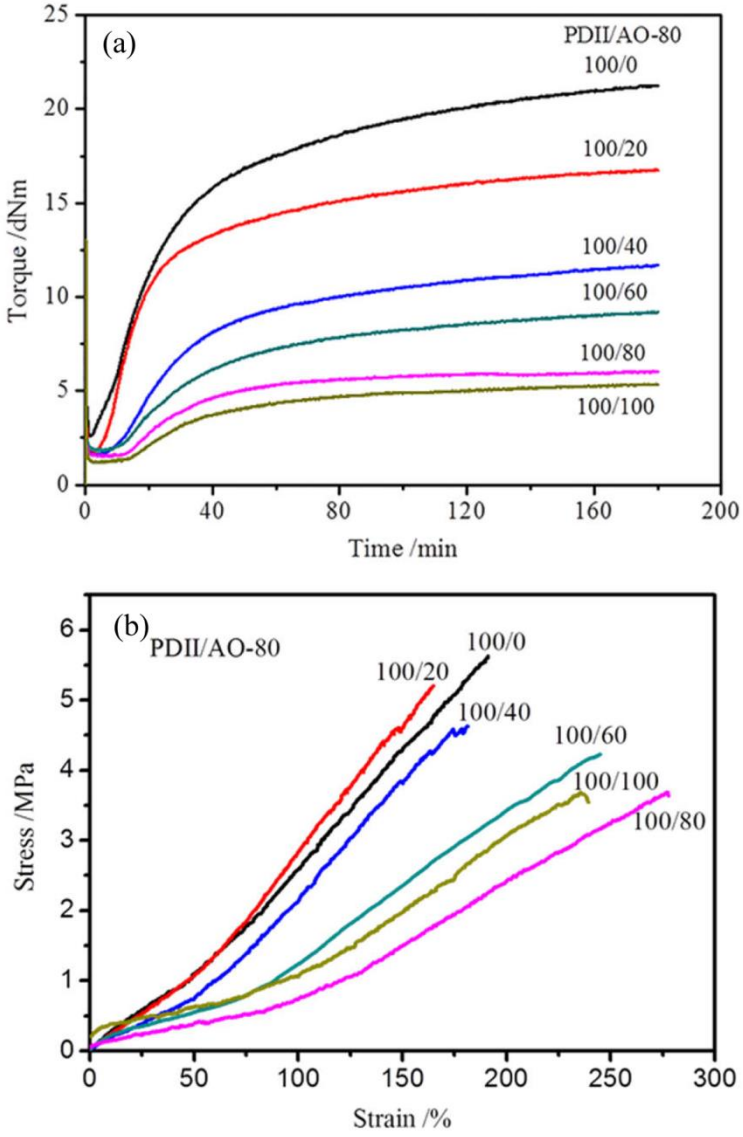

Figure 3-7. (a) Curing curves and (b) stress-strain curves of PDII/AO-80 hybrids with various mass ratio of PDII to AO-80.

Table 3-2. Mechanical properties of PDII/AO-80c hybrids.

Properties	**Loadings of AO-80**					
	0 phr	20 phr	40 phr	60 phr	80 phr	100 phr
Tensile strength (MPa)	5.64	5.20	4.63	4.25	3.69	3.70
Elongation at break (%)	199	166	190	246	278	250
Permanent set (%)	4	4	4	4	6	4
Hardness (Shore A)	62	64	70	75	77	80

4 Conclusions

A bio-based elastomer (PDII) with numerous ester groups was synthesized by a redox system and designed to form a bio-based damping material with a hindered phenol (AO-80). PDII/AO-80 crosslinked hybrids were successfully prepared by the melt blending technique. Most of the AO-80 dissolved in the PDII at the molecular level and formed strong intermolecular interactions with the PDII molecules. In addition, a sporadic aggregation of AO-80 molecules was observed in the PDII/AO-80c (100/60) hybrid. The structures and morphologies of the PDII/AO-80 hybrids in each preparation stage were systematically investigated. The mechanical properties of the PDII/AO-80 crosslinked hybrids with different mass ratios of PDII to AO-80 were studied. The results indicated that AO-80 was homogenously dispersed in the PDII/AO-80 crosslinked hybrids. The PDII/AO-80 crosslinked hybrids exhibited a single relaxation transition, high dynamic mechanical loss values, and decreased tensile strengths. As expected, the PDII/AO-80 crosslinked hybrids had strong intermolecular interactions and tunable damping properties. The tunable damping properties make these hybrids potential candidates for bio-based damping material of the future.

Ackonwledgements

This work was supported by the National Natural Science Foundation of China (50933001, 51221102), the National Outstanding Youth Science Fund (50725310), the National Basic Research Program (973 Program) of China (2011 CB606003), the Beijing Nova Program (Z131102000413015), and the Beijing Municipal Training Program Foundation for the Talents (2013D00303400041).

Chapter 4 Itaconate based carboxylic elastomers and their nanocomposites

In order to explore the applicability of itaconate based elastomers as tire tread materials, we introduced carboxylic groups into itaconate based elastomers to produce a bio-based carboxylic elastomer poly(dibutyl itaconate-*co*-isoprene-*co*-methacrylic acid) (PDIM). The introduction of the carboxylic groups was expected to improve the interfacial interaction between PDIM and silica, and thus guarantee good mechanical and dynamic properties.

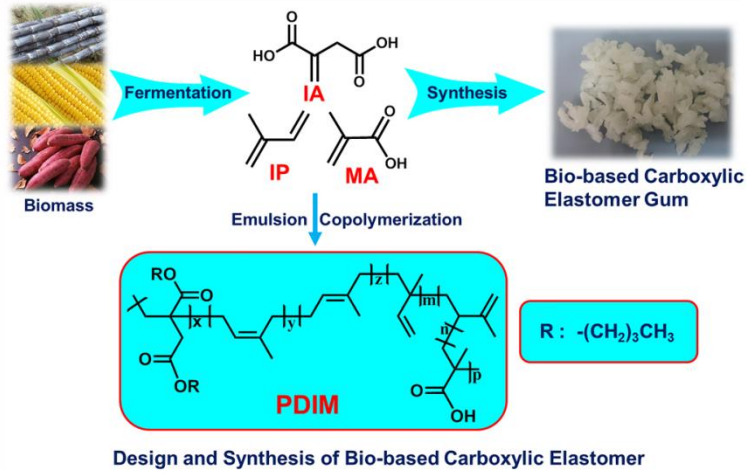

The first article will present the preparation and properties of the PDIM and the PDIM/silica nanocomposites. The chemical structure of the PDIM was determined by FTIR, NMR, DSC, and titration in non-proton solvent. The interfacial interaction between PDIM and silica was investigated by FTIR and RPA, which is a guarantee for good mechanical and dynamic properties.

The second article will focus on the preparation and properties of PDIM/HNTs nanocomposites, which was inspired by a sacrificial bonding mechanism in biological materials. The structure and properties of PDIM/HNTs nanocomposites were investigated carefully. A mechanism responsible for improvement in mechanical properties will be discussed in this part.

Design and synthesis by redox polymerization of a bio-based carboxylic elastomer for green tire

Abstract: Poly(dibutyl itaconate-*co*-isoprene-*co*-methacrylic acid) (PDIM) elastomer was designed and synthesized by redox emulsion polymerization under mild conditions. PDIM has high molecular weight, relatively high yield, and low glass transition temperature (T_g). The structure of PDIM was determined by FTIR and NMR, and the carboxyl content was obtained by titration in a non-proton solvent. Tensile strength and elongation at break increased with increasing carboxyl content. In addition, the interaction between PDIM and silica was elucidated by FTIR, Rubber Process Analyzer (RPA) and TEM, and the results showed that the silica-PDIM interaction was strong, unlike that of the silica-silica.

Keywords: Carboxylic rubber; Bio-based elastomer; Synthesis; Redox polymerization; Green tire.

1 Introduction

The tread is the only part of the tire that is in direct contact with the road and is thus responsible for motion and safety. The rolling resistance of the tread continues to be a primary driver of its development [106,107]. In order to further increase public awareness, the European Commission has introduced a new labeling system, which, from November 2012, making it a legal obligation to show the rolling resistance of a tire, together with other properties, including the pass-by noise and wet grip. The reduction in rolling resistance is important in optimizing a tread compound. Surface-modified carbon blacks with carboxylic solution SBR showed promising properties that significantly reduced hysteresis and rolling resistance [108]. However, the energy crisis and environmental awareness have served as catalysts for looking for greener solutions. As an eco-friendly filler, silica has become one of the most extensively used fillers in passenger tire tread compounds since the advent of so-called „green or energy tires" [109]. In tire treads, silica can provide a lower rolling resistance than carbon black at the same loading, without sacrificing wear resistance and wet grip [110]. In particular, the application of precipitated silica in high performance tires became a successful technology only after the dispersion problem was solved by coating the silica with a bifunctional silane by a complicated, multi-step procedure.

Currently, the basic building blocks of synthetic rubber, such as isoprene, butadiene, styrene, and chloroprene, are mainly derived from crude oil. In contrast, the development of non-petroleum-based rubbers, such as natural rubber and bio-based rubbers, [111] is an effective strategy to tackle the energy crisis and environmental pollution. Natural rubber is a renewable resource; however, the use of silica filler in tread compounds has not been taken up by the market [112]. In recent years interest has grown in the use of epoxidised natural rubber (ENR), which can be used in the tire tread to either partially or entirely replace synthetic rubbers [113,114]. At the 43rd Tokyo Motor Show 2013, Sumitomo launched the ENASAVE 100 as the first completely fossil resource free tire, which uses ENR in the tread, sidewall, and liner. The Tun Abdul Razak Research Centre has developed silica-filled ENR tire treads, which provide very low rolling resistance and excellent wet traction for vehicular applications [115]. The strong interaction between ENR and silica, which is significantly influenced by hydrogen bonding, is thought to be responsible for the low hysteresis exhibited by silica-filled ENR compounds. Although ENR can make a good tire tread compound, the output of natural rubber restricts the application of ENR in the tire industry. It is imperative to find new ways for reducing hysteresis in tire tread compounds with low rolling resistance.

In previous studies, the concept of bio-based engineering elastomer (BEE) was proposed [44]. Large-scaled bio-based monomers, such as sebacic acid, itaconic acid, succinate acid, 1, 3-propanediol, 1, 4-butanediol, and vegetable oils were chosen to generate polyester BEEs (PE-BEEs) [44], poly(diisoamyl itaconate-*co*-isoprene) BEE (PDII) [50], and poly(epoxidized soybean oil-*co*-decamethylene diamine) BEE (PESD) [45]. However, these BEEs were not designed and synthesized for the improvement of tire tread. Our objective was to design and synthesize a bio-based carboxylic elastomer that would provide reduced rolling resistance in tire tread compounds. The interfacial interactions are generally important in determining the end-use performance of polymer nanocomposites incorporated with inorganics. As polar groups, the carboxyl groups of carboxylated butadiene-styrene rubber can form hydrogen bonds with the Si-O groups located on the surface of halloysite nanotubes [116]. Accordingly, the bio-based elastomer functionalized with carboxyl groups along the chains can form strong interfacial interactions with silica joined with polar silanol groups on the surface. The use of silica as reinforcing filler for tread compounds is known to present problems with filler dispersion in rubber stocks because the surface silanol groups from different particles tend to self-associate, forming silica agglomerates. We assumed that the formation of silica agglomerates can be restrained by the strong interfacial interactions between the bio-based carboxylic elastomer and silica by which the dispersion of the silica phase could be improved. The strong interfacial interaction between the bio-based carboxylic elastomer and silica stands a good chance of resulting in a low hysteresis.

In this study, a poly(diisoamyl itaconate-*co*-isoprene-*co*-methacrylic acid) (PDIM) elastomer with high molecular weight was synthesized by redox emulsion polymerization based on dibutyl itaconate (DI), isoprene (IP), and methacrylic acid (MA). Itaconic acid and butyl alcohol are produced by the fermentation of a biomass like corn starch [15,117-119]. Bioisoprene technology was highly developed and reported by Genencor (Palo Alto, CA) and Amyris (Emeryville, CA) [54,120]. Small quantities of methacrylic acid (1-5 wt.%) was used to introduce the carboxyl groups into the macromolecular chains. Methacrylic acid is more hydrophobic and thus participates in emulsion polymerization more readily than itaconic acid [121]. In this study, a redox initiation system was used to generate free radicals by one-electron transfer reactions, which have found wide applications for initiating polymerization reactions and are industrially important. Besides a very short induction period (almost negligible), a lower energy of activation (40-80 kJ mol^{-1}) allows the redox polymerization to be carried out under milder conditions than those for thermal polymerization [122]. The

milder conditions lower the possibility of side chain reactions leading to high molecular weight polymers in high yields. The results indicated that it is easy to obtain a polymer with high molecular weight by redox polymerization. Carboxyl groups were successfully introduced into the synthesized PDIM elastomer. Such PDIM elastomer exhibits improved mechanical performances and strong interfacial interaction with silica.

2 Materials and methods

2.1 Materials

Dibutyl itaconate (purity of 96%) was purchased from Sigma-Aldrich Company. Isoprene (purity of 95%) was purchased from Alfa Aesar Company and distilled to remove the stabilizing agent before use. Ferric ethylenediaminetetraacetic acid salt (Fe-EDTA), sodium dodecyl benzene sulfonate (SDBS), sodium hydroxymethane sulfinate (SHS), tert-butyl hydroperoxide (TBH), potassium phosphate tribasic (K_3OP_4), potassium chloride (KCl), and hydroxylamine were purchased from Sigma-Aldrich Company and used without further purification. Standard solution of potassium hydroxide in ethanol was pre-pared in our lab according to Chinese Standard GB/T601-2002. All other chemicals and ingredients were purchased from China and used without further purification.

2.2 Redox initiation system

In this research, the combination of TBH and Fe-EDTA was used as the redox initiation system to generate radicals. A mechanism for the reaction between TBH and Fe-EDTA involves a one-electron transfer from the ferrous ion to the TBH with the dissociation of the oxygen-oxygen bond and the generation of one RO· radical and one RO- ion (Eq. (4-1)). For hydroperoxides, the primary step (Eq. (4-1)) is followed by further reduction of RO· (Eq. (4-2)), but when a monomer is present the RO· radicals are intercepted by the initiation of polymerization (Eq. (4-3)):

$$Fe^{2+} + ROOR \longrightarrow Fe^{3+} + RO^{-} + RO^{\cdot} \quad (4\text{-}1)$$

$$Fe^{2+} + RO^{\cdot} \longrightarrow Fe^{3+} + RO^{-} \quad (4\text{-}2)$$

$$RO^{\cdot} + M \longrightarrow RO\text{-}M^{\cdot} \xrightarrow{+nM} Polymer \quad (4\text{-}3)$$

where R is tert-butyl or H and M is monomer.

2.3 Synthesis of PDIM by redox-initiated emulsion polymerization

As summarized in Table 4-1, deionized water, SDBS, K_3PO_4 solution, KCl solution, Fe-EDTA solution, and SHS solution were added into a 0.5 L, three-necked flask fitted with a thermometer, a two-bladed anchor-type impeller, and a nitrogen inlet. Subsequently, dibutyl itaconate, isoprene, and methacrylic acid were mixed in advance and added into the flask under a nitrogen atmosphere. The mixture was stirred at high speed (350 rpm) for 60 min to form a stable and homogeneous latex. Later, the TBH solution was injected into the flask and the stirring speed was reduced to 250 rpm. The polymerization was allowed to proceed at 20^{o}C for 12 hours for obtaining the target PDIM latex, and the hydroxylamine solution was added to terminate the polymerization. The PDIM latex was coagulated by using calcium chloride solution (~1 wt.%), and the coagulation was dried at 60^{o}C in vacuum until a constant weight was obtained. The dosage of methacrylic acid is shown in Table 4-2. For all PDIM samples, the molecular weight, yield, and carboxyl content were determined. The polymerization equation is shown in Scheme 4-1.

Table 4-1. Recipe for redox emulsion polymerization.

Ingredients	Dosage (g)
Dibutyl itaconate	70.0
Isoprene	30.0
Methacrylic acid	variable
Deionized water	250.0
Sodium dodecyl benzene sulfonate (powder)	3.0
Potassium phosphate tribasic	0.2
Potassium chloride	0.5
SHS solution (10%)	2.0
Fe-EDTA solution (10%)	0.4
TBH toluene solution (10%)	0.5
Hydroxylamine solution (50%)	0.4

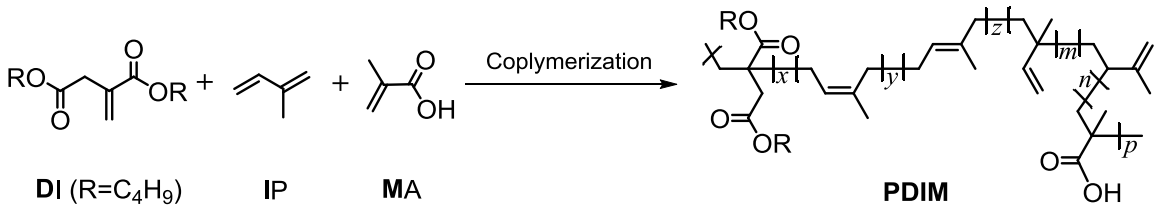

Scheme 4-1. Chemical equation for PDIM synthesis.

2.4 Preparation of crosslinked PDIM

On a 6-inch two-roll mill, the PDIM (100.0 phr) was blended with the additives zinc oxide (5.0 phr), stearic acid (0.5 phr), 2-mercaptobenzothiazole (0.7 phr), N-cyclohexyl-2-benzothiazole (1.0 phr), and sulfur (1.0 phr). The compound was cured at 15 MPa and 150^{o}C for an optimum period determined by a disk oscillating rheometer (P3555B2, Beijing Huanfeng Chemical Machinery Experimental Factory, China).

2.5 Measurements and characterization

The FTIR spectra of PDIM were recorded on a Bruker Tensor 27 spectrometer. ^{13}C NMR and ^{1}H NMR spectroscopic measurements of PDIM were carried out with a Bruker AV400 spectrometer, with $CDCl_3$ as solvent. Molecular weights of polymers were determined by gel permeation chromatography (GPC) on a Waters Breeze instrument equipped with three water columns (Styragel HT3_HT5_HT6E) and a Waters 2410 refractive index detector. Tetrahydrofuran (THF) was used as the eluent in the water columns, and a polystyrene standard was used for calibration in the refractive index detector. Differential scanning calorimetric (DSC) analysis was carried out on a Mettler-Toledo differential scanning calorimeter under N_2 flow (20 mL/min) and at a heating rate of 10^{o}C/min. Latex particle size measurements were conducted on a Malvern Zetasizer (Nano-ZS90). Tensile strength of the PDIMs were measured according to ASTM D412 (dumbbell-shape) on a LRX Plus tensile tester made by Lloyd Instruments, Ltd., UK. The dynamic storage modulus G' of the PDIM/silica compound was measured with a Rubber Process Analyzer (RPA2000, Alpha Technology). Strain sweeps from 0.28% to 400% were carried out at 60°C and 1 Hz. The dispersions of silica in the PDIM/silica compounds were investigated on a transmission electron microscope (TEM, FEI Tecnai G2 20 S Twin). The TEM specimens of the silica-filled PDIM compounds were prepared by cryogenic microtoming using a Reichert-Jung Ultracut Microtome and mounted on mesh copper grids.

2.6 Calculation of carboxyl content

Acidity is the most basic chemical property for carboxyl group. The carboxyl group in PDIM can react with alkali in a non-proton solvent. The carboxyl content in the PDIM can be determined by titration. Butanone, a non-proton solvent, was used to dissolve the PDIM, and the standard solution of potassium hydroxide in ethanol was used as titrant. Phenolphthalein was used as the indicator in the titration.

The following equation was used to calculate the carboxyl content of PDIM elastomer:

$$w = \frac{(V - V_0) \times c \times 45}{1000 \times m} \times 100\% \quad (4\text{-}4)$$

where w is the mass fraction of carboxyl group in the PDIM elastomer, c is the molar concentration of the standard solution of potassium hydroxide in ethanol, m is the mass of the PDIM dissolved into butanone, and V and V_0 are the volumes of the standard solution of potassium hydroxide in ethanol consumed in the PDIM butanone solution and the equivalent butanone, respectively.

3 Results and discussion

3.1 Synthesis of PDIM by redox emulsion polymerization

Table 4-2. Synthesis of PDIM elastomers by redox polymerization.

PDIMm[a]	Copolymerization feeds[b]			PDIM elastomers		
	DI (g)	IP (g)	MA (g)	Yield (%)	M_n[c] (g/mol)	PDI[c]
PDIM0	70.0	30.0	0	77	251 000	2.72
PDIM1	70.0	30.0	1.0	74	297 000	3.82
PDIM3	70.0	30.0	3.0	78	289 000	4.17
PDIM5	70.0	30.0	5.0	75	279 000	3.63

[a]m denotes the amount of methacrylic acid injected into the polymerization system. [b]The copolymerization was carried out at 20 °C for 12 hours by redox polymerization system. [c]Determined by GPC.

Redox emulsion polymerization was carried out under mild conditions to give high molecular weight polymers with greater yields. The number-average molecular weight (M_n) and the polydispersity index (PDI) affect the mechanical and processing properties of rubber. The M_n and PDI of the PDIM elastomers are given in Table 4-2. In all runs, PDIM elastomers with a

high molecular weight (M_n > 250 000 g/mol) were obtained in high yields by redox emulsion polymerization because a low energy of activation allows the redox polymerization to be carried out at low temperatures, omitting the possibility of side chain reactions. In addition, the PDI is also shown in Table 4-2.

The stability and homogeneity of the emulsion are important for the growth of macromolecular chains in the polymerization. Figure 4-1 shows the size distributions of latex particles measured by the Malvern Zetasizer after the terminated emulsions were left to stand for 48 hours. PDIM0 shows an average latex particle diameter (d) of 87 nm (Fig. 4-1*a*). On using MA as the third monomer, the average latex particle diameter of PDIM1 is larger than that of PDIM0. The average latex particle diameter of PDIM5 (d=106 nm) is much larger than both that of PDIM3 (d=94 nm) and that of PDIM1 (d=90 nm). MA is a methacryl type monomer, with noticeable steric effect. MA, having both methyl and carboxyl groups, may probably form uncompact particles and terpolymers. The small diameters of these particles make the PDIM emulsions qualify as mini-emulsions [123-125]. Moreover, with the increase of MA usage in the feed, the uncommon increase of latex particle diameter was observed although the increase was not so large and the mechanism of the uncommon increase was still unclear.

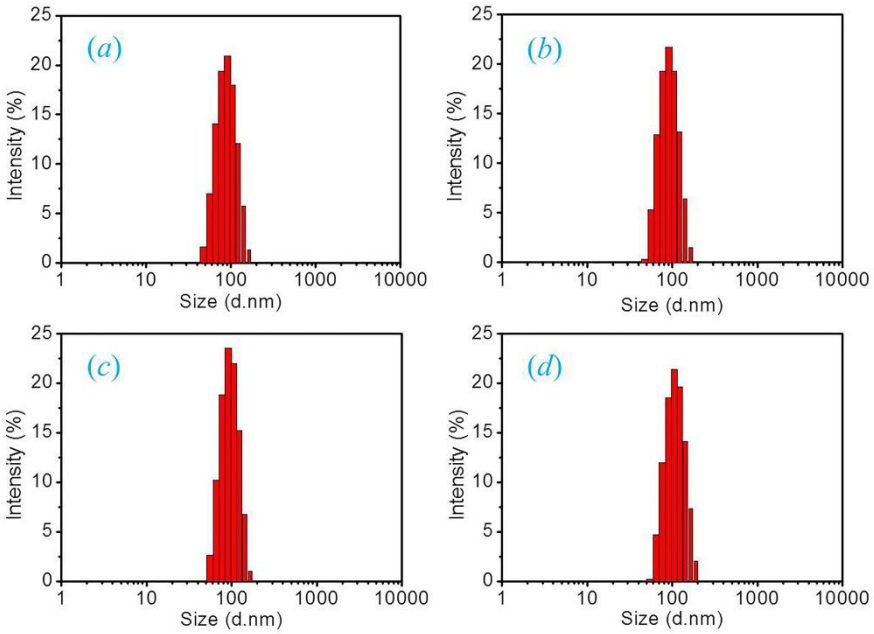

Figure 4-1. Size distributions of latex particles: (*a*) PDIM0 emulsion (d=87 nm), (*b*) PDIM1 emulsion (d=90 nm), (*c*) PDIM3 emulsion (d=94 nm), and (*d*) PDIM5 emulsion (d=106 nm).

The redox emulsion polymerization of PDIM5 was carried out at 20°C to investigate the effect of reaction time on the yield of the copolymerization. As shown in Fig. 4-2, the yield-time curve indicates that the yield increases with reaction time, reaching 75% after 12 hours. The reaction time was determined based on this result. The yields in emulsion polymerization were controlled in 70-80% to get the optimum mechanical properties for the PDIM elastomers, and the results were shown in Table 4-2.

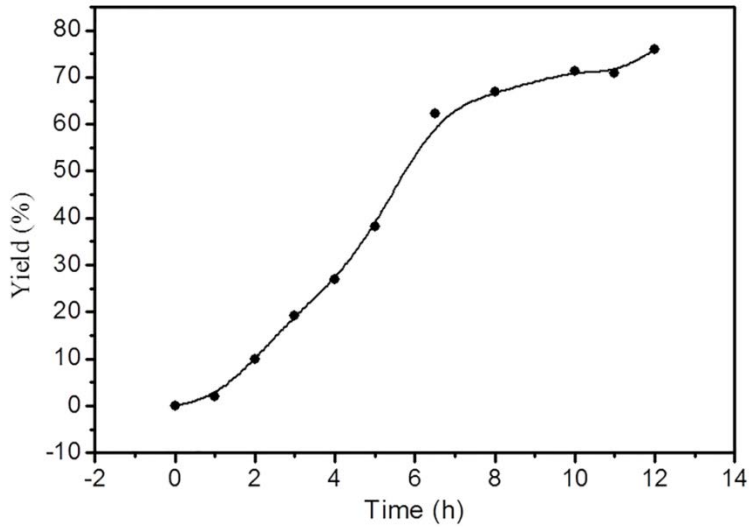

Figure 4-2. Time dependence of yield of PDIM5.

3.2 Characterization of carboxyl groups in PDIM

The carboxyl groups in PDIM are important for the dispersion of silica because they are expected to form strong interaction with the silanol on the surface of silica in the subsequent experiments. Titration results (Table 4-3) show that PDIM elastomers containing different amounts of carboxyl groups were successfully prepared. For each PDIM, the amount of meth-acrylic acid unit in macromolecular chains was consistently less than the initial amounts of methacrylic acid added into the polymerization system. Furthermore, mixed charging of monomers got larger amounts of carboxyl groups than the three monomers added separately, mainly because methacrylic acid can dissolve in both oily monomers and water [126]. It is well known that the first step for dissolution is a diffusion process of one solute into one solvent. Thus, methacrylic acid was added into a mixture of dibutyl itaconate and isoprene in advance and dissolved into the oily monomers by stirring. As a part of the mixture, a smaller amount of methacrylic acid was left to diffuse into the aqueous phase. The surplus amount of

meth-acrylic acid in the oil phase participated in the polymerization, resulting in an increased carboxyl content in PDIM.

Table 4-3. Contents of carboxyl and methacrylic acid unit in polymers.

PDIMm[a]	Content of carboxyl in polymer[b] (wt.%)	Content of methacrylic acid unit in polymer[c] (wt.%)
PDIM0	0	0
PDIM1	0.30±0.03	0.58±0.06
PDIM1[d]	0.23±0.03	0.44±0.06
PDIM3	1.37±0.02	2.62±0.04
PDIM3[d]	1.14±0.03	2.18±0.06
PDIM5	2.16±0.02	4.12±0.04
PDIM5[d]	1.96±0.02	3.75±0.04

[a]m denotes the amount of methacrylic acid injected into the polymerization system. [b]Calculated according to Eq. (4-4). [c]Calculated based on the recipe of polymerization. [d]First, dibutyl itaconate and isoprene were added, and then methacrylic acid was injected into the reaction system.

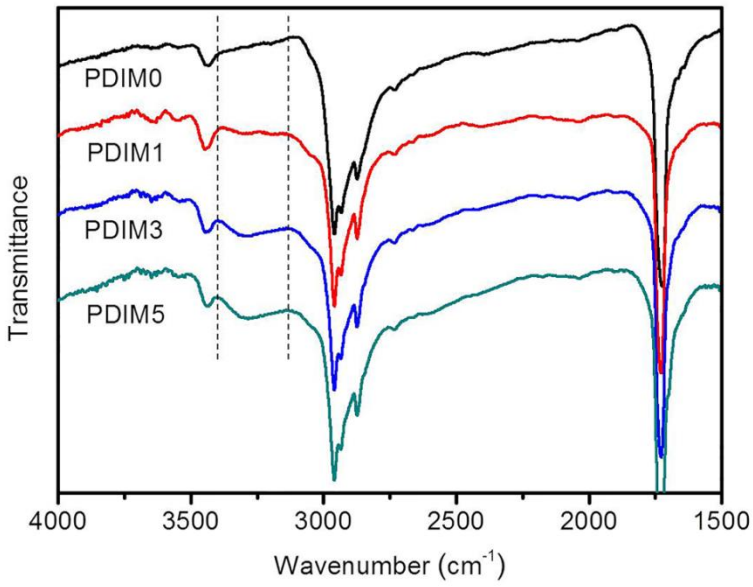

Figure 4-3. FTIR spectra of PDIM elastomers with different carboxyl contents.

Figure 4-3 shows the FTIR spectra of PDIM elastomers with different carboxyl contents. The strong absorption peak at 1740 cm^{-1} is associated with the stretching vibration of the carbonyl (C=O) of dibutyl itaconate, and the broad absorption peaks at 2960, 2925, and 2871 cm^{-1} are attributed to the stretching vibrations of $-CH_3$, $-CH_2$, and -CH in the terpolymers, respectively. The broad absorption peak at 3300 cm^{-1} corresponds to the -OH vibration in the carboxyl

groups of the PDIM samples except PDIM0, which does not contain any carboxyl group. Moreover, the increased intensity of the -OH vibration peak indicated the increased carboxyl contents in the PDIM elastomers.

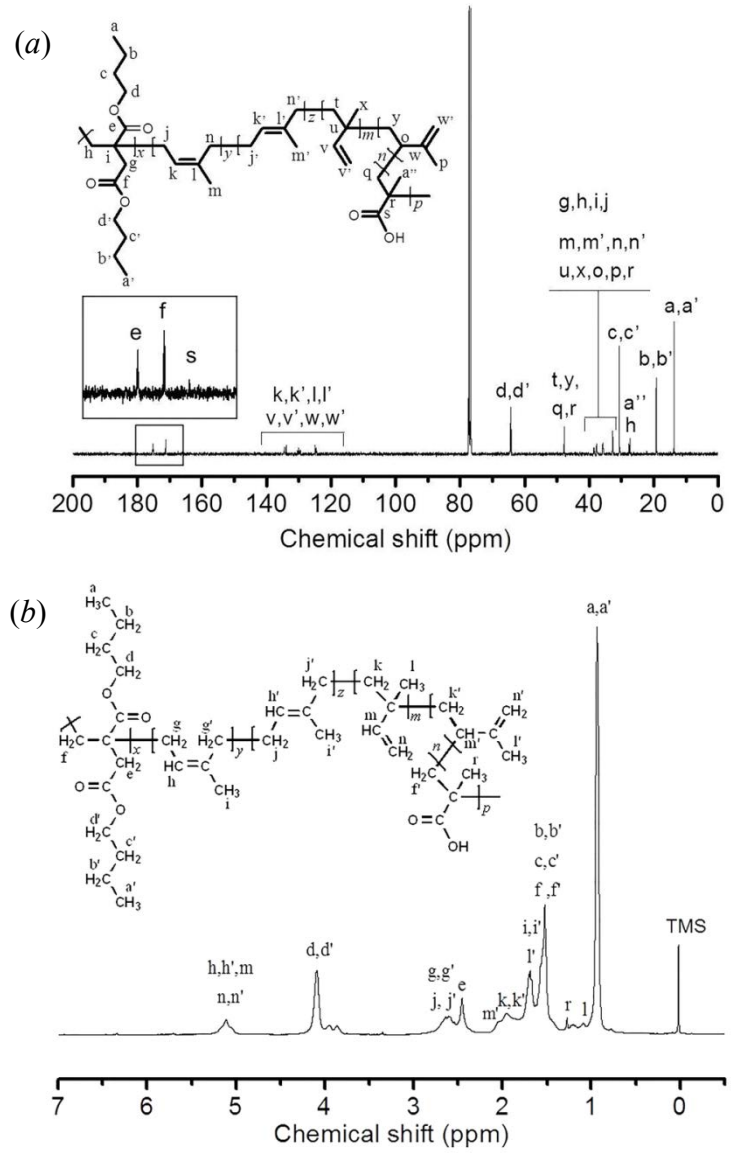

Figure 4-4. NMR spectra of PDIM5 elastomer: (*a*) ^{13}C NMR and (*b*) ^{1}H NMR (in $CDCl_3$).

PDIM5, with the highest carboxyl content, was characterized by ^{13}C NMR and ^{1}H NMR. Figure 4-4*a* shows the ^{13}C NMR spectrum of PDIM5. The peaks indicate the presence of dibutyl itaconate, isoprene, and methacrylic acid, further confirming the molecular structures of the terpolymer. In addition, the 1H NMR spectrum of PDIM5 is shown in Fig. 4-4*b*. The signals of the protons except CO_2H protons on the PDIM5 macromolecules are observed and used to confirm the molecular structures of the terpolymer. The absence of the signals of the labile CO_2H protons may be due to exchange reactions with the solvent [127,128].

3.3 Thermal properties of PDIM elastomers

The glass transition temperature (T_g) of an elastomer is much lower than room temperature because a polymer is rigid and inelastic at temperatures lower than T_g. An ideal T_g for elastomers should be lower than -30°C. The T_g values of the PDIM samples were determined by DSC, and their thermograms are shown in Fig. 4-5. Every PDIM sample did not show an obvious melting point, suggesting presence of some amorphous structures. Figure 4-5 shows that T_g increases with the increase of carboxyl content from -40°C to -32°C. The introduction of the carboxyl groups is responsible for the increase of T_g because this polar group can increase the interaction between the molecular chains and restrict the movement of polymer chain segments. These results indicate that PDIM with an amorphous structure and a low T_g can be used as an elastomer.

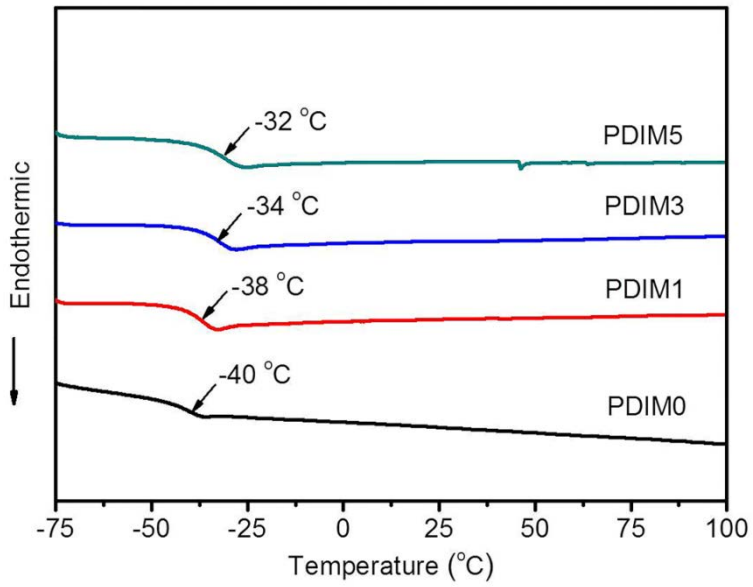

Figure 4-5. DSC curves of PDIM elastomers (for determination of T_g).

3.4 Curing characteristics and mechanical properties of PDIM elastomers

Vulcanization is a vital step for elastomer products. According to the literature [129-131], an elastomer with carboxyl groups can be crosslinked by metallic oxide. In this study, sulfur was used as the curing agent in the presence of zinc oxide. Figure 4-6 shows the curing curves for PDIM with different carboxyl contents at 150°C. From Fig. 4-6, PDIM0 and PDIM1 were cured in one step, and PDIM3 and PDIM5 were cured in two steps. From the cure curve (PDIM0, Fig. 4-6), it can be concluded that PDIM0 was cured by sulfur alone because carboxyl groups were not introduced into the PDIM0 chains. With the increase of the

carboxyl content, the curing process was delayed (PDIM1, Fig. 4-6) and even underwent two steps (PDIM3 and PDIM5, Fig. 4-6). The pendent carboxyl groups on the PDIM molecular chains can consume zinc oxide and the consumption of zinc oxide slows down the acceleration of the sulfur curing process. On the other hand, upon fully reacting, each mole of zinc oxide can neutralize two moles of carboxyl groups to form a crosslinked site (zinc ion aggregates) [130], contributing to the first step in the curing of PDIM3 and PDIM5. Apparently, the reversion phenomena can be observed in the curing of PDIM0 and PDIM1. Actually, the vulcanization process involves two competing processes, namely, crosslinking and desulfuration, and the reversion occurs when the desulfuration reaction is faster than the crosslinking reaction. As above mentioned, zinc ion aggregates were formed via neutralization in the curing of PDIM3 and PDIM5. Indeed, the neutralization is rapid process and responsibility for the very quick scorching in PDIM5.

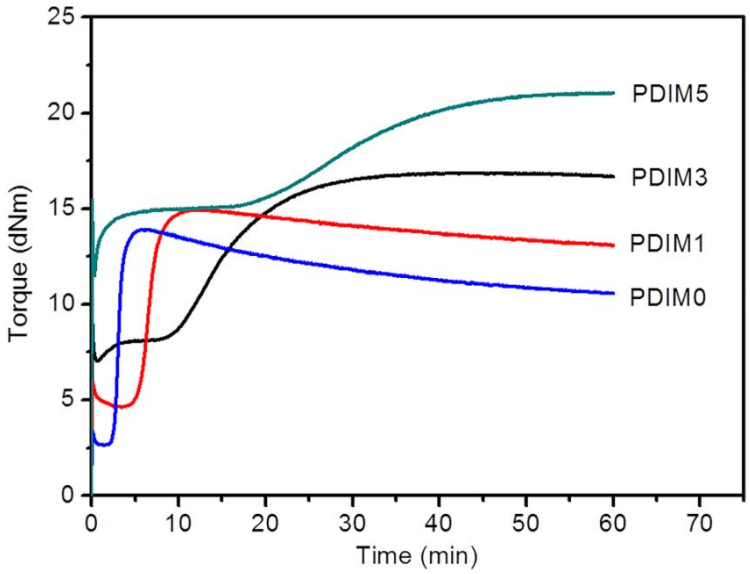

Figure 4-6. Curing curves for PDIM elastomers.

Figure 4-7 shows the stress-strain curves of the unfilled PDIM ealstomers with various carboxyl contents, and Table 4-4 summarizes the acquired data. The results demonstrate that with the increase of carboxyl content in PDIM, the tensile strength increases; besides increasing the elongation at break. Furthermore, the stress at 300% strain and the hardness (Shore A) also increase with the increase of carboxyl content. The small permanent set (Table 4-4) indicates that the PDIM elastomers have good recovery ability. The improvement of mechanical properties may be attributed to the increased intermolecular interaction or formation of zinc ion aggregates in PDIM5. In summary, the introduction of carboxyl groups

improved the mechanical properties of the PDIM elastomer, and these improvements made the PDIM elastomer an alternative rubber for tire tread applications in the future.

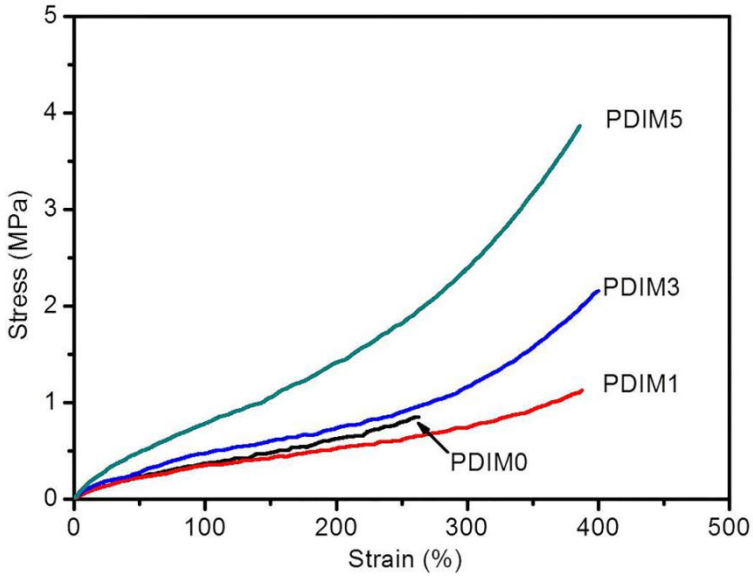

Figure 4-7. Stress-strain curves of PDIM elastomers.

Table 4-4. Mechanical properties of PDIM elastomers.

PDIM sample	PDIM0	PDIM1	PDIM3	PDIM5
Tensile stress (MPa)	0.9	1.2	2.2	3.9
Elongation at break (%)	255	389	435	402
Stress at 300% strain (MPa)	N/A[a]	0.8	1.2	2.4
Permanent set (%)	2	2	2	2
Hardness (Shore A)	24	27	35	47

[a]Not available due to low strain.

3.5 Interfacial interaction between PDIM and silica

A good interfacial interaction in the PDIM/silica nanocomposite is precondition for good mechanical properties. To investigate the interfacial interaction between PDIM and silica, a compound containing 100 phr of PDIM and 50 phr of silica was prepared on a two-roll mill firstly, denoted as PDIM/silica-a. Then, coupling reagent Si-69 and antioxidant were blended into the PDIM/silica-a, followed by a heat treatment under 120^{o}C for 5 min, denoted as PDIM/silica-b. Then next step was that the other additives, such as ZnO, SA, accelerators, and sulfur, were blended into the PDIM/silica-b to obtain the PDIM/silica nanocomposite.

FTIR technique was used to investigate the interfacial interaction between PDIM and silica, as shown in Fig. 4-8a. Figure 4-8a shows little differences in the peaks between 800 and 1400 cm^{-1} in FTIR spectra. The absorption peak at 1168 cm^{-1} which attributed to C-O-C stretching vibrations in PDIM chains shifts to 1163 cm^{-1} in the PDIM/silica compounds, while the absorption peak at 1106 cm^{-1} which attributed to Si-O-Si stretching vibration on silica surface shifts to 1100 cm^{-1} in the PDIM/silica compounds. These shifts indicate that hydrogen bonds might be formed between PDIM macromolecular chains (ester or carboxyl groups) and silica (silanol groups). However, a further direct verification on formation of the hydrogen bonds was not obtained due to the complicated system. A separate research on this topic will be done later. In addition, FTIR spectrum of PDIM/silica-b indicates that the adding coupling reagent would not make a difference on the shift of these absorption peaks.

A Rubber Process Analyzer (RPA) allows the reliable investigation of filler-polymer interaction [101,132]. It was found that both the initial modulus in the linear plateau (G'_0) and the infinite modulus at 400% strain (G'_∞) were the lowest for PDIM1 and increased with increasing carboxyl content, as shown in Fig. 8b. Additionally, G'_0 was almost constant from 0.56% to 20% strain for each PDIM elastomer. This phenomenon could hardly be observed in conventional silica-filled rubbers, such as SBR [133]. Generally, G'_0 is influenced by both filler-filler and filler-polymer interactions, which are two competing processes [134]. At low strain amplitudes, such as the 0.56% minimum strain specified for the RPA 2000, such filler-filler interactions can be particularly well measured. Far lower filler-filler interactions occur at higher strains [135]. In this study, all the G'_0 values remain almost constant for up to 20% strain, indicating that a strong filler network is not formed in the PDIM/silica compounds. The G'_0 is mostly affected by the interaction between PDIM and silica. The introduction of carboxyl groups is favorable to the formation of hydrogen bonds between the PDIM chains and silica surfaces. The hydrogen bonding can increase the interfacial interactions between PDIM and silica and decrease the filler-filler interactions, resulting in the good dispersion of fillers as indicated by the smallest decrease of modulus with strain, that is, the Payne effect (see PDIM1/silica, Fig. 4-8b). However, the increase of G'_0 and G'_∞ were observed with increasing carboxyl content (see PDIM3/silica and PDIM5/silica, Fig. 4-8b). In PDIM, these increases could be due to the covalent bonds between the carboxyl groups of PDIM and silica or the crosslinks in PDIM. In other words, the carboxyl groups can improve the interfacial interaction between PDIM and silica, resulting in a good dispersion of silica, which may play positive role in the reduction of rolling resistance.

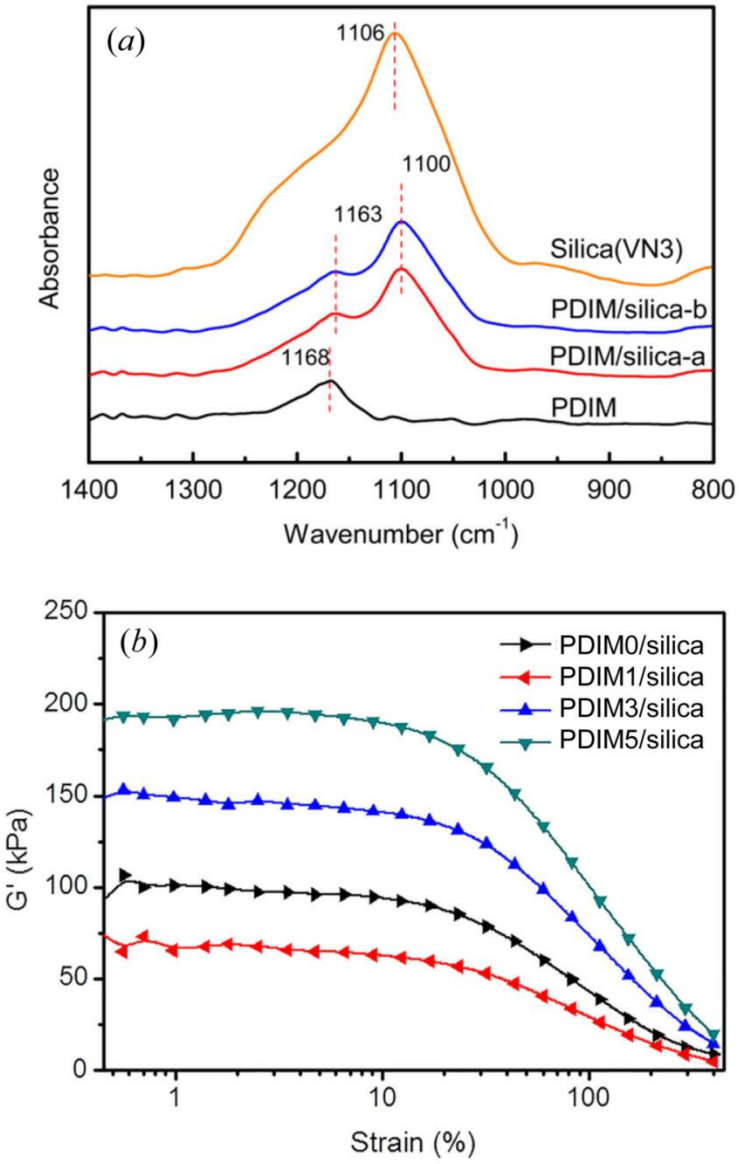

Figure 4-8. (*a*) FT-IR spectra of the PDIM, PDIM/silica compounds and silica; (*b*) Strain amplitude dependence of G' of PDIM/silica compounds.

To further investigate the dispersion of silica in the PDIM/silica compounds, representative fracture surfaces were studied by TEM. In Fig. 4-9, the light part represents the PDIM matrix and the dark part represents the filler particles that have been densely distributed in the matrix. Figure 4-9 shows that the dispersions of silica in the PDIM5/silica and the PDIM3/silica are more homogenous than those in the PDIM1/silica and the PDIM0/silica. As discussed above, the introduction of carboxyl groups is favorable to improve the interfacial interaction between PDIM and silica and the dispersion of silica in the PDIM/silica compounds.

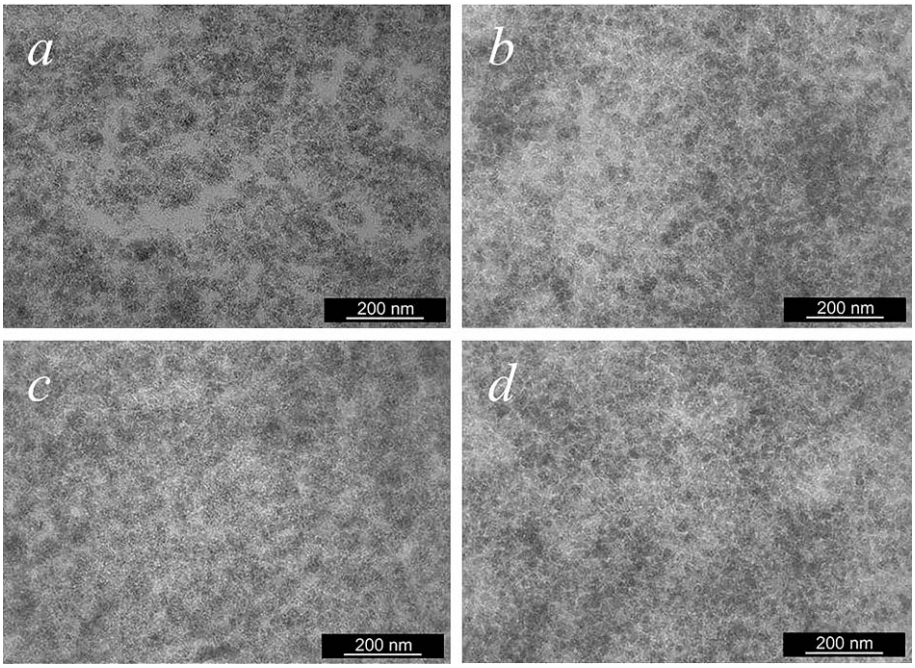

Figure 4-9. TEM observations of PDIM/silica compounds: (a) PDIM0/silica, (b) PDIM1/silica, (c) PDIM3/silica, (d) PDIM5/silica.

3.6 Curing characteristics and mechanical properties of PDIM/silica nanocomposites

Good mechanical properties are primary for PDIM/silica nanocomposites which are expected to be tire tread materials. PDIM0/silica, PDIM3/silica, and PDIM5/silica nanocomposites were used to investigate the mechanical properties of PDIM/silica nanocomposites. Most elastomer products are useless unless properly cured. Since the modulus of the elastomer increases dramatically during curing, it is used to monitor the curing progress. Figure 4-10*a* shows the characteristic curing curves for PDIM/silica nanocomposites at 150^{o}C. From the typical cure curves, it can be concluded that PDIM/silica nanocomposites could be effectively cross-linked by sulfur. Shapes of the curing curves of PDIM3/silica and PDIM5/silica nanocomposites are different compared with the PDIM0/silica nanocomposite, as shown in Fig. 4-10*a*. The delay of curing curves at initial stage for PDIM3/silica and PDIM5/silica nanocomposites can be explained by consumption of zinc oxide by carboxyl groups. The torque of PDIM0/silica nanocomposite increases during the whole curing process, because the PDIM0/silica nanocomposite is cured by sulfur alone. However, the PDIM3/silica and PDIM/silica nanocomposites were cross-linked by sulfur and zinc ion aggregates. The zinc ion aggregates can be decomposed at high temperature (*e.g.* 150^{o}C), resulting in a fast decrosslinking reaction. The fast decrosslinking reaction decreases the total crosslinking density at high temperature and makes the curing curves to be flat at later stage, leading to a

decreased torque. The mechanical properties of PDIM/silica nanocomposites are shown in Fig. 4-10*b* and Table 4-5. The tensile strength and stress at 100% strain of PDIM3/silica and PDIM5/silica nanocomposites are higher than those of PDIM0/silica nanocomposite, while the elongation at break of PDIM3/silica and PDIM5/silica nanocomposites is lower than that of PDIM0/silica nanocomposite. As mentioned above, the PDIM3/silica and PDIM5/silica nanocomposites were cross-linked by sulfur and zinc ion aggregates. The total crosslinking density of them should be higher than that of PDIM0/silica nanocomposite at room temperature. For rubber nanocomposites, high crosslinking density should generally lead to high tensile strength and low elongation at break. The PDIM5/silica nanocomposite has a high tensile strength (12.9 MPa) but a low elongation at break (131%), indicating that the PDIM/silica nanocomposites cannot be used as tire tread materials at present. More work on applications of PDIM elastomers should be done in future.

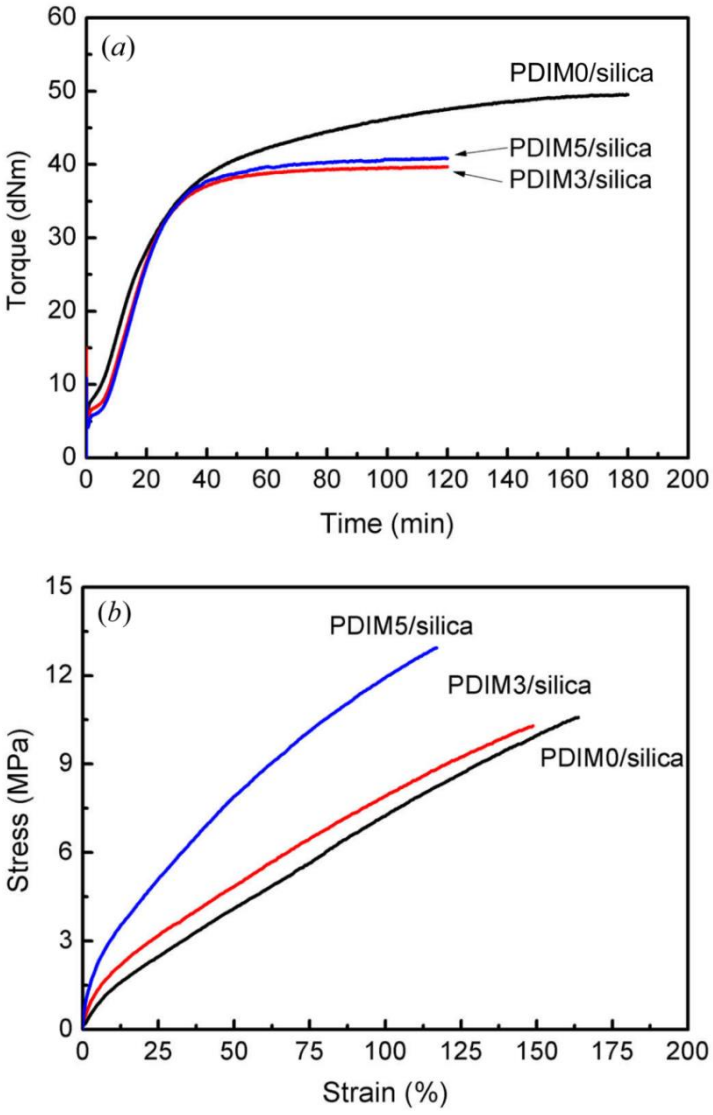

Figure 4-10. (*a*) Curing curves and (*b*) stress-strain curves of PDIM/silica nanocomposites.

Table 4-5. Mechanical properties of PDIM/silica nanocomposites.

PDIM/silica sample	PDIM0/silica	PDIM3/silica	PDIM5/silica
Tensile stress (MPa)	10.6	10.3	12.9
Elongation at break (%)	190	167	131
Stress at 100% strain (MPa)	7.3	7.9	11.9
Permanent set (%)	8	8	8
Hardness (Shore A)	78	84	92

3.7 Dynamic properties of PDIM/silica nanocomposites

Figure 4-11 shows the DMTA curves of PDIM/silica nanocomposites. Compared with that for the PDIM0/silica nanocomposite, the position of the loss factor (tan δ) peak for the PDIM3/silica and PDIM5/silica nanocomposites obviously shifts toward high temperature, indicating that the T_g of the PDIM macromolecular in the PDIM/silica nanocomposites was increased. The increase in T_g is mainly attributed to the strong interaction between carboxyl groups in PDIM chains and silanol groups on silica. Meanwhile, the amplitude of the tanδ peak obviously decreases, indicating that the moving ability of the polymer chains deteriorates. This may be attributed to increased crosslinking density from zinc ion aggregations. Unexpectedly, the tanδ at 60^{o}C of PDIM/silica nanocomposites increases with the increase of carboxyl groups in the PDIM chains, indicating an increased roll-resistance in tire tread applications. From the perspective of fuel consumption and CO_2 emission of road traffic, the PDIM/silica nanocomposites are not suitable for green tire applications.

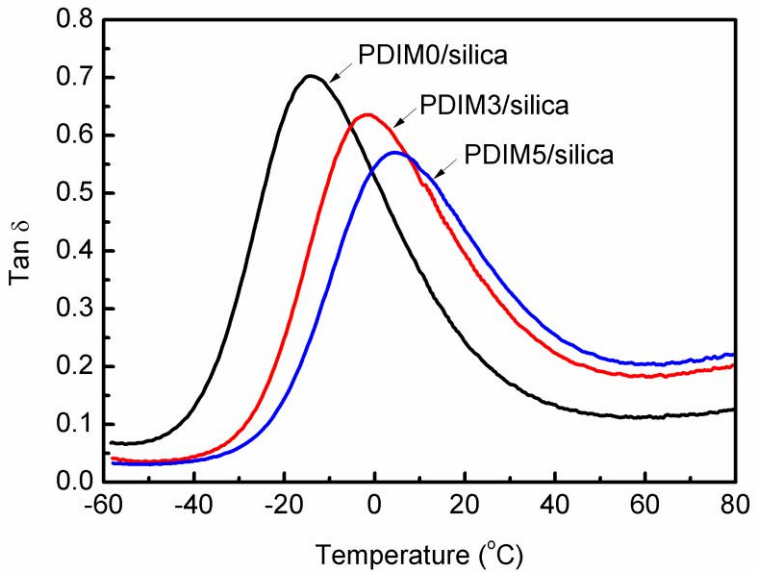

Figure 4-11. Temperature dependence of loss tangent (tanδ) for PDIM/silica nanocomposites.

4 Conclusions

Among the bio-based monomers, poly(dibutyl itaconate-*co*-isoprene-*co*-methacrylic acid) (PDIM) elastomer was synthesized successfully by redox emulsion polymerization under mild conditions. The yields of PDIM were over 70% after 12 hours in all runs. The PDIM elastomers had high number average molecular weight (>250 000 g/mol) and low glass transition temperatures (<-30^{o}C). The carboxyl contents in the PDIM elastomers were determined by butanone titration. With the increase of carboxyl content in the PDIM elastomers, the T_g was increased, with improved the physical properties and strong interfacial interaction between PDIM and silica. This resulted in a good dispersion of silica in the PDIM matrix, which might play a crucial role in reducing the rolling resistance. However, the investigation on mechanical and dynamic properties indicated PDIM/silica nanocomposites are not suitable for green tire tread materials.

Ackonwledgement: This work was supported by the National Natural Science Foundation of China (50933001, 51221102), the National Outstanding Youth Science Fund (50725310), the National Basic Research Program (973 Program) of China (2011 CB606003), the Beijing Nova Program (Z131102000413015), the Beijing Municipal Training Program Foundation for the Talents (2013D00303400041), and the Goodyear Tire & Rubber Company.

Preparation and performance of bio-based carboxylic elastomer/halloysite nanotubes nanocomposites with strong interfacial interaction

Abstract: Poly(dibutyl itaconate-*co*-isoprene-*co*-methacrylic acid) (PDIM)/halloysite nanotubes (HNTs) nanocomposites with strong interfacial interaction were prepared by co-coagulation of PDIM latex and HNTs aqueous suspension, followed by mechanical kneading with rubber additives. The interfacial interaction, thermal properties, morphology, and mechanical properties of the nanocomposites were investigated. The hydrogen bonds were confirmed in the nanocomposites. Morphology investigation showed uniform and individual dispersion of HNTs in the PDIM matrix. With the incorporation of HNTs into the PDIM matrix, the tensile strength and the fracture energy were significantly improved without sacrificing the extensibility. The improved mechanical properties were correlated to the co-coagulation and the strong hydrogen bonds. Especially, the morphology investigation of tensile fracture surfaces revealed a mechanism for the improved mechanical performance, in which the stress was efficiently transferred from PDIM to HNTs via hydrogen bonds and then the dissociation of the hydrogen bonds dissipated energy to increase the fracture energy of the nanocomposites.

Keywords: Biocomposite; Interface/interphase; Mechanical properties; Nanocomposites.

1. Introduction

One of the most important issues of material engineering in recent years has been the production of bio-based elastomers [91,136-141] and bio-based elastomer nanocomposites [142-146]. Bio-based elastomers derived from renewable resources are considered as potential substitutes for existing petroleum-based synthetic elastomers. The development of bio-based elastomers provides a feasible solution to the growing environmental threat and the depletion in fossil feedstocks. Various processable and crosslinkable bio-based elastomers have been designed and synthesized to meet engineering applications, such as poly(epoxidized soybean oil-*co*-decamethylene diamine) [45], polyester [46], and poly(di-alkyl itaconate-*co*-isoprene) (PDII) [50]. Different from other bio-based elastomers, cross-linkable PDII with high molecular weight was synthesized by emulsion polymerization, which is compatible with the traditional rubber synthetic process. To further increase the interfacial interaction between silica and PDII and improve the dispersion of silica in PDII, we used methacrylic acid as a third co-monomer to tailor PDII and prepared a bio-based carboxylic elastomer, poly(dibutyl itaconate-*co*-isoprene-*co*-methacrylic acid) (PDIM) [147].

Elastomers that do not contain any filler are practically insignificant in any application. Therefore, in practice an elastomer is commonly combined with fillers to form a composite. Significant improvement of mechanical properties of elastomer could be achieved through incorporation of nano-fillers into the elastomer matrix [148-156]. This improvement mainly depends on factors such as the dispersion state of the fillers as well as the interfacial interaction between the fillers and the elastomer matrix. Inorganic fillers, such as carbon black and silica [148-150], are mechanically introduced into an elastomer via milling. However, undesirable particulate agglomerates often remain even after rigorous milling. Layered silicates, such as montmorillonite [151-153] which has been widely used to reinforce an elastomer, belong to the structural family known as the 2:1 phyllosilicates. Stacking of the layers in layered silicates leads to a regular van der Waals gap between the layers. In addition, layered silicates are generally highly hydrophilic species and therefore are naturally incompatible with many types of elastomers. Improvement in strength, thermal and barrier properties was observed in elastomer/layered silicate nanocomposites [154]. However the preparation process and organic treatment of nanoclays are complex and costly [155]. Layered silicates need to be exfoliated to separate the layers, and good dispersion is needed for uniform distribution in the nanocomposites. In particular, one dimensional carbon nanotubes (CNTs) are considered to be one of the most promising reinforcement candidates for

elastomer modification due to their excellent mechanical, electrical and thermal properties [156]. Considering the relatively high cost and the difficulties in the preparation of CNTs and elastomer/CNTs nanocomposites, industrialization of CNTs-based nanocomposites in large scale is still pending.

Halloysite nanotubes (HNTs), one of naturally occurring clay minerals, is a new and prominent nano-filler composed of a multi-walled tubular-shaped crystalline nanostructure [157]. They combine the chemistry of montmorillonite and the geometry of carbon nanotubes. HNTs have an outer diameter of 40-70 nm, an inner diameter of 10-40 nm, and a length of 0.2-2 μm. Theoretically, the elastic modulus of HNTs is 230-340 GPa [159]. The environmental friendliness and economical availability make HNTs an important nano-filler for developing new organic/inorganic nanocomposites [158,159]. HNTs do not require exfoliation and can easily be dispersed in a polymer matrix. Additionally, HNTs have intrinsic hydrogen bonding interaction with polar polymers. In fact, in recent years they have been used to reinforce polymers and resins such as epoxy [160], polypropylene [161], polyamide [162], styrene rubber [163], natural rubber [164], and ethylene propylene diene monomer rubber [165]. However, a good HNTs dispersion and strong interfacial interaction in polymer/HNTs nanocomposites are still challenging due to the great polarity discrepancy and the chemical inertness of the rubbers. To obtain a good HNTs dispersion and strong interfacial interaction in polymer nanocomposites, modified methods for HNTs and various fabrication methods for polymer nanocomposites have been developed recently [159]. However, the natural raw HNTs have inhomogeneous quality worldwide. This limitation hinders large-scale industrialization of polymer/HNTs nanocomposite products.

In this study, PDIM/HNTs nanocomposites with improved mechanical properties were prepared by the co-coagulation of PDIM latex and HNTs aqueous suspension, followed by mechanical kneading with rubber additives on a two-roll mill at room temperature. PDIM, a polar bio-based elastomer, was synthesized by emulsion copolymerization and bare carboxyl groups in the chains. The co-coagulation of PDIM/HNTs aqueous suspension ensured the dispersion of HNTs in PDIM. The PDIM of the resulting nanocomposite was crosslinked by sulfur to form a covalently crosslinked network; meanwhile, the carboxyl groups of the PDIM formed hydrogen bonds with the oxygen-containing functional groups on the HNTs, which ensured strong interfacial interaction between PDIM and HNTs. As a result, the tensile modulus, tensile strength, and toughness of the PDIM/HNTs nanocomposites were significantly improved without sacrificing their extensibility.

2. Experimental

2.1 Materials

The poly(dibutyl itaconate-*co*-isoprene-*co*-methacrylic acid) denoted as PDIM, a bio-based carboxylic elastomer, was synthesized by redox emulsion copolymerization according to the following procedure. [147] Deionized water (250.0 g), sodium dodecyl benzene sulfonate (3.0 g), potassium phosphate tribasic (0.20 g), potassium chloride solution (0.50 g), Ferric ethylenediaminetetraacetic acid salt (0.04 g), and sodium hydroxymethane sulfonate (0.20 g) were added into a 0.5 L, three-necked flask fitted with a thermometer, a two-bladed anchor-type impeller, and a nitrogen inlet. Subsequently, dibutyl itaconate (70.0 g), isoprene (30.0 g), and methacrylic acid (5.0 g) were mixed in advance and added into the flask under a nitrogen atmosphere. The mixture was stirred at high speed (350 rpm) for 60 min to form stable and homogeneous latex. Later, the tert-butyl hydroperoxide (0.05 g) was injected into the flask and the stirring speed was reduced to 250 rpm. The polymerization was allowed to proceed at 20^{o}C for 12 hours for obtaining the target PDIM latex, and the hydroxylamine solution (50%, 0.4 g) was added to terminate the polymerization. The PDIM latex with a solid content of 29% was used to prepare PDIM/HNTs nanocomposites. The chemical structure of PDIM is shown in Scheme 4-1. The pristine HNTs were obtained from Hubei Province, China. Its structure is shown in Fig. 4-12. It was purified via a repeated dissolution/centrifugation process in the presence of sodium hexametaphosphate and then dried at 100^{o}C for 24 h. Zinc oxide, stearic acid, accelerators and sulfur were of industrial grade and used as-received.

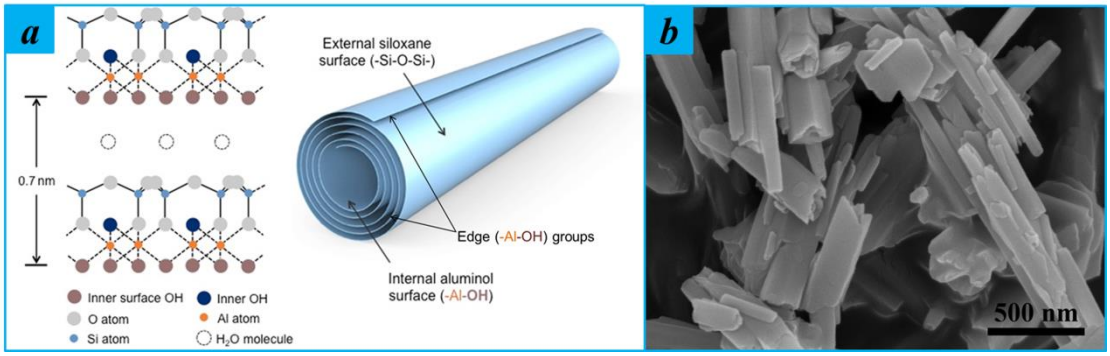

Figure 4-12. (*a*) Illustration of the structure and (*b*) SEM image of HNTs.

2.2 Preparation of PDIM/HNTs nanocomposites

The PDIM latex and HNTs aqueous suspension (10 wt.%) were mixed and stirred vigorously for 1h. The mixtures underwent ultrasonic treatment for 30 min, yielding a homogenous

reddish mixture. The resulting mixture was co-coagulated by gentle pouring into a calcium chloride aqueous solution (1 wt.%). The co-coagulated compounds were washed with de-ionized water for several times until no chlorine ions were detected. They were vacuum dried at 60^{o}C to a constant weight. The dried compounds were mechanically kneaded with rubber additives on a two-roll mill and then vulcanized at 150^{o}C under a pressure of 15MPa for optimum vulcanizing times as determined on a rotor-less rheometer. PDIM/HNTs *x* refer to a PDIM/HNTs nanocomposite with a HNTs theoretical content of *x* phr (parts per one hundred parts of rubber). For comparison, the vulcanizate of unfilled PDIM was also prepared. The compositions of the PDIM/HNTs nanocomposites are shown in Table 4-6.

Table 4-6. Compositions of PDIM/HNTs nanocomposites [a]

Sample	PDIM	PDIM/HNTs 5	PDIM/HNTs 10	PDIM/HNTs 15	PDIM/HNTs 20	PDIM/HNTs 30
PDIM (phr) [b]	100	100	100	100	100	100
HNTs [c] (phr)	0	5	10	15	20	30

[a] Rubber additives: zinc oxide (5.0 phr), stearic acid (0.5 phr), *N*-isopropyl-*N*′-phenyl-p-phenylenediamin (1 phr), 2-mercaptobenzothiazole (0.7 phr), *N*-cyclohexyl-2-benzothiazole (1.0 phr), and sulfur (1.0 phr). [b] phr: parts per hundred of rubber. [c] Theoretical content of HNTs in preparation of PDIM/HNTs compounds.

2.3 Measurements and characterization

The FTIR spectra of the co-coagulated PDIM/HNTs compounds without any other additives were conducted on a Bruker Tensor 27 spectrometer. They were acquired by scanning the specimens in the wavenumber range from 400 cm^{-1} to 4000 cm^{-1} for 128 times with a resolution of 2 cm^{-1}. X-ray photoelectron spectroscopy (XPS) measurements were carried out on an ESCALAB 250 XPS system (Thermo Electron Corporation, USA) with an Al Kα X-ray source (1486.6 eV photons). The core-level signals were obtained at a photo electron takeoff angle of 45^{o} with respect to the sample surface. The X-ray source was run at a reduced power of 150 W. The pressure in the analysis chamber was maintained at 1.33×10^{-6} Pa. Differential scanning calorimetric (DSC) analysis was carried out on a Mettler-Toledo differential scanning calorimeter under nitrogen flow (50 mL/min) at a heating rate of 10^{o}C/min. Thermogravimetric analysis (TGA) of PDIM/HNTs compounds was performed on a thermal gravimetric analyzer of Mettler-Toledo from 30 to 800^{o}C at a rate of 10^{o}C/min with a steady nitrogen flow of 50 mL/min. For calculating the HNTs contents in the PDIM/HNTs compounds, the TGA of HNTs as well as PDIM was also carried out under the same

conditions. The following equation was used to calculate the HNTs contents in the PDIM/HNTs compounds:

$$w = \frac{b-a}{c-b} \times 100 \quad (4\text{-}5)$$

where w is the parts per one hundred parts of PDIM in the PDIM/HNTs compound, and a, b and c are the residues of the PDIM gum, PDIM/HNTs compound and HNTs, respectively. Scanning electron microscopy (SEM) was performed on a Hitachi S-4800 scanning electron microscope (Hitachi, Japan). The surface of the sample was sputtered with a thin layer of gold prior to the analysis. The SEM analysis was carried out at an accelerating voltage of 5 kV. Transmission electron microscopy (TEM) images were recorded on FEI Tecnai G2 20 S Twin TEM at 200 kV. The ultrathin section specimens of PDIM/HNTs nanocomposites for the TEM observation were prepared using a cro-ultramicrotome (Leica EM UC6, Germany) and mounted on mesh copper grids. The vulcanizing times of the PDIM/HNTs nanocomposites were determined at 150^{o}C on a rotor-less rheometer MR-C3 (RAD Co., Ltd., Beijing, China). Tensile tests of the PDIM/HNTs nanocomposites were conducted according to ASTM standard (D412: dumbbell-shaped), and the specimens were tested on a tensile apparatus (CMT4104, Shenzhen SANS Testing Machine Co., Ltd., China) at 25^{o}C. The crosshead speed was 500 mm/min. For each sample, values obtained from five specimens were averaged.

3. Results and discussion

3.1 Interfacial interaction between HNTs and PDIM

In order to obtain good dispersion of HNTs in the PDIM, the PDIM/HNTs compounds were prepared by co-coagulation of PDIM latex and HNTs aqueous solution, which is depicted in Scheme 4-2. In this process, with the addition of the PDIM/HNTs aqueous suspension into a calcium chloride aqueous solution, the latex particles of PDIM coagulated promptly and consequently the HNTs among the particles were embedded in the coagulated PDIM. The co-coagulation effectively prevented the HNTs from aggregation and ensured their uniform dispersion in the PDIM matrix [102,166]. As controls, poly(dibutyl itaconate-*co*-isoprene) (PDI) and PDI/HNTs 20 nanocomposite were prepared following the same recipe and process.

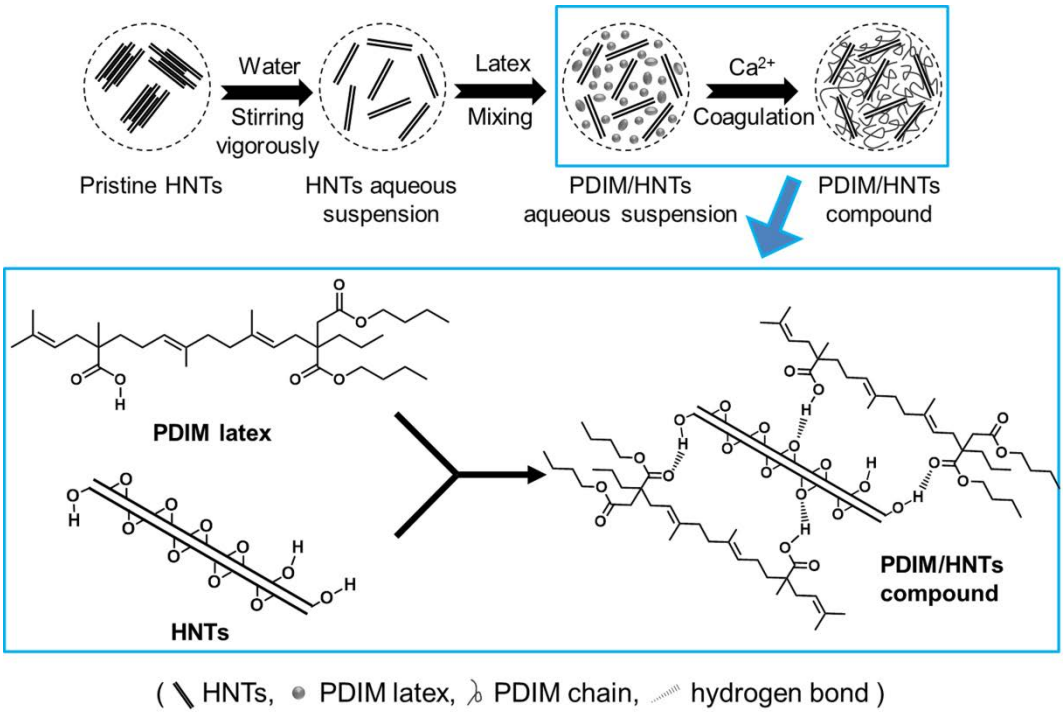

Scheme 4-2. Illustration of the co-coagulation in the preparation of PDIM/HNTs compounds.

Unlike other layered silicates (*e.g.* montmorillonite), HNTs exhibits a predominantly hollow tubular structure resulting from a mismatch in the two-layered alignment between the tetrahedral sheet of silica and the octahedral sheet of alumina. As a consequence, siloxane groups (Si-O-Si) are located on the external surface of HNTs and aluminol groups (Al-OH) are located on the inner surface and edges of HNTs, resulted in a curly structure [167]. FTIR technique was used to verify the formation of hydrogen bonds in the PDIM/HNTs compound. Figure 4-13 shows the ATR-FTIR spectra of HNTs, PDI/HNTs 20 and PDIM/HNTs 20 compounds. The absorption bands at 912 cm^{-1} and 1087 cm^{-1} are related to the inner Al-OH vibrations and in-plane Si-O-Si stretching vibrations in HNTs, respectively, while the absorption bands at 691 cm^{-1} and 754 cm^{-1} are related to the perpendicular Si-O-Si stretching vibrations [168]. In Fig. 4-13b, the absorption bands at 691, 754, and 1087 cm^{-1} are shifted to 688, 752, and 1080 cm^{-1} for the PDI/HNTs 20 compound, respectively, indicating that weak interfacial interaction exists between HNTs and PDI. This weak interfacial interaction may be caused by physical adsorption leading to formation of bound rubber in the PDI/HNTs 20 compound. Bound rubber is a common phenomenon in filler reinforced rubber composites, and the filler-polymer interaction involved in the formation of bound rubber is essentially a physical adsorption that is generally weaker than the hydrogen bonding interaction [169]. After introducing carboxyl groups (-COOH), the absorption bands at 691, 754, and 1087 cm^{-1} are further shifted to 684, 741, and 1070 cm^{-1} for the PDIM/HTNs 20 compound, respectively.

These obvious red-shifts demonstrate strong interfacial interaction exists in the PDIM/HNTs 20 compound due to the formation of hydrogen bonds between Si-O-Si at the surface of HNTs and -COOH in the PDIM chains. However, direct verification of hydrogen bonds between Al-OH at the inner surface of HNTs and -COOH at the PDIM chains seems challenging because the Al-OH inside the lumen of HNTs is not easily accessible to the PDIM chains, as indicated by the absorption bands at 912 cm^{-1} in Fig. 4-13. Thus, the FTIR results confirm the fact that the hydrogen bonds in the PDIM/HNTs compounds are formed between the siloxane groups on the HNTs and the carboxyl groups in the PDIM.

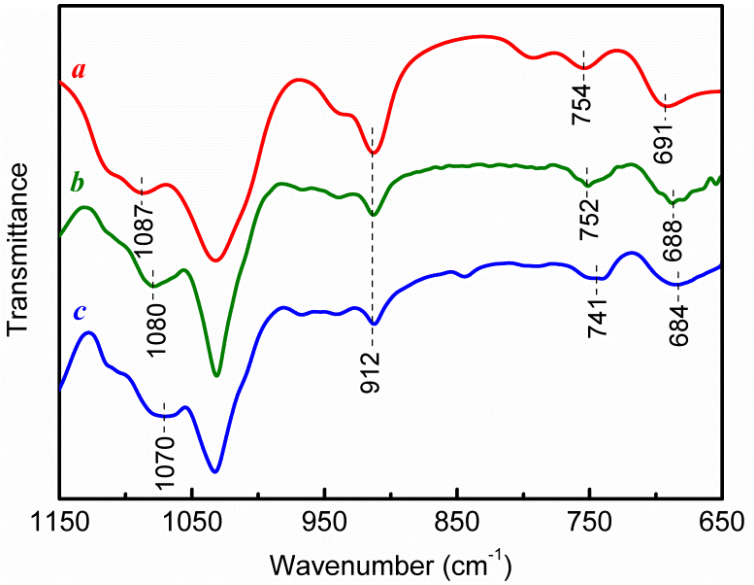

Figure 4-13. ATR-FTIR spectra of (*a*) HNTs, (*b*) PDI/HNTs 20 compound, and (*c*) PDIM/HNTs 20 compound.

Furthermore, XPS survey was utilized to characterize the formation of hydrogen bonds between HNTs and PDIM. It is believed that the formation of hydrogen bonds leads to the variation of the chemical environment for the hydrogen bond functionalities, which can be characterized by the variation of binding energy of the atoms related to the hydrogen bonds via XPS survey [116,170,171]. Figure 4-14 shows the high-resolution XPS spectra of aluminum and silicon atoms of HNTs, PDI/HNTs 20 and PDIM/HNTs 20 compounds, respectively. As shown in Fig. 4-14, there are characteristic negative shifts in the binding energies of aluminum atoms and silicon atoms, which are connected to the oxygen atoms in the hydrogen bonds. The characteristic peak of aluminum at 74.40 eV is shifted to 74.33eV for PDI/HNTs 20 compound and 74.32 eV for PDIM/HNTs 20 compound, while the characteristic peak of silicon at 102.58 eV is shifted to 102.47 eV for PDI/HNTs 20

compound and 102.13 eV for PDIM/HNTs 20 compound. There are no significant shifts in the aluminum spectra for both PDI/HNTs and PDIM/HNTs compounds, because only the Al-OH located on the edges of HNTs can form weak interfacial interaction with polymers. From the silicon spectra, the shift of binding energy of silicon atoms in the PDIM/HNTs compound (0.45 eV) is more significant than that in the PDI/HNTs compound (0.11 eV). The smaller shift of binding energy of silicon atoms for the PDI/HNTs compound should be attributed to weak interfacial interaction between surface silanol groups on the HNTs defects and ester groups on the PDI chains. Kerber *et al*. have demonstrated that the formation of hydrogen bonds can result in XPS binding energy shifts following certain pattern, *i.e.*, for **M**-**O**-**H**---**O**-**M'** hydrogen bonding system the binding energies of **M** and **M'** units will be decreased [169]. It is believed that the formation of hydrogen bonds between the Si-O-Si on the HNTs and the -COOH on PDIM chains results in the more significant shifts of the binding energy of silicon atoms for PDIM/HNTs compound. Consequently, the strong interfacial interaction in PDIM/HNTs compound is mainly attributed to the formation of hydrogen bonds between the HNTs and the PDIM. The analyzed results of XPS spectra are completely in accordance to that of FTIR spectra, and further confirm the formation of hydrogen bonds in the PDIM/HNTs compound, as illustrated in Scheme 4-2. In addition, some indirect verification of hydrogen bonds in the PDIM/HNTs nanocomposites were obtained from morphology analysis and mechanical performances, which further substantiate the formation of hydrogen bonds between HNTs and PDIM.

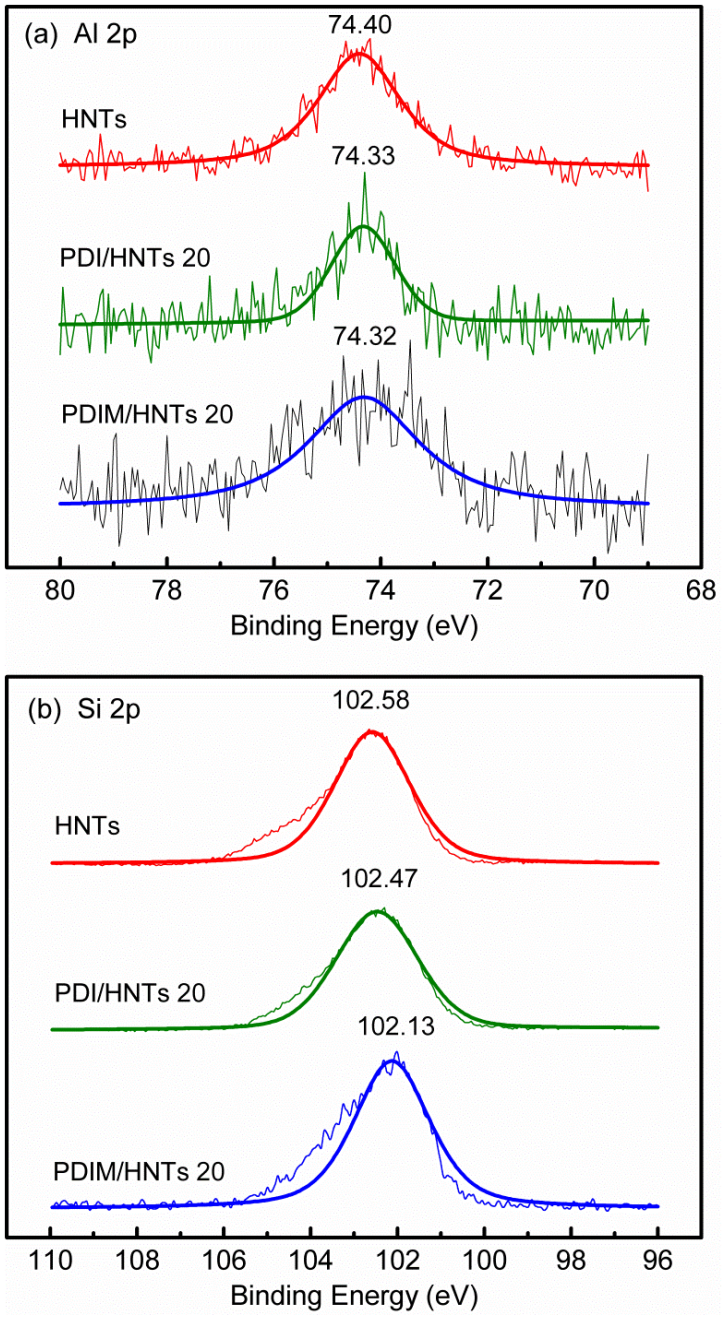

Figure 4-14. High-resolution XPS spectra of (a) aluminum and (b) silicon atoms in the pristine HNTs, PDI/HNTs 20 compound, and PDIM/HNTs 20 compound (bold lines: fitting data).

3.2 Thermal properties of PDIM/HNTs nanocomposites

Figure 4-15 shows typical DSC heating thermograms of the PDIM and PDIM/HNTs compounds. The PDIM gum is amorphous, with a glass transition temperature (T_g) of -32^{o}C. The T_g of the PDIM/HNTs 5 compound is the same as that of the PDIM. In other words, the

T_g of the PDIM of the PDIM/HNTs 5 compound is not affected by the presence of 5 phr of HNTs. In fact, the volume fraction of the HNTs in the PDIM/HNTs 5 compound could be much lower than the nominal value of the incorporated HNTs because HNTs might have partly lost during the co-coagulation (see the thermogravimetric analysis results). The small volume fraction of the HNTs does not allow forming enough hydrogen bonds with the PDIM chains to alter its T_g. As the volume fraction of the HNTs of the PDIM/HNTs compound increases, the T_g of the PDIM increases slightly with respect to that of the PDIM alone. The increase in T_g of the compounds might be due to (i) the effect of a small amount of dispersed HNTs on the free volume of the PDIM and (ii) the fact that the HNTs attached to the PDIM by hydrogen bonds restricts, partly, the segmental motion of the PDIM chains [172-174].

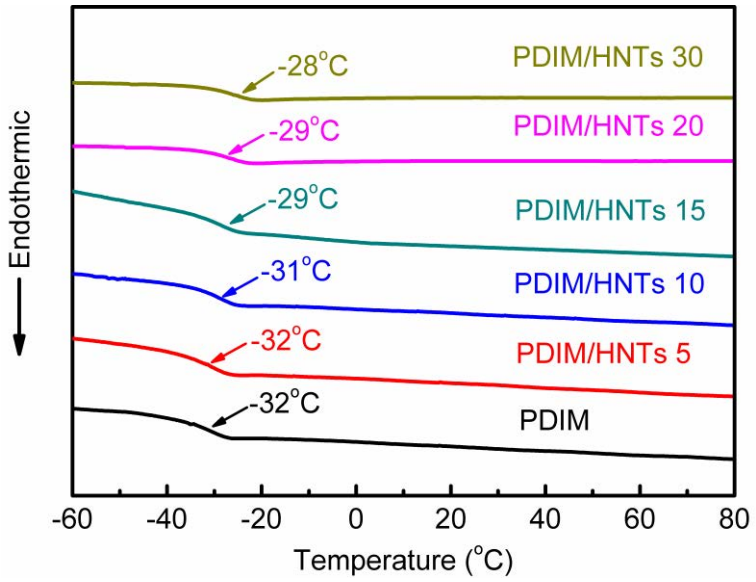

Figure 4-15. DSC curves of the PDIM gum and PDIM/HNTs compounds.

TGA and DTG curves of the PDIM, pristine HNTs, and PDIM/HNTs compounds are shown in Fig. 4-16. The content of the HNTs does not have a significant effect on the thermal stability of the PDIM/HNTs compounds. However, the integral procedural decomposition temperatures were slightly increased by increasing the content of HNTs in the PDIM/HNTs compounds， due to the higher thermal stability of HNTs (Fig. 4-16, dashed circle). Additionally, the TGA curves are used to determine HNTs contents of the PDIM/HNTs compounds. The residue of the PDIM/HNTs compound consists of the residue of the HNTs and that of the PDIM. Equation (4-5) is used to calculate the HNTs contents of all the PDIM/HNTs compounds, as shown in Table 4-7. The results reveal that the calculated HNTs contents of all the PDIM/HNTs compounds are systematically smaller than the nominal

values of the incorporated HNTs due to the HNTs or the PDIM losses during the co-coagulation.

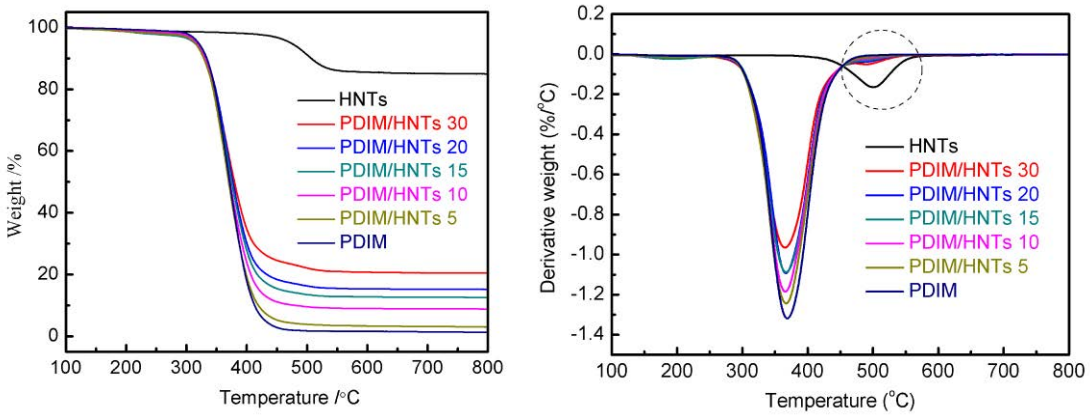

Figure 4-16. TGA (left) and DTG (right) curves of PDIM, HNTs, and PDIM/HNTs compounds.

Table 4-7. Calculated HNTs contents in the PDIM/HNTs compounds.

Samples	Residue [b] (%)	PDIM[c] (phr)	HNTs[d] (phr)	Volume fraction of HNTs (vol.%)
HNTs	85.26	/	100	/
PDIM	1.76	100	/	/
PDIM/HNTs 5[a]	3.31	100	1.9	1.0
PDIM/HNTs 10[a]	8.90	100	9.4	4.9
PDIM/HNTs 15[a]	12.85	100	15.3	7.7
PDIM/HNTs 20[a]	15.26	100	19.3	9.5
PDIM/HNTs 30[a]	21.59	100	31.1	14.5

[a] *m* in the PDIM/HNTs *m* denotes the nominal value of the incorporated HNTs (phr); [b] determined based on the TGA results; [c] set value of PDIM is 100 phr for the calculation of HNTs content; [d] calculated according to equation (1).

3.3 Morphology of PDIM/HNTs nanocomposites

Knowledge about phase morphologies is necessary for establishing a relationship between the microstructure and mechanical properties [175]. Generally, the state of dispersion nano-fillers in a polymer matrix is a decisive factor that dictates the ultimate properties of nanocomposites. Homogeneous dispersion of filler especially in a nano-scale leads to high mechanical properties of the resulting composites [172, 173]. On the contrary, aggregated fillers in the polymer matrix act as the stress-concentration points, leading to deterioration of mechanical

properties [176,177]. Therefore, representative fracture surfaces of the prepared PDIM/HNTs nanocomposites were studied by SEM and TEM. Figure 4-17 shows the state and degree of dispersion of the HNTs in the PDIM matrix. HNTs are uniformly dispersed in the PDIM at low filler content. At high filler content, the state of dispersion of HNTs is still good, since partial aggregation of the HNTs is almost inevitable (Fig. 4-17*d*). The individual dispersion of HNTs into PDIM is further confirmed by a TEM image of the PDIM/HNTs 20 nanocomposite (Fig. 4-17*c*). It is owing to the virtue of the co-coagulation and the hydrogen bonds between the HNTs and the PDIM. In addition, the HNTs in Fig. 4-17*c* shows a wide range of diameter and length, which was perhaps caused by the processing conditions. However, the HNTs before the compounding (Fig. 4-12*b*) shows the same as that after the compounding, indicating that the processing conditions had not significant influence on the dimension of the HNTs.

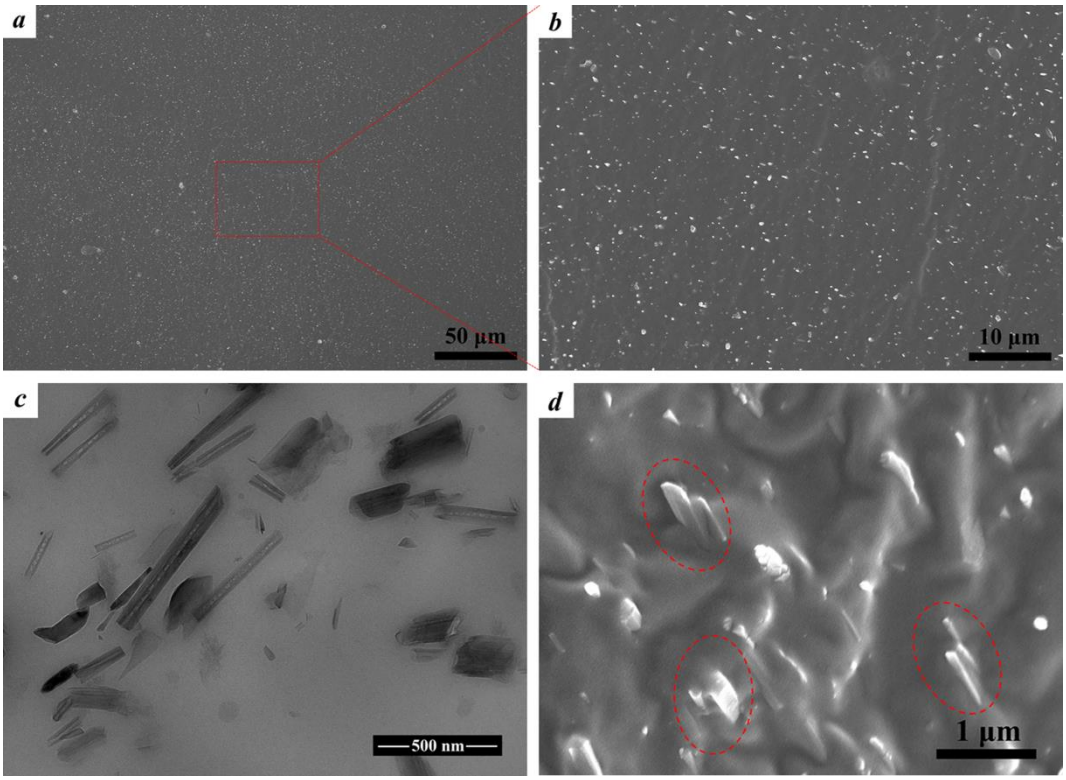

Figure 4-17. Morphologies of PDIM/HNTs nanocomposites. SEM images of (*a* and *b*) PDIM/HNTs 20 nanocomposite show a good dispersion state of HNTs in the PDIM matrix. TEM image of (*c*) PDIM/HNTs 20 nanocomposite shows individual dispersion of HNTs in the PDIM matrix. SEM image of (*d*) PDIM/HNTs 30 nanocomposite in high magnification shows partial aggregation (red dashed circle) of HNTs in the PDIM matrix.

3.4 Mechanical properties of PDIM/HNTs nanocomposites

Table 4-8. Optimum vulcanizing times for vulcanizations of PDIM/HNTs nanocomposites and unfilled PDIM

Samples	Optimum vulcanizing times (min)
PDIM	29.2
PDIM/HNTs 5	24.6
PDIM/HNTs 10	19.3
PDIM/HNTs 15	15.4
PDIM/HNTs 20	18.1
PDIM/HNTs 30	21.5

The PDIM/HNTs nanocomposites were vulcanized at 150^{o}C and 15 MPa for optimum vulcanizing times as determined on a rotor-less rheometer (Table 4-8). After the vulcanization, the PDIM/HNTs nanocomposites and the unfilled PDIM were stretched on the tensile tester. Figure 4-19(*a*) shows the tensile strength and the fracture energy of the PDIM/HNTs nanocomposites as a function of HNTs content. Figure 4-18 shows typical stress-strain curves of the PDIM/HNTs nanocomposites as well as the unfilled PDIM vulcanizate. Table 4-9 summarizes their mechanical properties. The unfilled PDIM vulcanizate has a tensile modulus (stress at 100% strain, similarly hereinafter) of 0.8 MPa, a tensile strength of 3.9 MPa, and an elongation at break of 386%. With the incorporation of the HNTs into the PDIM, the tensile modulus and tensile strength of the PDIM/HNTs nanocomposites are significantly improved without sacrificing their extensibility. For example, compared with the unfilled PDIM vulcanizate, the tensile modulus and tensile strength of the PDIM/HNTs 20 nanocomposite are increased to 1.7 MPa and 10.7 MPa, respectively, while the elongation at break is improved from 386% to 566%. Moreover, the fracture energy (the area surrounded by the stress-strain curve) of the PDIM/HNTs 20 nanocomposite is improved by a factor of 3.2, indicating an improvement in ductility [178,179]. As for the unsatisfactory mechanical properties of the PDIM/HNTs 5 nanocomposite, they should be due to the low HNTs content (see Table 4-7). The PDIM/HNTs 20 nanocomposite exhibits the best mechanical properties with a tensile strength of 10.7 MPa, an elongation at break of 566%, and fracture energy of 25.4 J/cm^3. The PDIM/HNTs 30 nanocomposite with a higher HNTs content, however, does not exhibit even better mechanical properties, but brings about a slight decrease in mechanical properties compared to the PDIM/HNTs 20 nanocomposite. Similar phenomena have also

been observed in a previous study [177]. This adverse phenomenon would originate from the inevitable aggregation of the HNTs in the PDIM/HNTs 30 nanocomposite (Fig. 4-17*d*). It is believed that the improvement in mechanical properties of the PDIM/HNTs nanocomposites largely depends on the dispersion of the HNTs, the interfacial interaction between the HNTs and the PDIM and the orientation of the HNTs. The pullout (Fig. 4-22*a* and *b*) of HNTs as well as the rupture (Fig. 4-22*c* and *d*) of interface between HNTs and matrix implies that the stress transfers efficiently from the PDIM to the HNTs via hydrogen bonds and that the dissociation of the hydrogen bonds dissipates much energy to improve the ductility of the nanocomposites. Moreover, orientation of the HNTs is observed from the SEM of the tensile fracture surface of the PDIM/HNTs 20 nanocomposite (Fig. 4-22*e* and *f*). It contributes to the improvement in modulus and strength. To find out the root cause of the orientation of HNTs, orthogonal fracture surfaces of the un-stretched PDIM/HNTs 20 nanocomposite were investigated by using SEM according to a previous method [180]. Figure 4-20 shows the SEM images of orthogonal fracture surfaces of the un-stretched PDIM/HNTs 20 nanocomposite. A certain degree of orientation of the HNTs is observed from the fracture surface along with the stretching direction, indicating that the processing condition is the main cause of the orientation of HNTs. Theoretically, testing condition is another cause of orientation of fillers in nanocomposites [181]. Thus, the high orientation of HNTs in PDIM/HNTs nanocomposites should attributed to both processing and testing conditions.

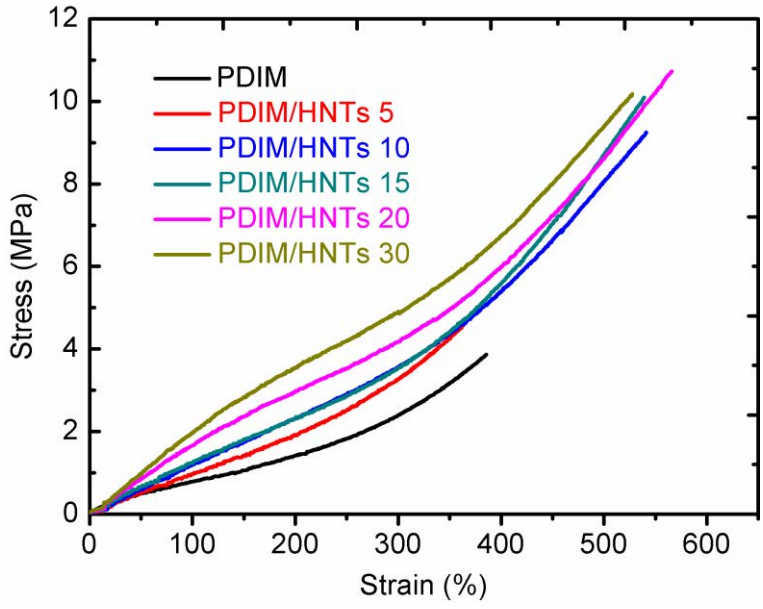

Figure 4-18. Stress-strain curves of unfilled PDIM vulcanizate and PDIM/HNTs nanocomposites.

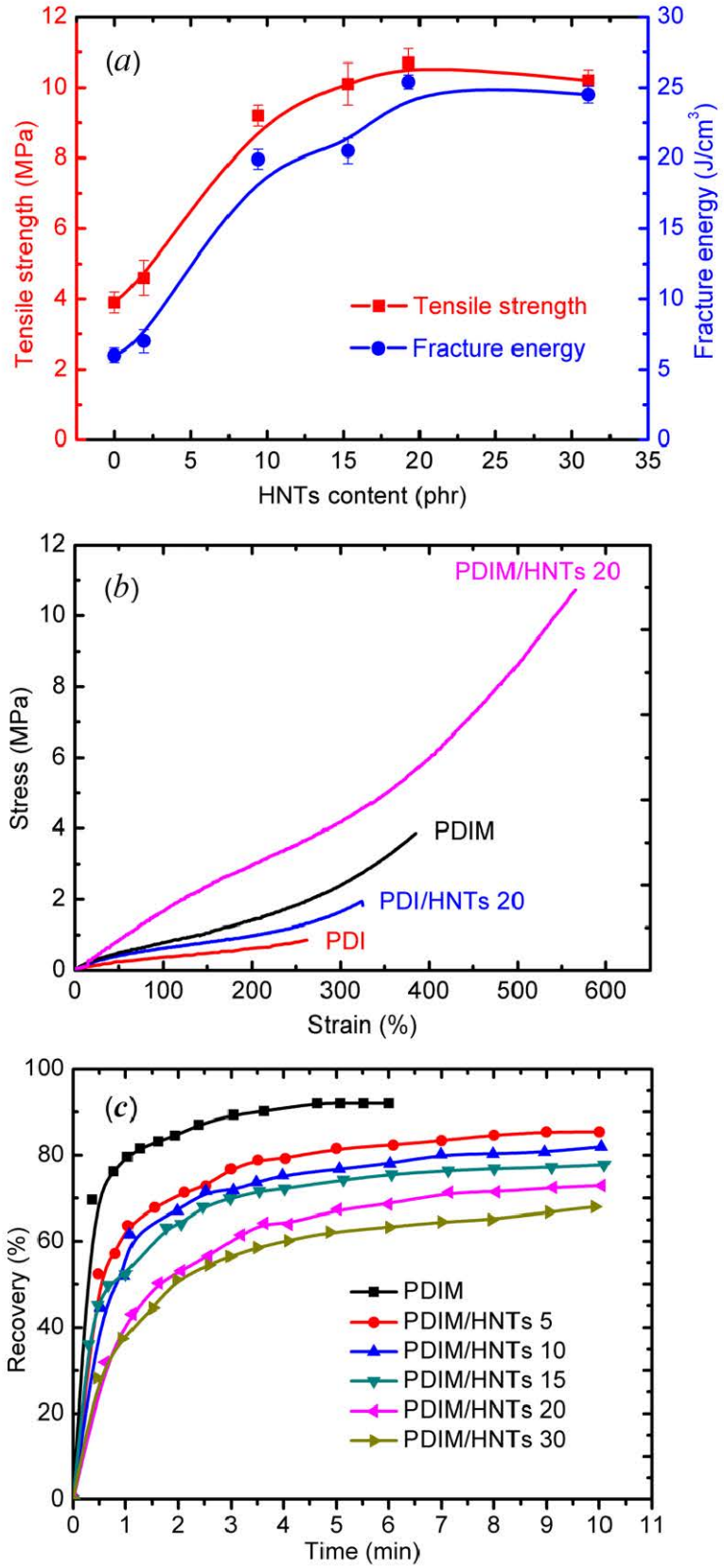

Figure 4-19. (a) Tensile strength and fracture energy of the PDIM/HNTs nanocomposites as a function of HNTs content. (b) Stress-strain curves of the controls (PDI and PDI/HNTs 20 nanocomposite) as well as PDIM and PDIM/HNTs 20 nanocomposite. (c) Recovery of the PDIM and the PDIM/HNTs nanocomposites as functions of time.

Table 4-9. Mechanical properties of the unfilled PDIM, the PDIM/HNTs nanocomposites and the controls.

Samples	Tensile modulus (MPa)	Tensile strength (MPa)	Elongation at break (%)	Fracture energy (J /cm^3)
PDIM	0.8±0.1	3.9±0.3	386±23	6.0±0.5
PDIM/HNTs 5	1.0±0.2	4.6±0.5	364±31	7.0±0.8
PDIM/HNTs 10	1.2±0.1	9.2±0.3	541±26	19.9±0.7
PDIM/HNTs 15	1.2±0.3	10.1±0.6	539±34	20.5±0.9
PDIM/HNTs 20	1.7±0.2	10.7±0.4	566±24	25.4±0.5
PDIM/HNTs 30	2.0±0.1	10.2±0.3	528±19	24.5±0.6
PDI	0.4±0.1	0.9±0.2	262±25	1.2±0.3
PDI/HNTs 20	0.6±0.1	1.9±0.3	325±28	2.9±0.5

The typical stress-strain curves of the control samples are shown in Fig. 4-19(*b*) and the data are summarized in Table 4-9. The strength and the elongation at break of PDI vulcanizate are 0.9 MPa and 262%, respectively. After the PDI is filled with 20 phr HNTs, the resulting PDI/HNTs nanocomposite exhibits unsatisfactory improvement in mechanical properties with a tensile strength of 1.9 MPa, an elongation at break of 325%, and the fracture energy of 2.9 J/cm^3, which are much inferior to those of the PDIM/HNTs nanocomposites. The investigation on morphology of the PDI/HNTs nanocomposite could give some explanation for its inferior mechanical properties. Aggregation of unoriented HNTs is observed from the SEM of the tensile fracture surface of the PDI/HNTs nanocomposite (Fig. 4-21), indicating the weak interfacial interaction between PDI and HNTs. PDI does not possess pendant carboxyl groups but only side ester groups. The ester groups on PDI chains are possible able to form hydrogen bonds with the rare Al-OH groups at the edges of HNTs but the abundant Si-O-Si at the surface of HNTs, which is why the interfacial interaction in PDI/HNTs nanocomposite is weak. The aggregation of HNTs and weak interfacial interaction between PDI and HNTs are responsible for the mechanical properties of PDI/HNTs nanocomposite.

Rubber elasticity, a well-known example of hyperelasticity, may be operationally defined as very large deformability with essentially complete recoverability. Figure 4-19c shows the recovery of the PDIM/HNTs nanocomposites as functions of time. Without HNTs, PDIM example takes a short time (5 min) to reach 90 % recovery. With HNTs, PDIM/HNTs nanocomposites need more and more time to reach their equilibrium state from fracture, and show lower and lower recovery. The rubber elasticity essentially depends on entropy change

of polymer chains in rubber networks. When the polymer chains are stretched, ideally, the entropy is reduced due to molecular conformation changes. Therefore, there is a restoring force in the polymer chains. Once the external force is removed, the restoring force will make the polymer chains to return to their equilibrium or un-stretched state, such as a high entropy random coil configuration. This is the reason why the PDIM sample takes a short time to reach a high recovery. After the PDIM/HNTs nanocomposites were stretched, the HNTs may be out of their original positions and the hydrogen bonds between the HNTs and the PDIM chains could be re-arranged. The position change of HNTs and the re-arrangement of the hydrogen bonds restrain the PDIM chains from returning to their un-stretched state, resulting in the weak recovery of the PDIM/HNTs nanocomposites.

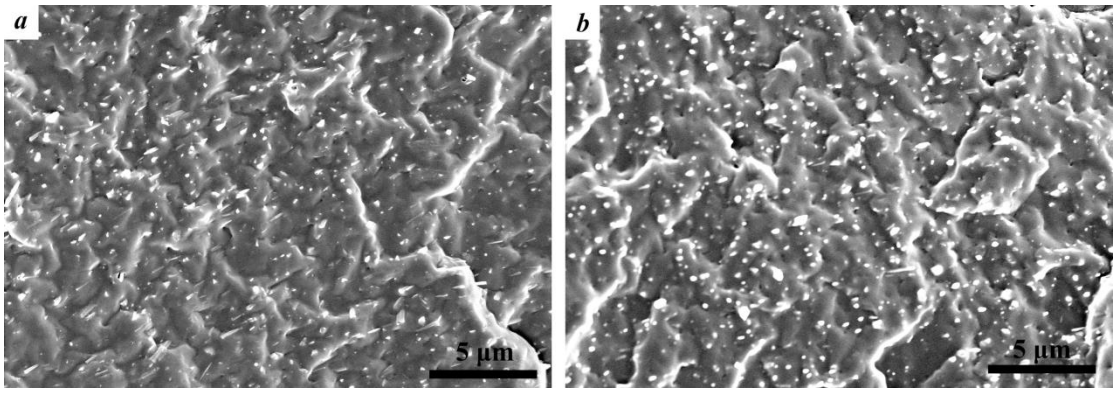

Figure 4-20. SEM images of un-stretched PDIM/HNTs 20 nanocomposite. (a) Fracture surface was along with the stretching direction. (b) Fracture surface was perpendicular to the stretching direction.

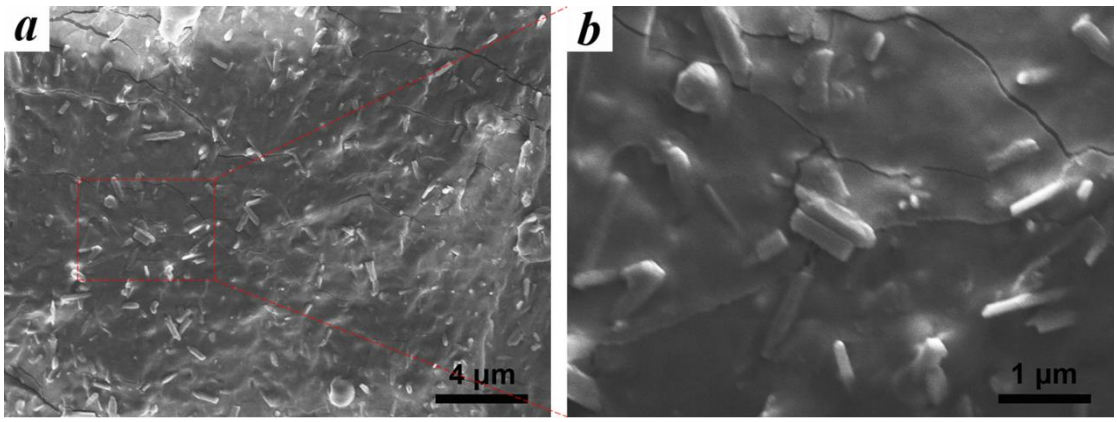

Figure 4-21. SEM images of PDI/HNTs 20 nanocomposite.

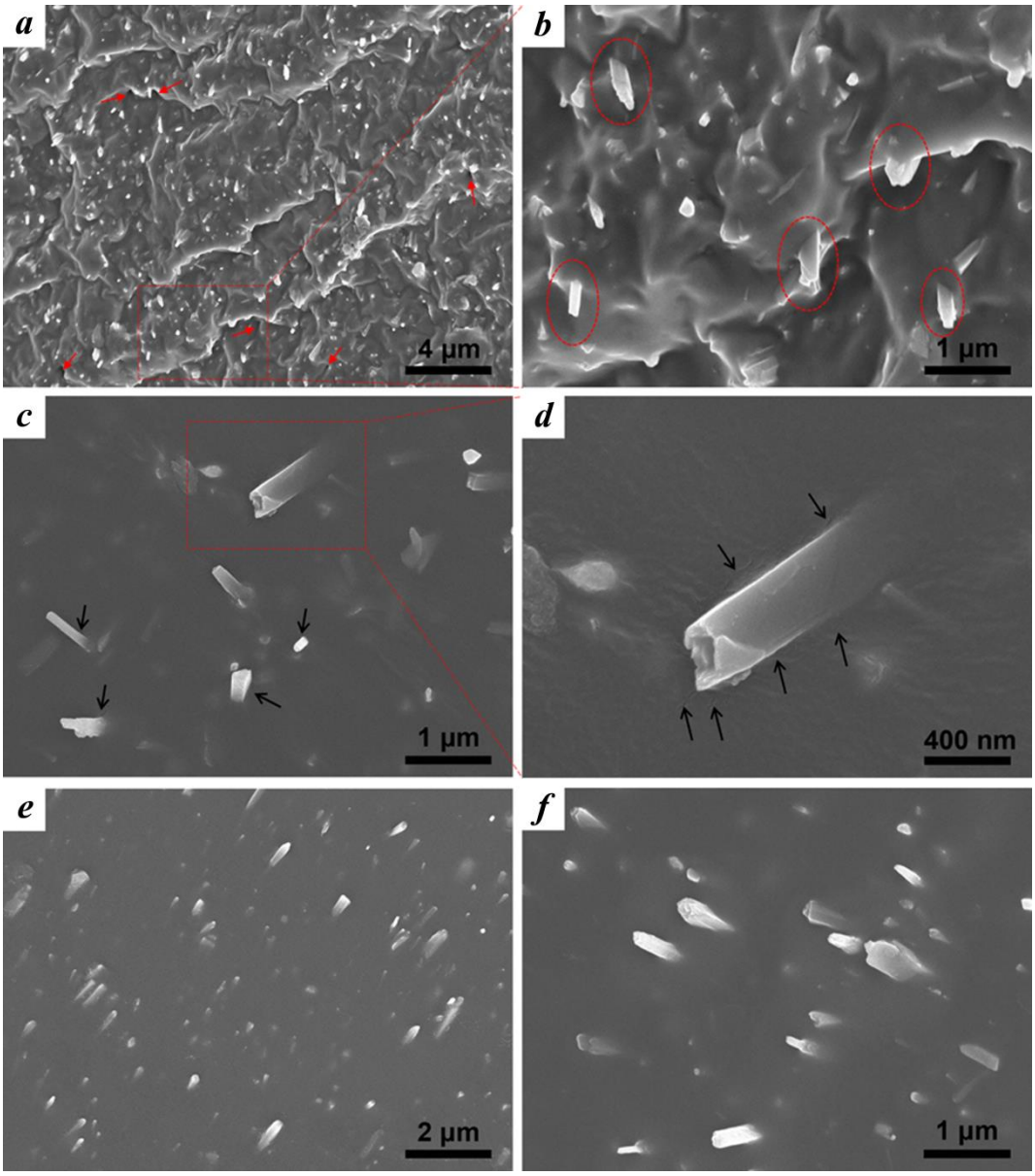

Figure 4-22. SEM images of the tensile fracture surface of the PDIM/HNTs 20 nanocomposite: (a and b) pullout of HNTs (red dashed circle), and holes and grooves remaining after pullout of HNTs (red arrows); (c and d) rupture of a HNT, indicating the load transfer between PDIM and HNTs via hydrogen bonds; (e and f) orientation of HNTs in PDIM/HNTs nanocomposites.

3.5 Mechanism responsible for improvement in mechanical properties

Unlike conventional rubber composites to which the addition of stiff fillers usually results in an increase in strength and a decrease in extensibility, the PDIM/HNTs nanocomposites exhibited improvement both in strength and extensibility. In the PDIM/HNTs nanocomposites,

the elastomeric architecture is held together by dual cross-linking bonds: covalent cross-linking bonds (chemical cross-linking) and hydrogen bonds between the HNTs and the PDIM (physical cross-linking) (Scheme 4-3a). The covalent cross-linking network imparts elasticity and keeps the permanent shape while the hydrogen bonds affords some mobility to the HNTs in the PDIM and serve as a load transfer from the PDIM to the HNTs. The orientation of HNTs was mainly caused by the processing condition, and the testing process further facilitated the orientation of HNTs. We suppose that during the successive uniaxial stretching, the alignment of PDIM chains further orients the HNTs along the loading direction (Scheme 4-3b), which was also observed in other HNTs-based polymer composites [176,182]. At the same time, the hydrogen bonds between the HNTs and the PDIM ensure efficient load transfer at the interface. A further increase in load finally dissociates these hydrogen bonds, providing energy dissipation (Scheme 4-3c). After the dissociation of hydrogen bonds, the PDIM chains that are coiled up in loops from the applied force by the hydrogen bonds are stretched to sustain a large deformation (Scheme 4-3d), which needs more energy to reduce entropy when PDIM segments are stretched [183]. Finally, the HNTs are pulled out from or rupture at the tensile fracture surface of the PDIM/HNTs nanocomposites. Consequently, the strength, the extensibility, and the ductility of the nanocomposites are simultaneously improved through the dissociation of hydrogen bonds.

It is critically important, but often challenging, to simultaneously improve the modulus, strength, and extensibility of polymer materials. Generally speaking, an improved strength conflicts with enhanced extensibility because a flexible network can sustain a large deformation but exhibits a shallow stress response, while a rigid or restricted network shows an enhanced strength but fails in small extension. Constructing hydrogen bonds at the interfaces of polymer/filler composites provides an effective solution to synergistically improve the modulus, strength, and extensibility. This can be a guideline for designing high-performance rubber composites.

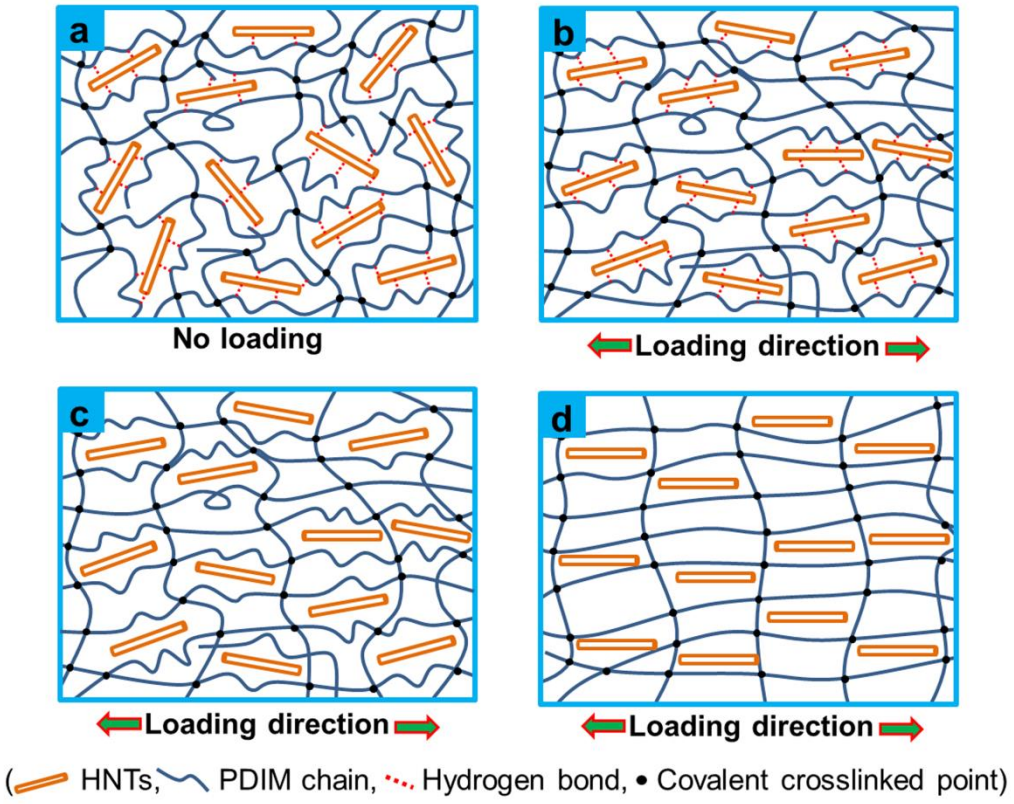

Scheme 4-3. Illustration for successive uniaxial stretching of PDIM/HNTs nanocomposites (a→b→c→d): (a) The PDIM is held together by dual cross-linking bonds, namely, covalent cross-linking bonds and hydrogen bonds; (b) The alignment of PDIM chains further orients the HNTs along the loading direction; (c) The dissociation of hydrogen bonds provides energy dissipation; (d) The stretching of PDIM chains that are coiled in loops dissipates much energy to sustain a large deformation and further orients the HNTs.

4. Conclusions

In this study, poly(dibutyl itaconate-*co*-isoprene-*co*-methacrylic acid) (PDIM)/halloysite nanotubes (HNTs) nanocomposites were prepared by the co-coagulation of PDIM latex and HNTs aqueous suspension and followed by mechanical kneading with rubber additives. The glass transition temperature of the PDIM/HNTs compound increased slightly with increasing HNTs content. The effective HNTs contents of all the PDIM/HNTs compounds were smaller than the nominal ones due to losses in the HNTs or the PDIM during the co-coagulation. Strong hydrogen bonds were formed in the PDIM/HNTs nanocomposites. The uniform dispersion of the HNTs in the PDIM/HNTs nanocomposites was obtained. With the incorporation of the HNTs into the PDIM, the tensile modulus, tensile strength, and fracture

energy of the PDIM/HNTs nanocomposites were simultaneously improved without sacrificing the extensibility. The improved mechanical properties were correlated to the formation strong hydrogen bonds. The investigation of the tensile fracture surface of the PDIM/HNTs nanocomposite revealed a mechanism responsible for improvement in mechanical properties which is composed of four steps: (1) alignment of the PDIM chains further orients the HNTs along the loading direction during the uniaxial stretching; (2) dissociation of the hydrogen bonds dissipates energy; (3) Coils of PDIM from the applied force by the hydrogen bonds are stretched to sustain a large deformation and dissipate energy; (4) finally, the HNTs are pulled out from or rupture at the tensile fracture surface of the PDIM/HNTs nanocomposites. Consequently, the strength and ductility of the nanocomposites are simultaneously improved without sacrificing the extensibility.

Acknowledgement

The authors thank the National 973 Basic Research Program of China (2015 CB654700), National Natural Science Foundation of China (50933001, 51503010), the China-France Cooperation Program of PHC CAI YUANPEI (CHINA SCHOLARSHIP COUNCIL, No. 201504490120), and the Goodyear Tire & Rubber Company (S2010-06) for their financial support.

Chapter 5 Synthesis and application of poly(dibutyl itaconate-*co*-butadiene)

From the conclusion of Chapter 4, the introduction of carboxylic groups did not make itaconate based elastomers good tire tread materials. Considering the super low rolling resistance of polybutadiene-based tire tread, we used butadiene instead of isoprene to copolymerize with dibutyl itaconate to produce poly(dibutyl itaconate-co-butadiene) (PDIB). We proposed the introduction of butadiene units in itaconate based elastomers would not only improve the mechanical properties but also reduce rolling resistance of PDIB-based tire tread.

The first article will focus on the synthesis and chemical structure of PDIB. Generally, chemical structure of a polymer will determine its final performance. In this part, the chemical structure of PDIB, especially the configuration of butadiene units, will be discussed in detail. The monomer sequence distribution of PDIB will also calculated according to the monomer reactivity ratios which will be determined by two classic linear methods. The molecular weight, glass transition temperature, and yield of PDIB will also be given in this part. The mechanical properties of un-filled PDIB will be assessed by tensile test.

In the second article, the PDIB/silica nanocomposites are prepared and evaluated systematically. Dynamic properties of PDIB/silica nanocomposites, especially loss tangent (tan δ) at 60^{o}C and at 0^{o}C, are investigated. The values of the tan δ at 60°C for filled elastomeric materials and the rolling resistance coefficients of tires are laboratory and industrial benchmarks for fuel consumption, respectively. Likewise, the value of the tan δ at 0^{o}C for filled elastomeric materials corresponds to the wet grip resistance coefficients of tires. Based on the mechanical and dynamic properties of PDIB/silica nanocomposites, a high-performance tire is manufactured and tested on a MTS tire rolling resistance measurement system.

A solvent-less green synthetic route toward sustainable bio-based elastomers: design, synthesis and characterization of poly(dibutyl itaconate-*co*-butadiene)

Abstract: A sustainable poly(dibutyl itaconate-*co*-butadiene) (PDIB) elastomer with curable double bonds was synthesized by environmentally benign emulsion polymerization of bio-based dibutyl itaconate with butadiene. The microstructure of PDIB elastomer was confirmed by FTIR and NMR. The resultant copolymers had predominately *trans*- and *vinyl*-polybutadiene in their chains, a molecular weight from 236, 000 to 392, 000 g/mol, and a glass transition temperature from -42 to -72^{o}C, depending on the feed weight percentage of butadiene. The reactivity ratios of dibutyl itaconate and butadiene determined by the classical Fineman-Ross method and Kelen-Tüdös one indicated a non-ideal copolymerization behavior with an azeotropic point at 0.383. The monomer sequence distribution indicated that butadiene could undergo self-propagation to form long flexible segments while dibutyl itaconate preferred to form short sequences with isolated, diad or triad moieties. The mechanical properties of PDIB could compete with or even surpass those of traditional synthetic rubbers. The stress and the elongation at break of unfilled PDIB40 (40 wt.% butadiene in feed) were over 2 MPa and 600%, respectively, indicating that PDIB elastomers could be good candidates for replacement of traditional synthetic rubbers based on fossil resources.

Keywords: Bio-based elastomer; Sustainable development; Emulsion polymerization; Reactivity ratio; Monomer sequence distribution.

1 Introduction

Polymers play a ubiquitous role in modern society because of their unique performances. More life without polymers is hardly imaginable. The majority of polymers in modern society are derived from fossil resources. Due to the continuous depletion of fossil fuels and associated environmental concerns, polymer scientists and engineers have developed sustainable synthetic polymers derived from renewable bio-based chemicals to compete with or replace those derived from petroleum-based chemicals. [93,184,185] The principle of "Use of Renewable Bio-based Chemicals" is important for sustainable polymer syntheses. Bio-based chemicals seem to be the most promising alternative to petroleum-based chemicals in terms of renewability, production and impact on the environment. [186] Up to now, several bio-based plastics derived from renewable chemicals, such as poly(lactic acid) (PLA), polyhydroxyalkanoate (PHA), and poly(butylene succinate) (PBS), have been developed and commercialized. However, compared with the rapid development in bio-based plastics, fewer research has been done on bio-based elastomers, especially on those targeted for engineering applications.[46,141,143] Considering the ever-stringent requirements for sustainable development and green chemistry, elastomers derived from bio-based chemicals, especially those which can match the performances of petroleum-based ones, should also have a bright future.

Itaconic acid can be produced in an industrial scale by fermentation of carbohydrates using *Aspergillus terreus* [15,187], and is one of most promising building blocks for fabricating bio-based polymers. Due to its novel chemical structure (being an unsaturated dicarbonic organic acid), huge annual production (more than 80,000 tons), and reasonable price (around 2 euros/kg) [15], itaconic acid has been listed as one of the "top 12" potential bio-based platform chemicals. [11] Itaconic acid and its derivatives can be readily incorporated into polymers as an ideal substitute for petroleum-based chemicals. By using its functional carboxylic acid groups, itaconic acid can undergo polycondensation with diamines and diols to produce polyamides [88,188] and polyesters [189,190], respectively. It has been proved that itaconic acid can be used as a building block to produce bio-based polyester elastomers. [44] Another approach for "use of itaconic acid" is radical homopolymerization or copolymerization of dialkyl itaconates with other unsaturated monomers. [191-195] Copolymerization of dialkyl itaconates with unsaturated monomers containing one double bond as well as homopolymerization of dialkyl itaconates yielded saturated polymers, which were hardly cross-linkable to form elastic networks. Moreover, those homopolymerization of

dialkyl itaconates and copolymerization with other unsaturated monomers were carried out in various organic solvents, such as benzene, chloroform, and *N*, *N*-dimethylformamide (DMF). [193] The use of such organic solvents was contrary to the requirements for sustainable development and green chemistry. Compared with solution polymerization, emulsion polymerization is solventless and environmentally benign, and is a desirable methodology for synthesizing sustainable polymers. [196,197] This polymerization technique offers many invaluable practical advantages, such as the absence of volatile organic solvents, the possibility to reach high molecular weight polymers with high conversion, and better control of heat transfer and a faster rate of polymerization than solution polymerization. The resultant latex can be used directly as an eco-friendly coating or as a dried polymer after removal of water.

Double bonds are essential to crosslink elastomers. Hence, dialkyl itaconates should be copolymerized with diene and terpenes to produce sustainable copolymers with unsaturated double bonds. However, only a handful of research has focused on the design and synthesis of sustainable bio-based elastomers, which must possess a sufficiently high molecule weight, a low glass transition temperature (T_g), and unsaturated double bonds, from dialkyl itaconates via emulsion polymerization. Sarkar and Bhowmick reported sustainable polymers derived from dibutyl itaconate and myrcene by emulsion polymerization with a molecular weight below 100 000 g/mol. [51] The alkyl length of dialkyl itaconates affects not only their polymerization but also the properties of the resultant polymers. Our previous studies demonstrated that dibutyl itaconate was the most promising itaconate for synthesizing sustainable bio-based elastomers. [50,142,198] It can be obtained by esterification of itaconic acid with *n*-butyl alcohol, both of which can derive from biomass via fermentation process. [199,200] In this study, sustainable bio-based poly(dibutyl itaconate-*co*-butadiene) (PDIB) elastomers with high molecular weights were synthesized by redox-initiated emulsion copolymerization of dibutyl itaconate with butadiene. Bio-butadiene technology has been developed rapidly in recent years. [186,201-203] Although petro-butadiene still dominates today‘s market, it is just around the corner to replace petro-butadiene with bio-butadiene. Thus, PDIB elastomers were prepared based on bio-based dibutyl itaconate and potential bio-based butadiene. Recently, green tires were made of a silica-filled PDIB elastomer nanocomposite. [142] However, the synthesis process, microstructure, and physical properties of PDIB elastomers were not investigated and the microstructure-properties relationship was still unclear. Therefore, this study focuses on the synthesis process, microstructure, and

physical properties of PDIB elastomers. The aim of investigating the synthesis process was to gain knowledge for potential commercialization of the PDIB elastomers. The microstructure of the PDIB elastomers was characterized by various spectroscopic techniques. Thermal performance of the PDIB elastomers was evaluated. The reactivity ratios of dibutyl itaconate and butadiene were calculated by Fineman-Ross (F-T) and Kelen-Tüdös (K-T) methods, respectively. In order to gain insight into the monomer sequence distribution of the copolymer chains, a simplified mathematical statistics model was performed. The curing characteristics and mechanical performance of PDIB elastomers were also examined, indicating that the PDIB elastomers were compatible with traditional rubber processing and might be good candidates for replacement of traditional synthetic rubbers based on petrochemical resources.

2 Experimental

2.1 Materials

Dibutyl itaconate (purity of 96%) was purchased from Sigma-Aldrich Company (USA). Butadiene (purity of 94%) was provided by Petrochemical Research Institute (Jilin Province, China). Disproportionated potassium rosinate and sodium soap were provided by the Petrochemical Research Institute. Phosphoric acid, potassium hydroxide, ethylene diamine tetraacetic acid (EDTA), EDTA ferric sodium salt, sodium formaldehyde sulfoxylate (SFS), sodium thiosulfate, hydroxylamine were purchased from Sigma-Aldrich Company and used without further purification. *p*-Menthane hydroperoxide was purchased from Hunan Songyuan Chemical Co., LTD (Hunan Province, China). All other chemicals were of reagent-grade commercial products and were used as received. Deionized water was used for all polymerization runs.

2.2 Sample preparation

2.2.1 Recipe for polymerization of PDIB elastomers

The physical properties of butadiene are differ from those of isoprene. For example, butadiene is a gas at ambient conditions. Therefore, the recipes and conditions for synthesis of PDII and PDIM elastomers are not suitable that of PDIB elastomers. Butadiene has been successfully polymerized with styrene to produce emulsion polymerized styrene-butadiene rubber (ESBR). In this work, a typical recipe for synthesis of ESBR was adapted to the synthesis of PDIB

elastomers. Table 5-1 shows a recipe used for redox-initiated polymerization of dibutyl itaconate with butadiene to obtain PDIB elastomers.

Table 5-1. Recipe for redox-initiated emulsion polymerization of dibutyl itaconate with butadiene to obtain PDIB elastomers.

Ingredient	Dosage (g)	Remarks
Dibutyl itaconate	Variable [a]	96 wt.%
Butadiene	Variable [a]	94 wt.%
Deionized water	150.0	Homemade
Emulsifier solution	33.33	Prepared as below
Electrolyte solution	8.33	Prepared as below
Activator solution	6.25	Prepared as below
Deoxidant solution	3.33	Prepared as below
Initiator solution	5.00	Prepared as below
Hydroxylamine	5.00	Terminator, 50 wt.% solution in water

[a] The total dosage of the monomers was fixed at 100.00 g, as shown in Table 5-2.

Preparation of the emulsifier solution Disproportionated potassium rosinate (15 wt.% aqueous solution) and sodium soap (13 wt.% aqueous solution) were used to prepare a compound emulsifier in the polymerization of PDIB elastomers, aiming to obtain a good emulsifying effect. The compound emulsifier was prepared by transferring 300.0 g of disproportionated potassium rosinate and 360.0 g of sodium soap into a 1000 mL volumetric flask. Deionized water was added in to complete the volume.

Preparation of the electrolyte solution Phosphoric acid (85 wt.% in aqueous solution), potassium hydroxide, and EDTA (white solid powder) were used to prepare the electrolyte solution, aiming to reduce the critical micelle concentration of the emulsifier and latex viscosity, and stabilize the latex. The electrolyte solution was prepared by transferring 9.24 g of phosphoric acid, 11.88 g of potassium hydroxide, and 0.9 g of EDTA into a 250 mL volumetric flask. Deionized water was added in to complete the volume.

Preparation of the activator solution EDTA ferric sodium salt and SFS were used to prepare the activator solution. The redox-initiated system composed of an activator and an initiator. The activator solution was prepared by dissolving 0.6 g of EDTA ferric sodium salt and 1.0 g of SFS in deionized water in a 250 mL volumetric flask.

Preparation of the deoxidant solution Sodium thiosulfate was used to prepare the deoxidant solution. Deoxidant was used to clear up residual oxygen in the polymerization system. The deoxidant solution was prepared by dissolving 2.64 g of sodium thiosulfate into 200 mL deionized water in a 250 mL sealed glass bottle in which the air was replaced by nitrogen.

Preparation of the initiator solution*p*-Menthane hydroperoxide was used to initiate the polymerization of PDIB elastomers. The initiator solution was prepared by dissolving 1.0 g of *p*-menthane hydroperoxide in dibutyl itaconate in a 100 mL volumetric flask.

2.2.2 Synthesis of PDIB elastomers

The polymerization reactor was a shake-bottle polymerization device, as shown in Fig. 5-1. According to the recipe in Table 1, deionized water, emulsifier solution, electrolyte solution, activator solution, and dibutyl itaconate were added into a reaction bottle. The latter was then sealed under nitrogen atmosphere. Subsequently, butadiene was pressed into the sealed reaction bottle, and the mixture in the bottle was *pre*-emulsified under nitrogen atmosphere for 4 hours. Later, the deoxidant solution was injected into the reaction bottle to eliminate the residual oxygen in the *pre*-emulsion, followed by the initiator solution. The polymerization was allowed to proceed under nitrogen atmosphere for 8 hours to form the target PDIB latex, followed by adding hydroxylamine solution to terminate the polymerization. The stirring speed and reaction temperature were 20 rpm and 5^{o}C, respectively. Figure 5-2 and Scheme 5-1 show the flow chart of the polymerization process and the polymerization equation, respectively. The PDIB latex was coagulated using ~1wt.% $CaCl_2$ aqueous solution. The moist PDIB was dried at 60^{o}C under vacuum until a constant weight was obtained. The PDIB gums with various dibutyl itaconate to butadiene ratios were prepared under the same conditions (Table 5-2).

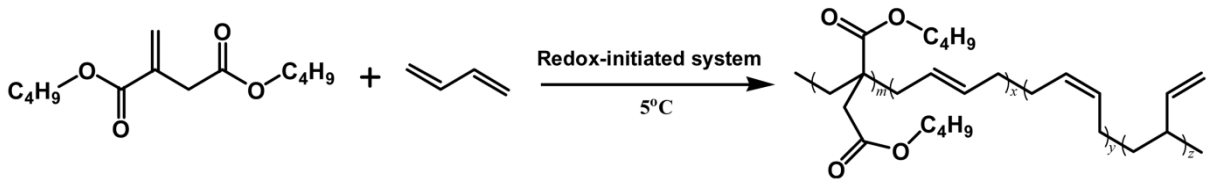

Scheme 5-1. Chemical equation for PDIB synthesis.

Figure 5-1. A shake-bottle polymerization device for PDIB elastomers. (a) Frontal view and (b) internal view.

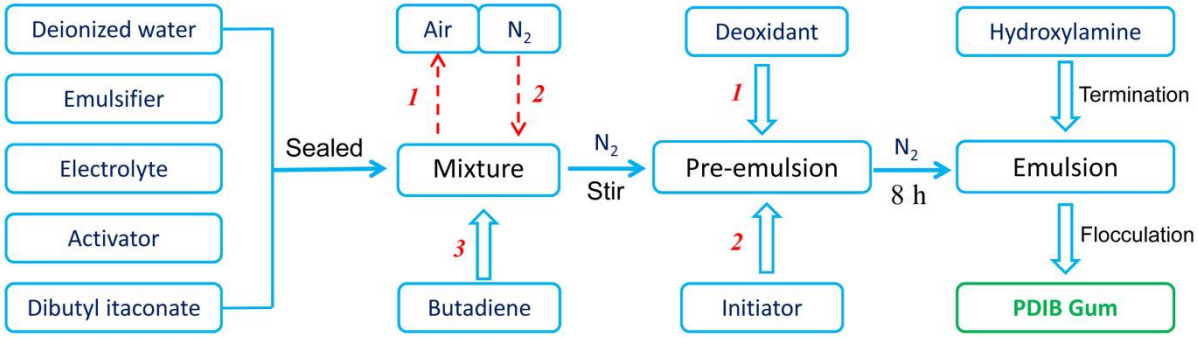

Figure 5-2. Flow chart of the polymerization process for PDIB elastomers.

Table 5-2. Feed compositions of the initiator and monomers for the polymerization of PDIB elastomers.

PDIB sample	Initiator (g)	Dibutyl itaconate (g)	Butadiene (g)
PDIB0 [a]	0.05	100	0
PDIB10	0.05	90	10
PDIB20	0.05	80	20
PDIB30	0.05	70	30
PDIB40	0.05	60	40
PDIB50	0.05	50	50
PDIB60	0.05	40	60
PDIB70	0.05	30	70
PDIB80	0.05	20	80
PDIB90	0.05	10	90
PDIB100	0.05	0	100

[a] The number represents the feed quantity of butadiene in a polymerization.

2.2.3 Preparation of cross-linked PDIB elastomers

On a 15.24 cm two-roll mill, the PDIB (100.0 phr) was blended with additives, *i.e.* zinc oxide (5.0 phr), stearic acid (0.5 phr), 2-mercaptobenzothiazole (0.7 phr), N-cyclohexyl-2-benzothiazole (1.0 phr), and sulfur (1.0 phr). The resultant compound was cured at 150^{o}C under 150 MPa for an optimum cure time as determined by an oscillating disk.

2.3 Measurements and characterization

Latex particle size measurement

The latex particle size and zeta potential measurements were conducted on a Malvern Zetasizer (Nano ZS) at 25^{o}C. The latex was diluted and dispersed in deionized water with ultrasonic treatment for 30 mins before testing.

Gel permeation chromatography (GPC)

The molecular weight of the PDIB were determined by GPC on a Waters Breeze instrument equipped with three water columns (Styragel HT3_HT5_HT6E) and a Waters 2410 refractive index detector. Chloroform was used as an eluent in the columns (1 mL/min), and a polystyrene standard was used for calibration in the refractive index detector.

Fourier transform infrared spectroscopy (FTIR)

The FTIR spectra of the PDIB gums were recorded on a Bruker Tensor 27 spectrometer. They were acquired by scanning the PDIB samples in the wavenumber range from 600 to 4000 cm^{-1} for 128 times with a resolution of 2 cm^{-1} with the Attenuated Total Reflection (ATR) technique.

Nuclear magnetic resonance (NMR)

The ^{13}C NMR and ^{1}H NMR spectra of the PDIM were recorded on a Bruker AV400 spectrometer at 25^{o}C, with $CDCl_3$ as a solvent.

Differential scanning calorimetry (DSC)

The DSC traces of the PDIB were recorded on a Mettle-Toledo differential scanning calorimeter under a nitrogen flow (50 mL/min). The samples were heated to 150^{o}C and

maintained for 5 min and then cooled down to -120°C. The heating and cooling rates were 10°C/min in all cases.

Thermogravimetric analysis (TGA)

The TGA of the PDIB was performed on a thermal gravimetric analyzer of Mettle-Toledo from 30 to 800°C with a steady nitrogen flow of 50 mL/min. The heating rate was 10°C/min for all cases.

Gel fractions

The gel fractions of the PDIB were determined by extraction with chloroform. All PDIB samples were extracted in a 2 L glass reactor for 8 hours with chloroform under reflux. The PDIB samples were dried after the extraction, and the gel fractions were calculated as the ratios of the weights of the dried polymers to their initial ones.

Vulcanization Test

The vulcanization tests of the PDIB compounds were carried out on a rotor-less rheometer at 150°C to determine their optimum vulcanization times.

Physical and mechanical tests

Hardness Test The hardness of PDIB vulcanizates was determined on a rubber durometer (Shore A) according to ASTM standard (D395). The specimens with 6 mm thick were tested for five times to determine the median of the hardness.

Tensile Test Tensile tests of PDIB vulcanizates were conducted according to ASTM standard (D412: dumbbell-shaped), and the specimens were tested on an LRX Plus tensile tester at 500 mm/min at room temperature (25°C). At least five specimens were tested to obtain an average value. During the testing process, the elongation of the gauge section was recorded against the applied force. The ultimate tensile strength (UST) or tensile strength (TS) in short and maximum elongation were directly measured via a tensile test.

The TS is measured by the maximum stress that a material can withstand under stretching until it failures. The stress (σ) is calculated by using the following equation:

$$\sigma = F / A \tag{5-1}$$

where F is the tensile force and A is the initial cross-section of the gauge section of the specimen. The elongation is used to calculate strain (ε) by using the following equation:

$$\varepsilon = \Delta L / L_0 = (L - L_0) / L_0 \tag{5-2}$$

where ΔL is the change in gauge length, L_0 is the initial gauge length, and L is the final length. Permanent set (δ) defined as the change in gauge length after recovery of the stretched specimen. The permanent set is expressed as a percentage of the initial gauge length:

$$\zeta = \Delta L' / L_0 \times 100 = (L' - L_0) / L_0 \times 100 \tag{5-3}$$

where $\Delta L'$ and L' are the change in gauge length and the final length after recovery of the stretched specimen, respectively.

Calculation of crosslinking density

The cross-linked PDIB were swollen in toluene for 72 h to obtain swollen samples at equilibrium. Soluble constituents were extracted during the swelling period. Excess solvent on the surfaces of the swollen samples was removed, and then the swollen samples were placed into sealed vials to reduce solvent evaporation. The swollen samples at equilibrium were weighed to determine their masses (m_{eq}). After dried in a vacuum oven at 60^{o}C for 48 h, the samples were weighed again to determine the masses of the dry networks (m_d).

The crosslinking densities of the swollen samples were calculated by using the Flory-Rehner equation:

$$v_e = -\frac{\ln(1 - v_2) + v_2 + \chi v_2^{\,2}}{V_s (v_2^{\,1/3} - 0.5 v_2)} \tag{5-4}$$

where v_e is crosslinking density of cross-linked PDIB, v_2 is the volume fraction of polymer at equilibrium swelling, χ is the polymer-solvent interaction parameter, and V_s is the molar volume of the solvent. The polymer volume fraction at equilibrium was calculated by using the following equation:

$$v_2 = \frac{m_d / \rho_r}{m_d / \rho_r + (m_{eq} - m_d) / \rho_s} \tag{5-5}$$

where ρ_r and ρ_s are the densities of the polymer and the solvent, respectively. The polymer-solvent interaction parameter was calculated based on Flory-Huggins theory by using the following equation:

$$\chi = \frac{V_s}{RT}(\delta_1 - \delta_2)^2 \tag{5-6}$$

where δ_1 and δ_2 are the solubility parameters for solvent and polymer, respectively, R is the molar gas constant, and T is the absolute temperature.

Calculation of monomer reactivity ratios in PDIB polymerization

The copolymerization of two monomers M_1 and M_2 may be described schematically as follows: [204]

$$\begin{aligned} M_1\bullet + M_1 &\xrightarrow{k_{11}} M_1M_1\bullet \\ M_1\bullet + M_2 &\xrightarrow{k_{12}} M_1M_2\bullet \\ M_2\bullet + M_2 &\xrightarrow{k_{22}} M_2M_2\bullet \\ M_2\bullet + M_1 &\xrightarrow{k_{21}} M_2M_1\bullet \end{aligned} \tag{5-7}$$

where $M_1\bullet$ and $M_2\bullet$ are the propagating radicals, and k_{11}, k_{12}, k_{22} and k_{21} are the rate constants for chain propagation. The monomer reactivity ratios are given by:

$$r_1 = \frac{k_{11}}{k_{12}} \qquad and \qquad r_2 = \frac{k_{22}}{k_{21}} \tag{5-8}$$

The copolymer composition equation which relates the polymer composition to the monomer composition is given as follows:

$$\frac{d[M_1]}{d[M_2]} = \frac{[M_1]}{[M_2]} \times \frac{r_1[M_1]+[M_2]}{r_2[M_2]+[M_1]} \tag{5-9}$$

where $[M_1]$ and $[M_2]$ refer to the concentrations of monomers, and $d[M_1]/d[M_2]$ refers to the concentration ratio of the copolymer components for low conversions (<10%). After introduction of

$$x = [M_1]/[M_2] \quad and \quad y = d[M_1]/d[M_2] \tag{5-10}$$

equation (5-9) becomes:

$$y = x \cdot \frac{1 + r_1 \cdot x}{r_2 + x} \tag{5-11}$$

The values of the monomer reactivity ratios, r_1 and r_2 in equation (5-8), were determined by classical linearization methods, more specifically the Fineman-Ross (F-R) and Kelen-Tüdös (K-T) ones.

Based on the F-R method, equation (11) may be linearized as:

$$G = r_1 \cdot H - r_2 \tag{5-12}$$

where the transformed variables are:

$$G = x(y-1)/y \quad \textit{and} \quad H = x^2/y \tag{5-13}$$

Graphical plotting of equation (5-12) gives r_1 as the slope and r_2 as the intercept.

Based on the K-T method, equation (5-11) may be linearized as:

$$\frac{G}{\alpha + H} = \left(r_1 + \frac{r_2}{\alpha}\right)\frac{H}{\alpha + H} - \frac{r_2}{\alpha} \tag{5-14}$$

where α denotes an arbitrary constant (α > 0) and its value is determined by:

$$\alpha = \sqrt{H_{max} \cdot H_{min}} \tag{5-15}$$

where the F_m and F_M stand for the lowest and the highest values calculated from the series of measurements, respectively. After introduction of

$$\eta = G/(\alpha + H) \quad \textit{and} \quad \xi = H/(\alpha + H) \tag{5-16}$$

equation (5-14) may be written as:

$$\eta = \left(r_1 + \frac{r_2}{\alpha}\right)\xi - \frac{r_2}{\alpha} \tag{5-17}$$

where the variable ξ is within the interval (0, 1). Plotting ε calculated from the experimental data as a function of ξ is expected to yield a straight line which allows for calculating the monomer reactivity ratios.

Monomer sequence distribution in PDIB copolymers

The monomer sequence distributions are of central importance for the study of copolymerization. The mathematical statistics theory of monomer sequence distributions in copolymers has been exhaustively reported in the 1960s [205,206] and 1970s [207,208]. This work used a simplified mathematical statistics model to study the monomer sequence distributions in PDIB copolymers by assuming that only the terminal unit of a propagating polymer chain affects the probability of monomer addition. The influence of configurations of butadiene moieties is neglected. In random copolymers, the monomer sequence of two monomers in a single polymer chain is irregular, while the monomer sequence of the same monomer in two polymer chains is different. In the copolymerization of dibutyl itaconate (M_1) with butadiene (M_2), the monomer sequence of M_1 (or M_2) with length l (l = 1, 2, 3… …) may be distributed according to the probability theory. The addition of M_1 to propagating radical M_1• and the addition of M_2 to propagating radical M_1• are competitive reactions, resulting in propagating radicals M_1M_1• and M_1M_2•, respectively. Define p_{11} and p_{12} as the conditional probabilities of propagating radicals M_1M_1• and M_1M_2•, respectively. Thus,

$$p_{11} = 1 - p_{12} = \frac{r_1[M_1]}{r_1[M_1] + [M_2]} \tag{5-18}$$

Likewise, the conditional probabilities of the propagating radicals M_2M_1• and M_2M_2• are defined as p_{22} and p_{21}:

$$p_{22} = 1 - p_{21} = \frac{r_2[M_2]}{r_2[M_2] + [M_1]} \tag{5-19}$$

The monomer sequence of M_1 with length l can be generated by adding (l-1) M_1 to propagating radical M_2M_1• followed by addition of a M_2, as shown below:

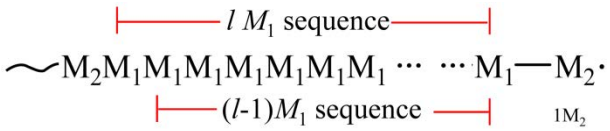

Based on the first-order Markov statistic model, the probability for generating M_1 sequence with length l (number of monomer moieties in sequence) is given:

$$\left(p_{M_1}\right)_l = p_{11}^{l-1} \cdot p_{12} = p_{11}^{l-1}\left(1-p_{11}\right) \tag{5-20}$$

which equals to the percentage of lM_1 sequence in all M_1 sequence in copolymers. Likewise, the probability for generating M_2 sequence with length l' is given:

$$\left(p_{M_2}\right)_{l'} = p_{22}^{l'-1} \cdot p_{21} = p_{22}^{l'-1}\left(1-p_{22}\right) \tag{5-21}$$

Equations (5-20) and (5-21) can be used to calculate the monomer sequence distribution of the PDIB copolymers in a certain monomer feed ratio. The number-average length of M_1 sequence and that of M_2 sequence are given below:

$$\bar{N}_{M_1} = \sum_{l=1}^{l} l\left(p_{M_1}\right)_l = \sum_{l=1}^{l} l p_{11}^{l-1}\left(1-p_{11}\right) = \frac{1}{1-p_{11}} \tag{5-22}$$

$$\bar{N}_{M_2} = \sum_{l'=1}^{l'} l'\left(p_{M_2}\right)_{l'} = \sum_{l'=1}^{l'} l' p_{22}^{l'-1}\left(1-p_{22}\right) = \frac{1}{1-p_{22}} \tag{5-23}$$

3 Results and discussion

3.1 Synthesis of PDIB by redox-initiated emulsion polymerization

The radical polymerization of vinyl monomers is known to be sensitive to the steric effect due to the substituents of monomers. However, radical polymerization of dibutyl itaconate at high temperature (> 50^{o}C) was found to yield polymers, despite its two bulky substituents. [192,193] From the perspective of a conventional elastomer network, homopolymers of itaconates are useless unless cross-linkable functional groups are introduced into them. In this study, butadiene was used to copolymerize with dibutyl itaconate to yield poly(dibutyl itaconate-*co*-butadiene) (PDIB). The incorporation of butadiene in the polymerization not only reduces the steric effect of dibutyl itaconate, but also introduces cross-linkable double bonds into PDIB chains, resulting in a novel cross-linkable and high molecular weight elastomer. Molecular weight is important for the mechanical properties of polymers, and typical number-average molecular weights (M_n) are above 200,000 for most conventional rubbers. In order to achieve a high molecular weight, redox-initiated emulsion polymerization of PDIB was carried out at low temperature (5^{o}C). Activators, *i.e.* EDTA ferric sodium and

sodium formaldehyde sulfoxylate, were introduced to decrease the activation energy of *p*-menthane hydroperoxide radical decomposition, ensuring sufficient free radical generation in the polymerization.

The PDIB elastomers in Table 5-3 were successfully synthesized according to the recipe in Table 5-1. Figure 5-3 shows the digital images of the flocculated PDIB with various butadiene contents. The molecular weights, polymer yields and gel contents of all PDIB were determined. As shown in Table 5-3, PDIB0, *i.e.* poly(dibutyl itaconate), had a M_n of 93,000 g/mol, a T_g of -4^oC, and a polydispersity index of 2.65. With increasing butadiene content, the M_n of PDIB elastomers ranged from 93,000 to 392,000 g/mol and reaches a maximum when the butadiene content was 40 wt.% in the feed. The increase in M_n could be explained as follows: the homopolymerization of dibutyl itaconate was restrained due to the steric effect of its bulky substituents. The latter was largely reduced by copolymerization with butadiene which is much less bulky. Moreover, an increase in butadiene content brought about an increase in polydispersity index due to an increase in chain transfer effect, an increase in gel content because of increased crosslinking between PDIB chains as a result of more double bonds, and a decrease in T_g as a result of the higher flexibility of the butadiene segments. For PDIB elastomers with a butadiene feed from 20 to 80 wt.%, the polymer yield was from 56.3 to 86.3%. As discussed above, PDIB0 cannot be used as an elastomer because of a lack of double bonds for crosslinking with sulfur. In addition, PDIB0 with a low yield is sticky (Fig. 5-3), resulting in difficulties in processing. Hereinafter, the work focuses on the PDIB copolymers, especially on those whose butadiene feed was from 20 to 80 wt.%. Figure 5-4 shows the digital images of the dried PDIB copolymers.

Figure 5-3. Digital images of the flocculated PDIB with various butadiene contents.

Table 5-3. Molecular weight, T_g, gel content, and yield of PDIB elastomers.

Sample	DBI /g	Bd /g	M_n /10^4	M_w/M_n	T_g /°C	Gel /%	Yield /%
PDIB0	100	0	9.3	2.65	-4	0	NA[a]
PDIB10	90	10	23.6	2,97	-42	2	60.5
PDIB20	80	20	31.4	3.23	-44	2	76.2
PDIB30	70	30	36.8	3.76	-48	3	80.7
PDIB40	60	40	39.2	3.81	-52	5	86.3
PDIB50	50	50	35.3	4.12	-55	6	84.7
PDIB60	40	60	33.7	3.96	-58	8	80.2
PDIB70	30	70	34.5	4.32	-63	11	70.8

PDIB80	20	80	32.6	4.29	-68	15	56.3
PDIB90	10	90	NA[b]	NA[b]	-72	21	45.4
PDIB100	0	100	NA[b]	NA[b]	-75	24	19.8

[a] Not available due to stickiness of PDIB0. [b] Not available due to very high gel contents.

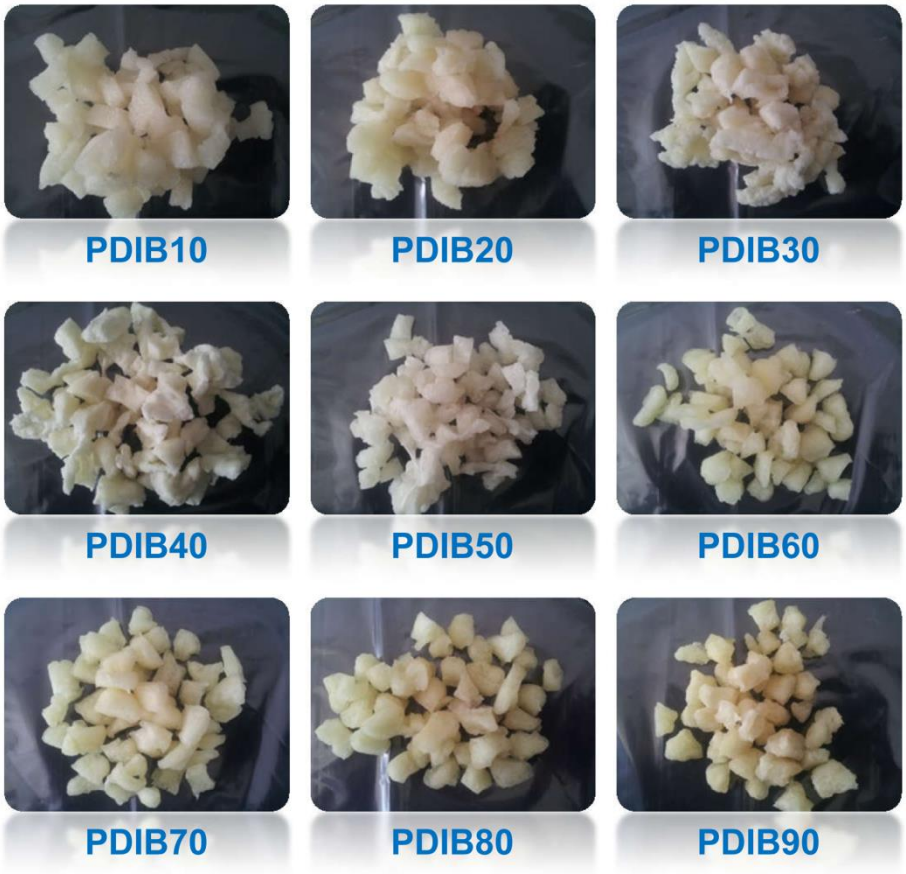

Figure 5-4. Digital images of PDIB copolymers with various butadiene contents.

3.2 Time dependence of PDIB synthesis

The effect of reaction time on the yield of the PDIB copolymerization was investigated upon carrying out the redox-initiated emulsion copolymerization of PDIB with various dibutyl itaconate to butadiene feed ratios. Figure 5-5 shows that the yield increased with increasing reaction time. For example, the yield of the PDIB40 copolymerization reached up to 90% after 9 hours. However, a further increase in the butadiene content brought about a decrease in polymer yield. The yield of the butadiene homopolymerization was even less than 20%. The product of dibutyl itaconate homopolymerization was sticky to the point that it was impossible to accurately determine its yield. The latter was estimated to be less than 25%. Those results showed that the homopolymerization of dibutyl itaconate and that of butadiene

under the specified conditions were not efficient. As discussed above, the steric effect of the bulky butyl groups in dibutyl itaconate should be responsible for the low yield and low molecular weight of PDIB0, while the chain transfer of the propagating radicals should be responsible for the low yield and high gel content of PDIB100 [209]. Furthermore, the values of the reactivity ratios of the monomers show that the two monomers tended to copolymerize rather than homopolymerize. Based on the kinetic results, the reaction time of PDIB copolymerization was chosen to be 8 hours for the subsequent studies.

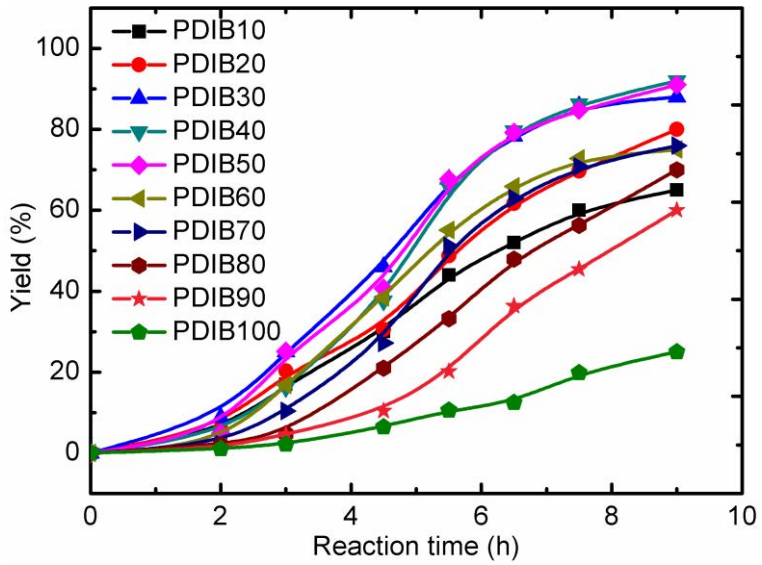

Figure 5-5. Time dependence of the yield of PDIB with various butadiene contents.

3.3 Latex particle size and zeta potential

The size and zeta potential of latex particles are important for the stability and homogeneity of the polymerization system. Figure 5-6 shows a narrow size distribution of PDIB latex particles measured via dynamic light scattering (DLS) after 2 months of storage. Polydispersity index (PdI) corresponds to the square of the normalized standard deviation of a Gaussian size distribution. It was calculated from a cumulants analysis of the DLS-measured intensity autocorrelation function. A PdI value of 1 indicates large variation in particle size; a PdI value of 0 indicates no variation in particle size. Generally, the PdI value larger than 0.5 indicates a high heterogeneity of the sample. From Fig. 5-6, all the PdI values of PDIB latices are less than 0.3, indicating the PDIB latices are homogeneity. Figure 5-7 shows the average diameter and zeta potential of the PDIB latex particles. The average diameter of latex particles increased with the butadiene content in the feed from 0% to 20 wt.% and then decreased. The zeta potential of PDIB latex particles was between -50 and -70 mV, indicating they repelled

each other electrostatically and consequently prevented themselves from coagulating. Those results confirmed the long term stability of homogeneity of the PDIB latices.

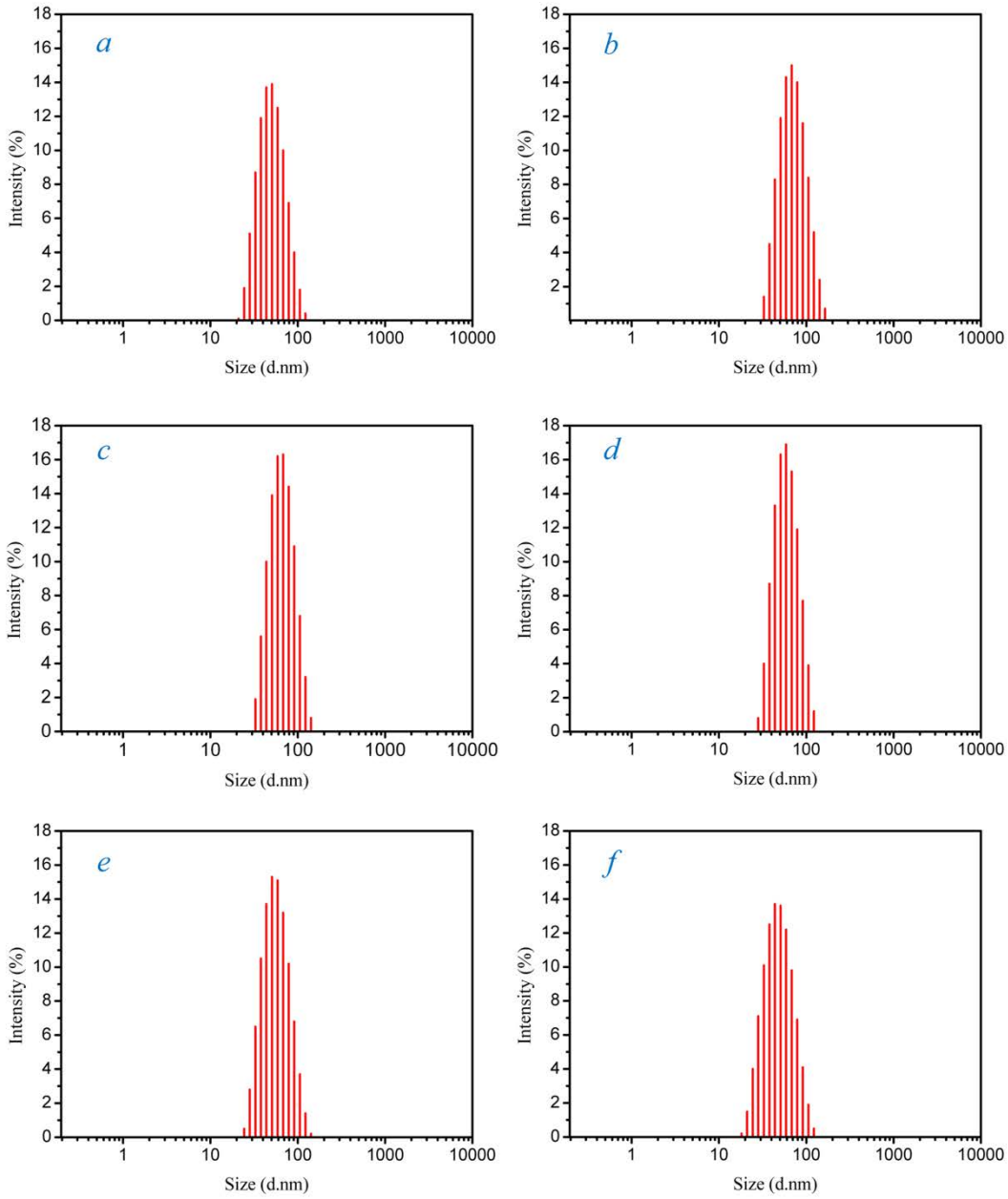

Figure 5-6. Size distributions of PDIB latex particles with small polydispersity indices (PdI): (*a*) PDIB0 latex (PdI: 0.198), (*b*) PDIB20 latex (PdI: 0.108), (*c*) PDIB40 latex (PdI: 0.115), (*d*) PDIB60 latex (PdI: 0.089), (*e*) PDIB80 latex (PdI: 0.185), and (*f*) PDIB100 latex (PdI: 0.303).

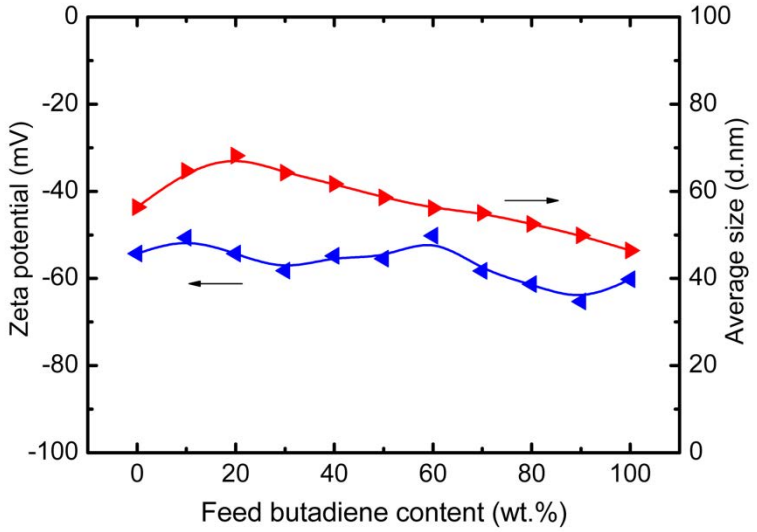

Figure 5-7. Average diameters and zeta potentials of PDIB latex particles with various feed butadiene contents.

3.4 FTIR and NMR characterization of PDIB

One of the disadvantages of emulsion polymerization is that surfactants and other polymerization ingredients remain in the polymers. The PDIB obtained from emulsion polymerization should be purified for subsequent determination of its chemical structure and composition via FTIR and NMR. The purification of the crude PDIB used a conventional method of dissolving the polymer in a solvent and precipitating it in an excess of non-solvent, as shown in Fig. 5-8.

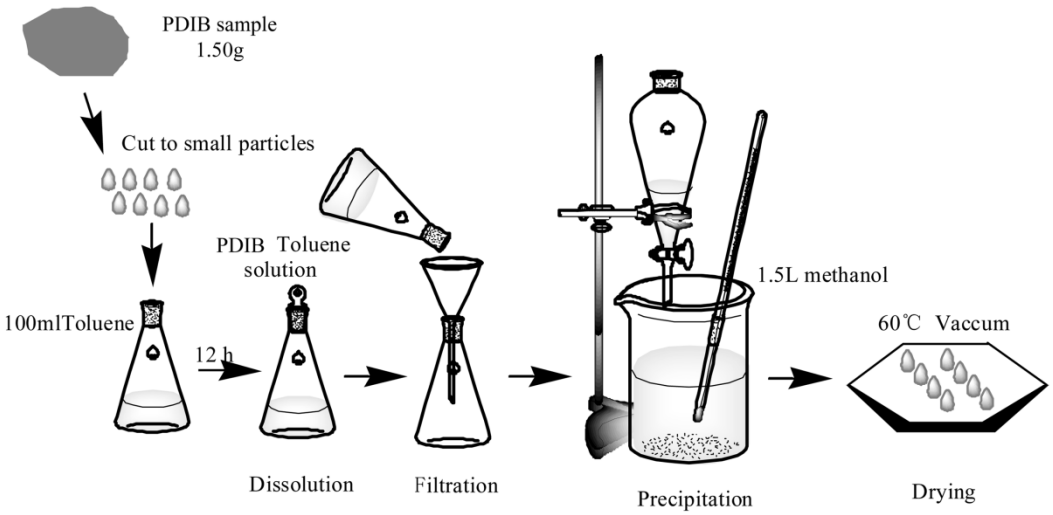

Figure 5-8. Purification process of PDIB by dissolution and precipitation.

Figure 5-9 shows the FTIR spectra of the poly(dibutyl itaconate), polybutadiene, and PDIB40. The absorption peaks at 1742 and 1178 cm^{-1} in Fig. 5-9*a* are associated with the C=O and -C-O- of the ester groups of poly(dibutyl itaconate), respectively. Those at 2959 and 2874 cm^{-1} are relative to the $-CH_3$ of the butyl groups, and those at 2933 cm^{-1} is relative to their $-CH_2$. In Fig. 5-9*c*, the absorptions at 1732 and 1177 cm^{-1} are due to the existence of dibutyl itaconate moieties that were introduced with the initiator solution. Those at 3075 and 911 cm^{-1} are attributed to the stretching vibration of -CH=$\underline{CH_2}$ and the wagging one of -$\underline{CH}$=CH_2, confirming the presence of *vinyl*-configuration in the polybutadiene. Those at 2915 and 2844 cm^{-1} correspond to the asymmetrical and symmetrical stretching vibrations of =C-$\underline{CH_2}$, respectively. The *trans*-configuration of polybutadiene is confirmed by the absorption at 966 cm^{-1} for the wagging vibration of -$\underline{CH}$=CH-. The absorption peak at 1640 cm^{-1} is relative to the double bonds which can be used as crosslinking sites. The presence of the absorptions mentioned above in the FTIR spectrum of PDIB40 confirms the copolymerization of dibutyl itaconate with butadiene (Fig. 5-9*b*). Figure 5-10 shows the spectra of the PDIB with various feed butadiene contents for reference.

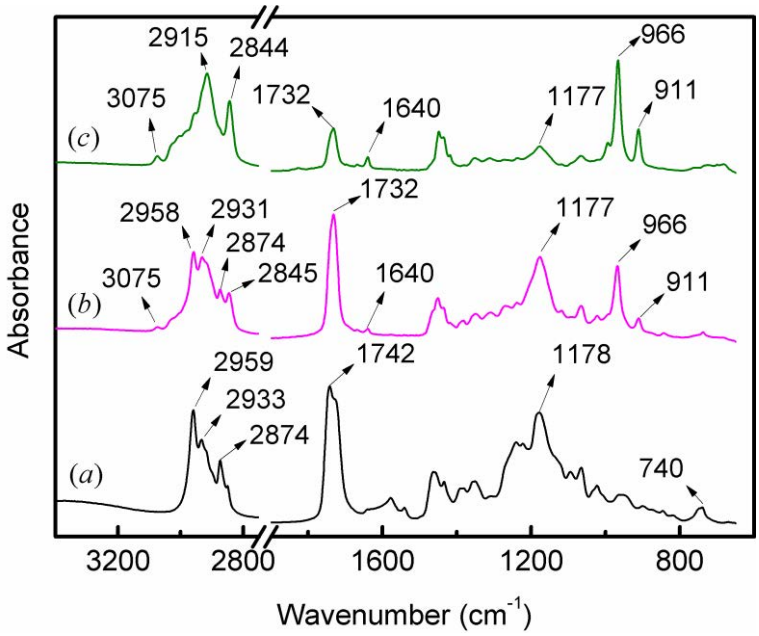

Figure 5-9. FTIR spectra of (a) poly(dibutyl itaconate) (PDIB0), (b) PDIB40, and (c) polybutadiene (PDIB100).

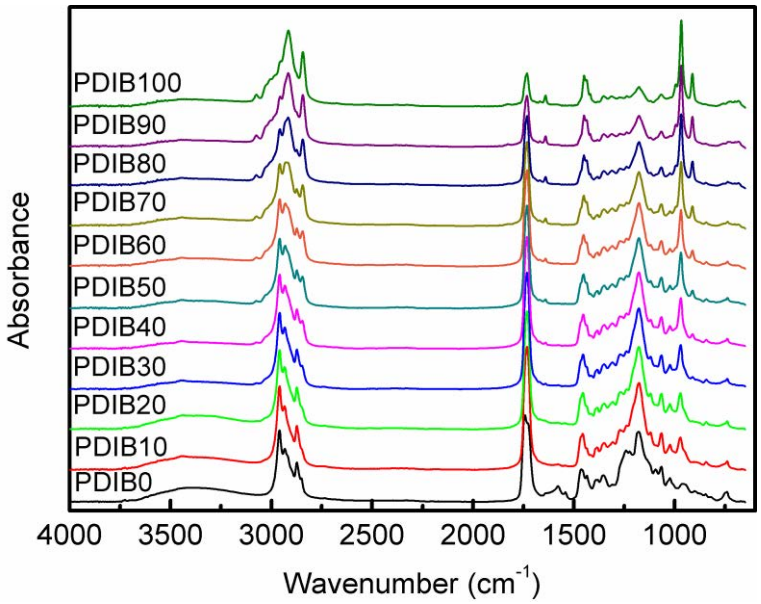

Figure 5-10. FTIR spectra of PDIB with various feed butadiene contents.

Figure 5-11 shows a ^{13}C NMR spectrum representative of a PDIB copolymer. The assignment of the resonance signals of the carbon atoms in the itaconate moieties has been verified by the distortionless enhancement by the polarization transfer (DEPT) technique with ζ of 135°, which permits the inversion of the methylene signals and suppression of the signals of quaternary carbons [210,211], as shown in Fig. 5-12. The resonance signals at 27.40 and 32.74 ppm are assigned to the methylene carbons in the *trans*-configuration (*l* and *m*) and *cis*-configuration (*j* and *k*) butadiene moieties, respectively. Those of the methylene and methine carbons in *vinyl*-configuration of butadiene moieties overlap with those of the methylene carbons of itaconate moieties in the region of 35-39 ppm. Those in the region of 124-135 ppm are attributed to the carbon-carbon double bonds of butadiene moieties. The triad sequence of the isomeric moieties of polybutadiene has been demonstrated to influence the assignment of the carbon-carbon double bonds of butadiene moieties [212,213]. In this study, the polymerization process was assumed to generate a random sequence distribution of monomeric moieties (itaconate moieties , and *trans*-, *cis*-, and *vinyl*-configurations of butadiene moieties), leading to very complicated triad sequences. Those complicated triad sequences make difficult the accurate assignment of the resonance signals of butadiene moieties.

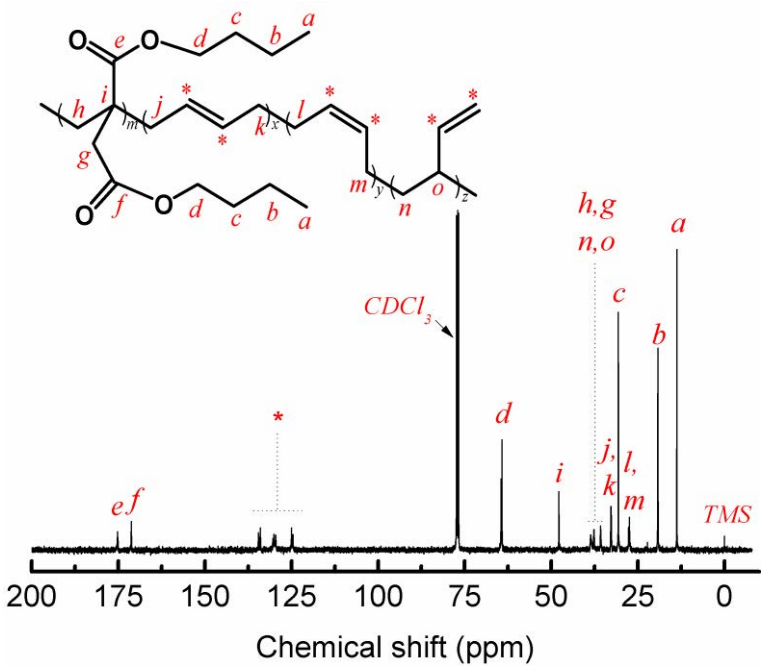

Figure 5-11. ^{13}C NMR spectrum of PDIB40 (in $CDCl_3$).

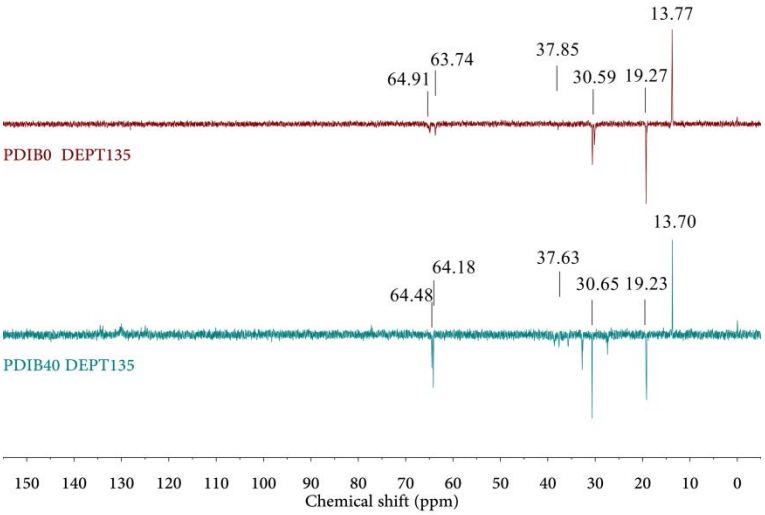

Figure 5-12. ^{13}C NMR spectra with DEPT135 of PDIB0 and PDIB40.

The chemical structures and compositions of the PDIB copolymers were further determined by using ^{1}H NMR spectroscopy. Figure 5-13 shows the ^{1}H NMR spectrum of PDIB40, a representative PDIB of this work. The signal at 0.93 ppm corresponds to the protons of the methyl groups (*b*) of dibutyl itaconate moieties. Those at 1.37, 1.60, 1.92, 2.02, 2.39, 2.5-2.7 and 4.04 ppm are assigned to the protons of the methylene groups of the PDIB chains. Those of the olefinic protons of *cis*-configuration (*l* and *m*) and *trans*-configuration (*h* and *i*) appear at 5.31 and 5.39 ppm, respectively. Those at 4.88-4.98 and 5.68 ppm originate from the olefinic protons of *vinyl*-configuration (*r* and *q*), showing the presence of pendent olefinic groups in the PDIB backbone. With increasing butadiene moieties in the PDIB copolymers,

the signal intensity of the *trans*- and *vinyl*-configurations increases and that of the *cis*-configuration decreases or even disappears, as shown in Fig. 5-14. Table 5-4 shows the compositions of the PDIB copolymers calculated from the relative peak areas of the protons of each structural moiety of the ^{1}H NMR spectra. The increase in proportion of *vinyl*-configuration with increasing butadiene content in the feed may be due to a corresponding decrease in bulky dibutyl itaconate content in the feed. The ^{1}H NMR results show that the microstructure of the PDIB copolymer strongly depends on the monomer feed ratio and their reactivity ratios, as described below.

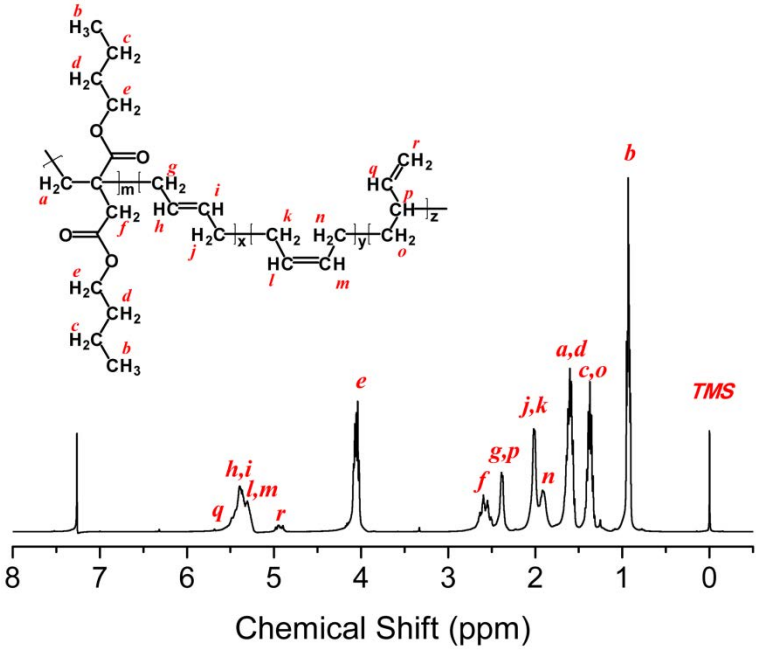

Figure 5-13. ^{1}H NMR spectrum of PDIB40 (in $CDCl_3$).

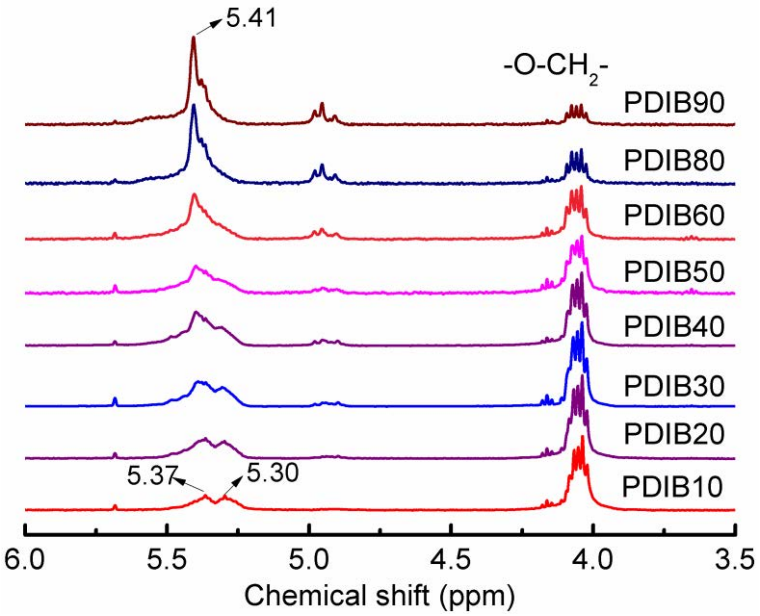

Figure 5-14. Expanded ^{1}H NMR spectra of PDIB (in $CDCl_3$).

Table 5-4. Percentages of itaconate and butadiene moieties in PDIB [a].

Sample	Molar percentages of itaconate moieties in PDIB (%)	Percentages of the different configurations of butadiene (total = 100%)			Mass ratio of itaconate moieties to butadiene ones in sampe
		trans-configuration (%)	*cis*-configuration (%)	*vinyl*-configuration (%)	
PDIB10	56.61	43.81	53.17	3.02	5.84
PDIB20	39.70	54.54	42.29	3.17	2.95
PDIB30	37.98	88.89	2.08	9.03	2.74
PDIB40	26.24	90.08	0.56	9.37	1.59
PDIB50	22.02	90.42	Negligible	9.58	1.26
PDIB60	18.94	89.48	Negligible	10.52	1.05
PDIB70	14.63	87.93	Negligible	12.07	0.77
PDIB80	8.87	86.67	Negligible	13.33	0.44
PDIB90	6.36	84.57	Negligible	15.43	0.30

[a] Calculated from integral ^{1}H NMR spectra.

3.5 Thermal properties of PDIB copolymers

Thermal properties such as glass transition temperature (T_g), thermal stability, and crystallization are critical for the applications of polymers. T_g determines whether a polymer is an elastomer at the end-use temperature. Figure 5-15 shows the DSC thermograms of the various PDIB polymers. None of the PDIB except for PDIB100 shows a melting point, implying they are amorphous. PDIB0 had the highest T_g, due to the bulky substituents on its PDIB0 chain. The incorporation of butadiene moieties obviously decreased the T_g of the PDIB because they are more flexible than dibutyl itaconate moieties. The T_g was -42^{o}C for PDIB10 and -72^{o}C for PDIB90. Because of their low glass transition temperatures and amorphous structures, the PDIB copolymers are rubbery at room temperature and are thus potential elastomers. The homopolymer of butadiene, *i.e.* PDIB100, had a T_g of -75^{o}C, a crystallization peak at -42^{o}C, and a melting peak at -18^{o}C. The crystallization and melting behavior of PDIB100 may be attributed to the abundant *trans*-configuration of butadiene moieties in the PDIB chain.

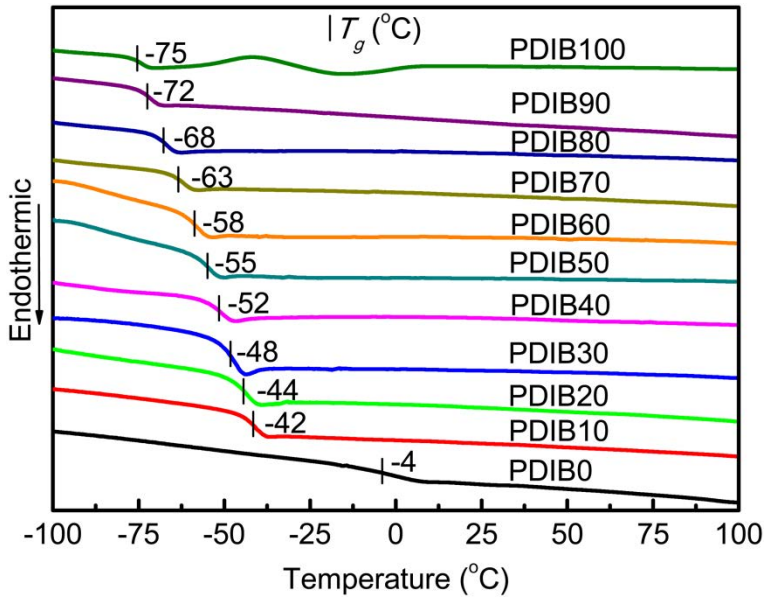

Figure 5-15. DSC thermograms of PDIB polymers.

The thermal stability of PDIB copolymers was evaluated by non-isothermal thermogravimetric (TG) analysis, as shown in Fig. 5-16*a*. The TG curves of the homopolymers of dibutyl itaconate and butadiene (PDIB0 and PDIB100) are also shown for comparison. Obviously, the thermal stability of PDIB increased with increasing butadiene content in it. The thermal degradation of PDIB occurred by depolymerization in two stages, as shown by the differential thermogravimetric (DTG) curves in Fig. 5-16*b*. The thermal degradation kinetics of the poly(dialkyl itaconate) was investigated previously. [214-216] The two DTG minima of PDIB0 can be ascribed to different depolymerization initiation modes. The first DTG minimum at 305°C corresponds to *β*-scission at the unsaturated chain ends, while the second one at 345°C is due to random main chain scission. The chain-end unsaturation originates mainly from termination by disproportionation during the radical polymerization. The chain transfer to monomer, which is another origin of the chain-end unsaturation, is suppressed in the radical polymerization due to steric hindrance of the ester substituents. As PDIB0 bear two *β*-hydrogens in the ester substituents, ester decomposition could occur during the thermolysis. However, the ester decomposition probably took place to a minor extent in the whole temperature range, which was independent of the sensitivity of poly(dialkyl itaconates) to side chain scission [214]. The thermal stability of the PDIB copolymers was obviously improved, depending on their composition. The *β*-scission at the unsaturated chain ends assigned to the first peak prevailed for PDIB copolymers with low molar percentages of butadiene moieties. This is because butadiene chain transfer to itaconate

monomers with allylic structure would be favored during the radical polymerization, resulting in unsaturated chain ends. [217-219] As dibutyl itaconate content in the feed decreased, the availability of the chain transfer to monomer during the radical polymerization decreased, while the termination by disproportionation was suppressed due to the generation of abundant allylic radicals in the propagating chains, [220] resulting in a decrease in unsaturated chain ends. This decrease can be read from Fig. 5-16*b* by the decrease in the first peaks for PDIB copolymers. As a result, the depolymerization initiated by random main chain scission was overwhelming for PDIB copolymers with high molar percentages of butadiene moieties, as shown by the increase in the second peaks. It is noted that the initial degradation temperature for all PDIB copolymers was above 300°C, which meets the general standard required for elastomer engineering materials.

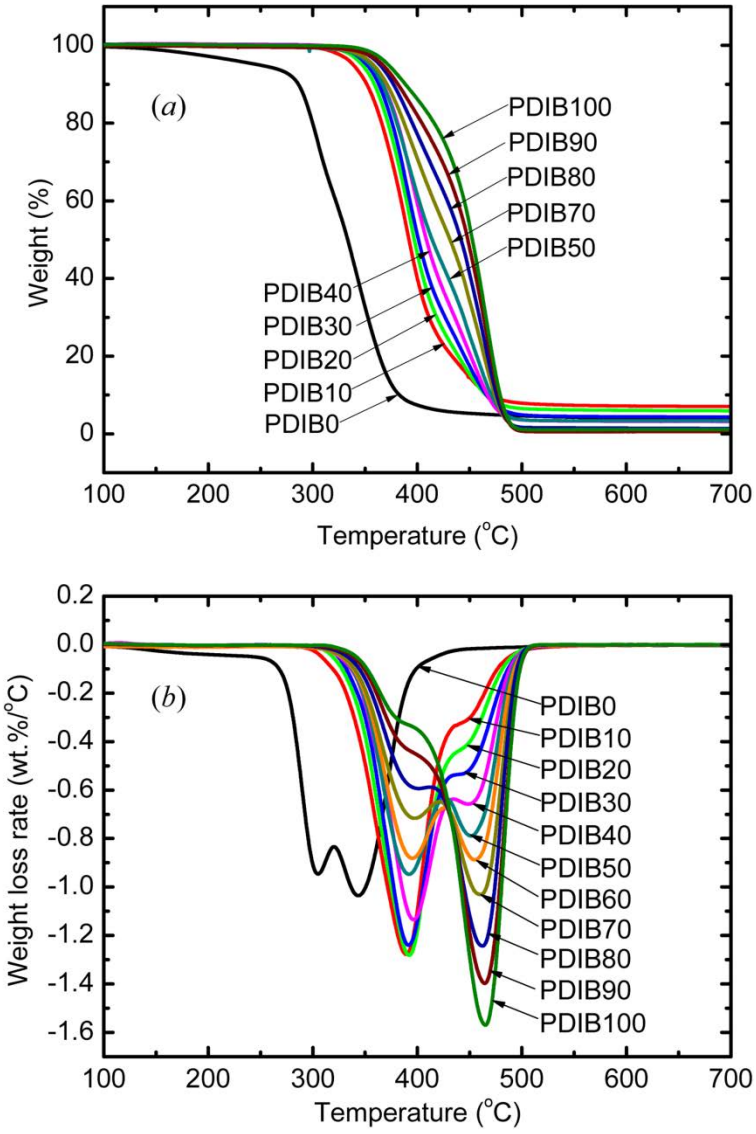

Figure 5-16. Non-isothermal TG curves (*a*) and DTG curves (*b*) for PDIB (co-)polymers.

3.6 Reactivity ratios of dibutyl itaconate and butadiene

The reactivity ratios of dibutyl itaconate (M_1) and butadiene (M_2) in the redox-initiated emulsion copolymerization were calculated by the linear F-R method and K-T one. A series of low conversion (<10 wt.%) experiments were performed for calculating the reactivity ratios, r_1 and r_2. The instantaneous copolymer compositions were determined by calculating the area of the peaks in ^{1}H NMR spectra via integration. The F-R and K-T parameters for the copolymers were calculated according to equations (5-10) to (5-17) and are presented in Table 5-5. As shown in Fig. 5-17, the correlation coefficients for the F-R and K-T plots were 0.9932 and 0.9976, respectively, indicating good linear relationships. In Table 5-6, the r_1 and r_2 values obtained from both methods were in good agreement with each other. $r_2 > r_1$ indicates that butadiene insertion was preferred when either dibutyl itaconate or butadiene was the last inserted. Moreover, the sequence distribution of PDIB copolymers shows that they were composed of long butadiene sequences with some isolated, diad, and triad dibutyl itaconate moities. Since the values of r_1 and r_2 were less than one, the copolymerization of dibutyl itaconate and butadiene belonged to a non-ideal copolymerization with an azeotropic point at 0.383, resulting in nearly random copolymers with high molecular weights.

Table 5-5. Parameters for the calculation of the reactivity ratios of dibutyl itaconate and butadiene[a].

Sample	$x=[M_1]/[M_2]$	$y = d[M_1]/d[M_2]$	$G = x(y-1)/y$	$H = x^2/y$	$\varepsilon = G/(\alpha+H)$	$\xi = H/(\alpha+H)$
PDIB10	2.1152	1.0588	0.1175	4.2256	0.0261	0.9374
PDIB20	0.9460	0.7419	-0.3291	1.2062	-0.2211	0.8104
PDIB30	0.5566	0.5957	-0.3778	0.5201	-0.4708	0.6482
PDIB40	0.3616	0.4615	-0.4219	0.2833	-0.7460	0.5009
PDIB50	0.2446	0.3571	-0.4404	0.1675	-0.9789	0.3724
PDIB80	0.0692	0.1333	-0.4499	0.0359	-1.4139	0.1129
PDIB90	0.0367	0.0714	-0.4773	0.0189	-1.5849	0.0626

[a] $\alpha = (H_{max} \times H_{min})^{1/2} = 0.2826$; $[M_1]$: molar fraction of dibutyl itaconate in the feed; $[M_2]$: molar fraction of butadiene in the feed; $d[M_1]$: molar fraction of dibutyl itaconate moiety in the copolymer; $d[M_2]$: molar fraction of butadiene moiety in the copolymer.

Table 5-6. Reactivity ratios of dibutyl itaconate and butadiene.

Method	r_1	r_2	$r_1 \times r_2$	azeotropic point[a]
Fineman-Ross	0.137	0.466	0.064	0.382
Kelen-Tüdös	0.141	0.466	0.066	0.383
Average	0.139	0.466	0.065	0.383

[a] Azeotropic point = $(1- r_2)/(2- r_1 - r_2)$

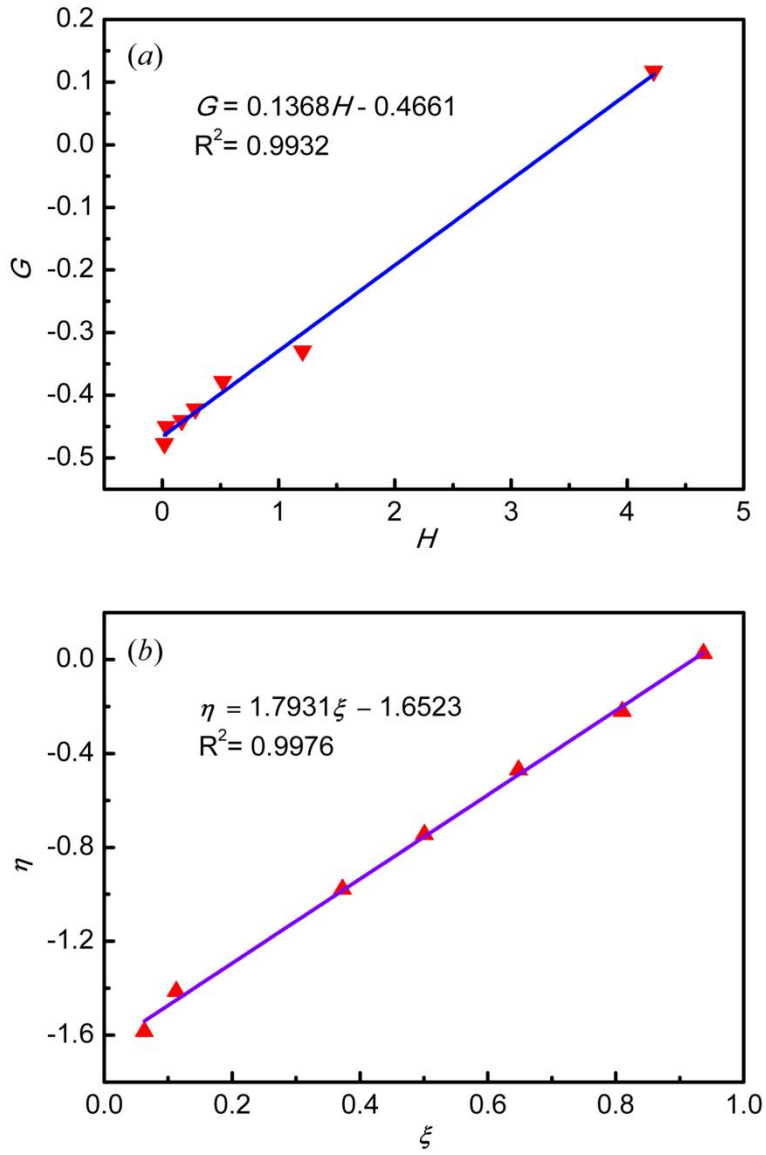

Figure 5-17. Calculations of the reactivity ratios of dibutyl itaconate and butadiene in redox-initiated emulsion copolymerization: (*a*) Fineman-Ross method, and (*b*) Kelen-Tüdös method.

3.7 Composition equation of PDIB copolymers

The composition equation of copolymers is usually used to describe the quantitative relationship between the monomer composition in the feed and the resultant copolymer composition. [221,222] The composition equation for the PDIB copolymers is given as follows:

$$F_1 = \frac{r_1 f_1 + f_1 f_2}{r_1 f_1^2 + 2 f_1 f_2 + r_2 f_2^2}$$

where F_1 is the ratio of the molar number of dibutyl itaconate moieties to the sum of the molar numbers of both monomer moieties in the copolymer, r_1 and r_2 are the monomer reactivity ratios as mentioned above, f_1 and f_2 are the ratios of the molar number of dibutyl itaconate moieties and that of butadiene moieties to the sum of the molar numbers of both monomers in the feed, respectively.

Figure 5-18 shows the relationship between the instantaneous copolymer composition F_1 and the monomer composition in the feed f_1. As discussed above, the copolymerization of dibutyl itaconate and butadiene belongs to a non-ideal copolymerization with an azeotropic point 0.383. If the molar feed fraction of dibutyl itaconate (f_1) is 0.383, the polymerization of PDIB will yield a copolymer of the same composition as the feed. A molar feed fraction of dibutyl itaconate less than 0.383 should yield a product with a higher fraction of dibutyl itaconate moieties than that of the feed, and a molar feed fraction of dibutyl itaconate higher than 0.383 should yield a product with a lower fraction of dibutyl itaconate moieties than that of the feed. Since the compositions of the copolymer and the feed monomer evolve during the copolymerization in a batch type of reactor for example, a drift in both compositions occurs.

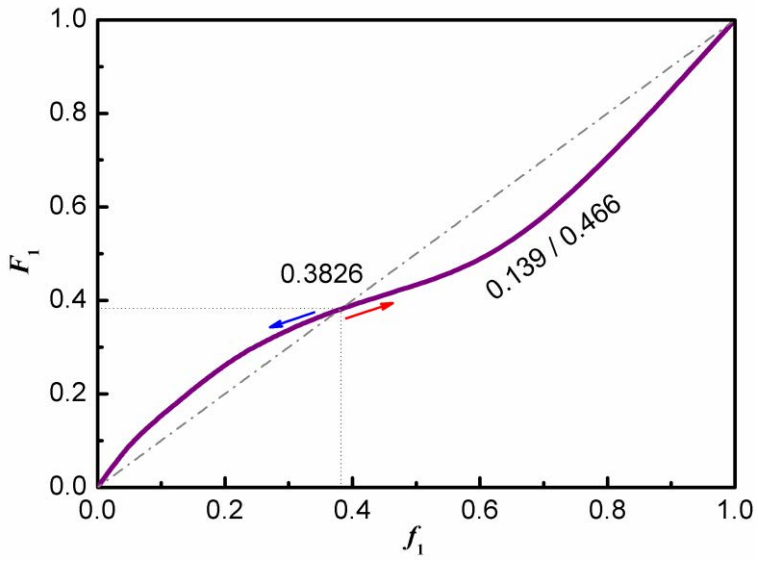

Figure 5-18. Instantaneous copolymerization behavior of the PDIB with an azeotropic point at 0.3826. F_1 represents the ratio of the molar number of dibutyl itaconate moieties to the sum of the molar numbers of both monomer moieties in the copolymer, and f_1 represents the molar ratio of the molar number of dibutyl itaconate to the sum of the molar numbers of both monomers in the feed.

3.8 Monomer sequence distribution in PDIB copolymers

The monomer sequence distributions of the PDIB copolymers were statistically investigated and are shown in Figure 5-19 and 5-20, and more statistical data are listed in Table 5-7. Figure 5-19 reveals the following information: (1) isolated dibutyl itaconate moiety (l = 1) accounted for 77.2, 88.3, 92.8, 95.2, 96.7, 97.7, 98.5, 99.0, and 99.5% of all dibutyl itaconate sequences in PDIB10, PDIB20, PDIB30, PDIB40, PDIB50, PDIB60, PDIB70, PDIB80, and PDIB90, respectively, indicating that the dibutyl itaconate sequences mainly exist in the form of isolated dibutyl itaconate moiety; (2) dibutyl itaconate sequences with more than 3 moieties ($l \geq 4$) can be neglected for all the PDIB copolymers, indicating dibutyl itaconate sequences are primarily isolated, diad, or triad moieties. As for the butadiene sequence distributions shown in Fig. 5-20, the percentage of isolated butadiene moiety in all butadiene sequences decreased form 81.8% for PDIB10 to 7.2% for PDIB90, and the long butadiene sequences with more than 40 moieties ($l' \geq 40$) existed in the copolymers. The monomer sequence distributions of the PDIB copolymers depended on steric hindrance, reactivity ratios, and feed molar ratios of monomers. The dibutyl itaconate was not prone to self-propagation due to its bulky substituents and small reactivity ratio and thus tends to copolymerizes with butadiene,

resulting in short dibutyl itaconate sequences. With a decrease in feed molar ratio of dibutyl itaconate to butadiene, the excess butadiene could self-propagate to form long flexible segments while dibutyl itaconate tended to be inserted into them in an isolated manner. This can also be seen from evolution of the number-average sequence lengths of the monomers in Table 5-7.

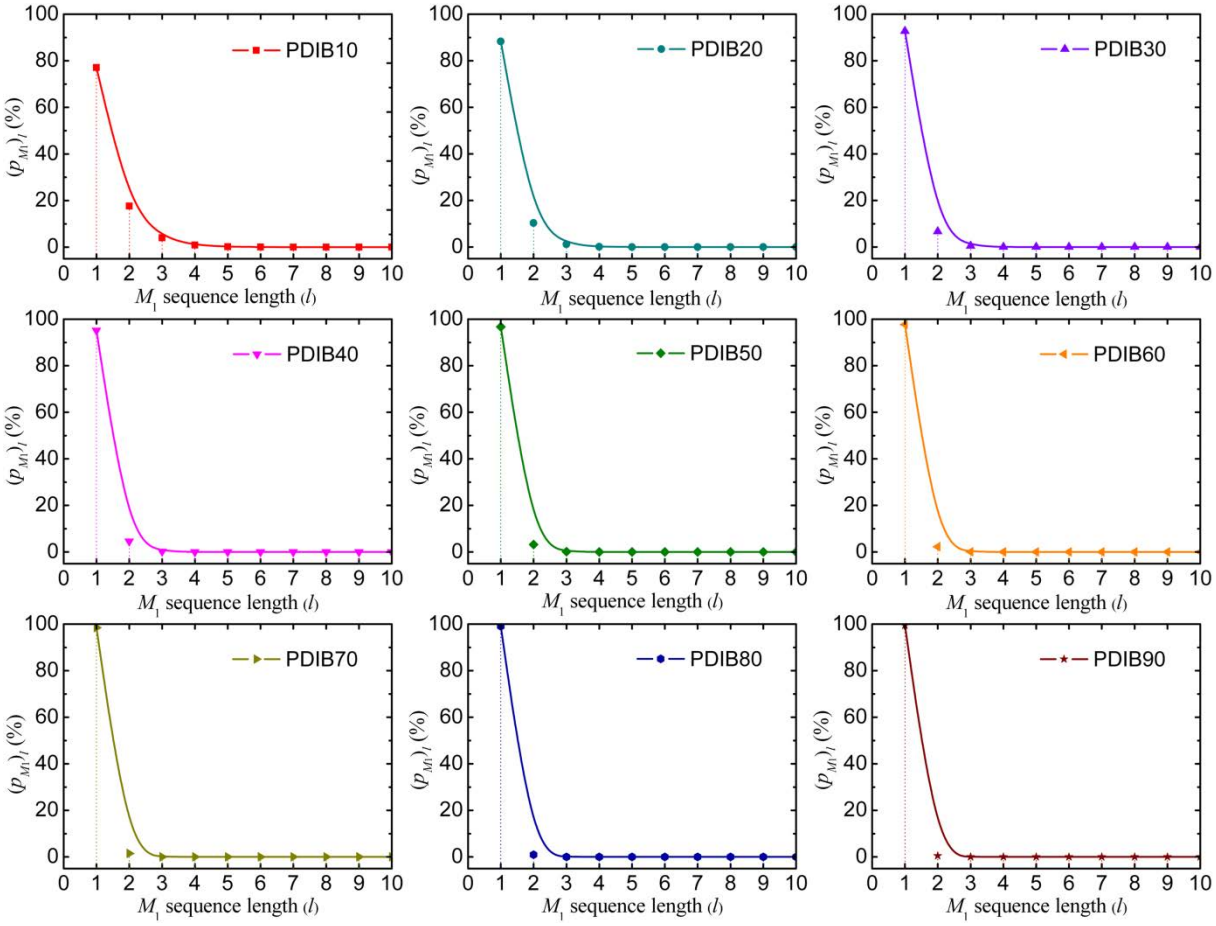

Figure 5-19. Dibutyl itaconate sequence distributions in PDIB copolymers.

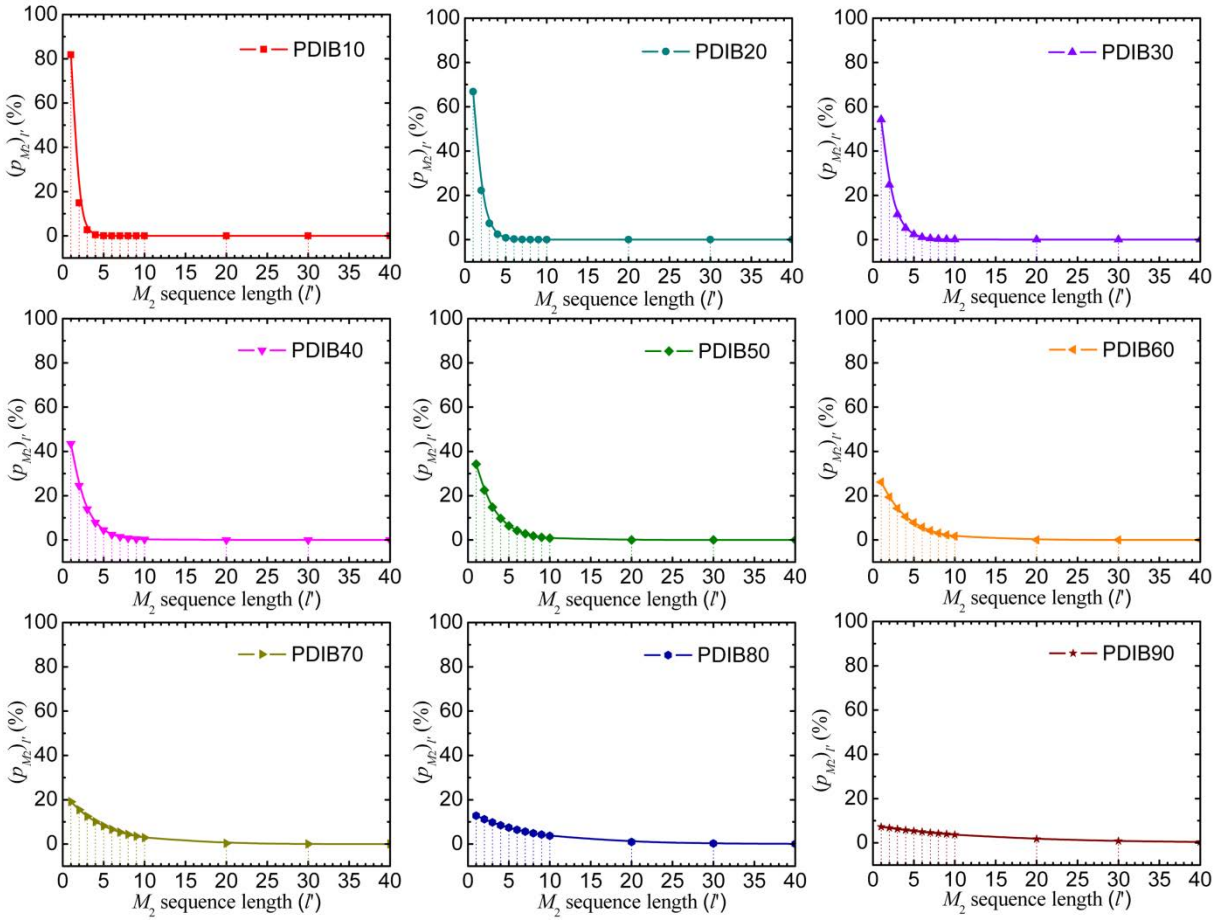

Figure 5-20. Butadiene sequence distributions in PDIB copolymers.

Table 5-7 Calculation for number-average lengths of monomer sequences of PDIB copolymer.

sample	M_1 (mol)	M_2 (mol)	p_{11}	p_{22}	$\bar{N}_{M1}$	$\bar{N}_{M2}$
PDIB10	0.235	0.111	0.227	0.773	1.29	1.22
PDIB20	0.210	0.222	0.116	0.330	1.13	1.49
PDIB30	0.186	0.333	0.072	0.456	1.08	1.84
PDIB40	0.161	0.444	0.048	0.563	1.05	2.29
PDIB50	0.136	0.556	0.033	0.656	1.03	2.90
PDIB60	0.111	0.667	0.023	0.737	1.02	3.77
PDIB70	0.086	0.778	0.015	0.808	1.02	5.20
PDIB80	0.062	0.889	0.010	0.871	1.01	7.74
PDIB90	0.037	1.00	0.005	0.927	1.00	13.70

3.9 Curing characteristics and mechanical properties of PDIB

Most elastomer products cannot be used as engineering materials unless properly cured. The curing characteristics of PDIB are shown in Fig. 5-21 and Table 5-8. From the typical curing curves, it can be concluded that PDIB could be effectively cross-linked by sulfur at 150^{o}C and could match current industrial applications for elastomers. An increase in curing time and a decrease in torque increase can be due to a loss of sulfur during blending of PDIB with additives. The mechanical properties of PDIB are shown in Fig. 5-22 and Table 5-9. The results show that the overall mechanical properties of PDIB matched or even surpassed those of traditional synthetic rubbers (tensile strength less than 1 MPa). The tensile strength and the elongation at break increased from 0.58 MPa and 414% for PDIB20 to 2.12 MPa and 484% for PDIB50, respectively. Those increases could be attributed to increased butadiene segments that increased the flexibility of PDIB chains and the number of their crosslinking sites. For PDIB60, PDIB70, and PDIB80, however, the tensile strength decreased and the elongation at break increased, due to a decrease in crosslinking density. Because PDIB were blended with additives on a two-roll mill, the loss of sulfur should be taken into account. Moreover, with increasing butadiene moieties, PDIB showed increased elasticity, resulting in that PDIB could readily burst apart during blending and consequently more loss of sulfur. The loss of sulfur caused a decrease in crosslinking density for PDIB60, PDIB70, and PDIB80. It is known that a higher crosslinking density leads to a higher tensile strength but a lower elongation at break for polymers. The result implies that the mechanical properties of PDIB could be influenced by the crosslinking density. The crosslinking density of PDIB was calculated by the Flory-Rehner expression shown in equation (5-4). In order to calculate the crosslinking density, the polymer-solvent interaction parameter (χ) should be determined first. For conventional elastomers, χ could be found in polymer handbooks. However, χ between PDIB and solvent (toluene) needed to be calculated according to the relationship for the solubility parameter shown in equation (5-6). The solubility parameter of PDIB was determined via a swelling method which was based on maxima in swelling using a series of solvents of varying and known solubility parameters. The assumption is that the interaction and swelling would reach a maximum when the solubility parameter of the polymer matched that of the solvent. Nine solvents with different solubility parameters were to calculate the solubility parameter δ of PDIB. A swelling ratio S ($V_{solution}/V_{PDIB}$) was used to characterize the swelling degree. As shown in Fig. 5-23, the solubility parameter δ of PDIB was 19.3 $(J/cm^3)^{1/2}$. The value of χ calculated based on the value of δ for PDIB was 0.0518. Then the crosslinking densities of the

PDIB were calculated using equation (5-4), and the results are listed in Table 5-11. As expected, the crosslinking density of the PDIB vulcanizates increased from PDIB20 to PDIB50, and then decreased from PDIB60 to PDIB80. The change in crosslinking density of PDIB vulcanizates was consistent with that of their tensile strength, confirming that the crosslinking density had a big impact on their mechanical properties.

Table 5-8. Curing parameters for the neat PDIB elastomers.

Sample	Scorch time (min:s)	Curing time (min:s)	Torque increase (dNm)
PDIB20	2:54	7:18	11.51
PDIB30	4:28	8:51	9.44
PDIB40	2:09	3:59	17.13
PDIB50	1:58	3:38	17.56
PDIB60	1:45	3:38	18.48
PDIB70	1:41	4:05	17.80
PDIB80	2:00	10.13	11.09

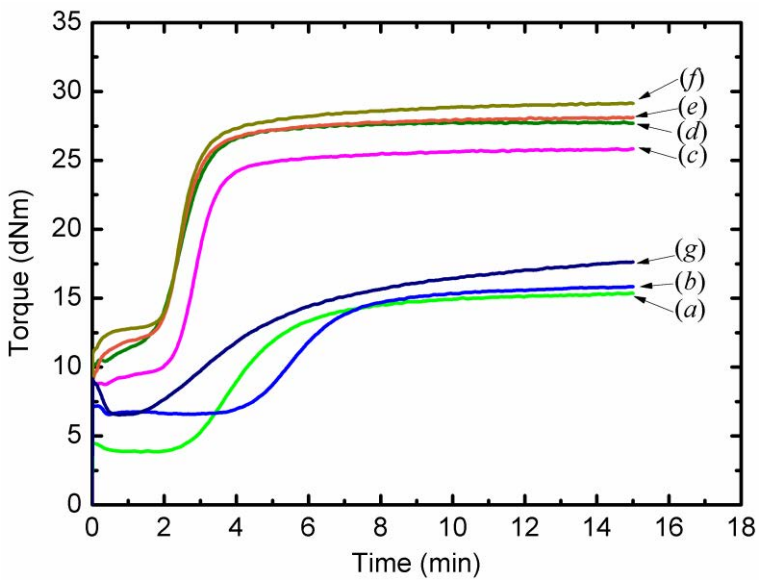

Figure 5-21. Curing curves of the neat PDIB elastomers: (*a*) PDIB20, (*b*) PDIB30, (*c*) PDIB40, (*d*) PDIB50, (*e*) PDIB60, (*f*) PDIB70, and (*g*) PDIB80.

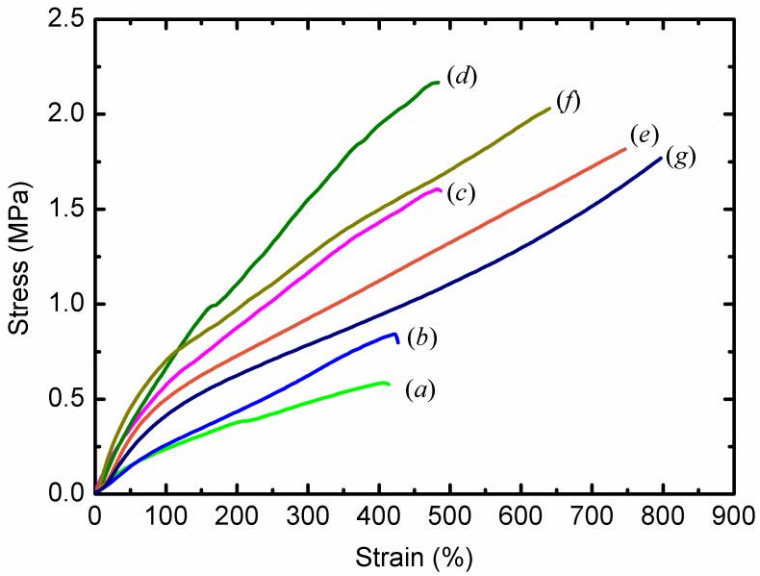

Figure 5-22. Stress-strain curves of the neat PDIB elastomers: (*a*) PDIB20, (*b*) PDIB30, (*c*) PDIB40, (*d*) PDIB50, (*e*) PDIB60, (*f*) PDIB70, and (*g*) PDIB80.

Table 5-9. Mechanical properties of the cross-linked PDIB elastomers.

sample	Tensile strength (MPa)	Elongation at break (%)	Permanent set (%)	Hardness (Shore A)
PDIB20	0.58±0.05	414±34	4±2	21
PDIB30	0.80±0.10	427±25	4±1	25
PDIB40	1.60±0.08	487±41	5±1	35
PDIB50	2.17±0.23	484±16	3±1	36
PDIB60	1.78±0.11	747±32	2±2	37
PDIB70	2.03±0.15	640±38	3±1	42
PDIB80	1.77±0.21	795±57	4±2	46

Table 5-10. Calculation of the solubility of PDIB.

Solvent	Density (g/cm^3)	δ_s ($J^{1/2}$ $cm^{-3/2}$)	m_0 (g) [a]	m_0' (g) [b]	*S*
n-Hexane	0.6594	14.9	0.1150	0.1908	0.9996
n-Heptane	0.6836	15.3	0.1209	0.2094	1.0708
Cyclohexane	0.7786	16.8	0.1187	0.3563	2.5709
Carbon tetrachloride	1.5940	17.8	0.1179	1.0758	5.0970

Toluene	0.8669	18.2	0.1180	0.6602	5.3004
Chloroform	1.4840	19.0	0.1168	1.1879	6.1795
n-Propanol	0.8036	24.5	0.1199	0.1780	0.6030
Ethanol	0.8160	26.5	0.1185	0.1439	0.2627
Methanol	0.7910	29.6	0.1187	0.1373	0.1981

[a] Mass of the dry network after the extraction of soluble materials. [b] Mass of the swollen network at equilibrium.

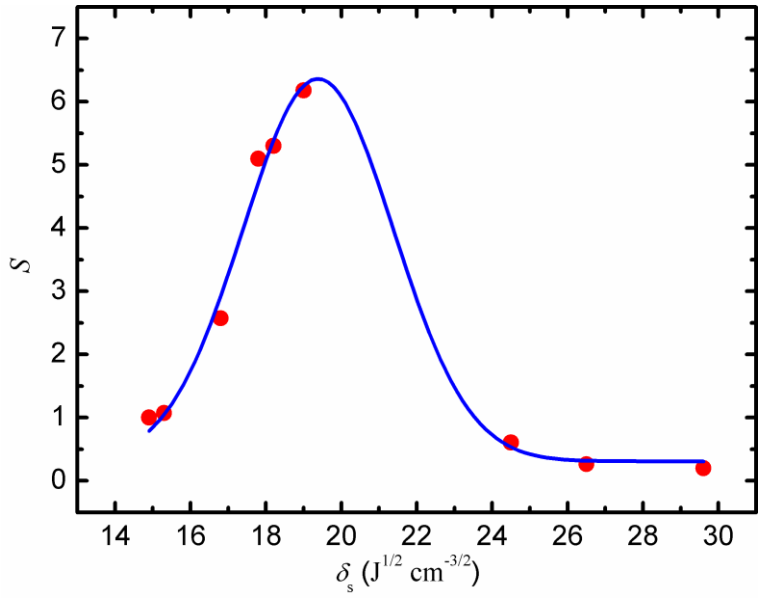

Figure 5-23. Relationship between the swelling ratio and solubility parameter.

Table 5-11. Densities and crosslinking densities of the PDIB vulcanizates.

Sample	Density (g/cm^3)	Crosslinking density (10^{-4} mol/cm^3)
PDIB20	1.12±0.03	1.48±0.11
PDIB30	1.10±0.01	1.45±0.17
PDIB40	1.13±0.04	2.21±0.14
PDIB50	1.08±0.05	2.90±0.21
PDIB60	1.08±0.02	2.29±0.19
PDIB70	1.05±0.01	2.52±0.26
PDIB80	1.06±0.02	1.12±0.15

4. Conclusions

Bio-based cross-linkable poly(dibutyl itaconate-co-butadiene) (PDIB) elastomers with high molecular weights and low glass transition temperatures were synthesized from dibutyl itaconate and butadiene by redox-initiated emulsion polymerization. With a feed butadiene content of 40 wt.%, the yield, the number-average molecular weight, and the glass transition temperature of the resultant PDIM copolymer were 86%, 392 000 g/mol, and -52^{o}C, respectively. The chemical structure of the PDIB was determined by FTIR and NMR. With an increase in butadiene moieties in PDIB, *trans*-configuration of butadiene moieties prevailed and *vinyl*-configuration increased. The reactivity ratios of both monomers calculated by the Fineman-Ross and the Kelen-Tüdös methods were less than one and were in agreement with each other, indicating that the copolymerization was non-ideal ith an azeotropic point at 0.383 and that the monomers tended to copolymerize to produce chains with high molecular weights. The monomer sequence distribution was investigated by using a simplified statistical model. With a decrease in the feed ratio of dibutyl itaconate to butadiene, the excess butadiene underwent self-propagation to form long flexible segments while the dibutyl itaconate tended to be inserted into them in an isolated manner. The mechanical properties of the PDIB could match or even surpass those of traditional synthetic rubbers. The stress and the elongation at break of unfilled PDIB50 were over 2 MPa and 450%, respectively, indicating that PDIB elastomers might be good candidates for replacement of traditional synthetic rubbers based on petrochemical resources.

Acknowledgement

The authors thank the National 973 Basic Research Program of China (2015 CB654700), National Natural Science Foundation of China (50933001, 51503010), and the China-France Cooperation Program of PHC CAI YUANPEI (CHINA SCHOLARSHIP COUNCIL, No. 201504490120) for their financial support. The authors also thank Jilin Petrochemical Research Institute for its great help.

High performance bio-based elastomers: energy efficient, sustainable materials for tires

Abstract: Globally, we face a massive growth in the number of urban vehicles. This growth comes at a cost of enormous fuel consumption, CO_2 emissions and air pollution, commonly seen as a haze. A strategy to overcome these issues is to fabricate low roll-resistance green tire elastomers using bio-based chemicals. A sustainable bio-based poly(dibutyl itaconate-*co*-butadiene) (PDIB) elastomer shows a potential for fabricating such green tires. By combining a molecular design with non-fossil based silica and an *in-situ* modification technique to tune the viscoelastic properties of the PDIB/silica nanocomposites, we successfully manufactured low roll-resistance green tires based on PDIB/silica nanocomposites. The results shown here open an important avenue for the synthetic rubber and automobile industry to improve a major challenge many cities worldwide, and also provide an effective route for resource sustainability.

Keywords: Bio-based nanocomposite; Green tire; Low resistance; Sustainable development.

1. Introduction

Passenger vehicles play a fundamental role in modern society. In 2015, approximately one billion passenger cars were in use around the world. [223] This widespread use of cars has far-reaching environmental and health-related consequences, including, but not limited to, CO_2 emission and progressively worsening urban haze. Tires, an essential component of all urban and rural vehicles and equipment, account for ~20% of fuel used. Rolling resistance of the tire accounts a startling 4% of worldwide carbon dioxide emissions from fossil fuel. [224,225] It is recognized that fuel consumption decreases by 2-3% when the rolling resistance coefficient decreases by 10%. [226] There are industrial guidelines on tire labelling to promote the fuel-efficiency of tires, for example, the EU Tire Labelling Regulation 1222/2009. Therefore, it is critical to develop low rolling resistance green tires.

Usually, elastomers need to be reinforced by fillers to ensure sufficient strength, wear resistance and elastic properties. However, viscous dissipation, resulting from the relaxation of polymer chains, in both unfilled and filled systems, account for a great amount of useless fuel consumption. [227-229] Many factors in filled polymeric systems, including macromolecular structure, aggregate structure, filler dispersion, and filler-elastomer interfacial interaction can affect the rolling resistance of tires. Values of the loss tangent at 60°C for elastomeric materials and the rolling resistance coefficients of tires are laboratory and industrial benchmarks for fuel consumption, respectively. Tread elastomer, which is the largest elastomeric component of the tire, is the primary target for fuel saving, wet grip resistance and wear-resistance. Wet grip resistance, dictated by the structure and properties of the tire composites, is of extreme practical important and a major concern for safety. Elastomeric materials with high loss tangents at 0^oC will exhibit good wet grip performance and the energy dissipation of automobile will be highly efficient during braking. However, simultaneously reducing the loss tangent at 60^oC and improving the loss tangent at 0^oC of elastomeric material is a major challenge. Silica-reinforced anionic solution polymerized styrene-butadiene rubber (SSBR) composites are widely used in the tire industry and have become the most important tread materials for present green tires, which have a relatively high 0^oC loss tangent and low 60^oC loss tangent. The properties of SSBR such as glass transition temperature (T_g) increase as the styrene and *vinyl* contents increase. However, SSBR with a high *vinyl* content shows less hysteresis heat than SSBR with a high styrene content even though they possess the same T_g. [230]

Synthetic elastomers used in tires now are derived mainly from petrochemicals, which are not sustainable. In 2014, the output of synthetic rubber reached 14.2 million tons, consuming ~35.5 million tons of crude oil [231] and emitting tremendous amounts of CO_2. The global climate change (global warming) and air pollution (smog or haze) strike directly at the intersection of societal environmental demands and economic needs. Environmentally-friendly solutions must be found. New strategies must be developed to produce polymer materials from renewable resources. [84,232] Bio-based polymers such as polylactide [233], polyhydroxyalkanoates [234], and poly(butylene succinate) [235] have been successfully industrialized. Soybean oil based elastomers [45], polyester elastomers [236], and poly(diisoamyl itaconateco-isoprene) elastomers [50] have already been investigated previously. However, bio-based synthetic elastomers for tire applications have yet to emerge. Major tire manufacturers plan to use sustainable resources for tires in a foreseeable future. [237] To meet this target, sustainable elastomers must be developed and non-renewable carbon black must be replaced with non-petroleum based fillers, like silica (Fig. 5-24).

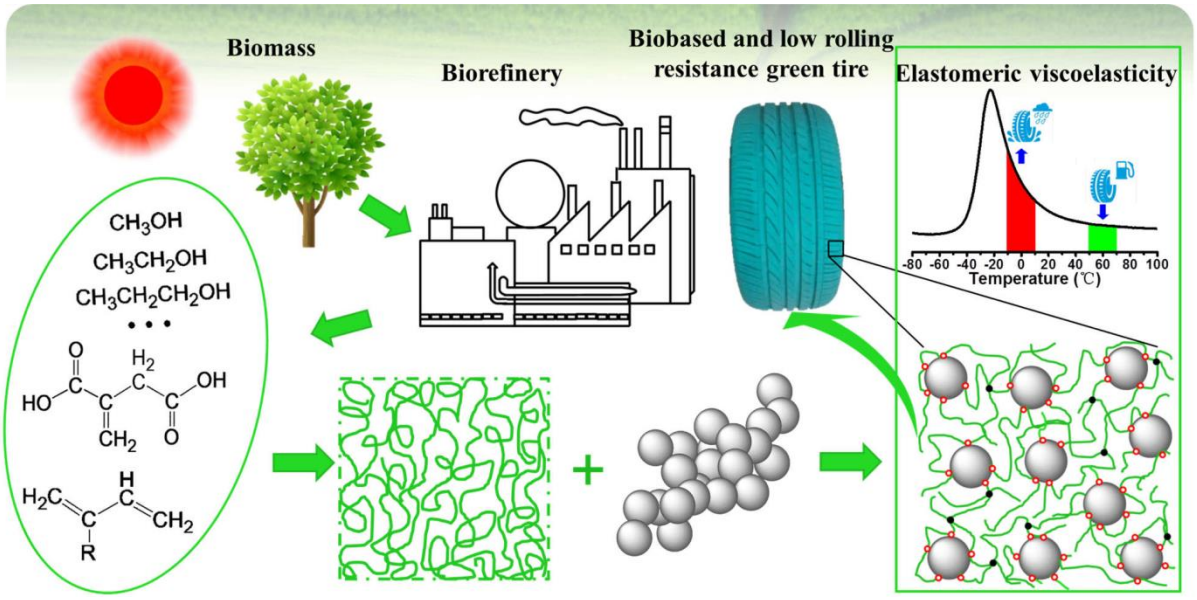

Figure 5-24. Integrated biomass-based chemicals with chemosynthesis-bio-based low rolling resistance elastomer pathway for sustainable resources and environmental protection.

In this study, PDIB/silica nanocomposites were prepared and investigated. The focus was on their mechanical performance, dynamic properties, and filler dispersion, which are decisive factors for the performance of resultant tires. A tire tread material was prepared based on PDIB/silica nanocomposites. The first low rolling resistance tire based on bio-based elastomer

was successfully fabricated and appeared to be a very interesting alternative for automobile tires.

2. Experimental

2.1 Materials

PDIB elastomers were synthesized according to the first part in Chapter 5. Silica (VN3) and silane (VP Si-363) were purchased from Evonik Degussa Co. All other chemicals and materials were reagent-grade commercial products and were used as received without further purification.

2.2 Preparation of PDIB/silica nanocomposites

The PDIB elastomer and additives were masticated in a 15.24 cm two-roll mill according to the formulation provided in Table 5-12 and the mixing procedure in Table 5-14. The resultant compound was cured in a XLB-D 350×350 hot press (Huzhou Eastmachinery Corporation, China) under 15 MPa at 150^{o}C for its optimum curing time as determined by a disk oscillating rheometer (P3555B2, Beijing Huanfeng Chemical Machinery Experimental Factory, China). The SSBR/silica nanocomposites were prepared using the above formulation and mixing procedure except that PDIB was substituted with SSBR.

Table 5-12. Formulation for the preparation of PDIB/silica nanocomposites.

Ingredient	Loading (phr) [a]
PDIB	100.0
Silica (VN3)	60.0
Si-363 (coupling reagent)	6.0
Zinc oxide	5.0
Stearic acid	0.5
Antioxidant 4020 [b]	1.0
Accelerator M [c]	0.7
Accelerator CZ [d]	1.0
sulfur	1.0

[a] phr stands for parts per 100 parts of rubber by weight. [b] N-1,3-dimethylbutyl-N'-phenyl-*p*-phenylenediamine. [c] 2-Mercaptobenzothiazole. [d] N-Cyclohexyl-2-benzothiazole.

2.3 Preparation of PDIB-BR/silica nanocomposites for green tires

The formulation (*c*) in Table 5-13 for preparing green tire composites was determined by evaluating the performance of PDIB-BR/silica nanocomposites which were prepared according to the formulations in Table 5-13 and the mixing procedure in Table 5-14. The tire tread compound, colored with phthalocyanine and titanium oxide, was prepared according to the formulation (*c*) in Table 5-13 and the mixing procedure in Table 5-14.

Table 5-13. Formulation of PDIB/silica compounds for green tires.

Ingredient	Loading (phr)		
	a	*b*	*c*
PDIB40	100.0	0	70.0
Polybutadiene (BR)	0	100	30.0
Silica (VN3)	50.0	50.0	50.0
Si-363	7.0	7.0	7.0
Zinc oxide	5.0	5.0	5.0
Stearic acid	2.0	2.0	2.0
Antioxidant 4020	1.0	1.0	1.0
Antioxidant RD	1.0	1.0	1.0
Wax	1.0	1.0	1.0
Accelerator CZ	1.0	1.0	1.0
Accelerator NS [a]	1.2	1.2	1.2
Sulfur	1.5	1.5	1.5

[a] N-tert-butylbenzothiazole-2-sulphenamide.

Table 5-14. Mixing procedure of PDIB/silica compound.

Stage I	Two-roll mill
1	PDIB40, BR
2	Antioxidant 4020 and antioxidant RD
3	1/2 silica, zinc oxide, stearic acid
4	1/2 silica, Si-363, wax
Stage II	Two-roll mill with heat equipment

0	Batch stage I
1	Heat treatment at 150°C, 5 min, stockpile for 2 hours
Stage III	Two-roll mill
0	Batch stage II
1	Titanium oxide, phthalocyanine
2	Accelerators, sulfur
3	Homogenization on two-roll mill

2.4 Measurements and characterization

Scanning electron microscopy (SEM) was performed on a Hitachi S-4800 scanning electron microscope (Hitachi, Japan). The surface of the sample was sputtered with a thin layer of gold prior to the analysis. The SEM analysis was carried out at an accelerating voltage of 5 kV. Transmission electron microscopy (TEM) images were recorded on an FEI Tecnai G2 20 S Twin TEM at 200 kV. Ultrathin section specimens of PDIB/silica nanocomposites for the TEM observation were prepared using a cryo-ultramicrotome (Leica EM UC6, Germany) and were mounted on mesh copper grids. The vulcanization times of the PDIB/silica nanocomposites were determined at 150°C on a rotor-less rheometer. Tensile tests of the PDIB/silica nanocomposites were conducted according to ASTM standard (D412: dumbbell-shaped), and the specimens were tested on a LRX Plus tensile tester at 25°C. The crosshead speed was 500 mm/min. The internal friction loss (tan δ) as a function of temperature was measured by a DMTA dynamic mechanical thermal analyzer (Rheometrics Scientific Inc., United States) in the rectangular tension mode. The measurements were carried out at a constant frequency of 10 Hz, a heating rate of 3°C/min, and an oscillating strain amplitude of 0.1% in the temperature range of -100 to 100°C. Each sample was 30 mm in length, 10 mm in width, and 2 mm in thickness. Strain sweep experiments (storage modulus (G‘) and loss factor (tanδ) as a function of scanning strain were performed on vulcanizates by a Rubber-Process-Analyzer (RPA, Alpha Technologies Corporation, Akron, Ohio, United States) at 60°C. The strain amplitude (ε %) was varied from 0.28 to 400% and the frequency was 1 Hz. Shore A hardness was measured according to ASTM D2240 by an XY-1 rubber hardness apparatus (4th Chemical Industry Machine Factory, Shanghai, China). In the Akron abrader (GT-7012-A, Gotech Testing Machines Co. Ltd., Taiwan), the contour of the circular test specimen,

mounted on a motor-driven spindle, was brought into contact with the periphery of an abrasive wheel (150 × 38 mm, abrasive media: 36# grit wheel), which was mounted on another spindle. Rotation of the specimen caused the abrasive wheel to rotate and the two were held together under a force of 26.66 N. The axis of the specimen and that of the abrasive wheel were at an angle of 15^{o}, which caused a rubbing action. The weight loss was recorded after a specified number of revolutions (1.61 km, 3418 revolutions) of the abrasive wheel. The specimen was first abraded by 800 revolutions before the Akron abrasion measurement. The abrasion resistance of the specimen was calculated from its volume loss according to the weight loss and tread density. The test temperature was 25^{o}C.

3. Results and discussion

3.1 Curing characteristics of PDIB/silica nanocomposites

As vulcanization is a critical step for elastomeric products, the effect of silica on the curing characteristics was studied. As the modulus of the elastomer increased dramatically during curing, it was used to evaluate the curing process. Figure 5-25 the torque of the PDIB/silica compounds as a function of curing time. It increased with increasing curing time as a result of the increasing crosslink density. Table 5-15 shows their curing characteristics in terms of scorch time, curing time, etc. based on Figure 5-25. The scorch time is the time interval corresponding to 10% torque increase and the curing time is the time interval corresponding to 90% torque increase.

Compared with the neat PDIB elastomer, PDIB/silica compounds had lower curing speed and higher torque. The lower curing speed was due to the adsorption of accelerators on the silica surfaces. As there were many hydroxyl groups on the silica surfaces, polar organic molecules such as accelerator molecules were prone to be adsorbed on them. Being rigid particles with a high modulus, the incorporation of silica resulted in a higher torque than that of the neat PDIB. PDIB90/silica and PDIB100/silica compounds seemed to need more time to achieve the equilibrium curing, probably because the curing speed was greater than the devulcanization one, resulting in a higher crosslink density. The scorch time indicates the prevulcanization trend of the compound. The longer the scorch time, the lower the prevulcanization trend, and therefore the more reliable the process of the elastomeric compounds on the mill. The curing time was used in the subsequent vulcanization of the PDIB/silica compounds.

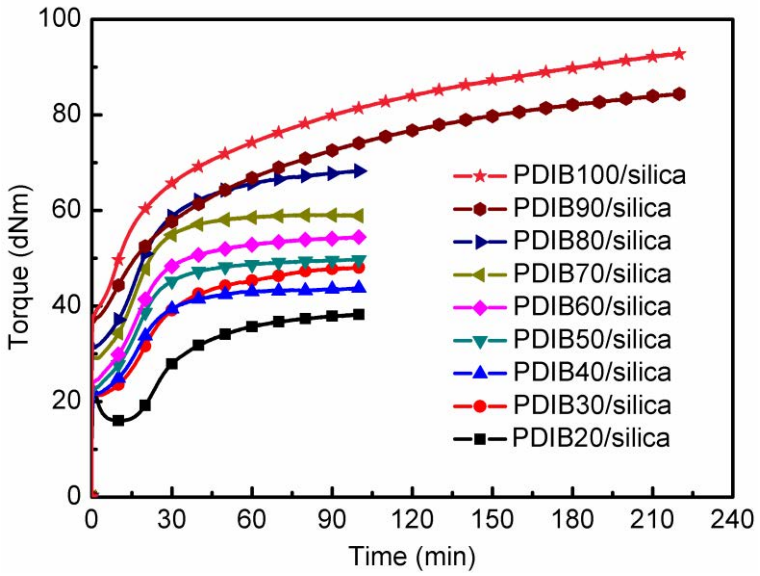

Figure 5-25. Torque of PDIB/silica nanocomposites as a function of curing time.

Table 5-15. Curing characteristics for PDIB/silica compounds.

Sample	Scorch time (min:s)	Curing time (min:s)	Torque min (dNm)	Torque max (dNm)	Torque increase (dNm)
PDIB20/silica	18:40	62:47	15.98	38.27	22.29
PDIB30/silica	10:55	61:18	21.30	48.12	26.82
PDIB40/silica	4:54	39:39	20.16	43.80	23.64
PDIB50/silica	4:51	38:30	21.75	49.78	28.03
PDIB60/silica	5:48	44:30	23.81	54.41	30.60
PDIB70/silica	7:15	34:29	29.04	59.15	30.11
PDIB80/silica	7:36	52:24	31.25	68.33	37.08
PDIB90/silica	6:21	78:00	36.85	76.14	39.29
PDIB100/silica	5:50	74:09	37.98	82.16	44.18

3.2 Filler-filler and filler-polymer interactions in PDIB/silica compounds

In order to promote chemical bonding of the PDIB elastomer to the silica, VP Si-363, a silane with a free mercapto group on the rubber-active site and a combination of an ethoxy and polymeric, amphiphilic substituents on the silica-active site, was used. The ethoxy was cleaved during the mixing process and the silane bonded covalently to the silica-surface through *in-situ* modification reaction (Scheme 5-2*a*). The polymeric chains were polar,

ensuring high silica affinity and fast adsorption and reaction on the silica surfaces. The mercapto group was responsible for the efficient coupling of the silane to the polymer chains through click reaction (Scheme 5-2*b*). [238,239]

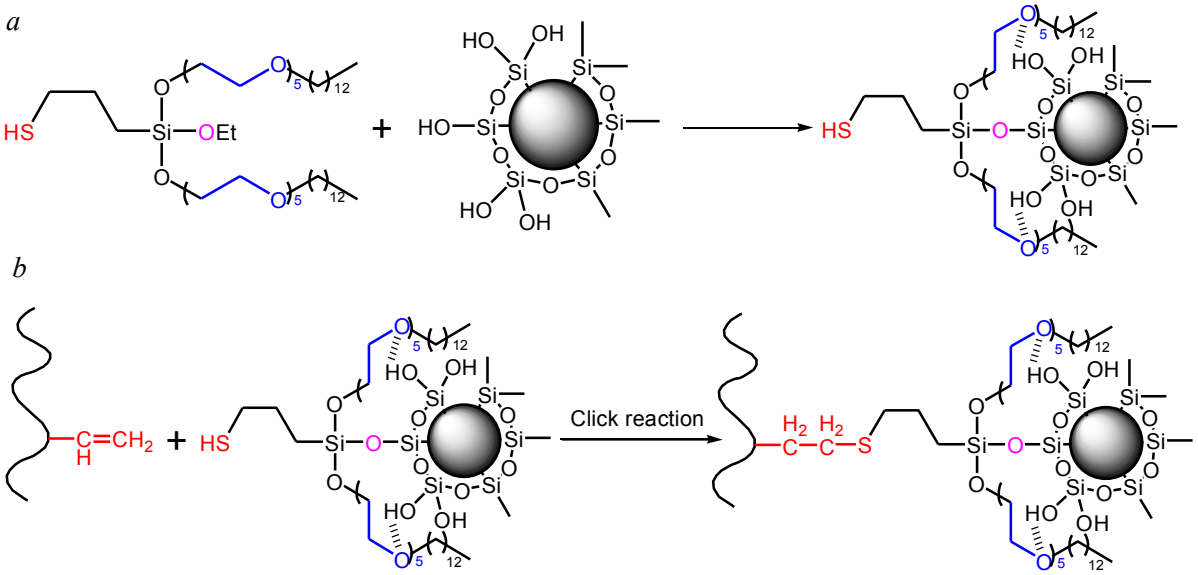

Scheme 5-2. (*a*) *In-situ* modification of silica with Si-363 and (*b*) covalent bonding of PDIB chains with modified silica via click reaction.

The Rubber-Process-Analyzer (RPA) allows investigating the strength of a filler network and filler-polymer interactions in a silica-filled elastomeric compound in a wide range of shear strain amplitudes. [101,132] Figure 5-26 shows the RPA curves of PDIB/silica compounds. The storage modulus of the PDIB/silica compounds decreased nonlinearly with increasing applied dynamic strain, due to stain-induced changes in the material‘s microstructure. As the butadiene moieties of the PDIB elastomers increased, the initial modulus G_0 increased more than the infinite modulus G_∞, resulting in a non-linear viscoelastic behavior known as Payne-effect (G_0-G_∞) (Fig. 5-26*a*). This increase was caused by the formation of filler-filler interactions which became stronger with increasing butadiene content. The *in-situ* modification technique allowed chemical bonding of PDIB chains to silica. Moreover, hydrogen bonding interactions could be formed between silanols on the silica surfaces and ester groups of the PDIB chains according to our previous studies. [96] This silica-PDIB interactions could prevent silica from aggregating to a filler network, resulting in a homogenous dispersion of silica. The number of ester groups per unit volume decreased with increasing butadiene content in the PDIB elastomer. Therefore, the silica-PDIB interactions weakened. The weakened silica-PDIB interactions imply an increased probability for the formation of silica network, resulting in an increase in Payne-effect and inhomogeneous

dispersion of silica. Figure 5-26*b* shows the strain dependence of loss tangent (tan δ) at 60°C. The values of the tan δ of PDIB/silica compounds at 60°C were low up to 20% strain, indicating that PDIB/silica nanocomposites were potential materials for tires with low rolling resistance.

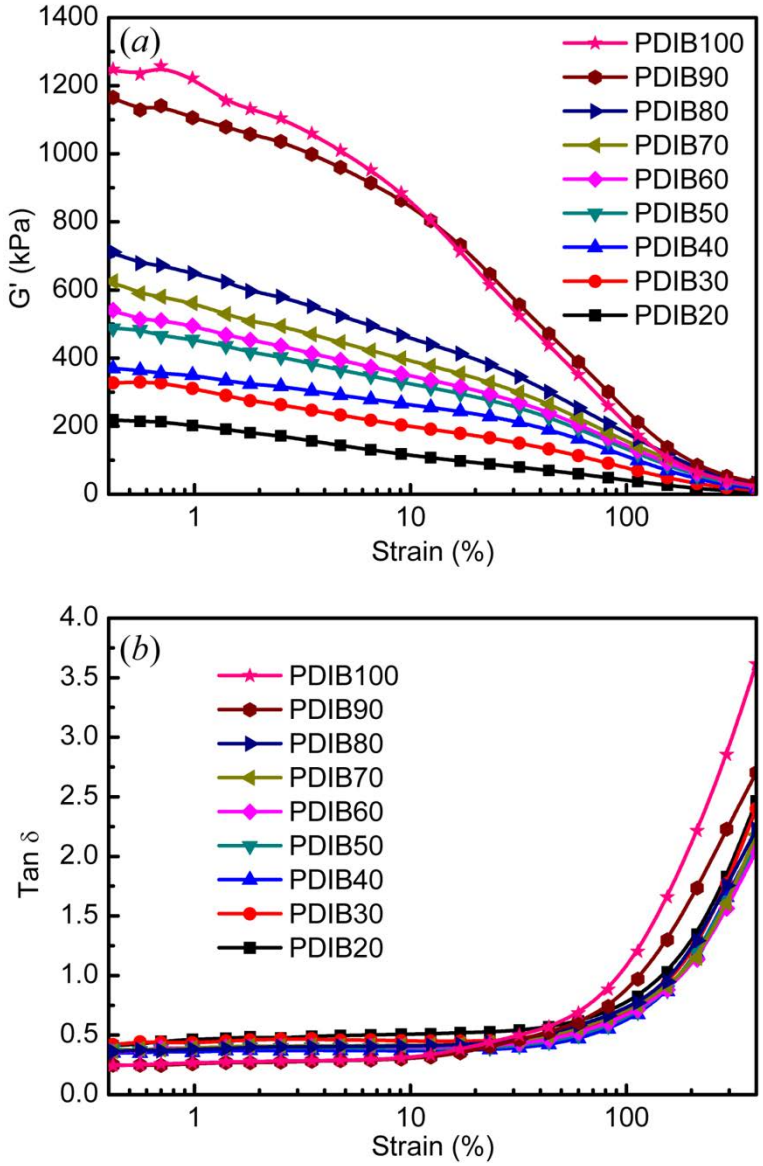

Figure 5-26. Strain dependence of (*a*) storage modulus and (*b*) loss tangent (tan δ) for PDIB/silica compounds.

3.3 Morphology of PDIB/silica nanocomposites

SEM and TEM were used to investigate the state of dispersion of silica in the PDIB/silica nanocomposite. The dark and light parts of the SEM images of Fig. 5-27*a-i* represent the PDIB matrix and silica particles, respectively. It is the opposite for the TEM images of Fig. 5-

27*a*'-*i*'. The SEM images of Fig. 5-27*a-i* show that the silica particles were spherical in shape and their diameter ranged from 20 to 50 nm. The state of dispersion of silica depended strongly on the filler-polymer interactions in PDIB/silica nanocomposites. As discussed above, the hydrogen bonding interaction could be formed between silanols and ester groups of PDIB/silica nanocomposites, resulting in dense and homogenous dispersion of silica, as shown in Fig. 5-27*a*'-*c*'. As the content of the ester groups in PDIB decreased, the silica-PDIB interaction weakened, resulting in the formation of silica networks and inhomogeneous dispersion, as shown in Fig. 5-27*g*'-*i*'.

3.4 Mechanical properties of PDIB/silica nanocomposites

Figure 5-28 shows the stress-strain curves of cross-linked PDIB/silica nanocomposites, and Table 5-16 gathers the most relevant data. The tensile strength and elongation at break of the PDIB/silica nanocomposites exceed 17 MPa and 500%, respectively, except for those of PDIB20/silica, PDIB90/silica, and PDIB100/silica nanocomposites. The deterioration of mechanical properties for PDIB90/silica and PDIB100/silica nanocomposites was attributed to the inhomogeneous dispersion of silica and the formation of silica networks. The aggregated silica in the PDIB90 and PDIB100 matrices acts as stress-concentration points, resulting in deterioration of the mechanical properties. The stress-strain curves of PDIB80/silica, PDIB90/silica, and PDIB100/silica nanocomposites exhibited a steep slope till 10% strain and then a weak yield phenomenon, indicating the presence of the filler network. The PDIB70/silica nanocomposite exhibited the best mechanical properties with a tensile strength of 25.0 MPa and an elongation at break of 774%. The tensile stress at 300% strain and the permanent set are also shown in Table 5-16. The mechanical properties of PDIB/silica nanocomposites meet most requirements of engineering applications.

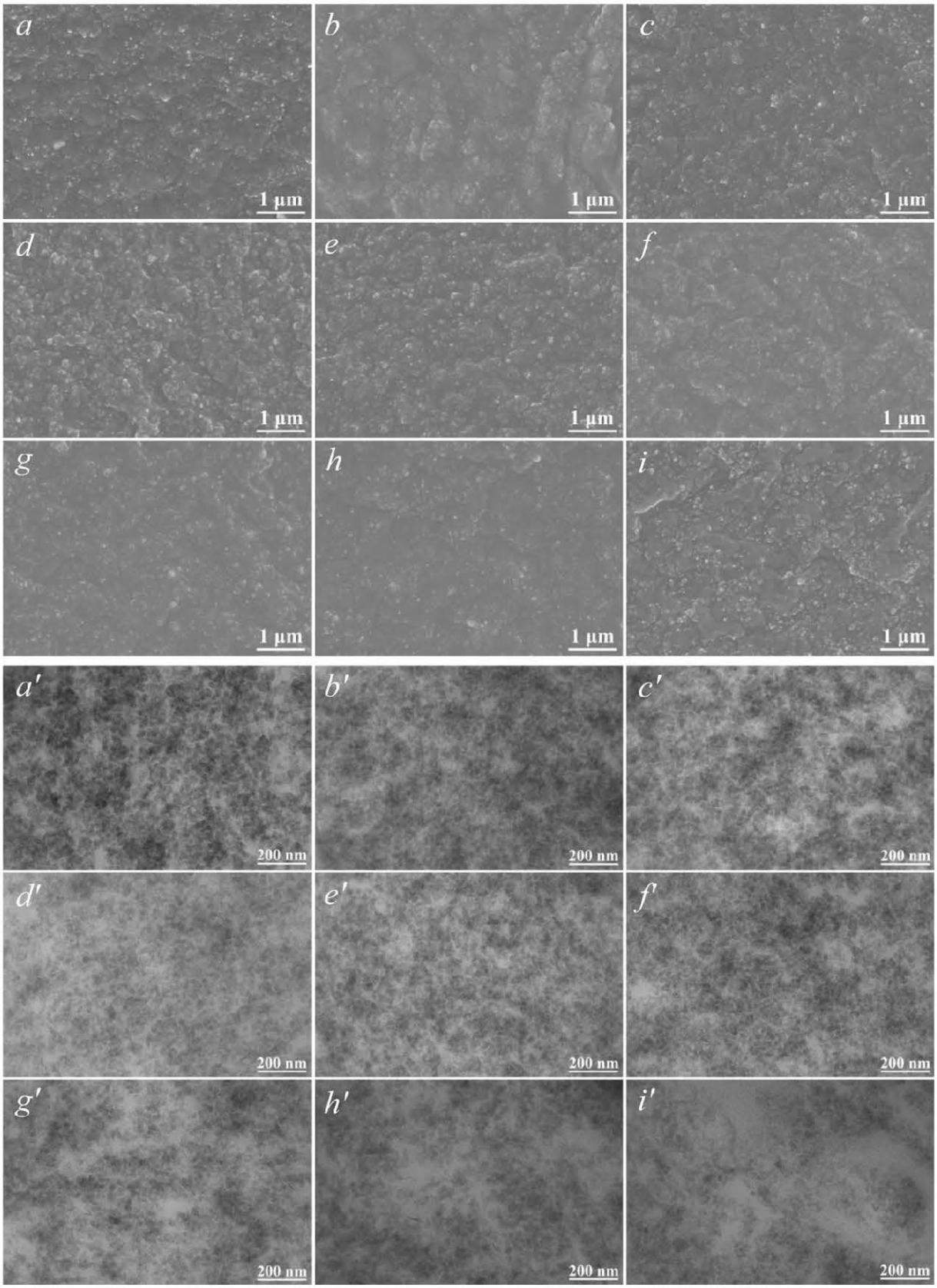

Figure 5-27. SEM (*a*-*i*) and TEM (*a*'-*i*') images for PDIB/silica nanocomposites: (*a*, *a*') PDIB20/silica, (*b*, *b*') PDIB30/silica, (*c*, *c*') PDIB40/silica, (*d*, *d*') PDIB50/silica, (*e*, *e*') PDIB60/silica, (*f*, *f*') PDIB70/silica, (*g*, *g*') PDIB80/silica, (*h*, *h*') PDIB90/silica, (*i*, *i*') PDIB100/silica.

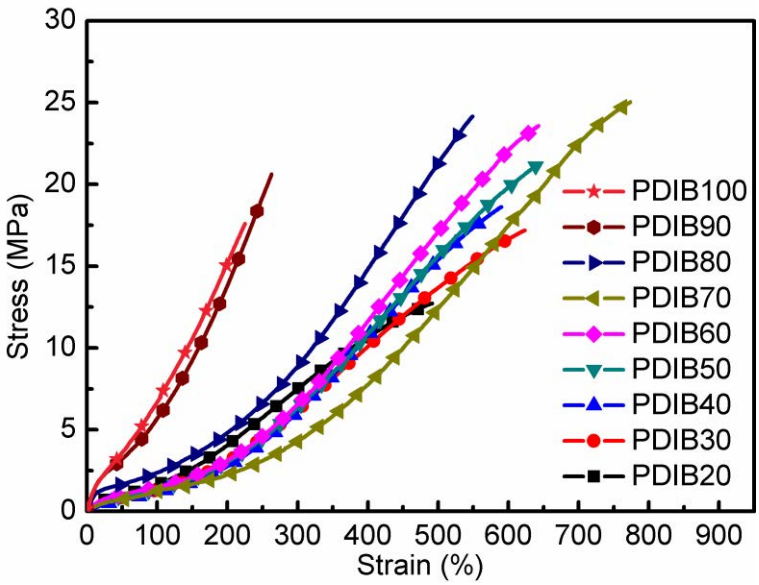

Figure 5-28. Stress-strain curves for PDIB/silica nanocomposites.

Table 5-16. Mechanical properties of PDIB/silica nanocomposites.

sample	Tensile strength (MPa)	Elongation at break (%)	300% Tensile stress (MPa)	Permanent set (%)
PDIB20/silica	12.7 ± 0.6	492 ± 38	7.5 ± 0.2	40 ± 4
PDIB30/silica	17.4 ± 1.3	509 ± 42	8.8 ± 0.3	32 ± 4
PDIB40/silica	18.6 ± 0.9	590 ± 43	6.1 ± 0.2	16 ± 2
PDIB50/silica	21.2 ± 1.1	640 ± 36	6.4 ± 0.1	16 ± 3
PDIB60/silica	23.6 ± 1.5	643 ± 27	6.5 ± 0.5	16 ± 2
PDIB70/silica	25.0 ± 1.4	774 ± 51	4.3 ± 0.3	16 ± 2
PDIB80/silica	24.8 ± 0.8	545 ± 46	9.3 ± 1.2	10 ± 1
PDIB90/silica	20.6 ± 2.2	263 ± 23	N/A	2 ± 1
PDIB100/silica	17.6 ± 2.6	255 ± 29	N/A	2 ± 1

3.5 Dynamic mechanical properties of PDIB/silica nanocomposites

DMTA analysis is an important technique to understand the performance of elastomers in the production of tires. The value of tan δ at 60^{o}C is used as a criterion for the rolling resistance, while that at 0^{o}C is used as a criterion for the wet grip resistance. An ideal material for production of high-performance tires should have a low tan δ value at 60^{o}C and a high tan δ

value at 0°C. Figure 5-29 shows the temperature dependence of the tan δ values of the crosslinked PDIB/silica nanocomposites, and Table 5-17 gathers most relevant data.

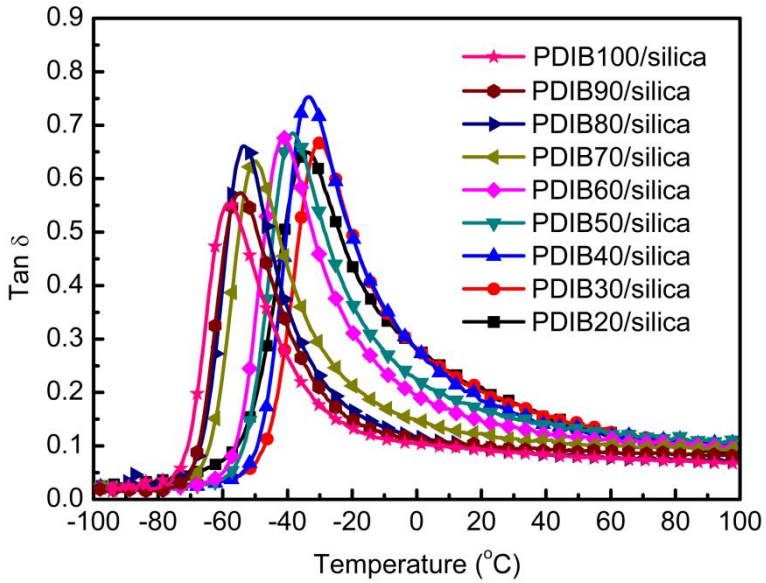

Figure 5-29. Temperature dependence of loss tangent (tan δ) for PDIB/silica nanocomposites.

Table 5-17. Dynamic mechanical thermal analysis of PDIB/silica nanocomposites.

sample	T_g (°C)	**Tan δ**		
		0°C	60°C	Max
PDIB20/silica	-34.6	0.282	0.125	0.652
PDIB30/silica	-30.2	0.284	0.125	0.667
PDIB40/silica	-33.4	0.280	0.119	0.754
PDIB50/silica	-38.3	0.227	0.121	0.686
PDIB60/silica	-41.0	0.196	0.113	0.676
PDIB70/silica	-50.0	0.149	0.102	0.633
PDIB80/silica	-53.2	0.116	0.078	0.661
PDIB90/silica	-54.5	0.113	0.090	0.574
PDIB100/silica	-58.8	0.104	0.077	0.551

The T_g of the PDIB/silica nanocomposites decreased with increasing butadiene content in the PDIB, resulting in a decrease in tan δ at both 60°C and 0°C for the PDIB/silica nanocomposite. The tan δ value of PDIB100/silica nanocomposite was the lowest at 60°C, indicating the lowest rolling resistance compared to the other PDIB/silica nanocomposites. This suggests

that PDIB100/silica nanocomposite would produce best fuel-efficient tire treads compared to the other PDIB/silica nanocomposites if the rolling resistance was the only consideration. However, in the tire tread application, the elastomer needs to combine good wet grip resistance and low rolling resistance. The lowest tan δ value of PDIB100/silica nanocomposite at 0^{o}C indicates the worst wet grip resistance, *i.e.*, the PDIB100 would produce most unsafe tire treads. Based on the mechanical properties, the wet grip resistance, and the rolling resistance, PDIB40 had best balanced properties and this emerged as a potential elastomer to produce high-performance bio-based tire treads.

3.6 Performance comparison between PDIB/silica and SSBR/silica nanocomposites.

SSBR is an ideal material for production of green tires in modern tire industry. In this work, two different types of SSBR, SSBR2503 and SSBR2416, were used to prepare SSBR/silica nanocomposites. The mechanical properties of the SSBR/silica nanocomposites are shown in Fig. 5-30*a*. Their dynamic properties are shown in Fig. 5-30*b* and the relevant data are gathered in Table 5-18. The mechanical and dynamic properties of the PDIB30/silica and PDIB40/silica nanocomposites are also shown in Fig. 5-30. The tensile strength and elongation at break of the PDIB/silica nanocomposites are higher than those of the SSBR/silica nanocomposites, while their moduli are lower than those of the SSBR/silica nanocomposites. Although the PDIB/silica nanocomposites exhibited lower moduli than SSBR/silica nanocomposites, they showed mechanical properties which satisfactorily met the basic requirements of tires. One of the reasons the SSBR was used to produce green tires was that SSBR/silica nanocomposites yielded low tan δ at 60^{o}C and high tan δ at 0^{o}C. From Fig. 5-30*b*, the tan δ value of the SSBR2416/silica nanocomposite was 0.071 at 60^{o}C and 0.311 at 0^{o}C, indicating that it was the most ideal material to produce a green tire. The tan δ value of the PDIB40/silica nanocomposite at 0^{o}C was well above that of the SSBR2503/silica nanocomposite, but 60^{o}C it was much lower. For the SSBR/silica and PDIB/silica nanocomposites, tan δ at 60^{o}C increased when the strain was less than 2%, which arose from polymer-polymer, polymer-filler and filler-filler frictions. For strains exceeding 2%, tan δ slowly increased and then leveled off, as shown in Fig. 5-31. At high strains, the silica networks were broken to keep with a decrease in energy dissipation produced by the filler-polymer viscous stress. Usually the tan δ value at 7% strain is closely related to the tire rolling resistance. The PDIB40/silica nanocomposite showed a tan δ value comparable with that of the SSBR/silica nanocomposites at high strains. Consequently, the PDIB40/silica nanocomposite would be used to manufacture tread materials for green tires.

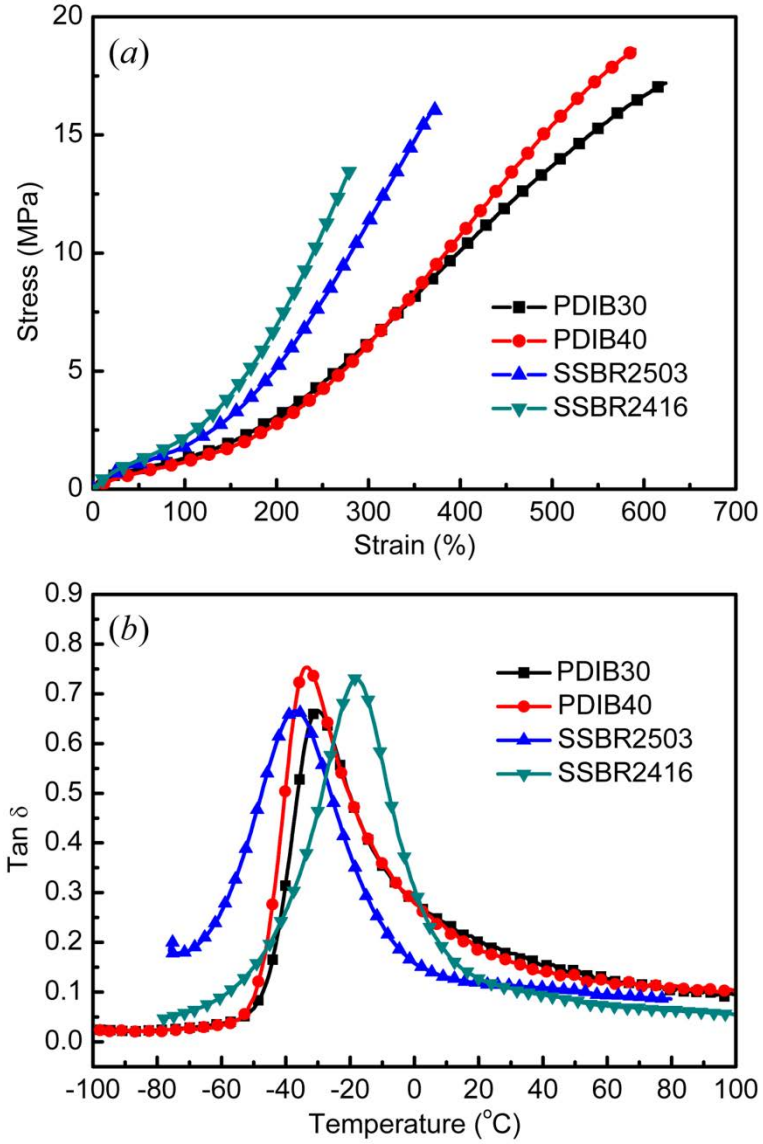

Figure 5-30. (a) Stress-strain curves of the PDIB/silica and SSBR/silica nanocomposites. (b) Temperature dependence of tan δ for PDIB/silica and SSBR/silica nanocomposites.

Table 5-18. Dynamic mechanical thermal analysis of the PDIB/silica and SSBR/silica nanocomposites.

sample	T_g (°C)	**Tan δ**		
		0°C	60°C	Max
PDIB30/silica	-30.2	0.284	0.125	0.667
PDIB40/silica	-33.4	0.280	0.119	0.754
SSBR2503/silica	-37.1	0.158	0.094	0.666
SSBR2416/silica	-18.5	0.311	0.071	0.730

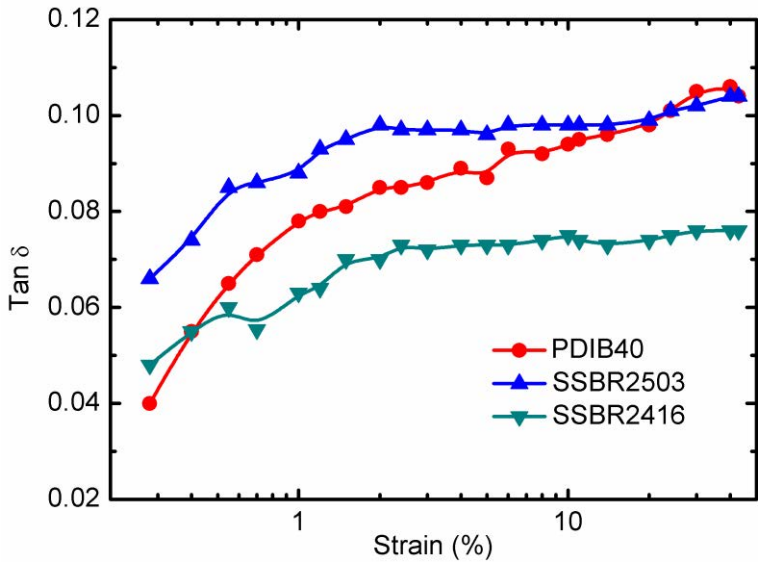

Figure 5-31. Strain dependence of tan δ for PDIB/silica and SSBR/silica nanocomposites.

It is desirable that a tire can transmit the maximum percentage of engine torque to the road. However, certain energy losses of elastomeric products undergoing a cyclic deformation are inevitable. The energy dissipated in the tire is ultimately converted into heat, [240] which leads to an increase in tire operating temperature. The relation between the energy loss and dynamic mechanical properties of elastomer materials can be obtained using a sinusoidal deformation. The dynamic stress and strain are given by $\sigma(t) = \sigma_a \sin \omega t$ and $\varepsilon(t) = \varepsilon_a \sin(\omega t - \delta)$, respectively. [240, 241] Energy loss per cycle per unit volume (H) under a controlled energy cycle is given below:

$$H = \int_0^{2\pi/\omega} \sigma(t) \frac{d\varepsilon(t)}{dt} dt = \pi \sigma_a \varepsilon_a \sin\delta \approx \pi \sigma_a \varepsilon_a \tan\delta$$

where ζ_a is the stress amplitude, ε_a is the strain amplitude, ω is the angular frequency, t is time, δ is the phase difference between strain and stress, and tan δ is the loss tangent. H is proportional to tan δ for equal energy consumption. Rubber rolling test results showed that the energy loss and temperature increase of the PDIB40/silica nanocomoposite were almost the same as those of the SSBR/silica nanotomposites (Fig. 5-32). Akron abrasion of the PDIB/silica nanocomposites ranged from 0.07 to 0.14 cm^3, which was comparable with that of the SSBR/silica nanocomposites. Those results suggest that bio-based PDIB40 reinforced with silica could be effectively used in tire industry for green tire treads.

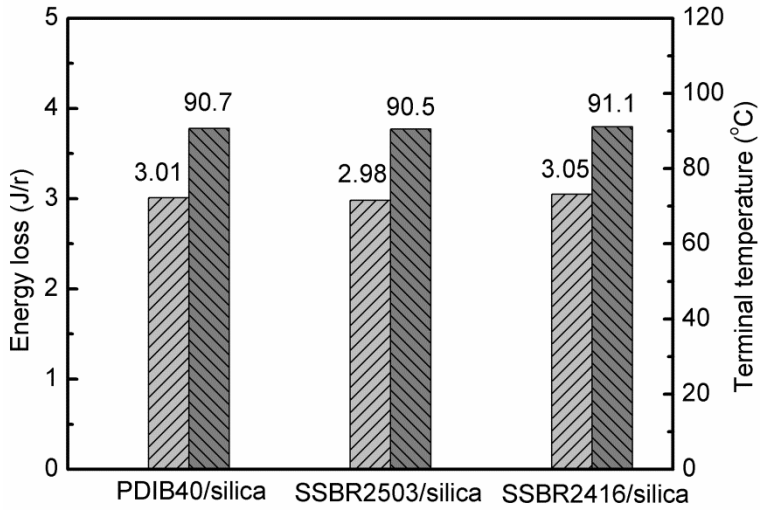

Figure 5-32. Energy loss test results for PDIB/silica and SSBR/silica nanocomposites.

3.7 Manufacturing of bio-based green tires

For a tire tread material, good rolling resistance which favors low energy loss and good wet grip resistance which favors high energy loss are contradictory. In order to balance these two opposing viscoelastic properties, mixtures of various types of synthetic and natural rubber are normally utilized in tire treads. For example, the mixture of SSBR and BR is commonly used as a rubbery material for green tire treads. BR is of good flexibility and resilience, which allows for low rolling resistance and high wear resistance.

In this study, a mixture of PDIB (70 wt.%) and BR (30 wt.%) was used as a rubbery material for bio-based green tire tread. The PDIB40/silica, BR/silica, and PDIB40-BR/silica nanocomposites were prepared according to the formulations in Table 5-13. The mechanical and dynamic properties of these nanocomposites are shown in Fig. 5-33 and Table 5-19. The tensile strength, elongation at break, and modulus (stress at 100% strain) for the PDIB40-BR/silica nanocomposite are 15.6 MPa, 368%, and 2.5 MPa, respectively. The mechanical properties of the PDIB40-BR/silica nanocomposite would meet the requirements of a tire tread. The tan δ value at 60^{o}C of the PDIB40-BR/silica nanocomposite was lower than that of PDIB40/silica and BR/silica nanocomposites, indicating a lower rolling resistance for a tire. The decrease in tan δ at 0^{o}C for the PDIB40-BR/silica nanocomposite was predictable. This means that the mixture of PDIB40 and BR could provide a lower rolling resistance upon sacrificing some wet grip resistance.

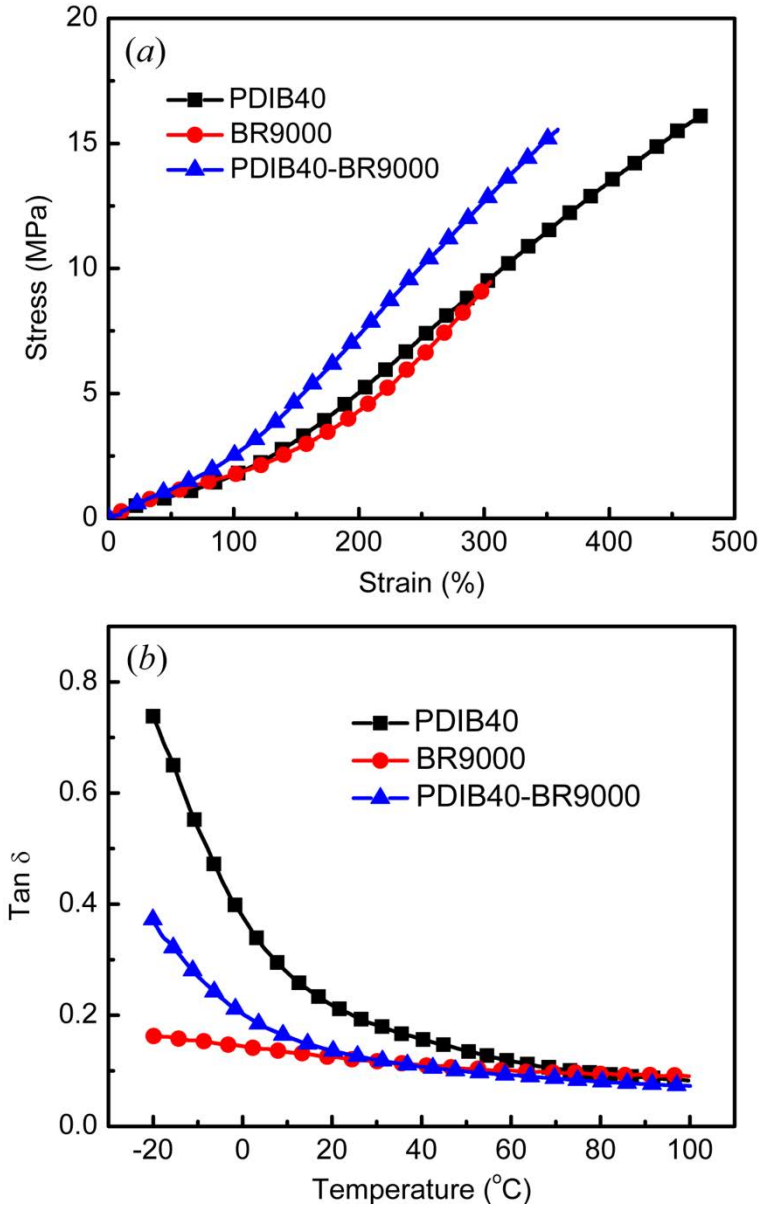

Figure 5-33. (a) Stress-strain curves and (b) tanδ-temperature curves for PDIB/silica, BR/silica, and PDIB-BR/silica nanocomposites.

Table 5-19. Mechanical properties and tan δ values of the PDIB40/silica, BR/silica, and PDIB40-BR/silica nanocomposites.

Property	Sample		
	PDIB40/silica	BR/silica	PDIB40-BR/silica
Stress at 100% strain (MPa)	1.7	1.8	2.5
Stress at 300% strain (MPa)	9.4	9.2	12.7
Tensile strength (MPa)	16.1	9.5	15.6
Elongation at break (%)	485	318	368

Permanent set (%)	20	20	20
Tan δ value at 0°C	0.38	0.14	0.21
Tan δ value at 60°C	0.12	0.10	0.09

A tire is a ring-shaped component that surrounds a wheel‘s rim to transfer a vehicle‘s load from the axle through the wheel to the ground. The radial tire technology developed by Michelin is now a standard design for almost all automotive tires. Radial tire construction uses body ply cords extending from the beads and across the tread so that the cords are laid at approximately right angles to the centerline of the tread, and parallel to each other, as well as at approximately right angle to the stabilizer belts directly beneath the tread. The advantages of this construction include a longer tread life, a better steering control, fewer blowouts, improved fuel economy, and a low rolling resistance. Materials for modern pneumatic tires are synthetic rubber, natural rubber, fabric and wire, along with filler and other chemical compounds. A tire carcass is composed of several parts: tread, bead, sidewall, shoulder, and ply. The tread is part of the tire that is in contact with the road. It is a thick rubber composite that provides an appropriate level of traction and does not wear away too quickly. The tread rubber is composed of three different rubbery materials, i.*e.* tread cap, tread base, and tread wing. In a tire factory, the three rubbery materials are simultaneously extruded in hundred kilograms scale. In this study, we scaled up the production of the PDIB40 elastomer in a reaction kettle and prepared the tire tread using the PDIB40-BR/silica nanocomposite. Therefore, the thread cap, tread base, and tread wing were prepared on a two-roll mill according to the tread design (Fig. 5-34). The tire tread was composed of one rubbery sheet of 212 mm wide × 4 mm high ×1900 mm long, one rubbery sheet of 200 mm wide × 2 mm high × 1900 mm long, and two rubbery sheets of 40 mm wide × 1.5 mm high × 1900 mm long. The chosen tire code was P225/40R18 92W, where P indicated the passenger car, 225 was the nominal section width of the tire in millimeters, 40 was the aspect ratio of the sidewall height as a percentage of the nominal section width of the tire, R indicated a radial tire, 18 was the diameter in inches of the wheel that the tire was designed to fit, 92 was the load index (the maximum load of 630 kg per tire), and W was the speed index (the maximum permitted speed was 270 km/h). The tire based on the PDIB40-BR/silica nanocomposite was manufactured and tested using a MTS tire rolling resistance measurement system (Fig. 5-35) in LingLong Tire Co. Ltd. The rolling resistance coefficient was 7.7 kg/ton (Fig. 5-36) and rated as a class

–B" according to the EU Tire Labelling Regulation 1222/2009, which is a high level since class –A" is few in the tire market.

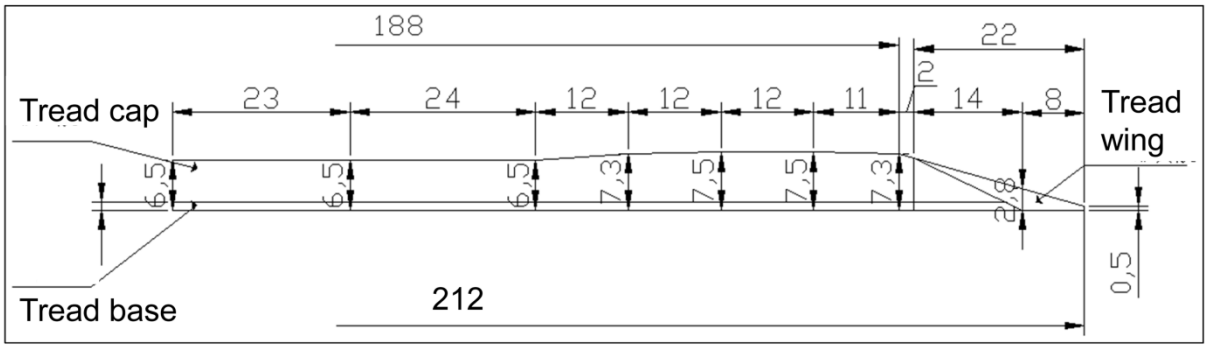

Figure 5-34. Size of the tire tread (tire code: P225/40R18 92W, unit: mm).

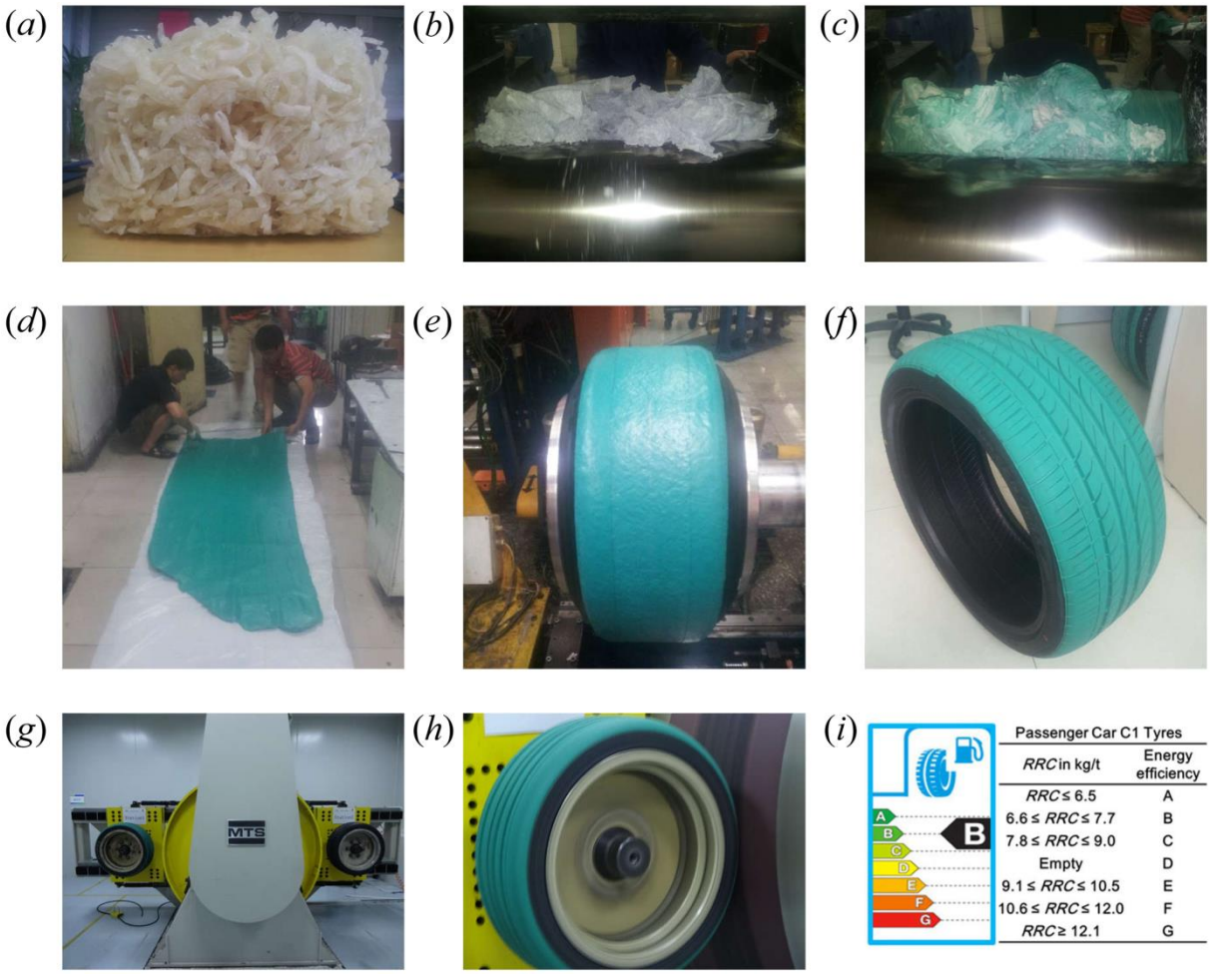

Figure 5-35. Manufacturing (*a-f*) and rolling resistance test (*g-i*) of bio-based green tires. (*a*) Synthetic PDIB40 elastomer; (*b*) mixing of PDIB40 with silica on a two-roll mill; (*c*) coloring with phthalocyanine and titanium oxide; (*d*) clipping of rubbery sheets; (*e*) tire assembling; (*f*)

bio-based tire; (*g* and *h*) tire rolling resistance test; (*i*) EU Tire Labeling Regulation 1222/2009, rolling resistance grading of the bio-based green tire.

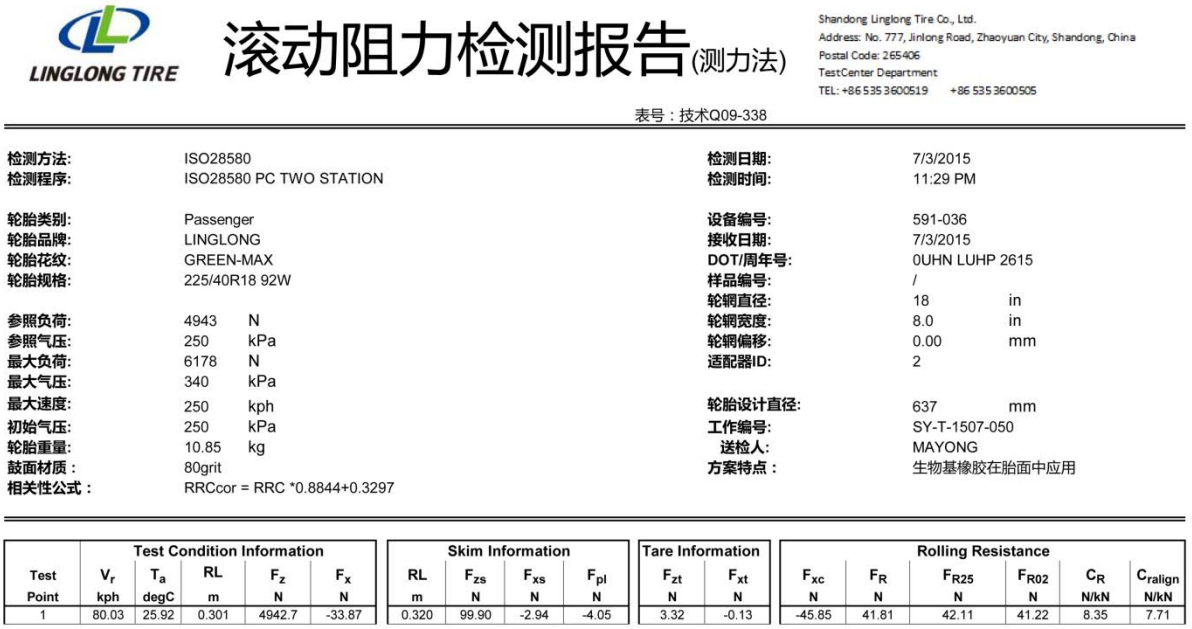

LINGLONG TIRE

滚动阻力检测报告(测力法)

Shandong Linglong Tire Co., Ltd.
Address: No. 777, Jinlong Road, Zhaoyuan City, Shandong, China
Postal Code: 265406
TestCenter Department
TEL: +86 535 3600519 +86 535 3600505

表号：技术Q09-338

检测方法:	ISO28580	检测日期:	7/3/2015
检测程序:	ISO28580 PC TWO STATION	检测时间:	11:29 PM
轮胎类别:	Passenger	设备编号:	591-036
轮胎品牌:	LINGLONG	接收日期:	7/3/2015
轮胎花纹:	GREEN-MAX	DOT/周年号:	0UHN LUHP 2615
轮胎规格:	225/40R18 92W	样品编号:	/
		轮辋直径:	18 in
参照负荷:	4943 N	轮辋宽度:	8.0 in
参照气压:	250 kPa	轮辋偏移:	0.00 mm
最大负荷:	6178 N	适配器ID:	2
最大气压:	340 kPa		
最大速度:	250 kph	轮胎设计直径:	637 mm
初始气压:	250 kPa	工作编号:	SY-T-1507-050
轮胎重量:	10.85 kg	送检人:	MAYONG
鼓面材质：	80grit	方案特点：	生物基橡胶在胎面中应用
相关性公式：	RRCcor = RRC *0.8844+0.3297		

	Test Condition Information					Skim Information				Tare Information		Rolling Resistance					
Test Point	V_r kph	T_a degC	RL m	F_z N	F_x N	RL m	F_{zs} N	F_{xs} N	F_{pl} N	F_{zt} N	F_{xt} N	F_{xc} N	F_R N	F_{R25} N	F_{R02} N	C_R N/kN	C_{ralign} N/kN
1	80.03	25.92	0.301	4942.7	-33.87	0.320	99.90	-2.94	-4.05	3.32	-0.13	-45.85	41.81	42.11	41.22	8.35	7.71

Figure 5-36. Report on the rolling resistance test for the bio-based green tire. The rolling resistance coefficient is 7.7 kg/ton.

4. Conclusions

Non-petroleum silica was used to reinforce the PDIB elastomers. Homogeneous dispersion of silica in the PDIB matrix was confirmed by SEM and TEM. The mechanical properties of the PDIB/silica nanocomposites were comparable with those of conventional rubber composites. DMTA results showed that the tan δ values of the PDIB/silica nanocomposites could be tuned according to the composition of the PDIB. Based on balanced mechanical properties, the wet grip resistance, and the rolling resistance, the PDIB40 emerged as a potential elastomer to produce a high-performance bio-based tire tread. A tire based on the PDIB40-BR/silica nanocomposite was manufactured and tested using a MTS tire rolling resistance measurement system. The rolling resistance coefficient was 7.7 kg/ton and rated as a class ~~B~~" according to the EU Tire Labelling Regulation 1222/2009. Combining bio-based chemicals and *in-situ* modification technology to develop green tires is an important step of the strategy for sustainable development.

Acknowledgement

The authors thank the National 973 Basic Research Program of China (2015 CB654700), National Natural Science Foundation of China (50933001, 51503010), and the China-France Cooperation Program of PHC CAI YUANPEI (CHINA SCHOLARSHIP COUNCIL, No. 201504490120) for their financial support. The authors also thank Jilin Petrochemical Research Institute and Linglong Tire Co. Ltd. for their great help.

Chapter 6 Sacrificial bonding mechanisms for strong polymeric materials---A review

Natural materials usually possess extraordinary mechanical properties. Preparation of high-performance synthetic materials via mimicking natural structures has been highly pursued. Recently, it has been revealed that the energy dissipating mechanism via sacrificial bonds is among the important factors which account for strong and tough attributes of natural materials. Essential progresses in synthesis of polymeric materials consisting sacrificial bonds have been achieved. This field is very important for breaking the bottlenecks in mechanical properties and extending the applications of polymeric materials.

This review describes the design of sacrificial bonds into polymeric materials and the related mechanisms. It emphasizes on mechanisms, design methods, and applications of sacrificial bonds in bulk polymers. We envision that this review may advance the real application of sacrificial bonds strategies in polymeric materials.

Progresses in bio-inspired sacrificial bonds in artificial polymeric materials

Abstract: Mimicking natural structures has been highly pursued in the fabrication of synthetic polymeric materials due to its potential in breaking the bottlenecks in mechanical properties and extending the applications of polymeric materials. Recently, it has been revealed that the energy dissipating mechanisms via sacrificial bonds are among the important factors which account for strong and tough attributes of natural materials. Great progresses in synthesis of polymeric materials consisting of sacrificial bonds have been achieved. The present review aims at: (1) summarizing progresses in mechanics and chemistry of sacrificial bonds bearing polymers, (2) describing mechanisms of sacrificial bonds in strengthening/toughening polymers based on studies by single-molecule force spectroscopy, chromophore incorporation and constitutive laws, (3) presenting synthesis methods for sacrificial bonding including dual-crosslink, dual/multiple-network, and sacrificial interfaces, (4) discussing on important advances in engineering sacrificial bonding into hydrogels, biomimetic structures and elastomers, and (5) suggesting future works on molecular simulation, viscoelasticity, construction of sacrificial interfaces and sacrificial bonds with high dissociative temperature. It is hoped that this review provides guidance for further development of sacrificial bonding strategies in polymeric materials.

Keyword: Sacrificial bonds; Energy dissipation mechanism; Polymeric materials; Biological materials; Mechanical properties.

Abbreviation for Materials

AMPS	2-acrylamido-2-methylpropanesulphonic acid
BPH	Byssus protein hydrolysate
CMC	Carboxymethylcellulose
CNC	Cellulose nanocrystal
CCNF	Carboxylated cellulose nanofibril
CB[8]	Cucurbit[8]uril
dGMP	2'-deoxyguanosine 5'-monophosphates
DMAEA-Q	Methyl chloride quarternized N,N-dimethylamino ethylacrylate
DMAPAA-Q	(3-Acrylamidopropyl)trimethylammonium chloride
EG-MA	Poly(ethylene glycol) methyl ether methacrylate
ENR-50	Epoxidized natural rubber with an epoxidization degree of 50%
EA	Ethyl acrylate
GN/PU	Graphene nanosheet/polyurethane
HPAMAM	Hyperbranched poly(amido amine)
IPN	Interpenetration polymer network
IR	*cis*-1,4-polyisoprene
MTM	Montmorillonite
MR gels	Microgel-reinforced hydrogels
MPTC	3-(methacryloylamino)propyl-trimethylammonium chloride
MA	Methyl acrylate
NHT	Synthetic sodium fluorohectorite
NaSS	Sodium *p*-styrenesulphonate
NaAMPS	Sodium 2-acrylamido-2-methylpropanesulfonate
PLA	Poly(lactic acid)
PDDA	Poly(diallyldimethylammonium chloride)
PAMPS	Poly(2-acrylamido, 2-methyl, 1-propanesulfonic acid)
PAAm	Polyacrylamide
PAAc	Poly(acrylic acid)
PNaAMPS	Poly(sodium 2-acrylamido-2-methylpropanesulfonate)
P(AAm-*co*-AAc)	Poly(acrylamide-*co*-acrylic acid)
P(DMAA-*co*-MAAc)	Poly(N,N-dimethylacrylamide-*co*-methacrylic acid)
P(DMAA-*co*-AAc)	Poly(N,N-dimethylacrylamide-*co*-acrylic acid)
PA	Polyampholyte
PIC	Polyion complexes
PEG	Poly(ethylene glycol)
PDGI	Poly(dodecylglyceryl itaconate)
PDMS	Poly(dimethylsiloxane)
PDCA	2,6-pyridinedicarboxamide
SSBR	Solution-polymerized styrene butadiene
UPy	2-ureido-4[1*H*]-pyrimidinone
UPy-MA	2-ureido-4[1*H*]-pyrimidone methacrylate
VPR	Butadiene-styrene-vinylpyridine rubber
ZDA	Zinc acrylate

1. Introduction

Biological materials, such as nacre in abalone shells, bone in mammals, and byssus in mollusks, are known for their extraordinary stiffness, strength and toughness with capability of self-repair.[242-246] The excellent performance of biological materials originates from a growing hierarchical structure with ordered arrangement of hard inorganic and soft organic building blocks.[247,248] For example, nacre consists of a ―brick-and-mortar" hierarchical structure, in which 95 wt.% hard aragonite tablets (brick) are glued together with 5 wt.% soft biopolymers (mortar), leading to synergistic mechanical performance.[249] The Young's modulus can reach up to 40-70 GPa, the tensile strength is as high as 80-170 MPa, and the toughness is 3,000 times that of monolithic aragonite.[250,251] Although the organic components in nacre are only 5 wt.%, they are thought to hold the key to the extraordinary toughness in nacre because the hard aragonite tablets alone cannot dissipate much energy.[3] Many studies used atomic force microscopy (AFM) to reveal a reversible toughening mechanism which often involves sacrificial bonds and hidden lengths within organic components in biological materials.[252-260] Sacrificial bonds are defined as bonds that rupture before strong bonds (often covalent bonds in the backbone) fail under deformation.[255] The hidden lengths are defined as the differences in length between unfolded and folded domains along polymer chains, or extra lengths released when sacrificial bonds within inter-chain or intra-chain break.[259] When a load is applied to biological materials, the rupture of sacrificial bonds and the release of hidden lengths dissipate a huge amount of energy; when the load is released, the biological materials can be self-repair due to the reversibility of the sacrificial bonds.

Inspired by the concept of sacrificial bonds and the hierarchical structures of biological materials, scientists have fabricated biomimetic materials with various kinds of inorganic and organic components. Recently, the concept of sacrificial bonds is also introduced to other artificial materials (*e.g.* hydrogels, elastomers) to obtain excellent performance, especially toughness. In the past several years, sacrificial bonds have found increasing applications in artificial polymeric materials. More and more studies show that engineering sacrificial bonds in an artificial polymeric material opens a new path to obtain a high-performance material. This review focuses on the designs, mechanisms, and applications of bio-inspired sacrificial bonds in artificial polymeric materials. The nature and mechanisms of the sacrificial bonds in biological materials are also summarized in order to help material scientists to understand

sacrificial bonding mechanisms and design bio-inspired sacrificial bonds in artificial polymeric materials.

2. Nature and Mechanisms of Sacrificial Bonds

2.1 Sacrificial Bonds in Biological Materials

It has been accepted that the high toughness of biological materials originates from the dynamics of the organic components: the rupture of sacrificial bonds and the release of hidden lengths dissipate a huge amount of energy. However this sacrificial bonding mechanism was unclear two decades ago. In 1997, Rief *et al.* reported on the mechanical properties of single titin chains by means of single-molecule force spectroscopy by AFM.[252] The characteristic saw-tooth pattern observed from force-extension curves reflected the successive unraveling of individual domains of a single titin molecule. That work did not discuss about the mechanism of the unraveling. Nevertheless, it showed that individual titin domains unravel once at a time, suggesting that AFM afforded a possibility of delineating sacrificial bonding mechanisms in biological materials.[253-257] To figure out the toughening mechanism of biological materials, Smith *et al.* used AFM to investigate organic molecules exposed on the surface of freshly cleaved nacre.[253] The force-extension curves of the nacre also exhibited a saw-tooth pattern and hysteresis was observed after a complete pulling cycle. This behavior was believed to reflect a sacrificial bonding mechanism which involved in a successive opening of intra-chain loops or folded domains within a single molecule, or a successive release of sacrificial inter-chain bonds holding a cross-linked multi-chain matrix together. To understand the sacrificial bonding mechanism, the authors discussed three different cases in which two surfaces were glued together with three different kinds of molecules (Fig. 6-1*a*).[253]

（1） When pulling two surfaces glued together with a short, inelastic molecule, the force increased rapidly with only a small extension of the molecule, leading to small energy dissipation.

（2） When the two surfaces were glued together with a long, elastic molecule, the force increased slowly till the long molecule was stretched to the point at which the contour length was reached, leading to large energy dissipation. Unfortunately, it is hard to produce such an ideal elastic material.

（3） In the case of two surfaces which were glued together with a long molecule folded or looped with sacrificial bonds of intermediate-strength, the force-extension curve exhibited a saw-tooth pattern. The force increased quickly with extension. When it reached a critical value above which the backbone of the molecule would break, the sacrificial bonds ruptured and the folded or looped molecules released, preventing the strong bonds of the backbone from rupturing. As the force further increased, all sacrificial bonds ruptured, and finally the strong bonds would rupture. In other words, the presence of sacrificial bonds makes the material both ―strong" and ―tough" as it allows for a big force over a large extension.

Sacrificial bonds in nacre are analogous to those in protein titin.[252,254-256] However, the nature of those sacrificial bonds remains unclear. Thompson *et al.* showed increased energy dissipation in successive pulling of the molecule of a collagen of bone if divalent Ca^{2+} ions were present in a buffer.[257] They contributed this phenomenon to the formation of sacrificial bonds in collagen molecules between negatively charged groups and the Ca^{2+} ions. It was found that Ca^{2+}-mediated sacrificial bonds in collagen of bone played a vital role in increasing stiffness and energy dissipation.[257-260] There are three types of hypothetical sacrificial bonds in bone tissue as shown in Fig. 6-1*b*: (1) within a molecule; (2) between two molecules; and (3) between a molecule and the surface of a mineral plate.[258] As discussed above, a sacrificial bonding system can dissipate a large amount of energy against an entropic force to toughen a biological material upon stretching out the hidden lengths that are exposed when sacrificial bonds rupture. Analogous sacrificial bonding systems were found in other biological materials, such as tendon,[261] silk,[262,263] gastroliths,[264] and byssus.[265-267] For example, hydrogen bonds and metal-ligand coordination bonds were found to be sacrificial bonds in spider silk proteins [263] and mussel byssal threads [268,269], respectively.

In conclusion, when a biological material is stretched or loaded, a large amount of energy is dissipated in the biopolymer through the rupture of sacrificial bonds and the release of hidden lengths, thereby ensuring high toughness of biological material. Moreover, these sacrificial bonds, such as ionic bonds, hydrogen bonds, and metal-ligand coordination bonds, are generally weaker than covalent bonds, and reversible. They can rupture prior to covalent bonds and self-repair to maintain the integrity of the biological materials.

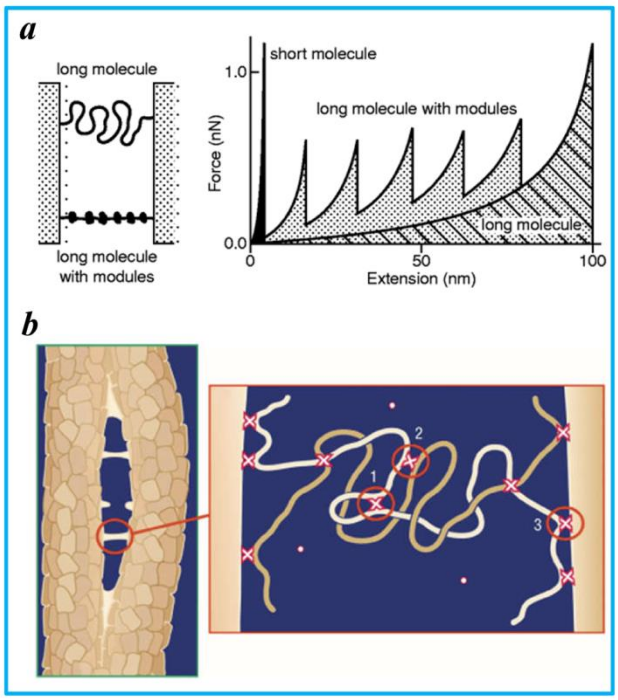

Figure 6-1. (*a*) Diagrams of a long polymer behaving as entropic springs and a long polymer with many modules held together with intermediate-strength sacrificial bonds (left). Force-extension curves for three different kinds of polymers (right). (Adapted with permission from ref. 253. Copyright 1999 Nature Publishing Group.) (*b*) Glue filaments could resist the separation of mineralized fibrils in bone (left). Suspected, calcium-mediated sacrificial bonds in bone could form between (1) two binding sites on one polymer, (2) two polymers, or (3) a polymer and a mineral plate (right). (Adapted with permission from ref. 258. Copyright 2005 Nature Publishing Group.)

To further understand the sacrificial bonding mechanism, several structural models were built up. Peridynamic models of nanofiber networks showed promise in numerically modeling and designing nanostructured materials with excellent performance that can replicate the high toughness of some biological materials.[270] Characteristic saw-tooth patterns of the peridynamic models were similar to the saw-tooth pattern in ultra-tough abalone nacre, indicating that the van der Waals forces acting between the fibers served as sacrificial bonds in the modeled nanofiber networks. A simple hierarchical chain model for spider capture silk was proposed by Zhou *et al.* to understand and reproduce the saw-tooth pattern in the force-extension curve of spider capture silk.[271] Although those works introduced the concept of sacrificial bonds, they did not provide any detailed sacrificial bonding mechanisms.[270-272] Fantner *et al.* discussed some of the possible implementations of sacrificial bonding

mechanisms and showed single-molecule force spectroscopy curves.[273] Close inspection of those curves allowed distinguishing fairly well pulling a single molecule with condensed domains and pulling several molecules in parallel (or one molecule with parallel branches) (Fig. 6-2*a*). They concluded that the increased stiffness and toughness of materials resulting from the sacrificial bonding mechanism did not depend only on molecules with condensed domains but rather on the presence of molecular loops formed by sacrificial bonds that were not stretched by the applied force. Nabavi *et al.* used Monte Carlo simulations to investigate the effects of the density, distribution, and topology of reversible sacrificial bonds on the mechanical performance of single-polymer chain model.[274-276] They observed characteristic saw-tooth patterns corresponding to the rupture of sacrificial bonds. Both the work to fracture and the energy dissipation increased not only with increasing density of sacrificial bonds, but also with change in their topology from the independent to the pseudo-knotted configuration (Fig. 6-2*b*). Moreover, the distribution of sacrificial bonds had a significant impact on the strength and apparent stiffness. The effective strength of sacrificial bonds was reduced by thermal fluctuations of the chain backbone.[274] The model of Nabavi *et al.* captured the essence of sacrificial bonds present in real systems. More recently, motivated by sacrificial ionic bonds in biological materials, Hartmann and Fratzl presented a model to describe the effect of the sacrificial bond distribution during shear deformation of biological materials.[277] In that model, negative charges were distributed on two parallel plates in an ordered or a random configuration. Divalent positively charged counter-ions which could move freely between the two plates ensured the charge neutrality of the whole system. In the case of the ordered configuration, all ionic bonds were loaded in exactly the same way and ruptured collectively when the ultimate strength of the system was reached, resulting in a nonlinear elastic and brittle behavior. In the case of the random configuration, however, the mechanical behavior of the system could be described by a stick-slip mechanism: the system deformed elastically until a critical load was reached, and then the plates started slipping. After some slipping, the system eventually found a new, more stable configuration that could withstand further elongation. Thus, the energy dissipation in the case of a random configuration was much effective than that in the case of an ordered one, indicating that sacrificial ionic bonds needed to be randomly distributed to toughen a material.[277]

In addition to the structural models, 3D printing technologies opens up a new path to investigate sacrificial bonding systems. Direct-write (DW) assembly is a 3D fabrication method that moves a computer-controlled ink deposition nozzle to create materials with

controlled architecture and composition.[278] A solvent-cast DW fabrication method was developed to fabricate 3D models of sacrificial bonding systems at room temperature.[279,280] Inspired by the molecular structure of spider silk proteins,[262] Guo *et al.* used the solvent-cast DW technique to fabricate high toughness micro-structured fibers with sacrificial bonds by extruding a polymer solution to a substrate moving perpendicularly at a speed that is smaller than that with which the fibers were extruded.[279] Sacrificial bonds in those micro-structured fibers played a role analogous to that of the sacrificial hydrogen bonds present in the molecular structure of the spider silk proteins.[262] High toughness of the micro-structure fiber based on the area under the force-extension curve was obtained due to the rupture of sacrificial bonds and the release of hidden lengths. Passieux *et al*. developed two DW techniques (instability-assisted fused deposition modeling and instability-assisted solvent cast printing) combined with a fluid rope coiling instability to fabricate micro-structured fibers featuring sacrificial bonds at different scales (Fig. 6-3*a*).[280] In the instability-assisted fused deposition modeling approach, a filament of PLA was fused and extruded before being cooled down and solidified in ambient air. In the instability-assisted solvent cast printing approach, a solution of PLA in dichloromethane was extruded in ambient air and solidified as the solvent evaporated. Both approaches allowed for the creation of sacrificial bonds whenever the fiber coiled on itself. The force-extension relationship exhibited a characteristic saw-tooth pattern (Fig. 6-3*c*), in which the dramatic drop of the force after the rupture of sacrificial bonds (α and β in Fig. 6-3*b*) corresponded to the release of the coiled loop hidden lengths.

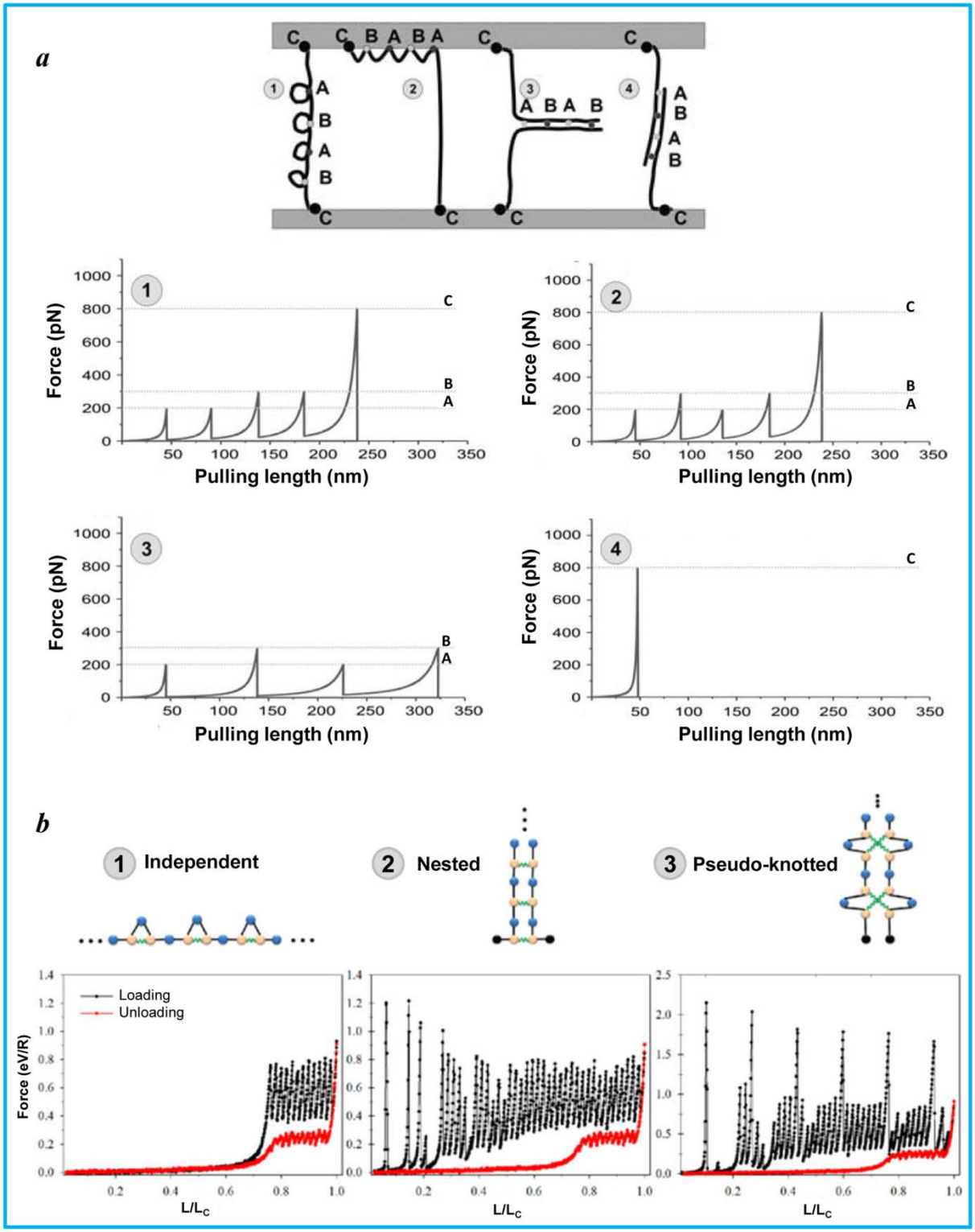

Figure 6-2. (*a*) Various sacrificial bonds on single strand connections. (①) When a force is applied on the molecule, the sacrificial bonds will rupture successively following the order of increasing bond strength. (②) When a force applied on the molecule, the sacrificial bonds rupture in the sequence that they are in on the molecule. (③) When a force applied on the molecule, the bonds rupture in the sequence that they are in on the molecule. (④) The

sacrificial bonds will all rupture once a force is reached the combined binding force. In this case, no hidden length is set free. (Adapted with permission from ref. 273. Copyright 2006 The Biophysical Society.) (*b*) Starting configurations (top) and force-extension curves (bottom) for three topologies of sacrificial bonds: (①) independent, (②) nested, and (③) pseudo-knotted. Black spheres denote fixed end beads; dark and light beads denote non-sticky and sticky sites, respectively. Straight connections correspond to the covalent backbone of the structure; zigzag connections denote closed sacrificial bonds. In the force-extension curves, the black line shows stretching of the different starting configurations until the contour length, and the red line shows subsequent unloading. (Adapted with permission from ref. 276. Copyright 2015 American Physical Society)

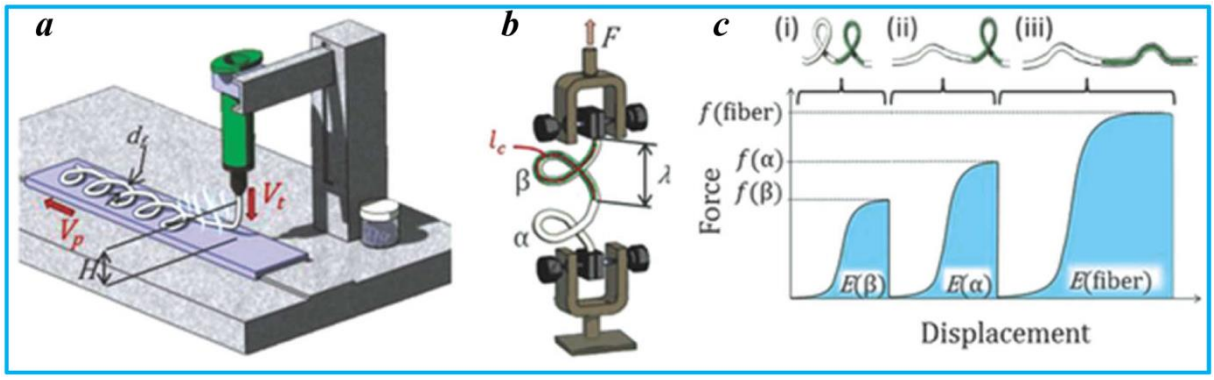

Figure 6-3. Schematic general view of the direct writing of micro-structured fibers with sacrificial bonds. (*a*) Schematic representation of the deposition process whose variables are the deposition height H, fiber diameter d_f, extrusion speed V_t, and platform speed V_p. (*b*) The produced fibers are characterized by a contour length l_c and a periodicity length λ. The behavior of fibers with sacrificial bonds (α, β) is characterized via tensile tests. (*c*) Sacrificial bonds breakage and hidden length unfolding events are illustrated with a schematic and result in a characteristic saw-tooth tensile curve. (Adapted with permission from ref. 280. Copyright 2015 WILEY-VCH Verlag GmbH & Co. KGaA, Weinheim.)

2.2 Constitutive Theories of Sacrificial Bonding Systems

The functioning of a sacrificial bonding system depends on the dynamic state of its sacrificial bonds. With the formation of hidden lengths (folded or looped chains), sacrificial bonds restrict part of the lengths from contributing to the end-to-end distance. This restriction corresponds to a reduction in the polymer chain entropy and an increase in the initial stiffness of the polymer chain. After the sacrificial bonds are ruptured, the hidden lengths are released

and a huge amount of energy is dissipated in reducing the chain entropy as the hidden lengths are straightened out. Computer simulation as well as modeling possesses a strong potential to provide insights into the behavior of sacrificial bonds and guide the design of bio-inspired sacrificial bonds. Recently, several constitutive theories have been developed to describe mechanical behavior of sacrificial bonding systems. For example, the worm like chain (WLC) model has been used to describe the mechanical behavior of a bone collagen polymer containing a sacrificial bonding system.[281-283] The latter is incorporated in the WLC model by introducing a dynamical variable: the available length.[281] In the presence of sacrificial bonds, the available lengths (L_a) and the contour length (L_c) are related by:

$$L_a = L_c - \sum_{i=1}^{n} l_i \tag{6-1}$$

Where l_i is the length of loop i shielded by the sacrificial bond i and n is the number of sacrificial bonds that are not broken yet.[281] Thus, the force-extension relationship of the polymer with sacrificial bonds and hidden lengths can be given by:

$$f = \frac{k_B T}{b}\left[\frac{1}{4}\left(1-\frac{x}{L_a}\right)^{-2} - \frac{1}{4} + \frac{x}{L_a}\right] \tag{6-2}$$

Where f is the force, x is the end-to-end distance, b is the persistence length, k_B is Boltzmann constant, and T is the temperature.[281] If a sacrificial bond ruptures, the available length then increases by the length of the loop segment that is released after the sacrificial bond rupture. Figure 6-4*a* shows an example of the force-extension relationship generated by this constitutive law for a polymer with a single sacrificial bond. However, this WLC model does not account for the rate dependence and the delay time dependence, which also influence the mechanical behavior of biological polymers with sacrificial bonds.

Lieou *et al.* developed a simple kinetic model to describe the rate dependence and delay time dependence of a sacrificial bonding system,[282] based on the WLC model and Bell's theory.[284,285] They found that the delay time dependence comes in only through the fraction of polymer chains attached at both ends at the beginning. The average force on each polymer chain $f(x, v)$ is independent of the delay time or the number of polymer chains:

$$f(x,v)=\begin{cases} f_p(v)\left(\dfrac{x}{x_p(v)}\right)^{s_1} & for \quad x \le x_p(v) \\ f_p(v)\left(\dfrac{x_c(v)-x}{x_c(v)-x_p(v)}\right)^{s_2} & for \quad x_p(v) < x < x_c(v) \\ 0 & for \quad x \ge x_c(v) \end{cases} \tag{6-3}$$

where $f_p(v)$, $x_p(v)$, and $x_c(v)$ are the rate-dependent peak force, end-to-end distance at peak force, and maximum pulling distance, respectively (labeled in Fig. 6-4*b*).[282] The constant s_1 and s_2 are approximatively 1.35 and 0.65, respectively.[282] The quantity $x_p(v)$ marks the transition from a strengthening to a weakening behavior, associated with the gradual detachment of polymer chains. Figure 6-4*b* shows how this constitutive law fits sample force-extension profiles. The kinetic model developed by Lieou *et al.* can be used to describe crack propagation in bone on the scale of mineralized collagen fibrils.[283] However, it does not explicitly account for the effect of cross-links and entanglements on the dynamic behavior of biopolymers in biological materials. This can be a subject of future investigation.

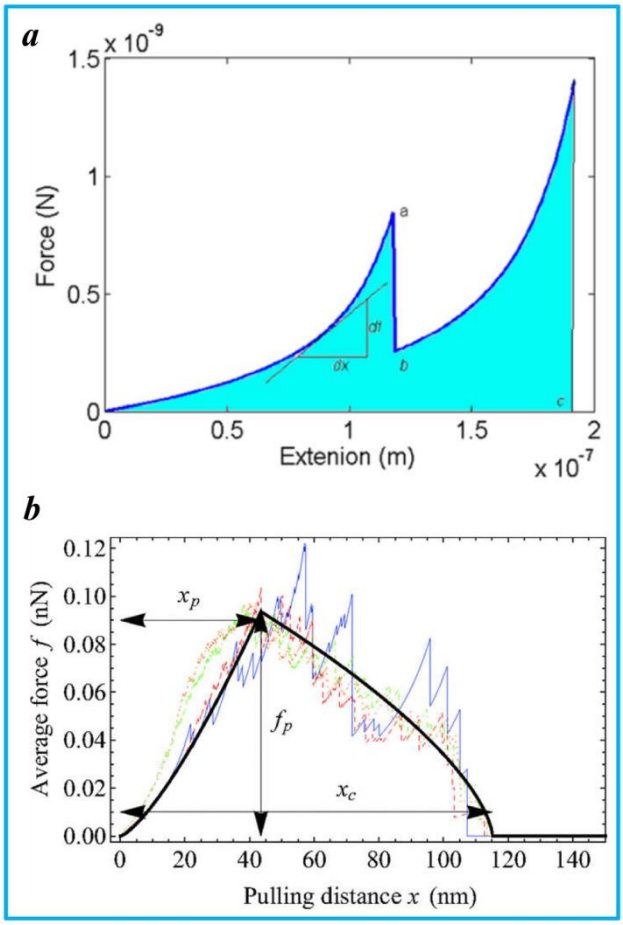

Figure 6-4. (*a*) The force-extension behavior generated from Equation (2) for an idealized polymer chain with a single sacrificial bond. The first force peak (point *a*) represents the strength of the sacrificial bond; point *b* represents the force supported by the chain just after the sacrificial bond has ruptured; and point *c* represents the maximum extension. (Adapted with permission from ref. 281. Copyright 2013 Elbanna, Carlson.) (*b*) The color lines represent force-extension behaviors of normalized modeled polymers involving sacrificial bonds for delay time t=2 s (blue), 5 s (red), 10 s (green), and 20 s (orange). The thick black line represents the fitting function (equation (3)) with parameter values given in Ref. 282. (Adapted with permission from ref. 282. Copyright 2013 American Physical Society.)

Hui's group focused on constitutive theories of high strength hydrogels with dynamic sacrificial bonding systems.[286-289] Those constitutive theories can accurately predict the mechanical behavior of a material with sacrificial bonding systems, and show promising guidance on the design of high strength materials. For example, Hui *et al*. developed a 3D finite strain constitutive model to study the mechanical behavior of a network hydrogel, in which a "primary network" was cross-linked with strong bonds (*e.g.* covalent bonds) while a

–secondary network" was cross-linked with weak bonds (*e.g.* ionic bonds).[287] In the –secondary network", the weak bonds could rupture and re-buildup in a sacrificial bonding manner. For uniaxial tensile testing, this constitutive model can be written as follow:

$$P_{11}/\mu = \left[1-\phi_2 q\left(J(\lambda)\right)\right]\left(1-\frac{J(\lambda)}{J_m}\right)^{-1}\lambda\left(1-\frac{1}{\lambda^3}\right) + 2\phi_2\int_1^{\lambda}\left.\frac{dq(J)}{dJ}\right|_{J(u)}\left[1-q\left(H(u,\lambda)\right)\right]\left(1-\frac{H(u,\lambda)}{J_m}\right)^{-1}\left(u-\frac{1}{u^2}\right)\left(\frac{\lambda}{u^2}-\frac{u}{\lambda^2}\right)du. \tag{6-4}$$

where P_{11}/μ is the normalized nominal stress, ϕ_2 is the number ratio of the weak bonds in the network hydrogel, λ is the stretch ratio, and the value for the other parameters can be found in the ref. 287. This constitutive model is capable of describing the macroscopic softening or hardening of a material with reversible sacrificial bonds. Additionally, the numerical results based on equation (6-4) showed the rate-dependent mechanical behavior of the material, as shown in Fig. 6-5*a*. The typical softening (necking) of the material is observed at low healing rate, whereas the softening is severely suppressed at sufficient high healing rate. For the reversible sacrificial bonding systems, there is a competition between the healing rate and the stretching rate. In other word, a low stretching rate will results in a high healing rate, because the sacrificial bonds have enough time to re-build up from rupture at a low stretching rate. Thus, this model can be used to explore the effect of sacrificial bonds on the rate-dependent mechanical behavior of a material. Furthermore, this constitutive model was developed and extended by combining kinetics of sacrificial bond rupturing and rebuilding and rate-dependent mechanical behavior.[288] Based on the developed constitutive model, the nominal stress ζ in a uniaxial tensile testing can be given by

$$\frac{\sigma}{\mu_0} = \left[(1-\rho)\varphi\left(\frac{t}{t_R}\right)+\rho\right]\left(\lambda(t)-\frac{1}{\lambda^2(t)}\right)+\int_0^t\frac{\gamma(\tau)}{N_0}\phi_B\left(\frac{t-\tau}{t_B}\right)\left[\frac{\lambda(t)}{\lambda^2(\tau)}-\frac{\lambda(\tau)}{\lambda^2(t)}\right]d\tau \tag{6-5}$$

where λ is the stretch ratio, μ_0 is the initial small strain shear modulus, ρ is the molar ratio between covalent cross-linked permanent chains and total chains, t_R and t_B are the characteristic times for breakage of original and rebuilt sacrificial bonds, N_0 is the number of the total chains, and $\gamma(\eta)$ is the reattachment rate of the temporary chains (*i.e.* the rebuilding rate of the sacrificial bonds).[288] The functions θ and ϕ_B are given:

$$\varphi\left(t/t_R\right)=\left(1+\left(\alpha-1\right)\left(t/t_R\right)\right)^{1/(1-\alpha)} \quad (6\text{-}6)$$

$$\phi_B\left(t/t_B\right)=\left(1+\left(\alpha_B-1\right)t/t_B\right)^{1/(1-\alpha_B)} \quad (6\text{-}7)$$

where α and α_B are a positive dimensionless material constants ($\alpha > 1$ and $2 > \alpha_B > 1$).[288] To predict mechanical behavior of a hydrogel cross-linked with covalent bonds and reversible sacrificial bonds, the kinetic parameters of sacrificial bond rupturing and rebuilding should be first determined by stress relaxation test and constant strain rate test. As a result, the mechanical behavior of the hydrogel was successfully and quantitatively predicted by this constitutive model (Fig. 6-5*b*). More importantly, this constitutive model shows great promising applicability to other polymeric materials cross-linked by covalent bonds and reversible sacrificial bonds. Guo *et al*. further developed and simplified this 3D constitutive theory by introducing a steady state kinetics.[289] Only four parameters in the simplified model should be determined from experimental results. The prediction of this simplified model on the mechanical behavior fits very well the experimental data of a dual cross-linked hydrogel at low stretching rate. The simplified model should be upgraded to predict the mechanical behavior of a material at relatively high stretching rate.

In addition to relaxation time, stretching rate, strain history, stress stiffening, steady state kinetics, and viscoelasticity, a rational consecutive model should consider the effects of physical entanglements (hidden lengths) and chain-chain interactions on the mechanical behavior.

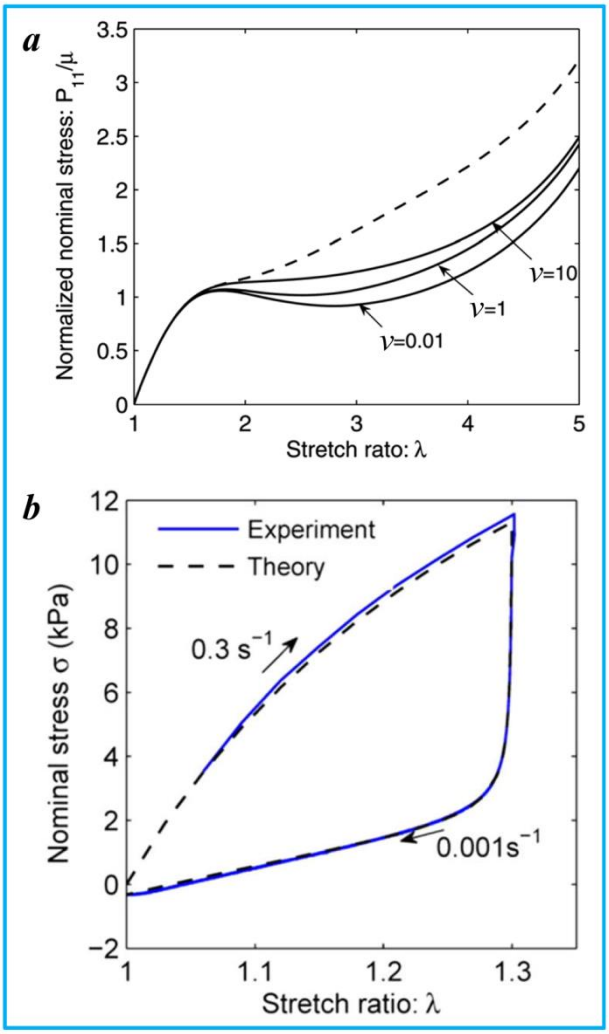

Figure 6-5. (*a*) Normalized nominal stress-stretch ratio behavior predicted from equation (6-4), where v is normalized healing rate. The dash line is the asymptotic result for $v\rightarrow\infty$. (Adapted with permission from ref. 287. Copyright 2012 The Royal Society of Chemistry.) (*b*) Comparison of model prediction (dash line) from equation (6-5) with experimental result (solid line) of cyclic tensile testing. The loading and unloading rates are 0.3 s^{-1} and 0.001 s^{-1}, respectively. (Adapted with permission from ref. 288. Copyright 2014 American Chemical Society.)

2.3 Inspired Sacrificial Bonds in Artificial Polymeric Materials

2.3.1 Sacrificial Covalent Bonds

Following the pioneering work by Gong *et al*. on double-network hydrogels (DN gels), it has widely been accepted that sacrificial covalent bonds in the first network is a mechanism to dissipate energy under deformation and protect the integrity of DN gels. Extensive studies on

the toughening mechanism of DN gels have suggested that introduction of any effective motifs of sacrificial bonds that dissipate energy under deformation will toughen the materials. One classical approach is to synthesize DN gels via a two-step polymerization method developed by Gong *et al*.[290] This approach allows preparing highly toughened soft materials with multiple networks, such as DN gels and elastomers, in which covalent bonds in the first brittle network act as ―sacrificial bonds" and the entangled polymer chains in the second/third ductile networks act as ―hidden lengths".[291] The first brittle network breaks into small clusters by sacrificing partial covalent bonds to dissipate a huge amount of energy at a relatively low stress. These small clusters serve as sliding cross-linking points in the ductile networks, in which the ―hidden lengths" of the second/third network chains are straightened by successive stretching. The concept of sacrificial bonding is reflected by a typical yielding and necking phenomenon in the loading-unloading tests of DN gels. The fracture of the covalent bonds in the first network dissipates a huge amount of energy during the elongation, leading to a large hysteresis of the DN gels during the first loading-unloading cycle. The necking phenomenon can be regarded as damage accumulation of the first brittle network. The DN gel is transformed into a very soft gel when its first network is broken into small clusters. A tearing test shows that the first brittle network is preferentially ruptured to increase the resistance to the crack propagation by forming a large damage zone around the crack tip,[292] similar to forming a crazing zone at the crack tip of glassy polymers. Additionally, the energy dissipation as well as the fracture process of the DN structures can be explained by the Brown-Tanaka model [293,294] which uses the Lake-Thomas theory [295] to describe energy dissipation due to rupture of covalent bonds in cross-linked polymers.

According to the Lake-Thomas theory, the fracture energy E_f dissipated due to rupture of covalent bonds in the first network in the fracture processing zone can be calculated by:

$$E_f = N n_1 n_2 U_f \tag{6-8}$$

where N is the number of polymer chains per unit volume in the fracture processing zone, n_1 is the average number of monomer units between adjacent crosslinks, n_2 is the number of covalent bonds in a monomer unit, and U_f is the average dissociation energy of the various covalent bonds.[295] The toughening mechanism of sacrificial covalent bonds requires that covalent bonds lying in the first brittle network be preferentially broken to dissipate mechanical energy. Since the stress is transmitted primarily via crosslinks, in order to preferentially break one covalent bond between adjacent crosslinks in the first network, it is

necessary to subject all polymer chains between adjacent crosslinks in the first network to pre-stretch. Actually, the polymer chains between adjacent crosslinks in the first network can be highly pre-stretched due to full swelling of the first network even when the resulting material is in the unstrained state. As the high fracture energy of the multiple-network-structured materials is a result of preferential rupture of covalent bonds in the first network to dissipate energy, the covalent bonds in the first network can be viewed as sacrificial bonds for the toughening of artificial materials. It is noted that apart from the fracture of the first network, the chain pulling and disentanglement of long polymer chains in the loosely cross-linked networks may also contribute to the toughness of artificial materials. Both the fracture of the sacrificial covalent bonds in the first network and the release of the hidden lengths in the second/third networks contribute to energy dissipation, endowing artificial materials with extraordinary toughness. Moreover, inter-network interactions are also important for the mechanical performance of artificial materials, because the stress is primarily transmitted between two networks via inter-network interactions.

It should be noted that when used as sacrificial covalent bonds, covalent bonds do not recover themselves from fracture, leading to irreversible and permanent damage of the materials. As a result, these materials exhibit softening and decreased hysteresis loops when subjected to repeated large deformation.[292,296]

2.3.2 Sacrificial Non-covalent Bonds

Sacrificial non-covalent bonds play a role of physical crosslinks in polymeric networks. Physical crosslinks based on non-covalent bonds are much weaker than chemical ones based on covalent bonds in a polymeric network. Sacrificial non-covalent bonds can preferably dissociate under a mechanical load or an external stimulus (*e.g.* temperature, pH, and ionic strength) to dissipate energy for the purpose of protecting the integrity of polymer chains. After dissociation of sacrificial non-covalent bonds, the detached polymer chains can relax and straighten under stress to further dissipate mechanical energy in polymer networks. Analogue to Lake-Thomas theory, the mechanical energy E_{dc} dissipated due to dissociation of sacrificial non-covalent bonds in the fracture process zone can be calculated by:

$$E_{dc} = Nn_1'U_{dc} / n_2' \tag{6-9}$$

Where $n_{1'}$ is the average number of bonding moieties in a polymer chain, n_2' is the number of bonding moieties forming a sacrificial non-covalent bond, and U_{dc} is the average dissociation energy of certain sacrificial non-covalent bonds. The dissociation energy U_{dc} in equation (6-9) should be smaller than U_f in equation (6-8).

Sacrificial non-covalent bonds can endow artificial materials with both high toughness due to dissipation of mechanical energy and recoverable and self-healing abilities due to the reversibility of sacrificed non-covalent bonds.[297-299] The reversibility of sacrificial non-covalent bonds can sustain the same hysteresis over cyclic loadings, leading to anti-fatigue materials.[300-303] However, since recovered sacrificial non-covalent bonds are usually out of their original positions, artificial materials that only use non-covalent bonds as crosslinks show plastic deformation under mechanical loads.[304] Therefore, elastic mechanisms should be introduced into reversible-crosslinked systems to maintain the shape of the artificial materials. This has been done by developing hybrid crosslinking systems as well as physical crosslinking systems with various crosslinking intensities upon following the methodologies of forming sacrificial non-covalent bonds described above. However, there have only been a few works on designing hidden lengths induced by sacrificial non-covalent bonds in polymeric networks. Therefore, it is challenging to design systems involving sacrificial non-covalent bonds and hidden lengths to meet prescribed requirements in terms of topological structures and properties.

3. Engineering of Sacrificial Bonds into Polymer Architectures and Mechanical Performance of Bio-inspired Materials

Sacrificial bonds have been found to endow biological materials with excellent performance, especially ultra-toughness and self-healing ability. However, sacrificial bonds in artificial materials cannot be generated the same way as those in biological materials because in the later cases sacrificial bonds are generated under the control of genes during the growth of biological materials. Fortunately, scientific and technological progresses allow engineering sacrificial bonds into bio-inspired materials. Table 6-1 lists three categories of bio-inspired materials associated with examples of sacrificial bonds. In what follows, the review will focus on these bio-inspired materials in terms of design methodology of sacrificial bonds and effects of sacrificial bonds on mechanical performance.

Table 6-1. Proposed sacrificial bonds in bio-inspired materials.

Bio-inspired Material	Example of Sacrificial Bond	Reference
Biomimetic Structures	Metal-ligand coordination bonds	330,331
	Ionic bonds (electrostatic bonds)	309,313
	Hydrogen bonds	317,323-325,329
High Strength Hydrogels	Covalent bonds	290-292, 347-351
	Metal-ligand coordination bonds	352-358
	Ionic bonds (electrostatic bonds)	56-59, 121
	Hydrogen bonds	359,360
	Hydrophobic associations	301,302,365-368
	Host-guest interactions	373-377
Elastomers	Covalent bonds	385
	Metal-ligand coordination bonds	183,390-392,397
	Hydrogen bonds	178,393-398
	π-π interactions	398

3.1 Sacrificial Bonds in Biomimetic Structures

Biomimetic structures, such as "mortar-brick" layered structures of nacre and metal ion mediated proteins, have served as sources of inspiration for scientists to develop high performance materials. The outstanding combination of high strength and high stiffness is closely related to the hierarchical structures of various nacres and bones.[249] However, the presence of sacrificial bonds has also been acknowledged as a common feature for such biological structures.[245,305,306] Recently, various sacrificial bonds have been engineered into organic layers for artificial biomimetic composites.

3.1.1 Design Methodology of Sacrificial Bonds in Biomimetic Structures

Ionic bonds are made of positively charged ions and negatively charged ions. In ionic compounds, the overall charge is zero. The force between oppositely charged ions is called electrostatic. Thus ionic bonds are also called electrostatic bonds. Ionic bonds are versatile in terms of the valence and size of the ion, and there is a large range of dynamic bond situations. Different from covalent bonds and hydrogen bonds, ionic bonds can be tuned by photo-induced valence changes or via electrochemistry.[307,308] Thus tuning nanoscale ionic interactions can tailor macroscopic mechanical performance. In the case of bones, it is shown

that ionic bonds serve as sacrificial bonds to dissipate a huge amount of energy during deformation.[257-260] This has inspired the design and development of nacre-mimetic composites involving sacrificial ionic bonds.

Sacrificial ionic bonds can be constructed between oppositely charged organic and inorganic components in organic/inorganic composites. Tang *et al.*[309] designed nacre-mimetic composite films from positively charged PDDA and negatively charged MTM platelets by the Layer-by-Layer (LBL) technique.[310-312] The LBL technique can realize charge reversal by means of sequential adsorption of PDDA and MTM dispersions. The PDDA and MTM layers had high compatibility because of strong electrostatic attractive interactions at the MTM/PDDA interface. The sacrificial ionic bonds were formed between the oppositely charged PDDA and MTM surface in the MTM/PDDA films (Fig. 6-6*a*). One negatively charged MTM surface could attract positively charged head-groups from different segments of the PDDA chain resulting in polymer loops (hidden lengths). Those nacre-mimetic composite films reproduced not only characteristic ―mortar-and-brick" architectures, but also the crucial effect of sacrificial bonds. This design strategy is applicable to different organic/inorganic building blocks resulting in nacre-mimetic materials. Na^+ cations are the major counter-ions in CMC/MTM nacre-mimetic composites due to the use of Na^+CMC and Na^+MTM. To introduce sacrificial, dynamic super-molecular crosslinks, the mono-valent Na^+ cations can be exchanged to multi-valent ones by infiltration of the latter in solution. Das *et al*. showed that super-molecular ionic interactions, introduced by infiltration of divalent Cu^{2+} cations, allow stabilization of the mechanical performance of self-assembled water-borne nacre-mimetics composed of alternating layers of Na^+CMC and Na^+MTM at high relative humidity (95%).[313] These super-molecular ionic interactions can form super-molecular ionic linkages between carboxylic acid groups within the CMC organic layer, and link carboxylates to the MTM surface (Fig. 6-6*b*).

Hydrogen bonds have been found to serve as sacrificial bonds in spider silk protein.[263] However, an isolated hydrogen bond is relatively weak (5-6 kcal/mol)[314] and does not resist much to force unless there are a large number of hydrogen bonds. Thus, sacrificial hydrogen bonds generally refer to multiple hydrogen bonds or clusters of hydrogen bonds. Moieties having several hydrogen bonding accepting and donating sites, such as dGMP and UPy,[315,316] are capable of forming multiple hydrogen bonds architectures. Actually, they have been successfully incorporated into artificial materials to form multiple hydrogen bonds severing as sacrificial bonds to dissipate a large amount of energy under deformation of the

materials. Martikainen *et al*. designed a facile route to prepare nacre-mimetic nanocomposites.[317] The anionic nanoclay (MTM) was first coated with a cationic polymer (PDDA) via electrostatic adsorption to form core-shell colloidal platelets. Subsequently the colloidal platelets were modified with anionic dGMP, resulting in an aligned and self-assembled nacre-mimetic nanocomposite denoted as MTM/PDDA/dGMP.[317] After modification with dGMP, the amino groups in the external surface of colloidal platelets were confirmed to complex with dGMP. The dGMP molecules containing multiple hydrogen bonding acceptors and donors formed multiple hydrogen bonds between the colloidal platelets in the nacre-mimetic nanocomposites (Fig. 6-6*c*). The multiple hydrogen bonds as well as the electrostatic bonds were shown to act as sacrificial bonds to improve synergistically mechanical performance of the nacre-mimetic nanocomposites via dynamic interactions between the platelets.

The UPy reported by Meijer‘s group are often used to build sacrificial hydrogen bonds because of their ability to form quadruple self-complementary hydrogen bonds.[179,318-321] Due to different secondary interactions, UPy dimers of donor-donor-acceptor-acceptor (DDAA) arrays are more stable than those of donor-acceptor-donor-acceptor (DADA) arrays. The DDAA and DADA dimers have four primary attractive hydrogen bonds. While the latter has six repulsive secondary interactions, the former has two repulsive and four attractive secondary interactions.[322] Based on the magnitude of the dimerization constant ($K_{dim} > 10^8$ M^{-1} in toluene),[320] the free energy required to break the UPy dimers is more than 10.9 kcal/mol,[179] which is comparable to protein unfolding energy and lower than typical covalent bond energies. Thus, the quadruple hydrogen bonds in UPy dimers can serve as sacrificial bonds to dissipate a large amount of energy when the hydrogen bonds break and the UPy moieties unfold. These sacrificial bonds would be constructed according to the supramolecular construction principle (Fig. 6-6*d*). Zhu *et al.* used sophisticated macromolecular engineering to introduce UPy moieties into a dynamic copolymer which was immediately self-mending when cut or ruptured due to the opening/rebinding of sacrificial bonds.[323,324] The dynamic copolymer denoted as EG-UPy was synthesized by reversible addition-fragmentation chain transfer copolymerization based on EG-MA and UPy-MA. Subsequently, the EG-UPy was assembled with high-aspect-ratio NHT nanoclay to fabricate hierarchical nacre-mimetic composite (EG-UPy/NHT) with a near-perfectly aligned structure.[323] McKee *et al*. developed one-component biomimetic nanocomposites based on rod-like CNCs grafted with long polymer brushes, involving UPy moieties on side chains to

form sacrificial hydrogen bonds within the grafted brush architecture.[325] UPy moieties can be incorporated in polymer chains either as pendant groups or telechelic moieties. In principle, larger hydrogen bonding systems could be designed and synthesized. One approach would be to pair up triple or quadruple hydrogen bonding units to form "dimers" which are capable of bonding with each other via six or eight hydrogen bonds, respectively. To date, many studies have developed multiple hydrogen bonding moieties and have shown the anticipated hydrogen bonding arrays. Very recently, there is a growing interest in incorporating multiple hydrogen bonding moieties into synthetic polymers to serve as reversible sacrificial bonds. Moreover, hyperbranched polymers are a special type of dendritic polymers and have attracted much attention due to their branched architectures as well as their high number of functional groups.[326] Because of the fact that hyperbranched polymers can bear a very large number of polar functional groups, they have a strong tendency to form hydrogen bond networks with neighboring molecules.[327] Therefore, hyperbranched polymers, such as hyperbranched polyglycerol [328] and poly(amido amine),[329] are of great potential to establish sacrificial hydrogen bonds in artificial materials and thus improve their toughness. Hao *et al*. developed ductile nacre-mimetic materials composed of HPAMAM and clay nanosheets.[329] Thanks to the numerous amine and amide groups, hydrogen bond networks were formed among the HPAMAM molecules. After crosslinking by genipin, a dual network was formed inside the nacre-mimetic materials and was responsible for the excellent mechanical properties of the nacre-mimetic materials.

Byette *et al*. developed mussel byssus-derived materials from a BPH, in which metal-ligand coordination bonds as well as salt bridges were shown to act as sacrificial bonds.[330] The treatment of the BPH materials at their isoelectric point using a citrate buffer (pH 4.5) led to the formation of salt bridges (interaction between carboxylate and ammonium functional groups), resulting in improvement of the mechanical performance of the BPH materials.[331] Three metal ions of different valences (Na^+, Ca^{2+}, and Fe^{3+}) were chosen to treat BPH materials at various pH values. With the addition of the metal ions, there was a competition between the bridging effect of the ions and screening of the salt bridges between charged amino acids. As a result, mono-valent Na^+ ion even had a negative impact on the mechanical performance of the BPH materials since it cannot act as a cross-linker but only moderately screens the salt bridges. On the contrary, multi-valent metal ions (Ca^{2+} and Fe^{3+}) formed metal-ligand complexes with more than one ligand, thus serving as sacrificial bonds to endow the BPH materials with high strength and toughness as well as self-healing ability. More

importantly, spectroscopic investigations showed existence of numerous Fe-ligand coordination bonds, indicating that the sacrificial metal-ligand bonds were efficiently formed in the BPH materials in the presence of Fe^{3+}. The use of multi-valent metal ions opens up a new avenue for to forming sacrificial bonds and therefore controlling the mechanical performance of artificial materials.

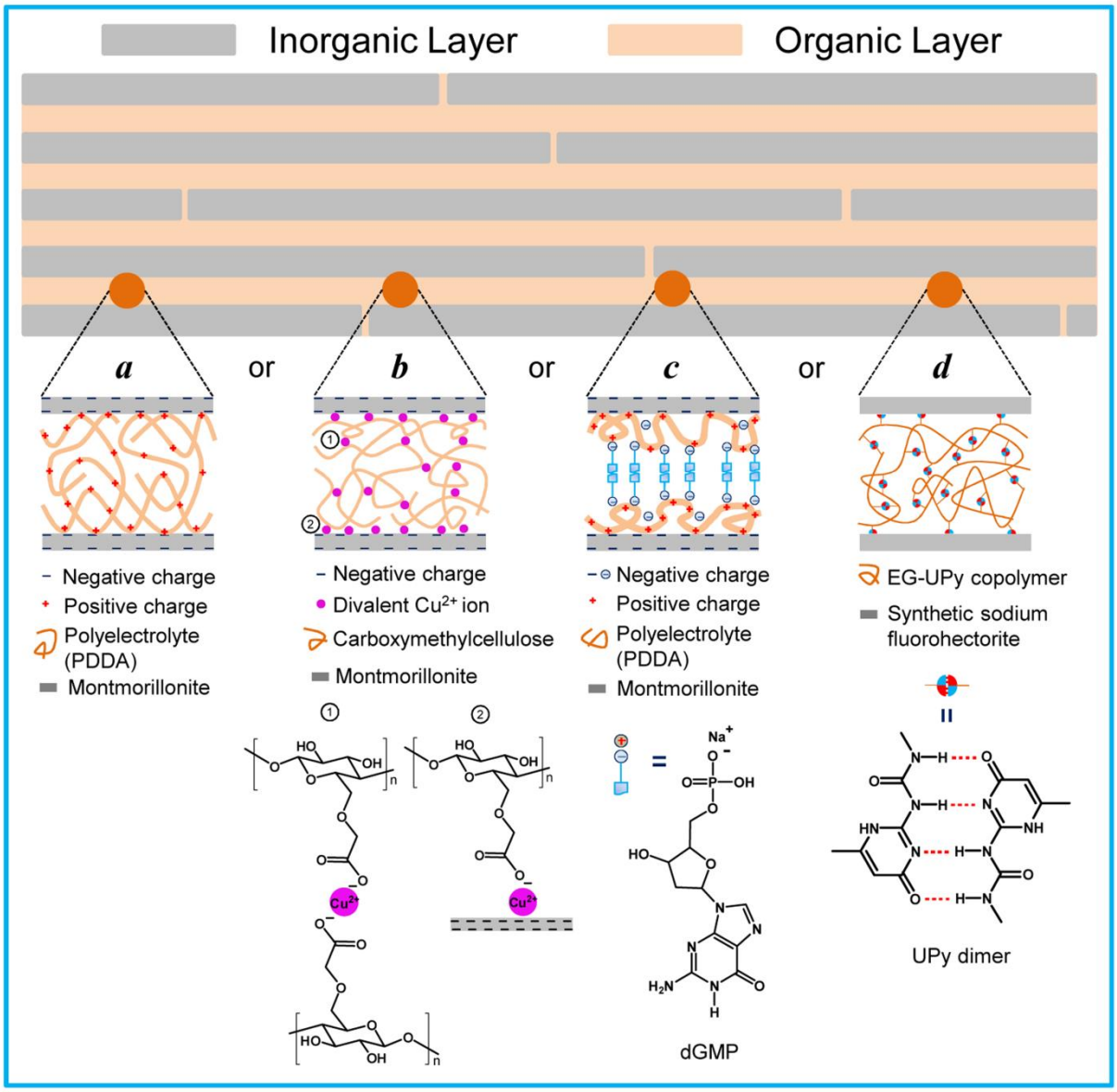

Figure 6-6. Schematic illustration of sacrificial bonds in nacre-mimetic composites. (*a*) Sacrificial ionic bonds were formed between opposite charges; (*b*) Sacrificial ionic bonds were formed between metal ions and acid groups as well as negatively charged MTM surface; (*c*) Sacrificial hydrogen bonds were formed between polymer-coated clays due to recognition sites on anionic dGMP; (*d*) Inter-chain and intra-chain hydrogen bonds were formed due to dimerization of the UPy moieties served as sacrificial bonds.

3.1.2 Effects of Sacrificial Bonds on Mechanical Performance of Biomimetic Composites

Nacre and bones are light-weight engineering materials with high stiffness, strength, and toughness. However, a combination of these properties is rarely found in artificial biomimetic composites. Generally, artificial biomimetic composites are composed of high volume fraction of inorganic platelets and several percentages of organic layers. The artificial biomimetic composites are generally stiff and strong but brittle because the inorganic platelets rupture prior to the organic layer yielding. Recently, engineering of sacrificial bonds into the organic layer as well as LBL assembly is used to result in the strong and tough artificial biomimetic composites. The nacre-mimetic MTM/PDDA films reported by Tang *et al*. reproduced structural and mechanical features of biological nacre.[309] Initial plastic deformation of MTM/PDDA film occurred and then abrupt hardening was observed with further stretching. The stress-strain curves of the nacre-mimetic films for 10 MPa < stress < 35 MPa exhibited a saw-tooth pattern similar to what would be observed for biological materials, indicating a sacrificial bonding mechanism. Regardless of stacking layers, the MTM/PDDA films exhibited high ultimate tensile strength (100 ± 10 MPa) and Young‘s modulus (11 ± 2 GPa), which should be compared with the ultimate tensile strength (130 MPa) and Young‘s modulus (64GPa) of biological nacre.[309] However, ultimate strain of the MTM/PDDA films increased with increasing stacking layers, indicating high toughness (Table 6-2). Martikainen *et al*. designed nacre-mimetic composites by first coating MTM with PDDA to prepare colloidal platelets and subsequently modifying the colloidal platelets with dGMP.[317] After modification with dGMP, the MTM/PDDA/dGMP composite exhibited higher ultimate tensile strength and Young‘s modulus than the MTM/PDDA composite without dGMP, due to the formation of sacrificial hydrogen bonds between the layers. The authors also considered the effect of relative humidity on the nacre-mimetic composites, analogically to the moist conditions of nacre. The relative humidity has a critical effect on the mechanical properties of the nacre-mimetic composites. The ultimate tensile strength and Young‘s modulus decreased with increasing relative humidity, due to the plasticizing effect of water molecules and screening effect of sacrificial bonds by polar water molecules.[309,317] At the same relative humidity, however, the MTM/PDDA/dGMP composites exhibited synergistic mechanical improvement.[317] For example, the MTM/PDDA/dGMP composite at 50% relative humidity had a tensile modulus of 13.5 GPa, a tensile strength of 67 MPa, a strain of 1.24%, and a work-to-failure of 0.58 MJ/m^3, which were all well above those of the MTM/PDDA composite (Table 6-2). The EG-UPy/NHT composite was another example on

mechanical improvement by engineering sacrificial hydrogen bonds into nacre-mimetic composites.[323] The mechanical properties of the EG-UPy/NHT composites could be tuned by controlling the sacrificial hydrogen bonds in EG-UPy copolymers. At 60% relative humidity, the tensile strength and the Young‘s modulus of the EG-UPy/NHT composite with 30 mol% UPy units were 13 and 22 times those of the EG-UPy/NHT composite without any UPy unit, respectively (Table 6-2). However, the brittleness of the former was indicated by low strain-to-failure and weak yielding, due to dense sacrificial hydrogen bonds with low exchange dynamics. With an intermediate fraction of UPy units (13 mol%), the EG-UPy/NHT composites exhibited synergistic improvement of tensile strength, Young‘s modulus, strain-to-failure, and work-to-failure as compared to the EG-UPy/NHT composite without any UPy unit, due to balanced exchange dynamics and strengthening effects of the UPy units.[323] Moreover, excellent gas barrier properties were obtained due to the high aspect ratio of the nanoclay (NHT, thickness ≈ 1 nm; aspect ratio ≈ 750).[332] Furthermore, the role of UPy unit as sacrificial bonds was indicated by the pronounced plastic behavior and non-catastrophic crack growth of one-component CNCs nanocomposite.[325] Recently, Hao *et al*. developed ductile nacre-mimetic HPAMAM/nanoclay composites, in which HPAMAM molecules formed sacrificial hydrogen bonds in organic phase and glued the clay nanosheets together.[329] However, the tensile strength of those nacre-mimetic composites was less than 20 MPa. After crosslinking by genipin, the resulting nacre-mimetic composites were tough (fracture toughness of 5 MJ/m^3) and strong (tensile strength of 153 MPa).[333] The authors showed that the structure of HPAMAM molecules played a key role in the cross-linked nacre-mimetic materials.

The mechanical properties of CMC/MTM composites are also listed in Table 6-2. As discussed above, the tensile strength and the Young‘s modulus of CMC/MTM composites decreased with increasing relative humidity. After modification with Cu^{2+}, they did not deteriorate much at high relative humidity. The ionic bonds in Cu^{2+}-modified CMC/MTM composites allowed for reduced deterioration of their mechanical properties against relative humidity. Especially, at 95% relative humidity, the stiffness, the strength, and the toughness of the Cu^{2+}-modified CMC/MTM composites were simultaneous improved as compared to the pristine CMC/MTM composites.[313]

Table 6-2. Overview of mechanical properties of nacre-mimetic composites.

Sample	Relative Humidity [%]	Young's Modules [GPa]	Tensile Strength [MPa]	Strain-to-Failure, [%]	Work-to-Failure [MJ/m^3]
LBL deposition of PDDA and MTM[a] [309]					
$(MTM/PDDA)_{100}$[b]	32	10±2	106±8	8.4±0.7	NA[e]
$(MTM/PDDA)_{200}$	32	13±2	109±8	10.0±0.5	NA
$(MTM/PDDA)_{100}$	92	3±0.5	52±8	18.0±0.9	NA
Core-shell colloidal self-assemble without/with modification with dGMP[a] [317]					
MTM/PDDA	Dry	21.9±0.6	120±5	1.17±0.11	0.94±0.13
MTM/PDDA/dGMP	Dry	31.9±1.4	149±4	0.73±0.04	0.64±0.05
MTM/PDDA	50	10.2±0.4	47.8±1.5	1.17±0.08	0.39±0.04
MTM/PDDA/dGMP	50	13.5±0.7	67±2	1.24±0.10	0.58±0.06
Core-shell colloidal self-assemble[a] [323,324]					
EG-UPy-0[c]/NHT	60	2±1	19±5	4.4±3.1	0.6±0.2
EG-UPy-13/NHT	60	22±4	67±23	8.2±3.4	3.8±0.8
EG-UPy-30/NHT	60	43±10	265±32	1.3±0.4	2.3±0.6
Core-shell colloidal self-assemble, subsequent infiltration of divalent Cu^{2+} ions[a] [313]					
Na^+-CMC/MTM (60/40)	95	1.5±0.3	19±3	1.5±0.3	0.2±0.02
Cu^{2+}-CMC/MTM (60/40)	95	13.5±1.6	125±6	1.5±0.2	1.3±0.1
Core-shell colloidal self-assemble, subsequent crosslinking with genipin[a] [329,333]					
G_0[d]-HPAMAM/nanoclay	NA	0.37±0.05	18.6±3.0	30.9±0.6	3.95±0.45
$G_{0.025}$-HPAMAM/nanoclay	NA	3.43±0.23	55.3±3.1	12.2±2.2	5.03±0.52
$G_{0.2}$-HPAMAM/nanoclay	NA	6.46±0.38	152.9±7.6	3.48±0.08	2.31±0.28

[a]Approach for preparation of nacre-mimetic composites; [b]Number of deposition cycles; [c]Molar fraction of UPy-MA units; [d]Percentage concentration of genipin aqueous solution; [e]Not available.

3.2 Sacrificial Bonds in High Strength Hydrogels

Hydrogels, consisting of three-dimensional polymer networks and a large amount of water (50-90%) inside the networks, are "soft and wet" materials. They have many unique properties such as transparency, flexibility, permeability, low surface friction, and stimuli-responsiveness. Because of these properties, hydrogels have great potential for use in many fields, such as biomedicine,[334,335] tissue engineering,[336-338] super absorbents,[339-341]

and environmental engineering.[342,343] However, conventional hydrogels, usually composed of a single-network (SN) of a hydrophilic polymer, are mechanically weak and brittle. The weak, brittle mechanical characteristics of hydrogels greatly restrict their extensive uses requiring better mechanical properties. Hydrogels are greatly expected as substitutes of existing load-bearing soft tissues such as cartilages,[344] ligaments,[345] and muscles.[346] Development of strong and tough hydrogels is significant for applications such as artificial load-bearing soft tissues.

3.2.1 Design Methodology of Sacrificial Bonds in Hydrogels

In biological materials, sacrificial bonds are often non-covalent and reversible bonds. Dynamics of these sacrificial bonds endows the biological materials with self-healing properties and excellent mechanical performance, especially extraordinary toughness. Normally, breaking a covalent bond may dissipate even much more energy than breaking a non-covalent bond. However, covalent bonds in biological materials do not serve as sacrificial bonds because biological materials lose inherent performance when covalent bonds of biopolymers are broken. Nevertheless, inspired by sacrificial bonding mechanisms in biological materials, researchers have developed super-toughed artificial materials by incorporating sacrificial covalent bonds into them. Gong and co-workers were the first to put forth the concept of sacrificial covalent bonds for tough DN gels (Fig. 6-7).[290] DN gels are generally synthesized by a two-step sequential free-radical polymerization following the design principles below: (1) a rigid and brittle polymer, such as a polyelectrolyte, serves as the first network, while a soft, ductile and neutral polymer serves as the second network; (2) the molar concentration of the monomer for the second network is 20-30 times that of the first network; and (3) the first network is tightly cross-linked while the second network is loosely cross-linked.[292] Therefore, the molecular weight of the second polymer has to be very high. In the first free-radical polymerization, the first network is tightly cross-linked in the presence of a high concentration of cross-linker. The first network is then fully swollen by an aqueous solution containing a high concentration of the second monomer aqueous solution and a low concentration of cross-linker. Further free radical polymerization leads to the formation of a loosely cross-linked second network inside the first tight network. Based on the design principles, enhanced mechanical performance has been realized in hydrogels with DN structures, of which the first network is brittle and imparts toughness by sacrificing its covalent bonds while the second network is ductile and sustain large deformation by extending its tangled polymer chains. A representative DN gel composed of PAMPS and

PAAm was prepared with PAMPS polyelectrolyte as the first network and PAAm neutral polymer as the second network.[290] However, in the first generation of DN gels, the first network should be a strong polyelectrolyte. This requirement greatly hindered the application of those gels. To address this issue, Nakajima *et al.* developed a general "molecular stent" method to synthesize tough DN gels (hereafter denoted as St-DN gels) in which any neutral polymer could be used to form the sacrificial first network.[347] Hu *et al*. developed strong and tough MR gels with a two-phase composite structure, where the disperse phase was rigid DN microgels, and the continuous phase was a soft PAAm matrix.[348-351] The MR gels were successfully prepared by salt-controlled swelling of highly cross-linked anionic PNaAMPS microgels and two-step sequential UV polymerization of lightly cross-linked neutral PAAm networks. In the case of MR gels, highly cross-linked microgels served as "sacrificial bonds" to replace the highly cross-linked polyelectrolyte network for DN gels.

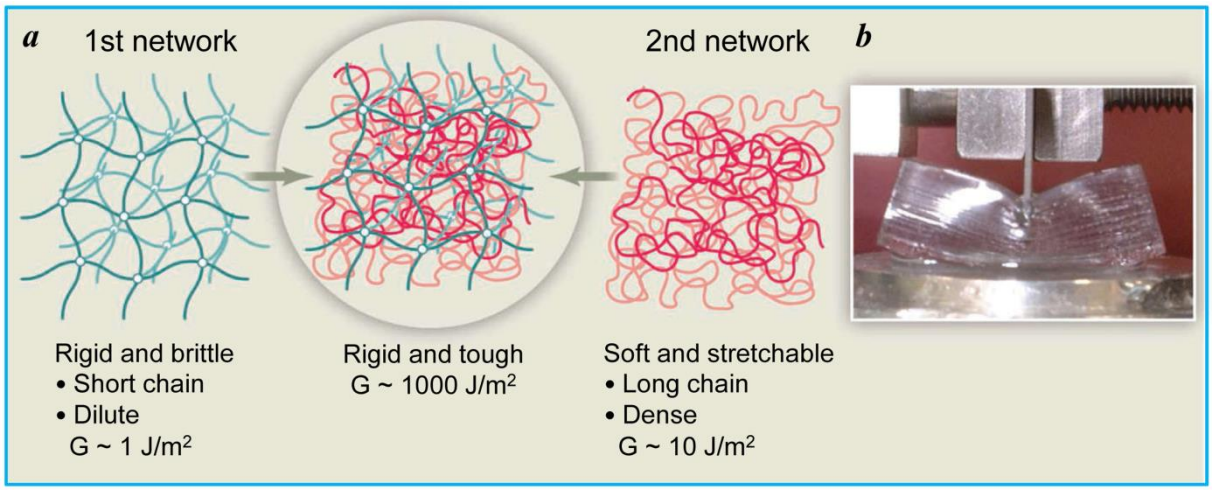

Figure 6-7. (*a*) Illustration of tough DN gels. (*b*) Optical photo of a tough DN gel containing 90 wt.% of water. The value of the fracture energy (G) is used to indicate material toughness. (Adapted with permission from ref. 291. Copyright 2014 American Association for the Advancement of Science.)

The high mechanical performance of the DN gels was achieved by sacrificing covalent bonds in the first rigid network under deformation. However, sacrificial covalent bonds do not recover from fracture, leading to irreversible and permanent damage of DN gels after loading. To address this issue, hybrid cross-linked gels with a combination of non-covalent and covalent cross-linkers were reported recently. The first network was physically cross-linked with non-covalent bonds, while the second network was chemically cross-linked with covalent bonds. Those physical bonds in the first network such as metal-ligand coordination

bonds, ionic bonds, and hydrogen bonds served as reversible sacrificial bonds to toughen the hybrid cross-linked gels with hysteresis and self-recovery potentials.

Metal-ligand coordination bonds in biological materials are thoroughly documented in the literature.[269] They are formed when the ligand donates lone pairs of electrons to the metal ion empty orbitals. From the perspective of sacrificial bonds, mono-valent metal-ligand coordination bonds are excluded because they will not break but slide when polymer chains involved in the ligand are stretched. Typical sacrificial metal-ligand coordination bonds are formed between di-valent/multi-valent metal ions (*e.g.* Zn^{2+}, Cu^{2+}, Ca^{2+}, and Fe^{3+}) and ligands capable of donating lone pairs of electrons (*e.g.* carboxylate groups, amino groups, and 3,4-dihydroxyphenylalanine).[269] Typically, tri-valent cations Fe^{3+} may be an ideal choice to form efficient sacrificial metal-ligand coordination bonds because of strong complexing strength. Sun *et al.* designed an extremely stretchable and tough hybrid hydrogel (alginate/PAAm gel) by combining an ionically cross-linked alginate network and a covalently cross-linked PAAm network (Fig. 6-8).[352] An alginate chain is composed of guluronic acid (G) segments, mannuronic acid (M) segments, and alternating G and M segments. In the presence of enough Ca^{2+} cations, zip-like metal-ligand coordinating crosslinks were formed between the G segments in different alginate chains. Besides Ca^{2+} cations, other multi-valent cations (Sr^{2+}, Ba^{2+}, Al^{3+}, Fe^{3+}) were used as ionically cross-linkers to develop stretchable and tough alginate/PAAm gels.[353] Lu *et al.* reported a highly stretchable and tough hydrogel, consisting of a carrageenan network cross-linked with cation-mediated (K^{+}/Ca^{2+}) coordination bonds and a PAAm network cross-linked with covalent bonds.[354] The metal-ligand coordination bonds that linked the carrageenan double helices served as reversible sacrificial bonds to stiffen and toughen the hydrogel through energy dissipation. In addition, the release of the hidden lengths of PAAm chains in the hydrogel dissipated much energy and allowed for ultrahigh extension of the hydrogel before failure during stretching. Panhuis‘s group developed a series of coordinative-covalent entanglement hydrogels based on IPNs of coordinative cross-linked polysaccharides and a covalent cross-linked neutral polymer.[355,356] For the above coordinative cross-linked hydrogels, polysaccharides such as alginate, gellan gum, and carrageenan were anionic polymers with abundant carboxyl groups in the main chains, and cations could form sacrificial coordination bonds with carboxyl groups in polysaccharides. Under a stress, those sacrificial coordination bonds were easily dissociated to dissipate energy, and thus toughen the hydrogels. When the stress was removed, the coordination bonds were able to reform and restore integrity of the

hydrogels. Lin *et al.* reported a novel dual P(AAm-*co*-AAc) hydrogel with dual networks by combining a covalent cross-linked network and a multi-valent ion pairing of Fe^{3+}-acrylic acid coordination.[357] With an excess of Fe^{3+} in the network, the Fe^{3+} would form a mixture of mono-, bi-, and tri-coordination bonds with acrylic group. The performance of the hydrogel with the multiple coordination bonds was limited due to the formation of an inhomogeneous coordinative cross-linked network. An immersion process was applied to remove excess Fe^{3+} and to allow forming more tri-coordination bonds between Fe^{3+} and acrylic group through reorganization of coordinates. The Fe^{3+}-acrylic acid coordination bonds were homogeneously distributed along the main polymer chains and served as reversible sacrificial bonds to dissipate energy efficiently. Menyo *et al*. developed an IPN hydrogel by incorporating a metal-ligand coordination network into a loosely cross-linked hydroxyethylacrylamide covalent scaffold.[358] The metal-ligand coordination bonds were formed between trivalent metal ions (Al^{3+}, Fe^{3+}, and In^{3+}) and 3-hydroxy-4-pyridinone moieties in modified PEG stars.

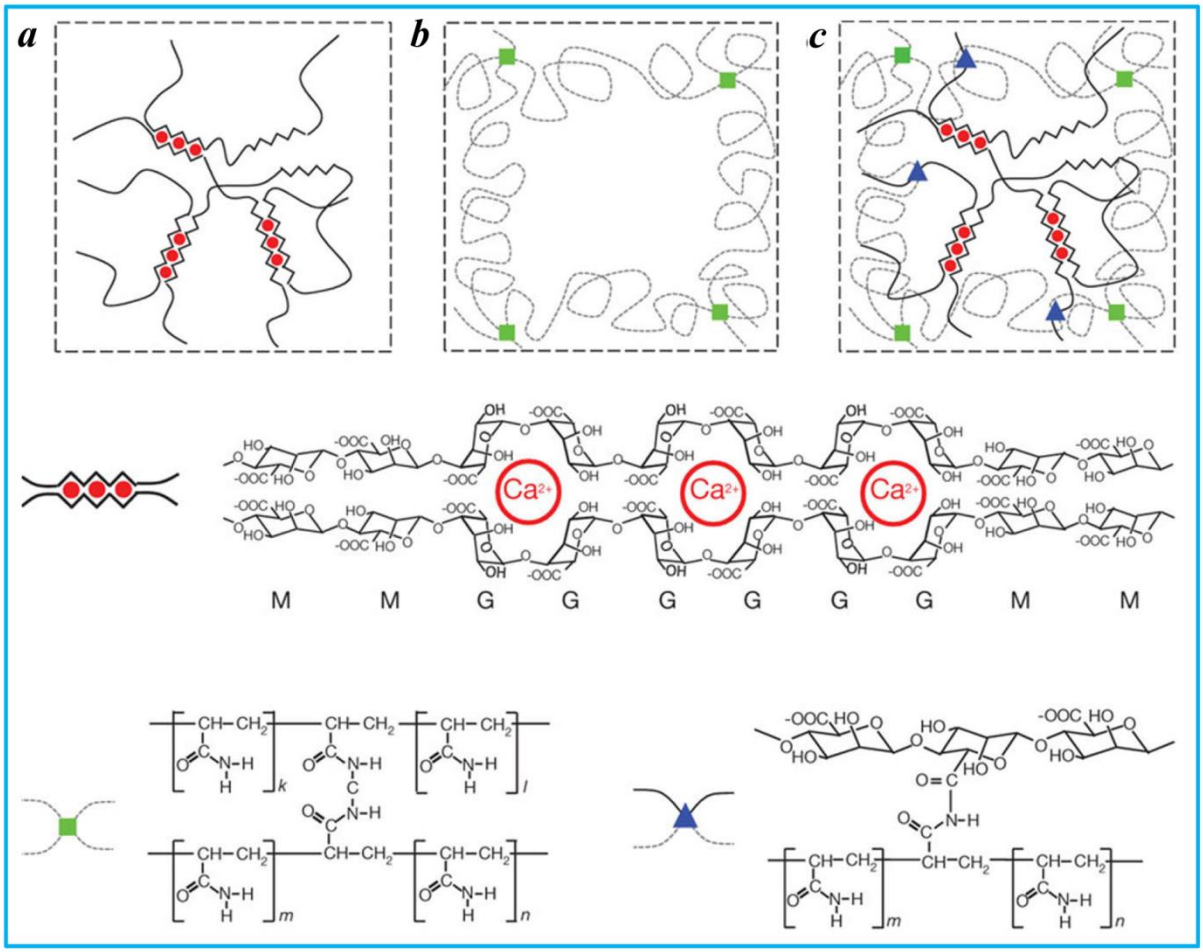

Figure 6-8. Schematic illustration of sacrificial metal-ligand coordination bonds in the alginate/PAAm hydrogels. ***a***, Alginate hydrogel cross-linked with Ca^{2+} ions. ***b***, PAAm

hydrogel cross-linked by covalent bonds. c, Alginate/PAAm hydrogel composed of the two types of polymer network. (Adapted with permission from ref. 352. Copyright 2012 Nature Publishing Group.)

Recently, weak hydrogen bonds were developed to serve as ―sacrificial bonds" in hydrogels.[359,360] Hu *et al.* designed a new hybrid network system based on a tunable composition of strong covalent bonds (as permanent crosslinks) and clusters of sacrificial hydrogen bonds (as recoverable transient crosslinks) with the following principle: (1) maintaining a high total number of crosslinks (permanent and sacrificial) to ensure a high modulus at a small strain <1%; (2) introducing a high fraction of multiple and reversible hydrogen bonds to ensure high energy dissipation due to recurring fracture of sacrificial network at large deformations; and (3) incorporating a small fraction of permanent crosslinks to ensure shape control and strain recovery after stress release.[359] They synthesized P(DMAA-*co*-MAAc) hydrogels by one-pot free-radical copolymerization of DMAA and MAAc. That monomer pair was chosen based on good match for forming hydrogen bonds (a strong hydrogen bond acceptor and a strong hydrogen bond donor) and chain transfer reaction in copolymerization process producing a low fraction of chemical crosslinks. As a result, the P(DMAA-*co*-MAAc) hydrogels were composed of a loose covalent cross-linked network and dense clusters of sacrificial hydrogen bonds (Fig. 6-9). Comparison between P(DMAA-*co*-MAAc) hydrogels and P(DMAA-*co*-AAc) ones shows that hydrogen-bonded clusters must be stabilized by hydrophobic interactions to ensure high rigidity of the hydrogels. Notably, the sacrificial hydrogen-bonded clusters were shown to have a broad distribution in terms of size and strength.

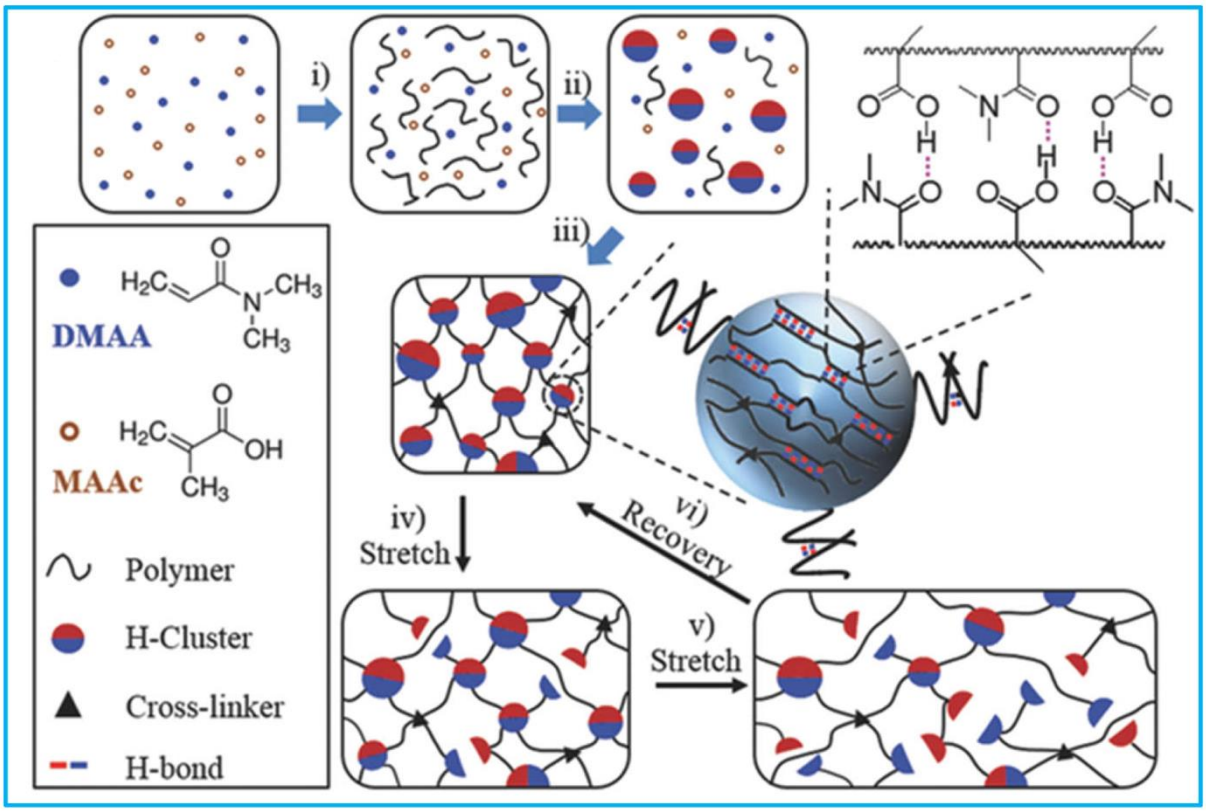

Figure 6-9. Schematic illustration of sacrificial hydrogen bonds in P(DMAA-*co*-MAAc) hydrogels. (Adapted with permission from ref. 359. Copyright 2015 WILEY-VCH Verlag GmbH & Co. KGaA, Weinheim.)

Sacrificial ionic bonds in hydrogels can be formed between oppositely charged polyelectrolytes in polymeric networks. Pendent cationic and anionic groups are randomly distributed along polyelectrolyte chains by random polymerization of ionic monomers. The randomly distributed charges form multiple ionic bonds of a wide distribution of strength through inter- and intra-chain interactions, in which strong ionic bonds act as permanent crosslinks to impart elasticity whereas weak ones act as reversible sacrificial bonds to toughen the materials. This approach for construction of sacrificial ionic bonds is applicable to various ionic monomer pairs with relatively bulky structures. Typical ionic monomers are MPTC, DMAEA-Q, DMAPAA-Q, NaSS, AMPS, and NaAMPS. It is noted that the performance of the resulting materials strongly depends on ion pair structures. This approach has been used to prepare a new class of physical hydrogels with sacrificial ionic bonds.[297-300] Sun *et al.* developed a new class of tough and viscoelastic physical PA hydrogels with excellent mechanical properties.[300] Those PA hydrogels were synthesized by one-step random copolymerization of oppositely charged ionic monomers at high total monomer concentration. The randomness of charges provided multiple ionic bonds with a wide distribution of strength,

through inter- and intra-chain complexation. Like ionic bonds, the PA hydrogels had super-molecular structures. The ionic bonds played two roles in the mechanical properties of the PA hydrogels, namely, strong bonds and weak ones. The strong ones served as permanent cross-links to impart elasticity, while the weak ones served as sacrificial cross-links to dissipate energy through reversible breakup and buildup. The physical PA hydrogels, however, had several drawbacks: (1) the charge sequence was random and not controllable. It depended on the reactivity ratio between oppositely charged monomers which might vary with monomer pairs; (2) inter-chain complexation that imparts elasticity to the hydrogel can only be formed at extremely high ion concentrations. To overcome those drawbacks, Luo *et al.* developed a PIC hydrogels which consisted of oppositely charged polyelectrolytes.[297-299] Strong and tough PIC hydrogels with self-healing property were synthesized by two-step sequential homopolymerization of cationic and anionic monomers (Fig. 6-10).[297] All the ionic bonds were formed through inter-chain complexation where the weak ionic bonds served as sacrificial bonds. Yang *et al.* developed an IPN hydrogels with improved toughness and time-dependent recovery capability by engineering ionically cross-linked CCNF-PEG complexes into covalently cross-linked PAAm networks.[361] Ionic bonds in the CCNF-PEG complexes ruptured preferentially prior to covalent bonds with increasing stress, resulting in stress transfer in the IPN hydrogels and fracture energy dissipation.

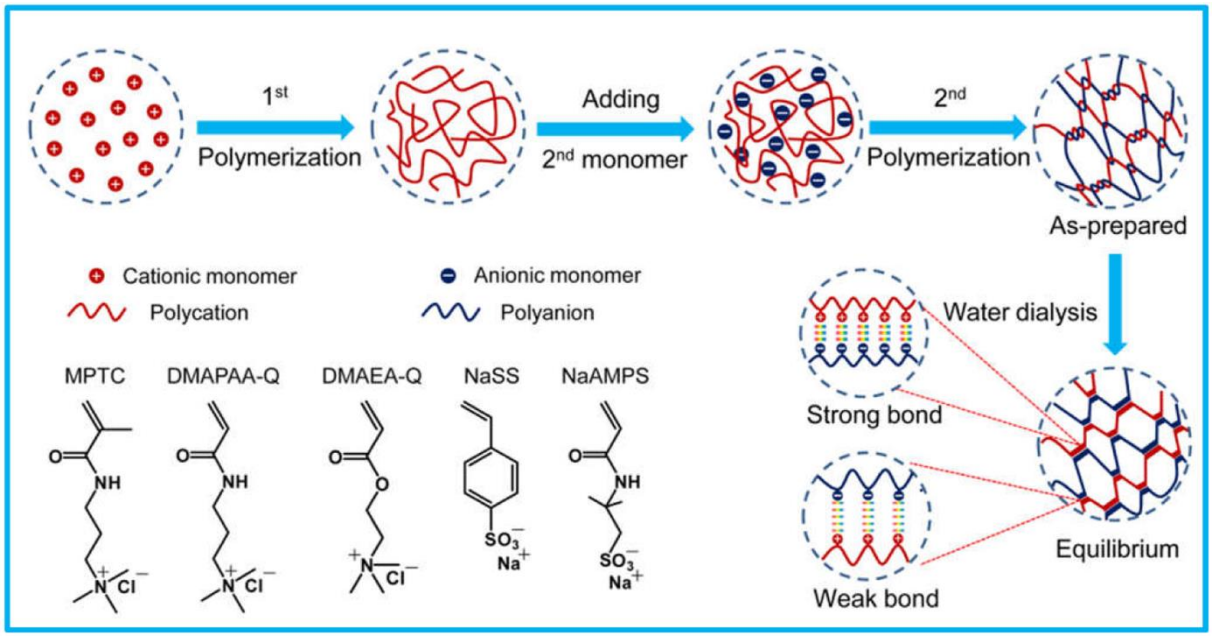

Figure 6-10. Schematic illustration of sacrificial ionic bonds in PIC hydrogels. (Adapted with permission from ref. 297. Copyright 2015 WILEY-VCH Verlag GmbH & Co. KGaA, Weinheim.)

Hydrophobic interaction is one of the significant driving forces for protein folding, cell membranes as well as many other biological assemblies in aqueous solutions.[362-364] In the case of protein folding, the hydrophobic effect is important to understanding the structures of proteins that have hydrophobic amino clustered together within the proteins. Structures of water-soluble proteins have a hydrophobic core in which side chains are buried from water, which stabilizes the folded state. Charged and polar side chains are located on the solvent-exposed surface where they interact with surrounding water molecules. Recently, hydrophobic interaction is widely applied to molecular self-assembly of hydrous artificial polymers. Gong‘s group demonstrated that hydrophobic association could serve as reversible sacrificial bonds in hydrophobic association hydrogels.[301,302,365,366] The latter are composed of amphiphilic polymers and water. Amphiphilic polymers are macromolecules that have both hydrophilic and hydrophobic segments. The molecular structure of amphiphilic polymers is critical to construct sacrificial hydrophobic association that results from self-assembly of pendent hydrophobic groups on a hydrophilic backbone. One strategy is to prepare amphiphilic polymers through radical copolymerization of water-soluble monomers and a small amount of co-monomers with extended hydrophobic groups.[367,368] Water-soluble monomers such as acrylamide and acrylic acid form hydrophilic polymer backbones, while co-monomers such as stearyl acrylate and octly phenol poyethoxy ether acrylate act as hydrophobic monomers to form hydrophobic associations (micelles) due to the self-assembly of their long alkyl chains. The resulting hydrophobic associations serve as reversible physical crosslinks of the copolymers. The molar fractions of hydrophobic monomers are controlled in several percentages to prevent excessive crosslinking. Another strategy is that amphiphilic monomers self-assemble into associated lamellar bilayers via hydrophobic interaction in an aqueous solution of hydrophilic monomers followed by co-polymerization in the presence of an initiator and a cross-linker. [301,302,365,366] As a result, the polymeric lamellar bilayers are entrapped inside the amorphous hydrophilic polymer networks, leading to the formation of lamellar hydrogels (Fig. 6-11).

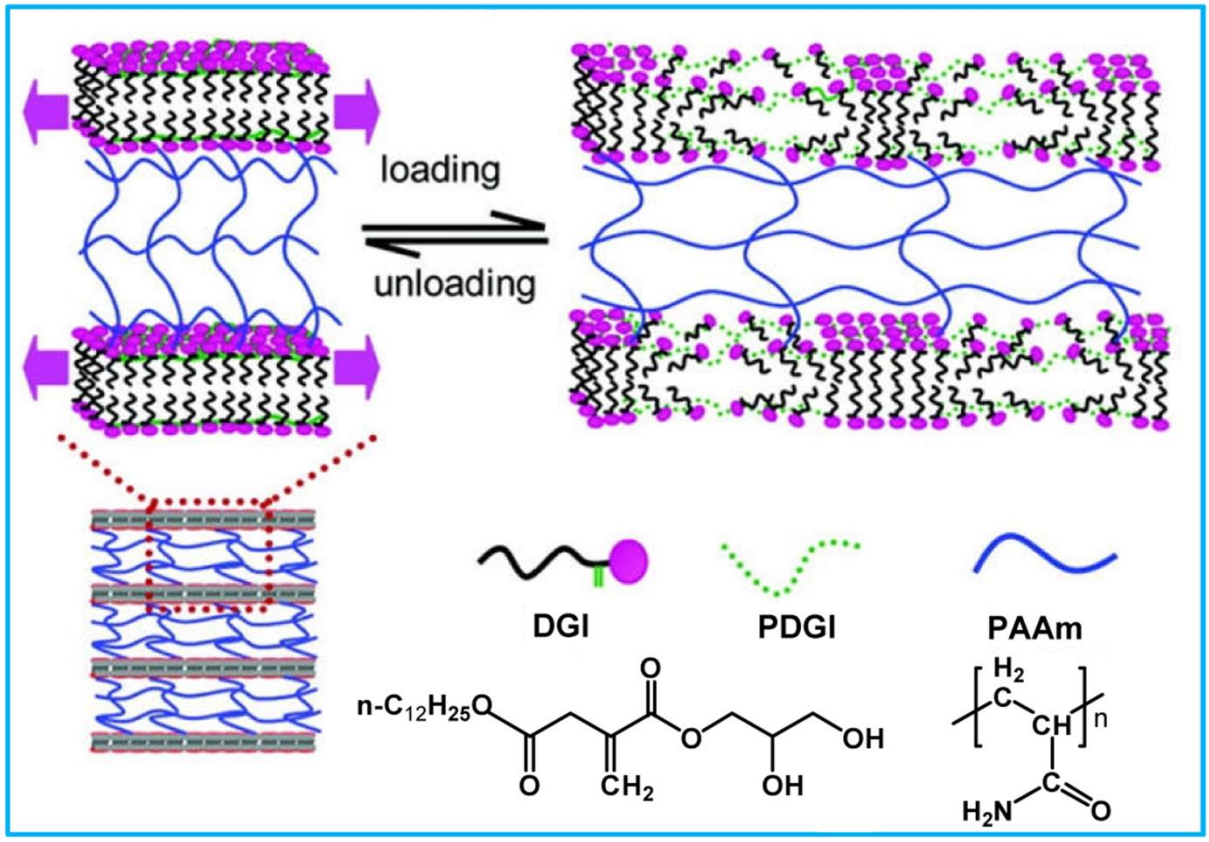

Figure 6-11. Schematic illustration of sacrificial hydrophobic associations in anisotropic lamellar hydrogels. (Adapted with permission from ref. 301. Copyright 2011 American Chemical Society.)

Host-guest complexes are generally composed of two molecules that are held together in unique structures through molecular recognition and non-covalent bonding. In principle, a host-guest complex consists of a receptor moiety (host) and a ligand moiety (guest) through non-covalent bonding. Common hosts include crown ethers, cyclodextrins, cucurbiturils, calixarenes, and pillararenes, while guests can be organic molecules, ions, and even nanoparticles. Host-guest complexes are formed by embedding guests into host cavities. To date, several excellent reviews have been published on the construction of host-guest complexes.[369-372] Constructing host-guest complexes into supramolecular systems can provide distinctive properties. Recently, host-guest complexes have been incorporated into supramolecular polymer networks to act in a sacrificing manner to endow the networks with high toughness as well as self-recovery.[373-377] The sacrificial host-guest complexes can usually be realized by "bottom-up" synthesis methodology and hierarchical construction in multiple length scales. Typical hosts for constructing sacrificial bonds include cyclodextrins [375-377] and cucurbiturils.[373,374] Guests should be selected based on association

constants of host-guest pairs. The higher the association constants, the more stable the host-guest complexes. Recently, based on the structure/function model of *titin*, Liu *et al*. reported an aqueous dual network, in which CB[8]-mediated dynamic host-guest interactions served as sacrificial bonds to toughen the network, while a small amount of covalent bonds served as permanent crosslinks to maintain its shape (Fig. 6-12).[374] In that dual network, one sacrificial host-guest complex was constructed by complexing two polymerizable guests (1-benzyl-3-vinylimidazolium) into one CB[8] with two relatively high association constants (K_{a1}=4.21×10^7 M^{-1}, K_{a2}=4.25×10^5 M^{-1}).[374] The sacrificial CB[8]-mediated host-guest complexes formed dynamic "hidden lengths (loops)" between two permanent crosslinks inside the artificial network. Therefore, the CB[8]-mediated host-guest complexes played several roles simultaneously: (1) they enhanced fracture resistance of the networks, thereby toughening the overall networks in a sacrificial bonding manner; (2) they endowed the networks with self-recovery due to the reversible host-guest complexes; (3) they increased energy dissipation by stretching dynamic "loops" inside the networks.[374] In addition, Nakahata *et al*. constructed sacrificial host-guest complexes using molecular recognition between cyclodextrin and hydrophobic guest molecules at polymer side chains, leading to a transparent, flexible, tough, and self-healing hydrogel.[375]

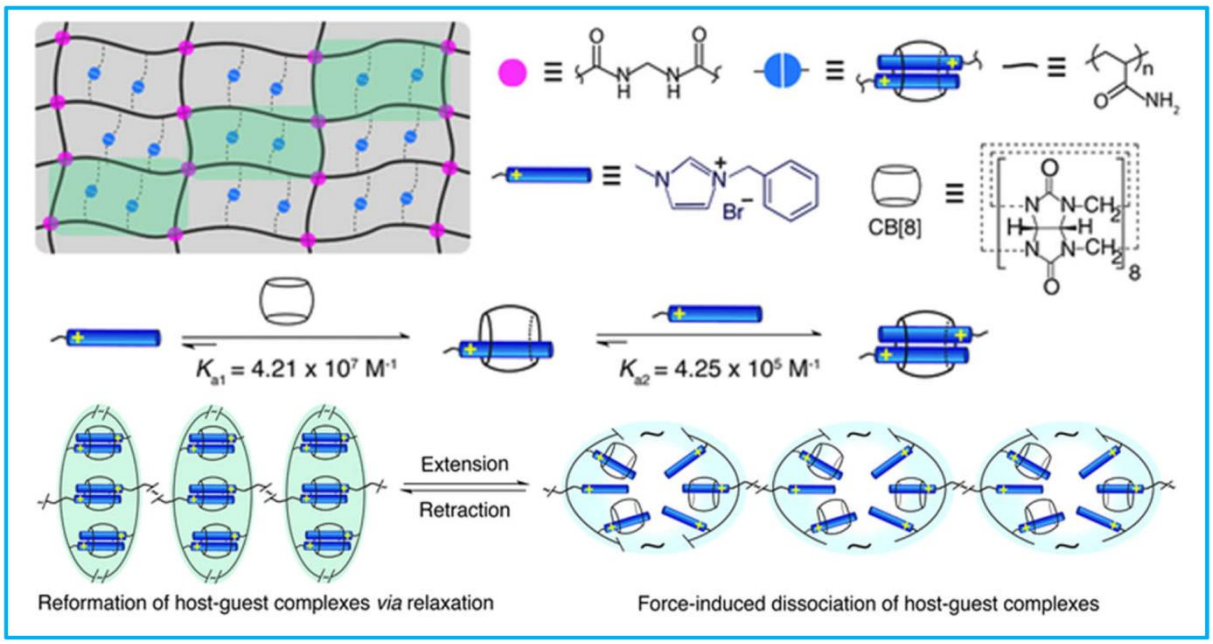

Figure 6-12. Schematic illustration of sacrificial host-guest complexes in CB[8]-mediated host-guest hydrogels. (Adapted with permission from ref. 374. Copyright 2017 WILEY-VCH Verlag GmbH & Co. KGaA, Weinheim.)

3.2.2 Effects of Sacrificial Bonds on Mechanical Performance of Hydrogels

Many effects have been made to develop strong and tough hydrogels with new approaches.[378-381] PAMPS/PAAm DN gels developed by Gong *et al*. are the most notable.[290] Optimized PAMPS/PAAm DN gels are of excellent hardness (elastic modulus of 0.1-1.0 MPa), strength (tensile fracture stress of 1-10 MPa), strain (100-3000%), and toughness (tearing energy of 100-4400 J/m^2).[292,382,383] In particular, the tearing energy of the DN gels is two and three orders of magnitude higher than that of PAAm SN gels (~10 J/m^2) and PAMPS SN gels (~0.1 J/m^2), respectively. Such improvement in toughness of PAMPS/PAAm DN gels is attributed to both the fracture of the sacrificial covalent bonds in the PAMPS network and the release of the hidden lengths in the PAAm network. The St-DN gels as well as MR gels also exhibited excellent mechanical properties, which were comparable to those of the conventional PAMPS/PAAm DN gels. Typically, the PDMAA/PAAm St-DN gels showed higher ultimate strength, strain-to-failure, and fracture energy than those of the conventional PAMPS/PAAm DN gels (Fig. 6-13*a*).[347] Similar to DN gels, MR gels showed irreversible energy dissipation in hysteresis measurement, showing permanent fracture of the covalent bonds in the rigid DN microgels.[350] The mesoscale fractures of the DN microgels phase were confirmed by monitoring the morphology change of the embedded DN microgels in MR gels during the real-time stretching process.[348,351] All the results indicated that the high mechanical performance of MR gels rooted in the fracture of the DN microgels during deformation.

The permanent damage of covalently cross-linked DN gels may severely limit their practical use. Fortunately, hybrid cross-linked gels with a combination of non-covalent and covalent cross-linkers were developed, and promise not only excellent mechanical properties but also reversible performance. The alginate/PAAm gels reported by Sun *et al*. exhibited excellent extensibility (beyond 20 times its initial length) and high fracture energy (maximum value of 8,700 J/m^2), but low tensile strength (~160 kPa).[352] When the alginate/PAAm gels were stretched, the PAAm network remained intact and stabilized the deformation, imparting elasticity; while the alginate network broke and dissipated energy by progressively unzipping sacrificial bonds and pulling out chains, imparting toughness. Furthermore, the hydrogels were also extremely notch-insensitive (the notched hydrogel could be pulled up to 17 times its initial length) and recoverable (the work on reloading was recovered to 74% of that of the first loading). The alginate/PAAm gels containing divalent or trivalent ionic bonds showed large hysteresis, indicating remarkable energy dissipation by unzipping the sacrificial bonds. All

those hydrogels exhibited exceptional mechanical performance. In particular, it was found that the alginate/PAAm gels cross-linked by trivalent cations were much stronger than those cross-linked by divalent ones (Fig. 6-13*b*).[353] The hybrid carrageenan/PAAm hydrogel could be stretched more than 20 times its initial length, and its fracture energy reached a high value of ~9,500 J/m^2.[354] Furthermore, the hydrogel could be completely healed upon restoring it in a short time at mild temperature.[354] With reorganization of Fe^{3+}-acrylic acid coordination bonds, the optimal dual cross-linked P(AAm-*co*-AAc) hydrogel was obtained with high tensile strength (~6 MPa), large elongation (~7 times), high toughness (~27 MJ/m^3), and good self-recoverability (~4 h at room temperature to 87.6%, at 3.5 MPa stress and 300% strain).[357]

As the sacrificial hydrogen-bonded clusters were broadly distributed in the P(DMAA-*co*-MAAc) hydrogels, different stresses were required to dissociate those hydrogel-bonded clusters of different sizes and strengths, as indicated by double yield points.[359] The P(DMAA-*co*-MAAc) hydrogels exhibited high stiffness (28 MPa), high strength (2 MPa), high fracture energy (9300 J/m^2) at a strain rate of 0.1 s^{-1}, and complete and fast recovery of strain and mechanical properties (100% recovery in 3 min at 37^{o}C). The excellent mechanical performance of the P(DMAA-*co*-MAAc) hydrogels was attributed to a good balance between the density of covalent crosslinks and strength of hydrogen-bonded clusters mediated by hydrophobic interactions.[359]

Oppositely charged ionic monomers were used to synthesize two kinds of tough physical hydrogels, which have a supramolecular topological structure with strong ionic bonds and weak ones.[297,300] The strong ones play the role of covalent bonds in DN gels. The weak ones had several simultaneous mechanical functions: enhancing the fracture resistance by bond rupture and thereby toughening the materials; improving the shock absorbance by generating high internal friction; reinforcing the fatigue resistance and self-healing by bond buildup. Accordingly, those weak ionic bonds served as reversible sacrificial bonds, providing the physical hydrogels with high toughness and self-recovery ability. One kind of the physical hydrogels is PA hydrogels from one-step random copolymerization of oppositely charged ionic monomers. A representative PA hydrogel is P(MPTC-*co*-NaSS) hydrogel, which had a fracture stress of 1.8 MPa, a strain of 750%, and a tearing energy of 4,000 J/m^2.[300] The obvious yielding in the tensile curves indicated the internal rupture of the weak ionic bonds. Moreover, the P(MPTC-*co*-NaSS) hydrogel could be completely self-recoverable without residual strain and therefore could possess very high fatigue resistance. Another kind of

physical hydrogels is PIC hydrogels from two-step sequential homopolymerization of cationic and anionic monomers. Their mechanical properties were much higher than those of the PA hydrogels. For example, the fracture stress (3.7 MPa) and the tearing energy (8600 J/m^2) of PMPTC/PNaSS PIC hydrogel were much higher than those of P(MPTC-*co*-NaSS) hydrogel, while the strain, the Young's modulus, and the work-to-failure of the PMPTC/PNaSS PIC hydrogel was up to 750%, 5.4 MPa, and 14.8 MJ/m^3, respectively.[297] The mechanical properties of the PMPTC/PNaSS PIC hydrogel were even comparable to those of elastomers. In addition, the yielding, the hysteresis, and the complete self-recovery were shown in the stress-strain curves of the PMPTC/PNaSS PIC hydrogel, which were similar to those of P(MPTC-*co*-NaSS) hydrogel (Fig. 6-13*c*). In addition, the PMPTC/PNaSS PIC hydrogel was so tough that it showed high notch-insensitivity, as shown in Fig. 6-13*d*.

The hydrophobic association hydrogels, especially the anisotropic lamellar hydrogels, are promising robust hydrogels with high mechanical performance. Haque *et al*. reported an anisotropic PDGI/PAAm hydrogel that had a macroscopic single-domain lamellar structure, composed of periodical stacking of several thousands of rigid, hydrophobic bilayers (PDGI) in the ductile and hydrophilic polymer (PAAm) matrix.[301,302,366] Because of the uniaxial orientation of the bilayer, the hydrogel possessed unique functions, such as one-dimensional swelling, anisotropic molecular permeation, anisotropic Young's modulus, and diffusion.[366] The PDGI/PAAm hydrogel also exhibited excellent tensile strength and toughness, self-recovery, and high fatigue resistance. The tensile stress (600 kPa), strain (2200%) and work-to-failure (5 MJ/m^3) of the PDGI/PAAm lamellar hydrogels were much higher than those of the PDGI/PAAm hydrogels without bilayer structure (Fig. 6-13*e*).[301] The unique PDGI bilayer structure, in which the polymer backbone of the PDGI was in random coil conformation while the side chains were physically associated in ordered structures, was responsible for those unique multi-functions. After a stress was loaded in parallel to the bilayer direction, rigid bilayers in the soft PAAm matrix retained the tensile stress and yielded at large stress due to the dissociation of the hydrophobic stacking of PDGI molecules. After the stress was released, the PDGI molecules recovered themselves to the associated state, as schematically shown in Fig. 6-11. The non-covalent hydrophobic associations in the bilayer served as reversible sacrificial bonds to ensure the excellent mechanical performance and self-recovery of the PDGI/PAAm hydrogels. The reversible nature of the sacrificial bonds was confirmed by consecutive hysteresis cycles and reversible structural color change.[301] That PDGI/PAAm hydrogel was superior to the tough DN gel. The latter showed permanent

damage and in which irreversible covalent bonds of brittle polyelectrolyte networks served as sacrificial bonds. By introducing a second network of PAAc into the PAAm layer of the PDGI/PAAm hydrogels to form an interpenetrating soft layer of PAAm-PAAc, Yue *et al.* reported a mechanically robust, lamellar photonic hydrogel (PDGI/PAAm-PAAc gel) with ternary (stress/strain, thermo, and pH) stimuli-responsive behavior.[384] The PDGI/PAAm-PAAc gel had a strain of 1300% and a tensile stress of 600 kPa, which were comparable to those of PDGI/PAAm hydrogels.

With the host-guest complexes as sacrificial bonds, the CB[8]-mediated host-guest hydrogel exhibited remarkable mechanical performance and self-recovery at room temperature.[374] For example, the CB[8]-mediated host-guest hydrogel could hold 500-fold its own weight, could be stretched up to 17-fold its original length and had excellent transparency. The sample with a blunted notch could even be stretched up to 7-fold its original length. In addition, the fracture energy of the CB[8]-mediated host-guest hydrogel was 750 J/m^2, which is a relatively high toughness. Notably, the dynamic dissociation and re-association of the CB[8]-mediated host-guest complexes should be responsible for uniaxial tensile behavior of the CB[8]-mediated host-guest hydrogels with different stretching rates. At high stretching rates (>100 mm/min), the tensile stress, the stain, and the work-to-failure simultaneously decreased because the CB[8]-mediated host-guest complexes did not have enough time to re-associate at the high stretching rates (Fig. 6-13*f*).[374]

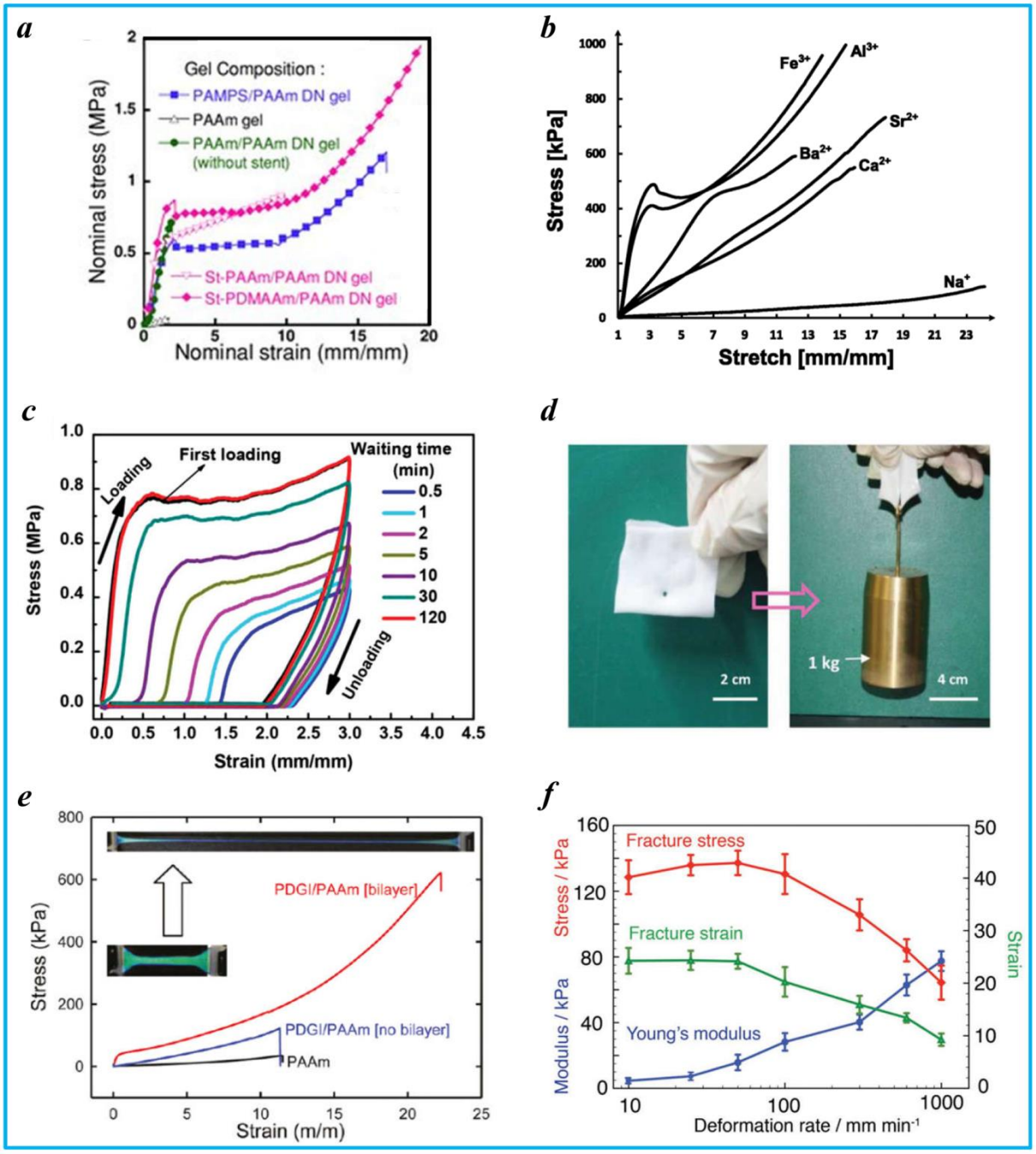

Figure 6-13. Mechanical performance of high strength hydrogels with different sacrificial bonds. (*a*) Stress-strain curves of various DN gels as well as PAAm SN gels. (Adapted with permission from ref. 347. Copyright 2012 WILEY-VCH Verlag GmbH & Co. KGaA, Weinheim.) (*b*) Stress-strain curves of alginate/PAAm gels ionically cross-linked by various metal cations. (Adapted with permission from ref. 353. Copyright 2013 American Chemical Society.) (*c*) Cyclic tensile testing curves of PMPTC/PNaSS PIC gel with different waiting time. (*d*) Notch-insensitive test of PMPTC/PNaSS PIC gel. A hole is made in the hydrogel, using a sharp awl and a 1 kg weight is hung to the gel via the hole. (Adapted with permission

from ref. 297. Copyright Copyright 2015 WILEY-VCH Verlag GmbH & Co. KGaA, Weinheim.) (*e*) Stress-strain curves of PAAm gel and PDGI/PAAm gel with and without a lamellar bilayer structure. The inserted images show the color change of the PDGI/PAAm gel with a bilayer structure. (Adapted with permission from ref. 301. Copyright 2011 American Chemical Society.) (*f*) Fracture stress, fracture strain, and Young‘s modulus as a function of deformation rate. (Adapted with permission from ref. 374. Copyright 2017 WILEY-VCH Verlag GmbH & Co. KGaA, Weinheim.)

3.3 Incorporation of Sacrificial Bonds into Elastomers

Elastomers are widely used as engineering materials in industrial applications because of their unique high elasticity and reversible deformability. However, the poor mechanical performance of most neat elastomers limits their use. Therefore, in practice, elastomers are commonly combined with nanofillers to form composites. Physical incorporation of nanofillers into elastomers significantly improves the mechanical performance of elastomers. However, compounding rubber with nanofillers faces several challenges including nanofiller dispersion/aggregation, interfacial adhesion control, and processability. Recently, remarkable progresses have been made in engineering sacrificial bonds into elastomers, aiming at significantly improving strength and toughness.

3.3.1 Design Methodology of Sacrificial Bonds in Elastomers

Although sacrificial strategy has been established to toughen network materials, it is not trivial to apply this concept to the non-hydrated elastomers. The first challenge is to form an interpenetrating double-network or dual-crosslinked structure, as elastomers are lacking of polyelectrolyte forms.[291] Another challenge is that elastomers usually have high molecular weight and are normally processed via mechanical kneading (shearing). In such case, it is difficult to form double network elastomers.

Inspired by design principle of DN gels, Ducrot *et al*. designed and prepared tough elastomers with a triple-network (TN), in which the first network plays a role of sacrificial bonds. To obtain an isotropically stretched first network, the first network was swollen with monomers of the second network.[385] The latter were fully polymerized, resulting in a DN elastomer of which the first network was pre-stretched. To further stretch the first network chains, the DN elastomer repeated the swelling-polymerization process, resulting in a TN elastomer. The first

network chains only had a several percent share and were highly stretched in the TN elastomer, whereas the second network chains were slightly stretched, and the third network chains were entangled and slightly cross-linked. Note that in the second and third polymerization steps, the occurrence of chain transfer reactions led to loose connections of the networks with each other, thus affecting stress transfer between the networks.

Reversibility of non-covalent bonds can endow polymeric materials with self-healing capability. As strong non-covalent bonds, metal-ligand coordination bonds were incorporated into polymeric materials to develop self-healing materials.[386-389] Typically, Li *et al*. reported a self-healing elastomer network of PDMS chains cross-linked by distinct metal-ligand coordination complexes.[390] In the coordination complexes, PDCA ligands containing a strong binding site adjacent to two weak binding sites in a single ligand could coordinate to Fe^{3+} cores through three different coordination bonds: a strong iron-pyridyl one (Fe-$N_{pyridyl}$, 145.0 kcal/mol), and two weak iron-carboxamido ones (Fe-N_{amido}, 82.7 kcal/mol; Fe-O_{amido}, 40.7 kcal/mol).[390] The iron-ligand coordination bonds could readily break to dissipate energy during stretching and re-build up to ensure self-healing capacity of the material. Additionally, the Fe^{3+} ions were still attached to the ligands by the stronger interactions to allow for a rapid bond re-buildup. First, the PDCA ligands were introduced into a linear PDMS backbone, and subsequently coordinated to Fe^{3+} ions, resulting in an elastomer network with coordination complexes denoted as Fe-HPDCA-PDMS. The PDMS chains were folded by the intra-chain iron-HPDCA coordination complexes and cross-linked by the inter-chain iron-HPDCA coordination complexes. Zhang *et al.* reported a facile way to incorporate Fe^{3+}-O coordination bonds into an ENR-50 networks (Fig. 6-14*a*).[391] The Fe^{3+}-O coordination bonds were first formed in ENR-50/$FeCl_3$ master batch by mixing ENR-50 and $FeCl_3$•$6H_2O$ in an excess of chloroform. Next, the master batch, ENR-50 and ZDA, were kneaded and hot-pressed to prepare ENR-50/ZDA/$FeCl_3$ samples. Inspired by the sacrificial bond concept in biological materials, Tang *et al*. designed a high-performance and macroscopically responsive diene-rubber by incorporating sacrificial metal-ligand coordination bonds into a chemically cross-linked VPR network.[183] VPR is a commercially available elastomer with pendent pyridine groups in the chains. The pyridine groups can provide lone pair electrons to metal ions to form metal-ligand coordination bonds. Thus, metal-ligand coordination bonds were introduced into the chemically cross-linked VPR network by adding metal salts during the preparation of VPR. The elastomeric architecture of the resulting VPR was held together by dual-crosslinking bonds of permanent covalent bonds

and dynamic metal-ligand coordination bonds. In practical applications, neat elastomers must be reinforced by nanofillers and used as nanocomposites. In elastomer nanocomposites, interfacial interactions between fillers and elastomer have a critical effect on the filler dispersion, stress transfer, and chain orientation. Huang *et al*. developed sacrificial metal-ligand coordination bonding interfaces in graphene/VPR nanocomposites.[392] The formation of metal-ligand bridges needed the introduction of ligands onto graphene surfaces. Tea polyphenols were used to introduce catechol groups into graphene surfaces. Thus, the pyridine-Zn^{2+}-catechol coordination bonds were constructed at the interface between VPR and modified graphene. The strategy of metal-ligand coordination bonds is applicable to other functionalized polymers, such as epoxidized polymers and hydroxylated ones.

As reversible sacrificial bonds, multiple hydrogen bonds are incorporated into biomimetic and hydrogel materials. Recently, it is found that the incorporation of sacrificial hydrogen bonds into elastomers can enhance the mechanical performance of the elastomers. Kushner *et al*. developed a biomimetic design of a reversibly unfolding modular cross-linker that could enhance mechanical performance of elastomers (Fig. 6-14*b*).[393] The modular cross-linker was based on the quadruple hydrogen bonding UPy moieties that served as a sacrificial bonding module in linear polymers.[321] The results showed that the rubber containing the UPy-based cyclic modular cross-linker exhibited significant improvement in mechanical performance (Fig. 6-14*b*). The UPy moieties were also incorporated into a polyurethane elastomer as physical cross-linkers.[394] The dimerization of the UPy moieties could form intra-chain loops and inter-chain cross-links. The disassociation of the UPy moieties could remarkably dissipate strain energy, thus leading to robust mechanical performance of the elastomer. Recent works showed that amide and urazole groups (hydrogen bonding moieties) could be incorporated into covalently cross-linked rubber networks to create dynamic sacrificial bonds, and thus improving the overall mechanical properties.[178,395] Huang *et al*. engineered sacrificial hydrogen bonds into a pre-crosslinked SSBR via subsequent triazolinedione (TAD) click chemistry.[396] This strategy eliminated the influence of the sacrificial bonds on the covalent network and allowed pendant urazole groups in the TAD modified SSBR distributed heterogeneously, leading to the formation of separated micro-phases involving hydrogen bond clusters. In previous studies, only one type of sacrificial bond was incorporated into elastomeric architectures for improving the mechanical performance and obtaining the functionalities. Recently, concepts of multi-networks were developed, in which two different types of sacrificial bonds were incorporated into

elastomeric architectures. Liu *et al*. engineered sacrificial hydrogen bonds and metal-ligand coordination bonds into a chemical cross-linked IR network.[397] Maleic anhydride (MAn) was first grafted onto IR chains to form reaction sites with 3-amino-1,2,4-triazole (ATA). The addition reaction of the MAn and the ATA resulted in amide triazole-carboxylic acid groups that are capable of forming metal-ligand coordination bonds with Zn^{2+} ions as well as multiple hydrogen bonds with each other. Because of different binding energies, the hydrogen bonds ruptured prior to the metal-ligand coordination bonds. Chen *et al*. developed elastomer composites by constructing sacrificial bonds and hidden lengths at the interfaces of GN/PU composites.[398] The PU oligomer chains were non-covalently bonded to the GN surface through the π-π interaction between pyrene derivatives and GNs, while part of the PU oligomer chains were covalently bonded to the GN surface through the reaction of residual hydroxyl and epoxide groups on GNs with isocyanate groups. Meanwhile, hydrogen bonding clusters were formed between the oligomer and adjacent PU chains (Fig. 6-14*c*). It was shown that the π-π interaction and hydrogen bonds served as sacrificial bonds in GN/PU composites while hidden lengths were formed in hydrogen bonding clusters. The covalent linkage of oligomer chains to GN surface not only improved the GN dispersion and load transfer efficiency, but also ensured the formation of hidden lengths in GN/PU composites.

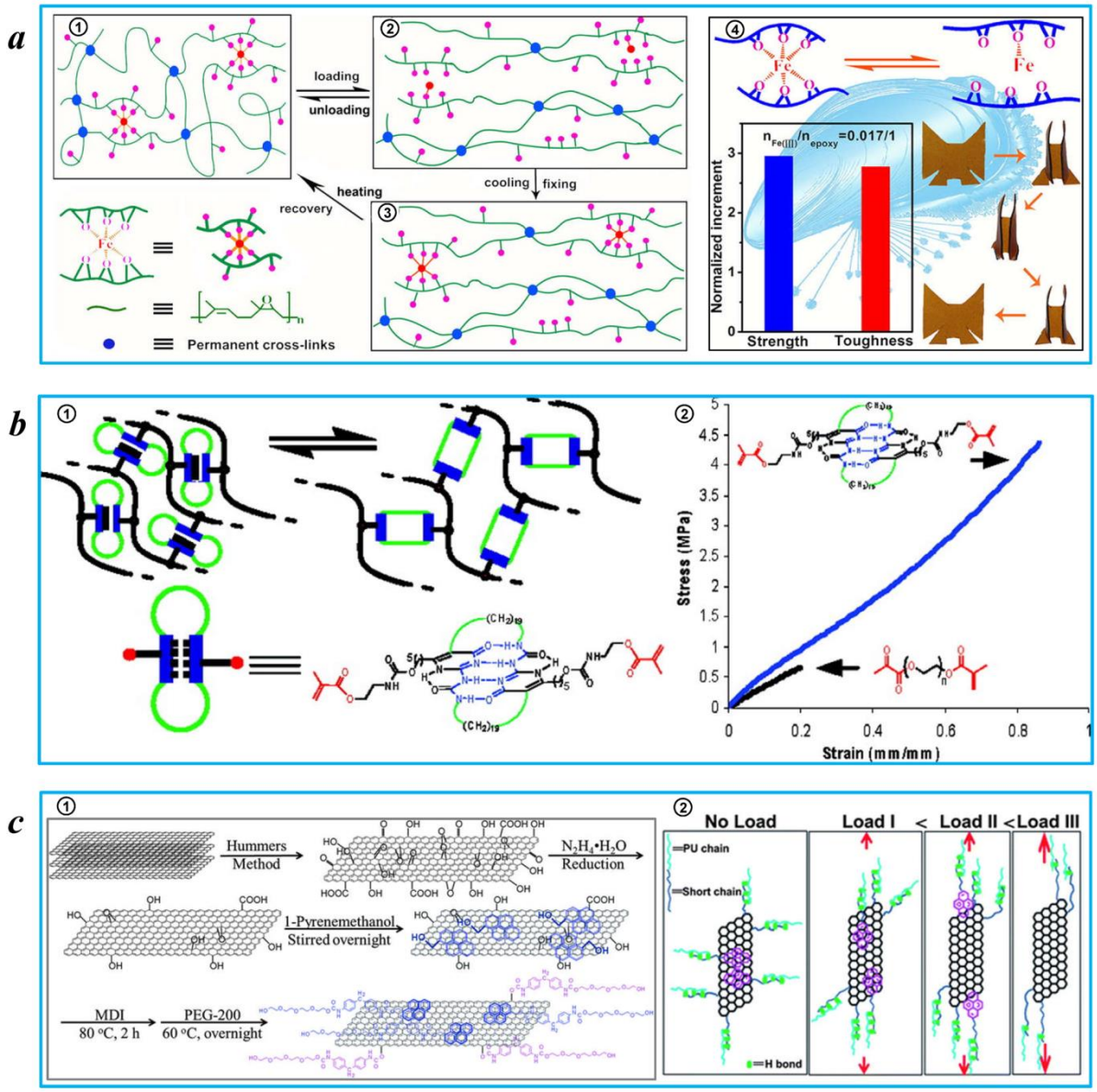

Figure 6-14. Schematic illustration of various sacrificial non-covalent bonds in elastomers. (*a*) ENR-50 networks with combination of permanent cross-links and Fe^{3+}-O coordination bonds (①②③). ENR-50 sample exhibits improved strength and toughness simultaneously as well as excellent triple shape memory performance (④). (Adapted with permission from ref. 391. Copyright 2016 American Chemical Society.) (*b*) Concept of biomimetic design of reversibly modular cross-linker (①) for enhancing network mechanical properties(②). (Adapted with permission from ref. 393. Copyright 2007 American Chemical Society.) (*c*) Synthesis route for covalently and non-covalently functionalized GNs (①). Toughening mechanism involving rupture of sacrificial bonds and release of hidden lengths in tensile test of GN/PU composites

(②). (Adapted with permission from ref. 398. Copyright 2012 The Royal Society of Chemistry.)

3.3.2 Mechanical Properties of Crosslinked Elastomers Incorporating Sacrificial Bonds

DN concept has been successfully applied to TN elastomers for reinforcement in stiffness and toughness. Alkyl acrylates were the first monomers to prepare the TN elastomers. Typically, EA was used to prepare the first network while MA was used in subsequent steps to prepare the second and third networks, resulting in EA_1MA DN elastomer and EA_1MAMA TN elastomer, respectively.[385] The Young's modulus (4.2 MPa) and the ultimate stress (29 MPa) of the EA_1MAMA TN elastomer were 2.8 times and 58 times higher those of EA_1 SN elastomer, respectively (Fig. 6-15*a*). In addition, the fracture toughness of the TN elastomer was 40-100 times that of the SN elastomer (Fig. 6-15*a*). Similar to the toughening mechanism of the DN hydrogels, the stretched covalent bonds in the first network served as sacrificial bonds to impart stiffness and toughness to the elastomers. Note that the combined mechanical performance of the TN elastomer is comparable to that of the natural rubber, which is due to strain-induced crystallization. However, it is hard to produce strain-induced crystallization in other elastomers. Thus, the TN elastomer is a new strategy to prepare strong elastomers.

Fe-HPDCA-PDMS elastomer was precisely designed and showed high stretchability, good mechanical strength, and autonomous self-healing, which was due to the re-buildup of the iron-HPDCA coordination bonds.[390] A maximum fracture strain of 4500% and an Young's modulus of 0.54 MPa were obtained. Pronounced hysteresis was observed in cyclic tensile tests, indicating the energy dissipation from iron-HPDCA coordination bond breakage. The breakage of those iron-HPDCA coordination bonds during stretching led to the unfolding and sliding of the polymer chains, thus toughening the elastomer. The fracture energy of the Fe-HPDCA-PDMS elastomer reached up to 2.6 kJ/m^2. Moreover, the Fe-HPDCA-PDMS elastomer was capable of excellent self-healing (Fig. 6-15*b*). For example, after two cut pieces were healed at room temperature for 48 hours, a fracture strain of 1700% and a healing ratio of 90% were obtained. The Fe-HPDCA-PDMS elastomer was even allowed self-healing at -20^oC with a healing ration of 68% after three days.[390] Single-molecule force spectroscopy was used to characterize those coordination bonds. Typical saw-tooth force-extension patterns of Fe-HPDCA-PDMS showed that the iron-HPDCA coordination bonds played the role of sacrificial bonds. With incorporation of the Fe^{3+}-O coordination bonds, the ENR-50/ZDA/$FeCl_3$ samples exhibited improved strength and toughness. For example, when

3 *phr* (parts per 100 parts of rubber) of $FeCl_3$ was incorporated, both the tensile strength and the fracture toughness of the resulting ENR-50/ZDA/$FeCl_3$ sample increased by about three-fold compared with those of the control ENR-50. Noticeably, the Fe^{3+}-O coordination bonds endowed the ENR-50 with new properties, such as highly damping and excellent triple shape memory performance (Fig. 6-14*a*).[391] With the incorporation of metal-ligand coordination bonds, the mechanical performance of the VPR samples was remarkably improved and could be conveniently tuned by varying the structural parameters of the covalently cross-linked network and the metal-ligand coordination bonds.[183] Significant hysteresis and full recovery in cyclic tensile tests confirmed that the metal-ligand coordination bonds played a role of sacrificial bonds by reversible breakup and buildup. The sacrificial metal-ligand coordination bonds preferentially ruptured prior to the covalent bonds under external load, leading to energy dissipation and chain orientation. With increasing metal-ligand coordination bonds, the Young‘s modulus, the tensile stress, and the work-to-failure of VPR samples increased from 4.9 MPa, 3.5 MPa, and 6.3 MJ/m^3 to 19.8 MPa, 27.8 MPa, and 38.7 MJ/m^3, respectively (Fig. 6-15*c*). In addition, the dynamic metal-ligand coordination bonds could endow the VPR with a thermally triggered shape memory behavior (Fig. 6-15*c*). The strong pyridine-Zn^{2+}-catechol coordination bonds in the VPR/graphene nanocomposites not only ensured uniform graphene dispersion and efficient stress transfer from the VPR to graphene, but also served as sacrificial bonds to dissipate additional energy and facilitate chain orientation.[392] As a result, the VPR/graphene nanocomposites exhibited both high strength and high toughness. A more recent study showed that sacrificial metal-ligand coordination bonds effectively promoted strain-induced crystallization of synthetic *cis*-1, 4-polyisoprene.[399] It is known that the fantastic mechanical performance of natural rubber is due to strain-induced crystallization. Incorporation of the sacrificial metal-ligand coordination bonds provided a new approach to mimic natural rubber to obtain crystallizable synthetic elastomers with high mechanical performance.

A polyurethane elastomer with UPy moieties exhibited robust mechanical performance with Young‘s modulus of 2 MPa, ultimate stress of 29 MPa, and strain of 900%, due to the disassociation of the UPy moieties.[394] The TAD modified SSBR exhibited promising triple-shape memory behavior as well as improved strength and toughness, due to the dynamic feature of sacrificial hydrogen bonds.[396] For example, the TAD modified SSBR showed high shape fixity (99%) at 25°C and high shape recovery ratio (94%) at 90°C (Fig. 6-15*d*). Notably, the combination of two types of sacrificial bonds with different binding

energies maximized the effect of sacrificial bonds on mechanical performance. The sacrificial hydrogen bonds and Zn^{2+}-ligand coordination bonds were incorporated into covalently cross-linked IR network to obtain a high-performance elastomer.[397] The preferential rupture and dynamic nature of the sacrificial bonds prevented the local stress concentration and facilitated the chain orientation, thus improving tensile modulus and fracture toughness. In addition, the excellent flex-cracking resistance of filled IR multi-network was also attributed to the energy dissipation of dynamic sacrificial bonds.[397] Under loading, both rupture of the sacrificial bonds and release of the hidden lengths endowed the GN/PU composites with high toughness and ductility nearly identical to those of the neat PU elastomer (strain at break > 900%). Compared with the neat PU, the GN/PU with 1wt.% GN content exhibited higher mechanical performance with an ultimate stress of 27.6 MPa, a tensile modulus of 18.7 MPa, and a fracture toughness of 130 $MP•m^{1/2}$, corresponding to 36, 122.6, and 36.8% increase, respectively.[398] The increase of the tensile modulus and the ultimate stress could be attributed to the reinforcing effect of GN, while the increase of the fracture toughness should be attributed to specific sacrificial bonds in the interface of GN/PU composite. The toughening mechanism is illustrated in Fig. 6-14*c*.

Single-molecule force spectroscopy by AFM has been used to study sacrificial bonds at the molecular scale.[390] Recently, a method was developed to directly observe the breakage of sacrificial bonds *in situ* by crosslinking the first network with chemoluminescent cross-linkers, which emitted light when they broke.[285,400] Figure 6-15*a* shows the image of the luminescence around the crack tip for SN, DN and TN elastomers. For the SN elastomer, the bond breakage was localized at the crack tip and it was difficult to observe the light emission. In the case of the DN elastomer, the bond breakage was still localized at the crack tip but the light emission was intense. As for the TN elastomer, the bond breakage extended over a large region inside the elastomer due to the preferred rupture of the first network and the light emission was more intense than that of the DN elastomer.[285] In addition, mechanophore spiropyran was also incorporated into polyurethane elastomer with sacrificial hydrogen bonds.[394] The spiropyran was used as a molecular probe to study the stress mapping and rupture of sacrificial bonds. However, it is still a challenge to study the sacrificial bonds *in situ* at molecular scale.

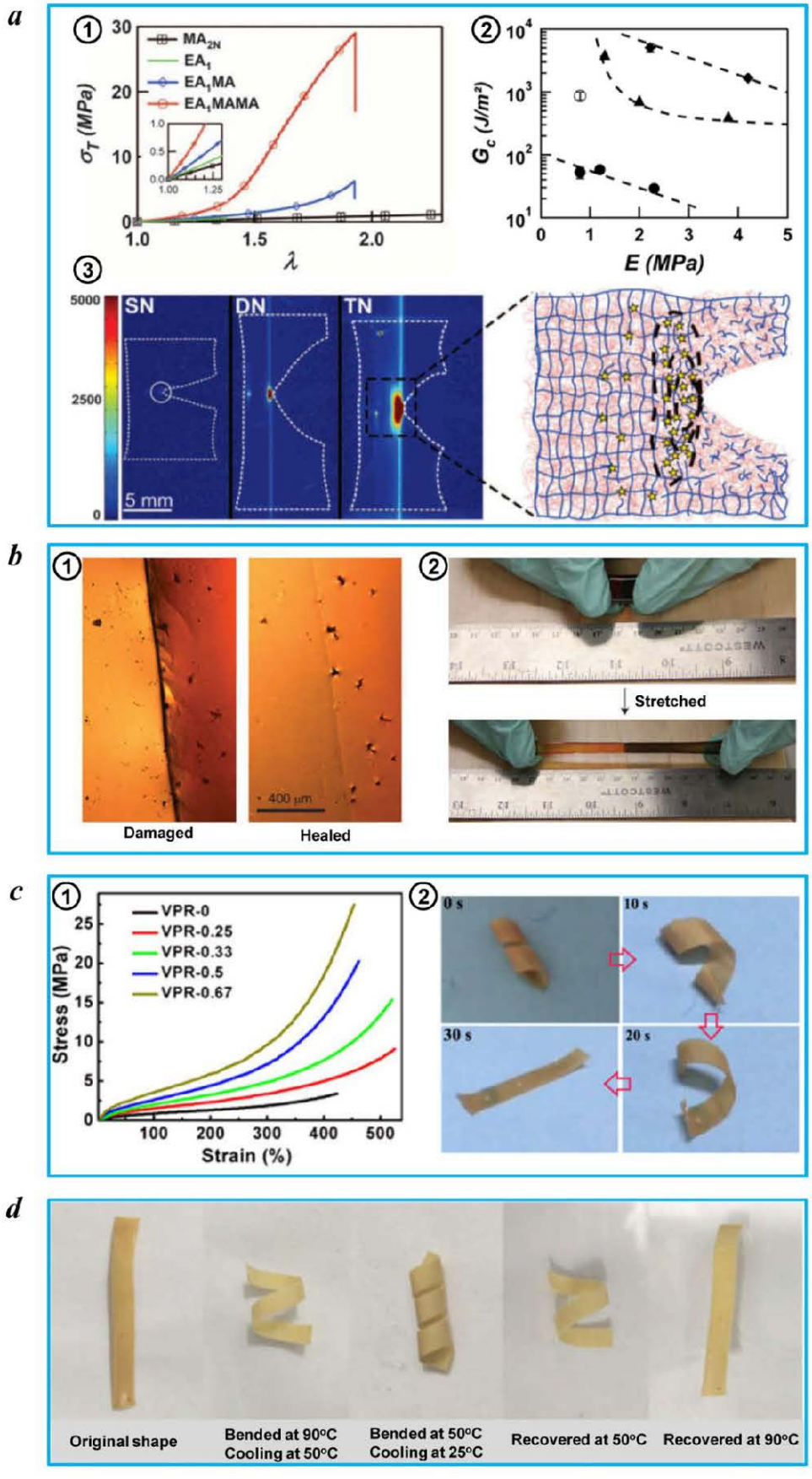
a
MA2N
EA1
EA1MA
EA1MAMA
σT (MPa)
λ
Gc (J/m²)
E (MPa)
SN
DN
TN
5 mm
b
Damaged
Healed
400 μm
Stretched
c
VPR-0
VPR-0.25
VPR-0.33
VPR-0.5
VPR-0.67
Stress (MPa)
Strain (%)
0 s
10 s
20 s
30 s
d
Original shape
Bended at 90°C
Cooling at 50°C
Bended at 50°C
Cooling at 25°C
Recovered at 50°C
Recovered at 90°C

Figure 6-15. Effect of sacrificial bonds on the performance of elastomers. (*a*) Mechanical properties of multi-network elastomers (①); fracture toughness of multi-network elastomers versus initial modulus for SN (solid circles), DN (triangles), and TN (diamonds) elastomers (②); intensity-colorized images of propagating cracks on notched samples containing chemoluminescent cross-linker in the first network and schematic for rupturing mechanism of sacrificial bonds in the crack tip for the DN and TN elastomer, the first network is represented in blue, and the second and the third network are in red (③). (Adapted with permission from ref. 285. Copyright 2014 American Association for the Advancement of Science.) (*b*) Optical microscope photos for damaged and healed samples (①) and optical photos for healed sample before and after stretching (②). (Adapted with permission from ref. 390. Copyright 2016 Nature Publishing Group.) (*c*) Typical tensile curves of VPR with various contents of sacrificial bonds (①) and optical photos displaying the shape recovery process of VPR sample (②). (Adapted with permission from ref. 183. Copyright 2016 American Chemical Society.) (*d*) Optical photos displaying the triple shape recovery process of SSBR with sacrificial bonds in water. (Adapted with permission from ref. 396. Copyright 2016 American Chemical Society.)

4. Concluding Remarks

Sacrificial bonds have been widely accepted as one of structural origins for the unique combination of high strength and high toughness for biological materials. The fracture process of sacrificial bonds and the subsequent release of hidden lengths have been revealed. Inspired by the sacrificial bonding structures in biological materials, scientists have engineered various non-covalent bonds as well as covalent ones as sacrificial bonds into artificial polymeric materials such as hydrogels and elastomers, resulting in significant improvements in strength and fracture toughness. Considering the large interfacial area (volume) of nanocomposites, the formation of sacrificial bonds at interface may greatly change the structure and performance of the nanocomposites, which will open a new avenue for high-performance polymeric nanocomposites. Except for the significantly improved mechanical properties, it has been demonstrated that the elastomers with sacrificial bonds can be used as highly damping materials. However, the dissociation temperature of most sacrificial bonds is still not sufficiently high (typically lower than 100^{o}C).

Concerning the mechanisms of sacrificial bonding, although many studies have been done, they remain unclear. The current understanding by single-molecule force spectroscopy is that the preferential rupture of the sacrificial bonds and the subsequent release of hidden lengths can dissipate a huge amount of mechanical energy to toughen materials. It is important to note that orientation of polymer chains is crucial for elastomer reinforcement. Therefore, we believe that the rupture of the sacrificial bonds can prevent the local stress concentration during stretching, thus facilitating the molecular chain orientation; during the orientation process, the dynamic sacrificial bonds can rebuild up from breaking. With further stretching, those re-buildup sacrificial bonds will break again, thus dissipating energy and further facilitating the molecular chain orientation consistently. It should be emphasized that the studies by single-molecule force spectroscopy have not given molecular evidence on the sacrificial bonding mechanism. The chemical monitoring *in situ* on the sacrificial bonds is developing. Although the introduced chromophores can be used to effectively monitor and demonstrate the rupture of weak bonds, the chemical design of polymers with chromophores is rather complicated. Therefore, it is very important to further develop chemical monitoring *in situ* during stretching for better understanding the sacrificial bonding mechanism. Although the constitutive laws can be used to calculate dynamic sacrificial bond content during stretching, molecular simulation is still lacking. We believe that molecular simulation is an alternative powerful method in raveling the sacrificial bonding mechanism. The authors

believe that future artificial polymeric materials with sacrificial bonds will be advanced by: (1) Mechanism studies: Exploring the molecular mechanism of sacrificial bonds by molecular simulation, and in-depth understanding the dynamic viscoelastic behavior of elastomers with sacrificial bonds; (2) Design and preparation: Exploring sacrificial bonds with higher dissociation temperatures for engineering applications, constructing interfacial sacrificial bonds in polymeric nanocomposites, designing biomimetic hierarchical structures by combining sacrificial strategy and material manufacturing techniques (such as layer-by-layer self-assembly).

Acknowledgement

The authors gratefully acknowledge financial support from the National 973 Basic Research Program of China (2015CB654700), National Natural Science Foundation of China (50933001, 51503010 and 51673065), the Major International Cooperation (51320105012) of the National Nature Science Foundation of China, and the China-France Cooperation Program of PHC CAI YUANPEI (CHINA SCHOLARSHIP COUNCIL, No. 201504490120).

Chapter 7 Conclusions and perspectives

7.1 Conclusions

This thesis focused on the preparation, properties and applications of itaconate based elastomers and their nanocomposites. Form the above investigations, the following conclusions can be drawn:

(1) 3,9-Bis[1,1-dim ethyl-2-{b-(3-tertbutyl-4-hydroxy-5-methylphenyl)propionyloxy}ethyl]-2,4,8,10-tetraoxaspiro-[5,5]-undecane, a rigid hindered phenol known as AO-80, was filled into poly(diisoamyl itaconate-co-isoprene) (PDII) elastomer to prepare a itaconate based elastomeric nanocomposite (or hybrid) by melt blending technique. The AO-80 was dissolved in the PDII matrix at the molecular level and formed strong hydeogen bonds with the PDII. Destruction and reconstruction of the hydrogen bonds could dissipate much mechanical energy under a dynamic load, indicating a good damping performance. The itaconate based elastomers show a great potential in damping appilications.

(2) Carboxylic groups were introduced into itaconate based elastomer to produce an itaconate based carboxylic elastomer poly(dibutyl itaconate-co-isoprene-co-methacrylic acid) (PDIM) by radical emulsion polymerization, aiming to exploring the feasibility of itaconate based elastomers as tire tread materials. The number-average molecular weight of the PDIM was higher than 250 000 g/mol, and its glass transition temperature was lower than -30^{o}C. The incorporation of the carboxylic groups improved the mechanical properties of the PDIM and the interfacial interaction between PDIM and silica. However, the investigation on the mechanical and dynamic properties indicated that the PDIM/silica nanocomposites would not be suitable for green tire tread materials.

(3) Inspired by the sacrificial bonding mechanism in biological materials, PDIM/halloysite nanotubes (HNTs) nanocomposites with strong hydrogen bonds at the interfaces were prepared by co-coagulation of PDIM latex and HNTs aqueous suspension, followed by mechanical blending with rubber additives. With the incorporation of the HNTs into the PDIM, the tensile modulus, tensile strength, and fracture energy of the PDIM/HNTs

nanocomposites were simultaneously improved without sacrificing the extensibility. A mechanism responsible for improvement in mechanical properties was composed of four steps: (1) alignment of the PDIM chains oriented the HNTs along the loading direction during the uniaxial stretching; (2) dissociation of the hydrogen bonds dissipated energy in a sacrificial bonding manner; (3) Coils (hidden lengthes) of the PDIM from the applied force by the hydrogen bonds were stretched to sustain a large deformation and dissipated energy; (4) finally, the HNTs were pulled out from or ruptured at the tensile fracture surface of the PDIM/HNTs nanocomposites.

(4) Considering the super low rolling resistance of polybutadiene-based tires, butadiene was used instead of isoprene to copolymerize with dibutyl itaconate to produce poly(dibutyl itaconate-co-butadiene) (PDIB) by redox-initiated emulsion polymerization. The resultant copolymers had predominately *trans*- and *vinyl*-polybutadiene in their chains, a molecular weight from 236 000 to 392 000 g/mol, and a glass transition temperature from -42 to -72^{o}C, depending on the feed weight percentage of butadiene. The reactivity ratios of dibutyl itaconate and butadiene determined by the classical Fineman-Ross method and Kelen-Tüdös one indicated a non-ideal copolymerization behavior with an azeotropic point at 0.383. The monomer sequence distribution indicated that butadiene could undergo self-propagation to form long soft segments while dibutyl itaconate preferred to form short sequences with isolated, diad or triad moieties. The mechanical properties of the unfilled PDIB could match or even surpass those of traditional synthetic rubbers. The stress and the elongation at break of unfilled PDIB40 were over 2 MPa and 600%, respectively, indicating that PDIB elastomers might be good candidates for replacement of traditional synthetic rubbers based on petrochemical resources.

(5) PDIB/silica nanocomposites were prepared according to traditional rubber processing. The silica was uniformly dispersed in the PDIB matrix. The mechanical properties of the PDIB/silica nanocomposites were comparable with those of conventional rubber/silica nanocomposites. Dynamic properties of PDIB/silica nanocomposites, especially loss tangents (tan δ) at 60 and 0^{o}C, were investigated. The values of the tan δ at 60°C for filled elastomeric materials and the rolling resistance coefficients of tires are laboratory and industrial benchmarks for fuel consumption, respectively. Likewise, the value of the tan δ at 0^{o}C for filled elastomeric materials corresponds to the wet grip resistance coefficient of tires. Based on the mechanical and dynamic properties of the PDIB/silica nanocomposites, a high-performance tire was manufactured and tested on a MTS tire rolling resistance measurement system. The rolling resistance coefficient was 7.7 kg/ton and rated as a class

–B" according to the EU Tire Labelling Regulation 1222/2009. This investigation showed manufacturing green tires from itaconate based elastomers would be a good strategy for sustainable development.

(6) A review focusing on the design and mechanisms of sacrificial bonds into polymeric materials was given in the last part of the thesis. It emphasized on the mechanisms, design methods, and applications of sacrificial bonds in bulk polymers. This field is very important for breaking the bottlenecks for mechanical properties and extending the applications of polymeric materials. We envision that this review may advance the real applications of sacrificial bonds strategies in polymeric materials.

7.2 Perspectives

Despite the progresses in itaconate based elastomers made in this thesis, much remains to be done and some perspectives are given below:

(1) The performances of itaconate based elastomers are comparable with those of conventional synthetic rubbers. It would be interesting to further develop itaconate based elastomers for other engineering applications for seal and insulation for example.

(2) The itaconate based elastomers were synthesized by a laboratory-scale emulsion polymerization process. The next step would be to scale up the process to a pilote and an indusrrial scale.

(3) The itaconate based elastomers bear numerous ester groups. Their chemical structure is similar to that of acrylate rubbers, while their mechanical properties are superior to those of the latter. Therefore, it would be interesting to explore the possibility of substituteing itaconate based elastomers for acrylate rubbers in oil-resistant applications. Itaconate based elastomers with high diene content could be used in cold environments. However, the excess of unsaturated double bonds would go against oil-resistance and ageing resistance. This problem could be solved by the mature hydrogenation technology.

(4) Sacrificial bonding mechanisms are responsible for the super mechanical performances of biological materials. One important scientific spotlight is to engineer sacrificial bonds into itaconate based elastomers for high mechanical and functional performances. Itaconate based elastomers incorporated with sacrificial bonds may be used as seismic materials because the breakdown of the sacrificial bonds can dissipate a huge amount of energy.

References

[1] Clark J H. Green chemistry for the second generation biorefinery-sustainable chemical manufacturing based on biomass. J. Chem. Technol. Biot., 2007, 82(7): 603-609.

[2] Hatti-Kaul R, Törnvall U, Gustafsson L, Börjesson P. Industrial biotechnology for the production of bio-based chemicals-a cradle-to-grave perspective. Trends Biotechnol., 2007, 25(3): 119-124.

[3] de Jong E, Higson A, Walsh P, Wellisch M. Bio-based chemicals value added products from biorefineries. IEA Bioenergy, Task42 Biorefinery. 2012.

[4] Kajaste R. Chemicals from biomass–managing greenhouse gas emissions in biorefinery production chains–a review. J. Clean. Prod., 2014, 75: 1-10.

[5] Sanders J P, Clark J H, Harmsen G J, Heeres H J, Heijnen J J, Kersten S R, van Swaaij W P, Moulijn J A. Process intensification in the future production of base chemicals from biomass. Chem. Eng. Process., 2012, 51: 117-136.

[6] Fiorentino G, Ripa M, Ulgiati S. Chemicals from biomass: technological versus environmental feasibility. A review. Biofuel. Bioprod. Bior., 2016, 11 (1): 195-214.

[7] Gallezot P. Conversion of biomass to selected chemical products. Chem. Soc. Rev., 2012, 41(4): 1538-1558.

[8] Straathof A J. Transformation of biomass into commodity chemicals using enzymes or cells. Chem. Rev., 2014, 114 (3): 1871-1908.

[9] Besson M, Gallezot P, Pinel C. Conversion of biomass into chemicals over metal catalysts. Chem. Rev., 2014, 114(3): 1827-1870.

[10] Werpy T, Petersen G, Aden A, Bozell J, Holladay J, White J, Manheim A, Eliot D, Lasure L, Jones S. Top value added chemicals from biomass. Volume 1-Results of screening for potential candidates from sugars and synthesis gas. Department of Energy Washington DC, 2004 Aug.

[11] Bozell J J, Petersen G R. Technology development for the production of biobased products from biorefinery carbohydrates-the US Department of Energy‘s “Top 10” revisited. Green Chem., 2010, 12(4): 539-554.

[12] Baup S. Ueber eine neue pyrogen-citronensäure, und über benennung der pyrogen-Säuren überhaupt. Eur. J. Org. Chem., 1836, 19(1): 29-38.

[13] Kinoshita K. Über eine neue Aspergillus Art, A. itaconicus. Bot. Mag. Tokyo., 1931, 45:45-50.

[14] Willke T, Vorlop K D. Biotechnological production of itaconic acid. Appl. Microbiol. Biot., 2001, 56(3): 289-295.

[15] Okabe M, Lies D, Kanamasa S, Park E Y. Biotechnological production of itaconic acid and its biosynthesis in Aspergillus terreus. Appl. Microbiol. Biot., 2009, 84(4): 597-606.

[16] Klement T, Büchs J. Itaconic acid-a biotechnological process in change. Bioresource Technol., 2013, 135:422-431.

[17] Global Industry Analysts Inc., 2011. Global itaconic acid market to reach US$398.3 million by 2017, according to a report by Global Industry Analysts, Inc. In: PRweb <http://www.prweb.com/releases/itaconic_acid/ renewable_chemicals/prweb8831422.htm> (accessed 25.10.2017).

[18] Hasunuma T, Kondo A. Development of yeast cell factories for consolidated bioprocessing of lignocellulose to bioethanol through cell surface engineering. Biotechnology Adv., 2012, 30(6): 1207-1218.

[19] Wisselink H W, Toirkens M J, Wu Q, Pronk J T, van Maris A J. Novel evolutionary engineering approach for accelerated utilization of glucose, xylose, and arabinose mixtures by engineered Saccharomyces cerevisiae strains. Appl. Environ. Microb., 2009, 75(4): 907-914.

[20] Munasinghe P C, Khanal S K. Biomass-derived syngas fermentation into biofuels: opportunities and challenges. Bioresource Technol., 2010, 101(13): 5013-5022.

[21] Abubackar H N, Veiga M C, Kennes C. Biological conversion of carbon monoxide: rich syngas or waste gases to bioethanol. Biofuel. Bioprod. Bior., 2011, 5(1): 93-114.

[22] Atsumi S, Hanai T, Liao J C. Non-fermentative pathways for synthesis of branched-chain higher alcohols as biofuels. Nature. 2008, 451(7174): 86-89.

[23] Shen C R, Liao J C. Metabolic engineering of Escherichia coli for 1-butanol and 1-propanol production via the keto-acid pathways. Metab. Eng., 2008, 10(6): 312-320.

[24] Jain R, Yan Y. Dehydratase mediated 1-propanol production in metabolically engineered Escherichia coli. Microb. Cell Fact., 2011, 10(1): 97.

[25] Jones D T, Woods D R. Acetone-butanol fermentation revisited. Microbiol. Rev., 1986, 50(4): 484-524.

[26] Berezina O V, Zakharova N V, Yarotsky C V, Zverlov V V. Microbial producers of butanol. Appl. Biochem. Microbiol., 2012, 48(7): 625-638.

[27] Donaldson G K, Eliot A C, Huang L L, Nagarajan V, Nakamura, C E. Pat. Appl. WO2007130518, November 15, 2007.

[28] Donaldson G K, Eliot A C, Maggio-Hall L A, Nagarajan V, Nakamura C E, Tomb J F. Pat. Appl. WO2009134376, November 5, 2009.

[29] Smith K M, Liao J C. An evolutionary strategy for isobutanol production strain development in Escherichia coli. Metab. Eng., 2011, 13(6): 674-681.

[30] Bandres M, Thiebaud-Roux S, Borredon M E. Green syntheses of biobased solvents. C. R. Chim., 2011, 14: 636-646.

[31] Piang-Siong W, de Caro P, Lacaze-Dufaure C, Sing A S C, Hoareau W. Effect of catalytic conditions on the synthesis of new aconitate esters. Ind. Corp. Prod., 2012, 35: 203-210.

[32] Fortman J L, Chhabra S, Mukhopadhyay A, Chou H, Lee T S, Steen E, Keasling J D. Biofuel alternatives to ethanol: pumping the microbial well trends. Biotechnol., 2008, 26: 375-381.

[33] Wang Y, Ameer G A, Sheppard B J, Langer R. A tough biodegradable elastomer. Nat. Biotechnol., 2002, 20(6): 602-606.

[34] Sundback C A, Shyu J Y, Wang Y, Faquin W C, Langer R S, Vacanti J P, Hadlock T A. Biocompatibility analysis of poly (glycerol sebacate) as a nerve guide material. Biomaterials, 2005, 26(27): 5454-5464.

[35] Nijst C L, Bruggeman J P, Karp J M, Ferreira L, Zumbuehl A, Bettinger C J, Langer R. Synthesis and characterization of photocurable elastomers from poly(glycerol-co-sebacate). Biomacromolecules, 2007, 8: 3067-3073.

[36] Yang J, Webb A R, Ameer G A. Novel citric acid-based biodegradable elastomers for tissue engineering. Adv. Mater., 2008, 16(6): 511-516.

[37] Kang Y, Yang J, Khan S, Anissian L, and Ameer G A. A new biodegradable polyester elastomer for cartilage tissue engineering. J. Biomed. Mater. Res. A, 2006, 77(2): 331-339.

[38] Yang J, Webb A R, Pickerill S J, Hageman G, Ameer G A. Synthesis and evaluation of poly (diol citrate) biodegradable elastomers. Biomaterials, 2006, 27(9): 1889-1898.

[39] Prabhakaran M P, Nair A S, Kai D, Ramakrishna S. Electrospun composite scaffolds containing poly (octanediol-co-citrate) for cardiac tissue engineering. Biopolymers, 2012, 97(7): 529-538.

[40] Du Y, Ge J, Shao Y, Ma P X, Chen X, Lei B. Development of silica grafted poly (1, 8-octanediol-co-citrates) hybrid elastomers with highly tunable mechanical properties and biocompatibility. J. Mater. Chem. B, 2015, 3(15): 2986-3000.

[41] Zeimaran E, Mohan S, Pourshahrestani S, Pingguan-Murphy B, Kadri N A, Murali M R, Raghavendran H R, Hasikin K, Kamarul T, Towler M R. Osteogenic differentiation of mesenchymal stem cells on a poly (octanediol citrate)/bioglass composite scaffold in vitro. Mater. Design, 2016, 109: 434-442.

[42] Zeimaran E, Pourshahrestani S, Pingguan-Murphy B, Kong D, Naveen S V, Kamarul T, Kadri N A. Development of poly (1, 8-octanediol citrate)/chitosan blend films for tissue engineering applications. Carbohyd. Polym., 2017, 175: 618-627.

[43] Ding T, Liu Q, Shi R, Tian M, Yang J, Zhang L. Synthesis, characterization and in vitro degradation study of a novel and rapidly degradable elastomer. Polym. Degrad. Stabil., 2006, 91(4): 733-739.

[44] Wei T, Lei L, Kang H, Qiao B, Wang Z, Zhang L, Coates P, Hua K C, Kulig J. Tough bio-based elastomer nanocomposites with high performance for engineering applications. Adv. Eng. Mater., 2012, 14(1-2): 112-118.

[45] Wang Z, Zhang X, Wang R, Kang H, Qiao B, Ma J, Zhang L, Wang H. Synthesis and characterization of novel soybean-oil-based elastomers with favorable processability and tunable properties. Macromolecules, 2012, 45(22): 9010-9019.

[46] Wang Z, Yuan L, Trenor N M, Vlaminck L, Billiet S, Sarkar A, Du Prez F E, Stefik M, Tang C. Sustainable thermoplastic elastomers derived from plant oil and their ―click-coupling" via TAD chemistry. Green Chem., 2015, 17(7): 3806-3818.

[47] Bajaj P, Sreekumar T V, Sen K. Effect of reaction medium on radical copolymerization of acrylonitrile with vinyl acids. J. Appl. Polym. Sci., 2001, (9): 1640-1652.

[48] Bajaj P, Sreekumar T V, Sen K. Thermal behaviour of acrylonitrile copolymers having methacrylic and itaconic acid comonomers. Polymer, 2001, 42(4): 1707-1718.

[49] Barrett D G, Merkel T J, Luft J C, Yousaf M N. One-step syntheses of photocurable polyesters based on a renewable resource. Macromolecules, 2010, 43(23): 9660-9667.

[50] Wang R, Ma J, Zhou X, Wang Z, Kang H, Zhang L, Hua K C, Kulig J. Design and preparation of a novel cross-linkable, high molecular weight, and bio-based elastomer by emulsion polymerization. Macromolecules, 2012, 45(17): 6830-6839.

[51] Sarkar P, Bhowmick A K. Green approach toward sustainable polymer: synthesis and characterization of poly (myrcene-co-dibutyl itaconate). ACS Sustainable Chem. Eng., 2016, 4(4): 2129-2141.

[52] Chappell J. The biochemistry and molecular biology of isoprenoid metabolism. Plant Physiol., 1995, 107(1): 1-6.

[53] Whited G M, Feher F J, Benko D A, Cervin M A, Chotani G K, McAuliffe J C, LaDuca R J, Ben-Shoshan E A, Sanford K J. Technology update: Development of a gas-phase bioprocess for isoprene-monomer production using metabolic pathway engineering. Ind. Biotechnol., 2010, 6(3): 152-163.

[54] Yang J, Zhao G, Sun Y, Zheng Y, Jiang X, Liu W, Xian M. Bio-isoprene production using exogenous MVA pathway and isoprene synthase in Escherichia coli. Bioresource Technol., 2012, 104: 642-647.

[55] Zhao Y, Yang J, Qin B, Li Y, Sun Y, Su S, Xian M. Biosynthesis of isoprene in Escherichia coli via methylerythritol phosphate (MEP) pathway. Appl. Microbiol. Biot., 2011, 90(6): 1915.

[56] Morschbacker A. Bio-ethanol based ethylene. Polym. Rev., 2009, 49(2): 79-84.

[57] Ezeji T, Qureshi N, Blaschek H P. Production of acetone-butanol-ethanol (ABE) in a continuous flow bioreactor using degermed corn and Clostridium beijerinckii. Process Biochem., 2007, 42(1): 34-39.

[58] Fischer C R, Peterson A A, Tester J W. Production of C3 hydrocarbons from biomass via hydrothermal carboxylate reforming. Ind. Eng. Chem. Res., 2011, 50(8): 4420-4424.

[59] van Leeuwen B N, van der Wulp A M, Duijnstee I, van Maris A J, Straathof A J. Fermentative production of isobutene. Appl. Microbiol, Biot., 2012, 93(4): 1377-1387.

[60] Syu M J. Biological production of 2, 3-butanediol. Appl. Microbiol. Biot., 2001, 55(1): 10-18.

[61] Haveren J, Scott E L, Sanders J. Bulk chemicals from biomass. Biofuel. Bioprod. Bior., 2008, 2(1): 41-57.

[62] Sonnenschein M F, Ginzburg V V, Grzesiak A L, Schiller K, Wendt B L. Design, polymerization, and properties of polyurethane elastomers from miscible, immiscible,

and hybridized seed-oil derived soft segment blends. J. Polym. Sci. Pol Chem., 2015, 53(1): 93-102.

[63] Hazmi A S, Pauzi N N, Maurad Z A, Abdullah L C, Aung M M, Ahmad A, Salleh M Z, Tajau R, Mahmood M H, Saniman S E. Understanding intrinsic plasticizer in vegetable oil-based polyurethane elastomer as enhanced biomaterial. J. Therm. Anal. Calorim., 2017, 130(2): 919-933.

[64] Lee A, Deng Y. Green polyurethane from lignin and soybean oil through non-isocyanate reactions. Eur. Polym. J., 2015, 63: 67-73.

[65] Finegan I C, Gibson R F. Recent research on enhancement of damping in polymer composites. Compos. Struct., 1999, 44(2-3): 89-98.

[66] Harris J A. Design principles for vibration isolation and damping with elastomers including nonlinearity. Rubber Chem. Technol., 1989, 62(3): 515-528.

[67] Kang S, Hong S I, Choe C R, Park M, Rim S, Kim J. Preparation and characterization of epoxy composites filled with functionalized nanosilica particles obtained via sol-gel process. Polymer, 2001, 42 (3): 879-887.

[68] Sperling L H, Fay J J. Factors which affect the glass transition and damping capability of polymers. Polym. Adv. Technol., 1991, 2 (1): 49-56.

[69] Fradkin D G, Foster J N, Sperling L H, Thomas D A. Molecular demixing in poly [cross-(ethyl acrylete)]-inter-poly [cross-(methyl methacrylate)] interpenetrating polymer networks brought about by selective decrosslinking and annealing. Polym. Eng. Sci., 1986, 26(11): 730-735.

[70] Ungar E E. Loss factors of viscoelastically damped beam structures. J. Acoust. Soc. Am., 1962, 34(8):1082-1089.

[71] Manoj N R, Ratna D, Dalvi V, Chandrasekhar L, Patri M, Chakraborty B C, Deb P C. Interpenetrating polymer networks based on carboxylated nitrile rubber and poly (alkyl methacrylate)s. Polym. Eng. Sci., 2002, 42(8):1748-1755.

[72] Mathew A P, Groeninckx G, Michler G H, Radusch H J, Thomas S. Viscoelastic properties of nanostructured natural rubber/polystyrene interpenetrating polymer networks. J. Polym. Sci., Part B: Polym. Phys., 2003, 41(14):1680-1696.

[73] Chern Y C, Tseng S M, Hsieh K H. Damping properties of interpenetrating polymer networks of polyurethane-modified epoxy and polyurethanes. J. Appl. Polym. Sci., 1999, 74(2): 328-335.

[74] Manoj N R, Chandrasekhar L, Patri M, Chakraborty B C, Deb P C. Vibration damping materials based on interpenetrating polymer networks of carboxylated nitrile rubber and poly (methyl methacrylate). Polym. Adv. Technol., 2002, 13(9): 644-648.

[75] Perera M S, Ishiaku U S, Ishak Z M. Characterisation of PVC/NBR and PVC/ENR50 binary blends and PVC/ENR50/NBR ternary blends by DMA and solid state NMR. Eur. Polym. J., 2001, 37(1): 167-178.

[76] Yamada N, Shoji S, Sasaki H, Nagatani A, Yamaguchi K, Kohjiya S, Hashim A S. Developments of high performance vibration absorber from poly (vinyl chloride)/chlorinated polyethylene/epoxidized natural rubber blend. J. Appl. Polym. Sci., 1999, 71(6):855-863.

[77] Qin C L, Cai W M, Cai J, Tang D Y, Zhang J S, Qin M. Damping properties and morphology of polyurethane/vinyl ester resin interpenetrating polymer network. Mater. Chem. Phys., 2004, 85(2): 402-409.

[78] Chu H H, Lee C M, Huang W G. Damping of vinyl acetate-n-butyl acrylate copolymers. J. Appl. Polym. Sci., 2004, 91(3): 1396-1403.

[79] Wu C, Yamagishi T A, Nakamoto Y, Ishida S, Nitta K H, Kubota S. Organic hybrid of chlorinated polyethylene and hindered phenol. I. Dynamic mechanical properties. J. Polym. Sci., Part B: Polym. Phys., 2000, 38(17): 2285-2295.

[80] Wu C, Otani Y, Namiki N, Emi H, Nitta K H, Kubota S. Dynamic properties of an organic hybrid of chlorinated polyethylene and hindered phenol compound. J. Appl. Polym. Sci., 2001, 82(7): 1788-1793.

[81] Wu C, Akiyama S. Dynamic properties of carbon black filled chlorinated polyethylene/hindered phenol blends. Polym. Int., 2003, 52(8): 1249-1255.

[82] Wu C. Effects of a hindered phenol compound on the dynamic mechanical properties of chlorinated polyethylene, acrylic rubber, and their blend. J. Appl. Polym. Sci., 2001, 80(13): 2468-2473.

[83] Zhao X Y, Xiang P, Tian M, Fong H, Jin R, Zhang L Q. Nitrile butadiene rubber/hindered phenol nanocomposites with improved strength and high damping performance. Polymer, 2007, 48(20): 6056-6063.

[84] Corma A, Iborra S, Velty A. Chemical routes for the transformation of biomass into chemicals. Chem. Rev., 2007, 107(6): 2411-2502.

[85] Binder J B, Raines R T. Simple chemical transformation of lignocellulosic biomass into furans for fuels and chemicals. J. Am. Chem. Soc., 2009, 131(5): 1979-1985.

[86] Tong X, Ma Y, Li Y. Biomass into chemicals: conversion of sugars to furan derivatives by catalytic processes. Appl. Catal., A., 2010, 385(1): 1-3.

[87] Besson M, Gallezot P, Pinel C. Conversion of biomass into chemicals over metal catalysts. Chem. Rev., 2013, 114(3): 1827-1870.

[88] Wang Z, Wei T, Xue X, He M, Xue J, Song M, Wu S, Kang H, Zhang L, Jia Q. Synthesis of fully bio-based polyamides with tunable properties by employing itaconic acid. Polymer. 2014, 55(19): 4846-4856.

[89] Ma Q, Liu X, Zhang R, Zhu J, Jiang Y. Synthesis and properties of full bio-based thermosetting resins from rosin acid and soybean oil: the role of rosin acid derivatives. Green Chem., 2013, 15(5):1300-1310.

[90] Yamaguchi S, Tanha M, Hult A, Okuda T, Ohara H, Kobayashi S. Green polymer chemistry: lipase-catalyzed synthesis of bio-based reactive polyesters employing itaconic anhydride as a renewable monomer. Polym. J., 2014, 46(1): 2-13.

[91] Satoh K, Lee D H, Nagai K, Kamigaito M. Precision synthesis of bio-based acrylic thermoplastic elastomer by raft polymerization of itaconic acid derivatives. Macromol. Rapid Commun., 2014, 35(2): 161-167.

[92] Gandini A, Lacerda T M, Carvalho A J. A straightforward double coupling of furan moieties onto epoxidized triglycerides: synthesis of monomers based on two renewable resources. Green Chem., 2013, 15(6): 1514-1519.

[93] Xia Y, Larock R C. Vegetable oil-based polymeric materials: synthesis, properties, and applications. Green Chem., 2010, 12(11): 1893-1909.

[94] Jiang L, Kang H, Wang Z, Zhang L, Mao L, Wang Y. Studies on chain extension of a novel bio-based engineering elastomer using 4, 4-diphenyl methane diisocyanate as a chain extender. J. Appl. Polym. Sci., 2014, 131(18): 40756.

[95] Fang B, Kang H, Wang R, Wang Z, Wang W, Zhang L. Aging behavior and mechanism of bio-based engineering polyester elastomer nanocomposites. J. Appl. Polym. Sci., 2014, 131(19): 40862.

[96] Wang R, Yao H, Lei W, Zhou X, Zhang L, Hua K C, Kulig J. Morphology, interfacial interaction, and properties of a novel bioelastomer reinforced by silica and carbon black. J. Appl. Polym. Sci., 2013, 129(3): 1546-1554.

[97] Yao H, Qiao H, Xing Q, Gao N, Chu J, Zhang L, Hua K C, Kulig J, Wang R. Enhancing the air impermeability of a biobased poly (di-isoamyl itaconate-co-isoprene) elastomer via the cocoagulation of latex and natural layered silicates. J. Appl. Polym. Sci., 2014, 131(17): 40682.

[98] Guo W, Shen Z, Guo B, Zhang L, Jia D. Synthesis of bio-based copolyester and its reinforcement with zinc diacrylate for shape memory application. Polymer. 2014, 55(16): 4324-4331.

[99] Chang M C, Thomas D A, Sperling L H. Group contribution analysis of the damping behavior of homopolymers, statistical copolymers, and interpenetrating polymer networks based on acrylic, vinyl, and styrenic mers. J. Polym. Sci., Part B: Polym. Phys., 1988, 26(8): 1627-1640.

[100] Gauthier C, Reynaud E, Vassoille R, Ladouce-Stelandre L. Analysis of the non-linear viscoelastic behaviour of silica filled styrene butadiene rubber. Polymer, 2004, 45(8): 2761-2771.

[101] Rattanasom N, Saowapark T, Deeprasertkul C. Reinforcement of natural rubber with silica/carbon black hybrid filler. Polym. Test., 2007, 26(3): 369-377.

[102] Wu Y P, Wang Y Q, Zhang H F, Wang Y Z, Yu D S, Zhang L Q, Yang J. Rubber-pristine clay nanocomposites prepared by co-coagulating rubber latex and clay aqueous suspension. Compos. Sci. Technol., 2005, 65(7): 1195-1202.

[103] Sui G, Zhong W H, Yang X P, Yu Y H, Zhao S H. Preparation and properties of natural rubber composites reinforced with pretreated carbon nanotubes. Polym. Adv. Technol., 2008, 19(11): 1543-15459.

[104] Flory P J, Rehner Jr J. Statistical mechanics of cross-linked polymer networks I. Rubberlike elasticity. J. Chem. Phys., 1943, 11: 512-520.

[105] Flory P J, Rehner Jr J. Statistical mechanics of cross-linked polymer networks ii. swelling. J. Chem. Phys., 1943, 11: 521-526.

[106] Hall D E, Moreland J C. Fundamentals of rolling resistance. Rubber Chem. Technol., 2001, 74(3): 525-539.

[107] Ghosh S, Sengupta R A, Heinrich G. Investigations on rolling resistance of nanocomposite based passenger car radial tyre tread compounds using simulation technique. Tire Sci. Technol., 2011, 39(3): 210-222.

[108] Herd C, Edwards C, Curtis J, Crossley S, Schomberg K C, Gross T, Steinhauser N, Kloppenberg H, Hardy D, Lucassen A. Use of surface-treated carbon blacks in an elastomer to reduce compound hysteresis and tire rolling resistance and improve wet traction. United States Patent, 20130046064 A1, 2013-2-21.

[109] Rauline R. Rubber compound and tires based on such a compound. European Patent, 0501227 (A1), 1992-09-02.

[110] Wolff S. Silanes in tire compounding after ten years—a review. Tire Sci. Technol., 1987, 15(4): 276-294.

[111] Zhu L, Wool R P. Nanoclay reinforced bio-based elastomers: synthesis and characterization. Polymer, 2006, 47(24): 8106-8115.

[112] Job K A. Trends in green tire manufacturing. Rubber World, 2014, 249(6): 32-38.

[113] Sengloyluan K, Sahakaro K, Dierkes W K, Noordermeer J W M. Silica-reinforced tire tread compounds compatibilized by using epoxidized natural rubber. Eur. Polym. J., 2014, 51: 69-79.

[114] Chattopadhyay P K, Basuli U, Chattopadhyay S. Studies on novel dual filler based epoxidized natural rubber nanocomposite. Polym. Compos., 2010, 31(5): 835-846.

[115] Chapman A V. Natural rubber and NR-based polymers: renewable materials with unique properties. Transport., 2007, 5: 8.

[116] Du M, Guo B, Lei Y, Liu M, Jia D. Carboxylated butadiene–styrene rubber/halloysite nanotube nanocomposites: interfacial interaction and performance. Polymer, 2008, 49(22): 4871-4876.

[117] Reddy C S K, Singh R P. Enhanced production of itaconic acid from corn starch and market refuse fruits by genetically manipulated Aspergillus terreus SKR10. Bioresour. Technol., 2002, 85(1): 69-71.

[118] Jang Y S, Lee J, Malaviya A, Seung D Y, Cho J H, Lee S Y. Butanol production from renewable biomass: rediscovery of metabolic pathways and metabolic engineering. Biotechnol. J., 2012, 7(2): 186-198.

[119] Green E M. Fermentative production of butanol—the industrial perspective. Curr. Opin. Biotechnol., 2011, 22(3): 337-343.

[120] Singh R. Facts, growth, and opportunities in industrial biotechnology. Org. Process. Res. Dev., 2010, 15(1): 175-179.

[121] Abdollahi M, Sharifpour M. Effect of carboxylic acid monomer and butadiene on particle growth in the emulsifier-free emulsion copoly-merization of styrene–butadiene–carboxylic acid monomer. Polymer, 2007, 48(7): 2035-2045.

[122] Sarac A S. Redox polymerization. Prog. Polym. Sci., 1999, 24(8): 1149-1204.

[123] Antonietti M, Landfester K. Polyreactions in miniemulsions. Prog. Polym. Sci., 2002, 27(4): 689-757.

[124] Qi G, Jones C W, Schork F J. Enzyme-initiated miniemulsion polymerization. Biomacromolecules, 2006, 7(11): 2927-2930.

[125] Ishimoto K, Arimoto M, Okuda T, Yamaguchi S, Aso Y, Ohara H, Kobayashi S, Ishii M, Morita K, Yamashita H, Yabuuchi N. Biobased polymers: synthesis of graft copolymers and comb polymers using lactic acid macromonomer and properties of the product polymers. Biomacromolecules, 2012, 13(11): 3757-3768.

[126] Vijayendran B R. Effect of carboxylic monomers on acid distribution in carboxylated polystyrene latices. J. Appl. Polym. Sci., 1979, 23(3): 893-901.

[127] Carbajo R J, Neira J L. NMR for Chemists and Biologists. Springer, 2013, 36-38.

[128] Wang W, Chang Z, Wang M, Zhang, Z. Effect of carboxyl on vulcanization and mechanical properties of carboxylated acrylic rubber prepared by 60Co-γ-ray-induced polymerization. J. Appl. Polym. Sci., 2006, 102(6): 5587-5594.

[129] Ibarra L, Alzorriz M. Ionic elastomers based on carboxylated nitrile rubber and calcium oxide. J. Appl. Polym. Sci., 2003, 87(5): 805-813.

[130] Hamed G R, Hua K C. Effect of ZnO particle size on the curing of carboxylated NBR and carboxylated SBR. Rubber Chem. Technol., 2004, 77(2): 214-226.

[131] Smejda-Krzewicka A, RZYMSKI W M. Crosslinking of new elastomers functionalized with carboxyl groups. Polimery, 2006, 51(1): 66-68.

[132] Wu Y, Zhao Q, Zhao S, Zhang L. The influence of in situ modification of silica on filler network and dynamic mechanical properties of silica–filled solution styrene–butadiene rubber. J. Appl. Polym. Sci., 2008, 108: 112-118.

[133] Ramier J, Gauthier C, Chazeau L, Stelandre L, Guy L. Payne effect in silica–filled styrene–butadiene rubber: influence of surface treatment. J. Polym. Sci. Pol. Phys., 2007, 45(3): 286-298.

[134] Fröhlich J, Niedermeier W, Luginsland H D. The effect of filler-filler and filler-elastomer interaction on rubber reinforcement. Compos. Part A, 2005, 36(4): 449-460.

[135] Payne A R. Effect of dispersion on dynamic properties of filler-load rubbers. Rubber Chem. Technol., 1966, 39(2): 365-374.

[136] Cordier P, Tournilhac F, Soulié-Ziakovic C, Leibler L. Self-healing and thermoreversible rubber from supramolecular assembly. Nature, 2008, 451(7181): 977-980.

[137] Kalita H, Karak N. Bio-based elastomeric hyperbranched polyurethanes for shape memory application. Iran. Polym. J., 2012, 21(4): 263-271.

[138] Gopalakrishnan S. Influence of polyols on properties of bio-based polyurethanes. B. Mater. Sci. 2012, 35(2): 243-251.

[139] Zhang J, Li L, Boonkerd K, Zhang Z, Kim J K. Formation of bio-based elastomer from styrene-butadiene copolymer and epoxidized soybean oil. J. Polym. Res., 2014, 21(4): 1-11.

[140] Boonkerd K, Moon B K, Kim M C, Kim J K. Formation of a novel bio-based elastomer from polybutadiene and epoxidized soybean oil via post-living anionic polymerization. J. Elastom. Plast., 2014, 46(7): 644-661.

[141] Sarkar P, Bhowmick A K. Synthesis, characterization and properties of a bio-based elastomer: polymyrcene. RSC Adv., 2014, 4(106): 61343-61354.

[142] Lei W, Zhou X, Russell T P, Hua K C, Yang X, Qiao H, Wang W, Li F, Wang R, Zhang L. High performance bio-based elastomers: energy efficient and sustainable materials for tires. J. Mater. Chem. A, 2016, 4(34): 13058-13062.

[143] Wang R, Zhang J, Kang H, Zhang L. Design, preparation and properties of bio-based elastomer composites aiming at engineering applications. Compos. Sci. Technol., 2016, 133: 136-156.

[144] Qiao H, Wang R, Yao H, Zhou X, Lei W, Hu X, Zhang L. Preparation of graphene oxide/bio-based elastomer nanocomposites through polymer design and interface tailoring. Polym. Chem., 2015, 6(34): 6140-6151.

[145] Qiao H, Wang R, Yao H, Wu X, Lei W, Zhou X, Hu X, Zhang L. Design and preparation of natural layered silicate/bio-based elastomer nanocomposites with improved dispersion and interfacial interaction. Polymer, 2015, 79: 1-11.

[146] Zhou X, Cai L, Lei W, Qiao H, Liu C, Zhao X, Chen J, Wang R, Zhang L. Preparation and intermolecular interaction of bio-based elastomer/hindered phenol hybrid with tunable damping properties. Pure Appl. Chem., 2015, 87(8): 767-777.

[147] Zhou X, Wang R, Lei W, Qiao H, Ji H, Zhang L, Hua K-C, Kulig J. Design and synthesis by redox polymerization of a bio-based carboxylic elastomer for green tire. Sci. China Chem., 2015, 58(10): 1561-1569.

[148] Omnès B, Thuillier S, Pilvin P, Grohens Y, Gillet S. Effective properties of carbon black filled natural rubber: experiments and modeling. Compos. Part A, 2008, 39(7): 1141-1149.

[149] Zou Y, Sun Y, He J, Tang Z, Zhu L, Luo Y, Liu F. Enhancing mechanical properties of styrene-butadiene rubber/silica nanocomposites by in situ interfacial modification

with a novel rare-earth complex. Compos. Part A, 2016, 87: 297-309.

[150] Li Y, Han B, Wen S, Lu Y, Yang H, Zhang L, Liu L. Effect of the temperature on surface modification of silica and properties of modified silica filled rubber composites. Compos. Part A, 2014, 62: 52-59.

[151] Arroyo M, Lopez-Manchado M A, Herrero B. Organo-montmorillonite as substitute of carbon black in natural rubber compounds. Polymer, 2003, 44(8): 2447-2453.

[152] Zheng H, Zhang Y, Peng Z, Zhang Y. Influence of clay modification on the structure and mechanical properties of EPDM/montmorillonite nanocomposites. Polym. Test, 2004, 23(2): 217-223.

[153] Kader M A, Kim K, Lee Y S, Nah C. Preparation and properties of nitrile rubber/montmorillonite nanocomposites via latex blending. J. Mater. Sci., 2006, 41(22): 7341-7352.

[154] Mittal V. Polymer layered silicate nanocomposites: a review. Materials, 2009, 2(3): 992-1057.

[155] Alexandre M, Dubois P. Polymer-layered silicate nanocomposites: preparation, properties and uses of a new class of materials. Mater. Sci. Eng. R-Rep., 2000, 28(1): 1-63.

[156] Ponnamma D, Ramachandran R, Hussain S, Rajaraman R, Amarendra G, Varughese K T, Thomas S. Free-volume correlation with mechanical and dielectric properties of natural rubber/multi walled carbon nanotubes composites. Compos. Part A, 2015, 77: 164-171.

[157] Joussein E, Petit S, Churchman J, Theng B, Righi D, Delvaux B. Halloysite clay minerals-a review. Clay Miner., 2005, 40(4): 383-426.

[158] Dong Y, Marshall J, Haroosh H J, Mohammadzadehmoghadam S, Liu D, Qi X, Lau K T. Polylactic acid (PLA)/halloysite nanotube (HNT) composite mats: Influence of HNT content and modification. Compos. Part A, 2015, 76: 28-36.

[159] Liu M, Jia Z, Jia D, Zhou C. Recent advance in research on halloysite nanotubes-polymer nanocomposite. Prog. Polym. Sci., 2014, 39(8): 1498-1525.

[160] Ye Y, Chen H, Wu J, Chan C M. Evaluation on the thermal and mechanical properties of HNT-toughened epoxy/carbon fibre composites. Compos. Part B, 2011, 42(8):

2145-2150.

[161] Ning N, Yin Q, Luo F, Zhang Q, Du R, Fu Q. Crystallization behavior and mechanical properties of polypropylene/halloysite composites. Polymer, 2007, 48(25): 7374-7384.

[162] Prashantha K, Schmitt H, Lacrampe M F, Krawczak P. Mechanical behaviour and essential work of fracture of halloysite nanotubes filled polyamide 6 nanocomposites. Compos. Sci. Technol., 2011, 71(16): 1859-1866.

[163] Guo B, Chen F, Lei Y, Liu X, Wan J, Jia D. Styrene-butadiene rubber/halloysite nanotubes nanocomposites modified by sorbic acid. Appl. Surf. Sci., 2009, 255(16): 7329-7336.

[164] Zhong B, Jia Z, Luo Y, Guo B, Jia D. Preparation of halloysite nanotubes supported 2-mercaptobenzimidazole and its application in natural rubber. Compos. Part A, 2015, 73: 63-71.

[165] Ismail H, Pasbakhsh P, Fauzi M A, Bakar A A. Morphological, thermal and tensile properties of halloysite nanotubes filled ethylene propylene diene monomer (EPDM) nanocomposites. Polym. Test, 2008, 27(7): 841-850.

[166] Potts J R, Shankar O, Murali S, Du L, Ruoff R S. Latex and two-roll mill processing of thermally-exfoliated graphite oxide/natural rubber nanocomposites. Compos. Sci. Technol., 2013, 74: 166-172.

[167] Singh B. Why Does Halloysite Roll?—A New Model. Clays Clay Miner., 1996, 44(2): 191-196.

[168] Pasbakhsh P, Ismail H, Fauzi M N A, Bakar A A. EPDM/modified halloysite nanocomposites. Appl. Clay Sci., 2010, 48(3): 405-413.

[169] Wolff S, Wang M J, Tan E H. Filler-elastomer interactions. Part VII. Study on bound rubber. Rubber Chem. Technol., 1993, 66(2): 163-177.

[170] Kerber S J, Bruckner J J, Wozniak K, Seal S, Hardcastle S, Barr T L. The nature of hydrogen in x-ray photoelectron spectroscopy: General patterns from hydroxides to hydrogen bonding. J. Vac. Sci. Technol. A, 1996, 14(3): 1314-1320.

[171] Liu S, Chan C, Weng L, Jiang M. Surface segregation in polymer blends and interpolymer complexes with increasing hydrogen bonding interactions. J. Polym. Sci. Part B: Polym. Phys., 2005, 43(14): 1924-1930.

[172] Lu H, Nutt S. Restricted relaxation in polymer nanocomposites near the glass transition. Macromolecules, 2003, 36(11): 4010-4016.

[173] Liu L, Barber A H, Nuriel S, Wagner H D. Mechanical Properties of Functionalized Single-Walled Carbon-Nanotube/Poly (vinyl alcohol) Nanocomposites. Adv. Funct. Mater., 2005, 15(6): 975-980.

[174] Liang J, Huang Y, Zhang L, Wang Y, Ma Y, Guo T, Chen Y. Molecular-level dispersion of graphene into poly (vinyl alcohol) and effective reinforcement of their nanocomposites. Adv. Funct. Mater., 2009, 19(14): 2297-2302.

[175] Bee S T, Ratnam C T, Sin L T, Tee T T, Hui D, Kadhum A A H, Rahmat A R, Lau J. Effects of electron beam irradiation on mechanical properties and nanostructural-morphology of montmorillonite added polyvinyl alcohol composite. Compos. Part B, 2014, 63: 141-153.

[176] Manchado M L, Valentini L, Biagiotti J, Kenny J M. Thermal and mechanical properties of single-walled carbon nanotubes–polypropylene composites prepared by melt processing. Carbon, 2005, 43(7): 1499-1505.

[177] Liu C, Luo Y, Jia Z, Li S, Guo B, Jia D. Structure and properties of poly (vinyl chloride)/halloysite nanotubes nanocomposites. J. Macromol. Sci. Part B, 2012, 51(5): 968-981.

[178] Neal J A, Mozhdehi D, Guan Z. Enhancing mechanical performance of a covalent self-healing material by sacrificial noncovalent bonds. J. Am. Chem. Soc., 2015, 137(14): 4846-4850.

[179] Guan Z, Roland J T, Bai J Z, Ma S X, McIntire T M, Nguyen M. Modular domain structure: a biomimetic strategy for advanced polymeric materials. J. Am. Chem. Soc., 2004, 126(7): 2058-2065.

[180] Ma J, Feng Y X, Xu J, Xiong M L, Zhu Y J, Zhang L Q. Effects of compatibilizing agent and in situ fibril on the morphology, interface and mechanical properties of EPDM/nylon copolymer blends. Polymer, 2002, 43(3): 937-945.

[181] Yao S H, Yuan J K, Zhou T, Dang Z M, Bai J. Stretch-modulated carbon nanotube alignment in ferroelectric polymer composites: characterization of the orientation state and its influence on the dielectric properties. J. Phys. Chem. C, 2011, 115(40): 20011-20017.

[182] Ji Z, Luo Y, Yang S, Guo B, Du M, Jia D. Morphology, interfacial interaction and properties of styrene-butadiene Rubber/Modified halloysite nanotube nanocomposites. Chin. J. Polym. Sci., 2009, 27(06): 857-864.

[183] Tang Z, Huang J, Guo B, Zhang L, Liu F. Bioinspired engineering of sacrificial metal-ligand bonds into elastomers with supramechanical performance and adaptive recovery. Macromolecules, 2016, 49(5): 1781-1789.

[184] Raquez J M, Deléglise M, Lacrampe M F, Krawczak P. Thermosetting (bio) materials derived from renewable resources: a critical review. Prog. Polym. Sci., 2010, 35(4): 487-509.

[185] Isikgor F H, Becer C R. (2015). Lignocellulosic biomass: a sustainable platform for the production of bio-based chemicals and polymers. Polym. Chem., 2015, 6(25): 4497-4559.

[186] Sheldon R A. Green and sustainable manufacture of chemicals from biomass: state of the art. Green Chem., 2014, 16(3): 950-963.

[187] Yahiro K, Shibata S, Jia S R, Park Y, Okabe M. Efficient itaconic acid production from raw corn starch. J. Ferment. Bioeng., 1997, 84(4): 375-377.

[188] Ali M A, Tateyama S, Oka Y, Kaneko D, Okajima M K, Kaneko T. Syntheses of high-performance biopolyamides derived from itaconic acid and their environmental corrosion. Macromolecules, 2013, 46(10): 3719-3725.

[189] Ma S, Liu X, Jiang Y, Tang Z, Zhang C, Zhu J. Bio-based epoxy resin from itaconic acid and its thermosets cured with anhydride and comonomers. Green Chem., 2013, 15(1): 245-254.

[190] Dai J, Ma S, Wu Y, Han L, Zhang L, Zhu J, Liu X. Polyesters derived from itaconic acid for the properties and bio-based content enhancement of soybean oil-based thermosets. Green Chem., 2015, 17(4): 2383-2392.

[191] Otsu T, Yamagishi K, Yoshioka M. Determination of absolute rate constants for radical polymerization of dialkyl itaconates with various ester groups by electron spin resonance spectroscopy. Macromolecules, 1992, 25(10): 2713-2716.

[192] Sato T, Inui S, Tanaka H, Ota T, Kamachi M, Tanaka K. (1987). Kinetic and ESR studies on the radical polymerization of di-n-butyl itaconate in benzene. J. Polym. Sci. Pol. Chem., 1987, 25(2): 637-652.

[193] Sato T, Morita N, Tanaka H, Ota T. (1989). Solvent effect on the radical polymerization of di-n-butyl itaconate. J. Polym. Sci. Pol. Chem., 1989, 27(8): 2497-2508.

[194] Mahdavian A R, Abdollahi M, Mokhtabad L, Reza Bijanzadeh H, Ziaee F. Kinetic study of radical polymerization. IV. Determination of reactivity ratio in copolymerization of styrene and itaconic acid by 1H-NMR. J. Appl. Polym. Sci., 2006, 101(3): 2062-2069.

[195] Fernández-García M, Madruga E L, Cuervo-Rodríguez R. A kinetic study on the radical copolymerization of dimethyl itaconate and methyl methacrylate in benzene. Polymer, 1996, 37(2): 263-268.

[196] Tsarevsky N V, Matyjaszewski K. "Green" atom transfer radical polymerization: from process design to preparation of well-defined environmentally friendly polymeric materials. Chem. Rev., 2007, 107(6): 2270-2299.

[197] Qiu J, Charleux B, Matyjaszewski K. Controlled/living radical polymerization in aqueous media: homogeneous and heterogeneous systems. Prog. Polym. Sci., 2001, 26(10): 2083-2134.

[198] Lei W, Russell T P, Hu L, Zhou X, Qiao H, Wang W, Wang R, Zhang L. Pendant chain effect on the synthesis, characterization, and structure-property relations of poly (di-n-alkyl itaconate-co-isoprene) bio-based elastomers. ACS Sustainable Chem. Eng., 2017, 5(6): 5214-5223.

[199] Reilly J, Hickinbottom W J, Henley F R, Thaysen A C. The products of the "acetone: n-butyl alcohol" fermentation of carbohydrate material with special reference to some of the intermediate substances produced. Biochem. J., 1920, 14(2): 229-251.

[200] Zheng J, Tashiro Y, Wang Q, Sonomoto K. Recent advances to improve fermentative butanol production: genetic engineering and fermentation technology. J. Biosci. Bioeng., 2015, 119(1): 1-9.

[201] Posada J A, Patel A D, Roes A, Blok K, Faaij A P, Patel M K. Potential of bioethanol as a chemical building block for biorefineries: preliminary sustainability assessment of 12 bioethanol-based products. Bioresource Technol. 2013, 135: 490-499.

[202] Bender C, Hellstern S, Roman G. Bio-Butadiene from Waste Carbon Monoxide. Senior Design Reports (CBE), 2014, April 15.

[203] Abdelrahman O A, Park D S, Vinter K P, Spanjers C S, Ren L, Cho H J, Vlachos D G, Fan W, Tsapatsis M, Dauenhauer P J. Biomass-derived butadiene by dehydra-decyclization of tetrahydrofuran. ACS Sustainable Chem. Eng., 2017, 5(5): 3732-3736.

[204] Mayo F R, Lewis F M. Copolymerization. I. A basis for comparing the behavior of monomers in copolymerization; the copolymerization of styrene and methyl methacrylate. J. Am. Chem. Soc., 1944, 66(9):1594-1601.

[205] Price F P. Copolymerization mathematics and the description of stereoregular polymers. J. Chem. Phys., 1962, 36(1): 209-218.

[206] Ito K, Yamashita Y. Copolymer composition and microstructure. J. Polym. Sci. Pol. Chem., 1965, 3(6): 2165-2187.

[207] Pyun C W. Comonomer and stereosequence distributions in high polymers. J. Polym. Sci. Pol. Phys., 1970, 8(7): 1111-1126.

[208] Carman C J, Harrington R A, Wilkes C E. Monomer sequence distribution in ethylene-propylene rubber measured by 13C NMR. 3. Use of reaction probability model. Macromolecules. 1977, 10(3): 536-544.

[209] Weerts P A, German A L, Gilbert R G. Kinetic aspects of the emulsion polymerization of butadiene. Macromolecules. 1991, 24(7): 1622-1628.

[210] Doddrell D M, Pegg D T, Bendall M R. Distortionless enhancement of NMR signals by polarization transfer. J. Magn. Reson., 1982, 48(2):323-327.

[211] Franot C, Benezra C, Lepoittevin J P. Synthesis and interaction studies of 13 C labeled lactone derivatives with a model protein using 13 C NMR. Bioorgan. Med. Chem., 1993, 1(5): 389-397.

[212] Elgert K F, Quack G, Stutzel B. On the structure of polybutadiene: 4. 13C NMR spectrum of polybutadienes with cis-1, 4-, trans-1, 4-and 1, 2-moieties. Polymer. 1975, 16(3): 154-156.

[213] Sato H, Takebayashi K, Tanaka Y. Analysis of carbon-13 NMR of polybutadiene by means of low molecular weight model compounds. Macromolecules, 1987, 20(10): 2418-2423.

[214] Popovic J G, Katsikas L, Velickovic J S. The thermal degradation kinetics of poly (di-n-alkylitaconates). J. Therm. Anal. Calorim., 1992, 38(4): 953-959.

[215] Popović I, Katsikas L. The thermal degradation of some polymeric di-alkyl esters of itaconic acid. J. Serb. Chem. Soc., 2013, 78(12): 2179-2200.

[216] Fernández-Garcia M, La Fuente D, Luis J, Madruga E L. Thermal behavior of poly (dimethyl itaconate) and poly (di-n-butyl itaconate) copolymerized with methyl methacrylate. Polym. Eng. Sci., 2001, 41(9): 1616-1625.

[217] Popović I G, Katsikas L, Voloshchuk K A, Schrötter S, Veličković J S. The thermal degradation of poly (di-n-hexyl itaconate) prepared in the presence of n-dodecyl mercaptan. Polym. Degrad. Stabil., 1993, 42(3): 345-349.

[218] Popović I G, Katsikas L, Weller H, Schrötter S, Veliĉković J S. Polymerization studies: The application of differential thermogravimetric analysis. J. Appl. Polym. Sci., 1993, 50(8): 1475-1482.

[219] Tomić S L, Filipović J M, Katsikas L, Popović I G. The polymerisation kinetics of lower dialkyl itaconates. Macromol. Chem. Phys., 1999, 200(10): 2421-2427.

[220] Korth H G, Trill H, Sustmann R. [1-2H]-Allyl radical: barrier to rotation and allyl delocalization energy. J. Am. Chem. Soc., 1981, 103(15): 4483-4489.

[221] Zhang Z, Zheng H, Huang F, Li X, He S, Zhao C. Template polymerization of a novel cationic polyacrylamide: sequence distribution, characterization, and flocculation performance. Ind. Eng. Chem. Res., 2016, 55(37): 9819-9828.

[222] Zhang M, Carnahan E M, Karjala T W, Jain P. Theoretical analysis of the copolymer composition equation in chain shuttling copolymerization. Macromolecules, 2009, 42(21): 8013-8016.

[223] Data reports from The International Organization of Motor Vehicle Manufacturers. http://www.oica.net/.

[224] Chu S, Majumdar A. Opportunities and challenges for a sustainable energy future. Nature, 2012, 488(7411): 294-303.

[225] Tullo A H. Stretching tires'magic triangle. Chem. & Eng. News, 2009, 87 (46): 10-14.

[226] Holmberg K, Andersson P, Erdemir A. Global energy consumption due to friction in passenger cars. Tribol. Int., 2012, 47: 221-234.

[227] Batistakis C, Michels M A, Lyulin A V. Confinement-induced stiffening of thin elastomer films: linear and nonlinear mechanics vs local dynamics. Macromolecules, 2014, 47 (14): 4690-4703.

[228] Mackay M E, Tuteja A, Duxbury P M, Hawker C J, Van Horn B, Guan Z, Chen G, Krishnan R S. General strategies for nanoparticle dispersion. Science, 2006, 311(5768): 1740-1743.

[229] Merabia S, Sotta P, Long D R. A microscopic model for the reinforcement and the nonlinear behavior of filled elastomers and thermoplastic elastomers (Payne and Mullins effects). Macromolecules, 2008, 41 (21): 8252-8266.

[230] Byers J T. Fillers for balancing passenger tire tread properties. Rubber Chem. Technol., 2002, 75 (3): 527-548.

[231] Data reports from Rubber Statistical Bulletin (International rubber study group, october-december 2015 edition, Singapore), http://www.rubberstudy.com/documents/WebSiteData_Nov2015.pdf.

[232] Ragauskas A J, Williams C K, Davison B H, Britovsek G, Cairney J, Eckert C A, Frederick W J, Hallett J P, Leak D J, Liotta C L, Mielenz J R. The path forward for biofuels and biomaterials. Science, 2006, 311 (5760): 484-489.

[233] Dusselier M, Van Wouwe P, Dewaele A, Jacobs P A, Sels B F. Shape-selective zeolite catalysis for bioplastics production. Science, 2015, 349 (6243): 78-80.

[234] Li Z, Loh X J. Water soluble polyhydroxyalkanoates: future materials for therapeutic applications. Chem. Soc. Rev., 2015, 44 (10): 2865-2879.

[235] Ullah M H, Mahadi W N, Latef T A. Aerogel poly (butylene succinate) biomaterial substrate for RF and microwave applications. Scientific Reports, 2015, 5: 12868.

[236] Van Lith R, Gregory E K, Yang J, Kibbe M R, Ameer G A. Engineering biodegradable polyester elastomers with antioxidant properties to attenuate oxidative stress in tissues. Biomaterials, 2014, 35 (28): 8113-8122.

[237] Data reports from http://www.continental-tires.com/car/searchpage?q=sustainability#, and http://www.bridgestone.co.jp/csr/eco/environmental_report/pdf/BS_EnvReport2012.pdf.

[238] Sengloyluan K, Sahakaro K, Dierkes W K, Noordermeer J W M. Reinforcement efficiency of silica in dependence of different types of silane coupling agents in natural rubber-based tire compounds. KGK Kautschuk, Gummi, Kunststoffe, 2016, 69: 44-53.

[239] Klockmann O L. Processing of new rubber silane VP Si 363. 2006 International Tire Exhibition and Conference of Rubber & Plastics News, Akron, OH, September 16-18, 2006, Paper No. 29B.

[240] Willett P R. Heat generation in tires due to the viscoelastic properties of elastomeric components. Rubber Chem. Technol., 1974, 47 (2): 363-375.

[241] Futamura S. Deformation index-concept for hysteretic energy-loss process. Rubber Chem. Technol., 1991, 64 (1): 57-64.

[242] Fratzl P. Biomimetic materials research: what can we really learn from nature9s structural materials?. J. R. Soc. Interface, 2007, 4(15): 637-642.

[243] Ritchie R O. The conflicts between strength and toughness. Nat. Mater., 2011, 10(11): 817-822.

[244] Sun J, Bhushan B. Hierarchical structure and mechanical properties of nacre: a review. RSC Adv., 2012, 2(20): 7617-7632.

[245] Meyers M A, McKittrick J, Chen P Y. Structural biological materials: critical mechanics-materials connections. Science, 2013, 339(6121): 773-779.

[246] Suhre M H, Gertz M, Steegborn C, Scheibel T. Structural and functional features of a collagen-binding matrix protein from the mussel byssus. Nat. Commun., 2014, 5: 3392.

[247] Mayer G. Rigid biological systems as models for synthetic composites. Science, 2005, 310(5751): 1144-1147.

[248] Meyers M A, Chen P Y, Lin A Y, Seki Y. Biological materials: structure and mechanical properties. Prog. Mater. Sci., 2008, 53(1): 1-206.

[249] Espinosa H D, Rim J E, Barthelat F, Buehler M J. Merger of structure and material in nacre and bone–Perspectives on de novo biomimetic materials. Prog. Mater. Sci., 2009, 54(8): 1059-1100.

[250] Walther A, Bjurhager I, Malho J M, Ruokolainen J, Berglund L, Ikkala O. Supramolecular control of stiffness and strength in lightweight high-performance nacre-mimetic paper with fire-shielding properties. Angew. Chem. Int. Ed., 2010, 49(36): 6448-6453.

[251] Jackson A P, Vincent J F, Turner R M. The mechanical design of nacre. Proc. R. Soc. London, Ser. B, 1988, 234(1277): 415-440.

[252] Rief M, Gautel M, Oesterhelt F, Fernandez J M, Gaub H E. Reversible unfolding of individual titin immunoglobulin domains by AFM. Science, 1997, 276(5315): 1109-1112.

[253] Smith B L, Schäffer T E, Viani M, Thompson J B, Frederick N A, Kindt J, Belcher A, Stucky G D, Morse D E, Hansma P K. Molecular mechanistic origin of the toughness of natural adhesives, fibres and composites. Nature, 1999, 399(6738): 761-763.

[254] Evans E, Ritchie K. Strength of a weak bond connecting flexible polymer chains. Biophys. J., 1999, 76(5): 2439-2447.

[255] Li H, Oberhauser A F, Fowler S B, Clarke J, Fernandez J M. Atomic force microscopy reveals the mechanical design of a modular protein. Proc. Natl. Acad. Sci. U. S. A., 2000, 97(12): 6527-6531.

[256] Oberhauser A F, Hansma P K, Carrion-Vazquez M, Fernandez J M. Stepwise unfolding of titin under force-clamp atomic force microscopy. Proc. Natl. Acad. Sci. U. S. A., 2001, 98(2): 468-472.

[257] Thompson J B, Kindt J H, Drake B, Hansma H G, Morse D E, Hansma P K. Bone indentation recovery time correlates with bond reforming time. Nature, 2001, 414(6865): 773-776.

[258] Fantner G E, Hassenkam T, Kindt J H, Weaver J C, Birkedal H, Pechenik L, Cutroni J A, Cidade G A, Stucky G D, Morse D E, Hansma P K. Sacrificial bonds and hidden length dissipate energy as mineralized fibrils separate during bone fracture. Nat. Mater., 2005, 4(8): 612-616.

[259] Currey J. Biomaterials: sacrificial bonds heal bone. Nature, 2001, 414(6865): 699.

[260] Hansma P K, Fantner G E, Kindt J H, Thurner P J, Schitter G, Turner P J, Udwin S F, Finch M M. Sacrificial bonds in the interfibrillar matrix of bone. J. Musculoskeletal Neuronal Interact., 2005, 5(4): 313-315.

[261] Gutsmann T, Hassenkam T, Cutroni J A, Hansma P K. Sacrificial bonds in polymer brushes from rat tail tendon functioning as nanoscale velcro. Biophys. J., 2005, 89(1): 536-542.

[262] Becker N, Oroudjev E, Mutz S, Cleveland J P, Hansma P K, Hayashi C Y, Makarov D E, Hansma H G. Molecular nanosprings in spider capture-silk threads. Nat. Mater., 2003, 2(4): 278-283.

[263] Oroudjev E, Soares J, Arcidiacono S, Thompson J B, Fossey S A, Hansma H G. Segmented nanofibers of spider dragline silk: atomic force microscopy and single-molecule force spectroscopy. Proc. Natl. Acad. Sci. U. S. A., 2002, 99 (suppl 2), 6460-6465.

[264] Thormann E, Mizuno H, Jansson K, Hedin N, Fernández M S, Arias J L, Rutland M W, Pai R K, Bergström L. Embedded proteins and sacrificial bonds provide the strong adhesive properties of gastroliths. Nanoscale, 2012, 4(13): 3910-3916.

[265] Vaccaro E, Waite J H. Yield and post-yield behavior of mussel byssal thread: a self-healing biomolecular material. Biomacromolecules, 2001, 2(3): 906-911.

[266] Harrington M J, Waite J H. Holdfast heroics: comparing the molecular and mechanical properties of Mytilus californianus byssal threads. J. Exp. Biol., 2007, 210(24): 4307-4318.

[267] Harrington M J, Gupta H S, Fratzl P, Waite J H. Collagen insulated from tensile damage by domains that unfold reversibly: In situ X-ray investigation of mechanical yield and damage repair in the mussel byssus. J. Struct. Biol., 2009, 167(1): 47-54.

[268] Reinecke A, Bertinetti L, Fratzl P, Harrington M J. Cooperative behavior of a sacrificial bond network and elastic framework in providing self-healing capacity in mussel byssal threads. J. Struct. Biol., 2016, 196(3): 329-339.

[269] Degtyar E, Harrington M J, Politi Y, Fratzl P. The mechanical role of metal ions in biogenic protein-based materials. Angew. Chem. Int. Ed., 2014, 53(45): 12026-12044.

[270] Bobaru F, Silling S A, Jiang H. Peridynamic fracture and damage modeling of membranes and nanofiber networks. Proc. XI Int. Conf. Fracture, Turin, 2005, 5748, 1-6.

[271] Zhou H, Zhang Y. Hierarchical chain model of spider capture silk elasticity. Phys. Rev. Lett., 2005, 94(2): 028104.

[272] Buehler M J. Molecular nanomechanics of nascent bone: fibrillar toughening by mineralization. Nanotechnology, 2007, 18(29): 295102.

[273] Fantner G E, Oroudjev E, Schitter G, Golde L S, Thurner P, Finch M M, Turner P, Gutsmann T, Morse D E, Hansma H, Hansma P K. Sacrificial bonds and hidden length: unraveling molecular mesostructures in tough materials. Biophys. J., 2006, 90(4): 1411-1418.

[274] Nabavi S S, Harrington M J, Paris O, Fratzl P, Hartmann M A. The role of topology and thermal backbone fluctuations on sacrificial bond efficacy in mechanical metalloproteins. New J. Phys., 2014, 16(1): 013003.

[275] Nabavi S S, Harrington M J, Fratzl P, Hartmann M A. Influence of sacrificial bonds on the mechanical behaviour of polymer chains. Bioinspired, Biomimetic Nanobiomater., 2014, 3(3): 139-145.

[276] Nabavi S S, Fratzl P, Hartmann M A. Energy dissipation and recovery in a simple model with reversible cross-links. Phys. Rev. E, 2015, 91(3): 032603.

[277] Hartmann M A, Fratzl P. Sacrificial ionic bonds need to be randomly distributed to provide shear deformability. Nano Lett., 2009, 9(10): 3603-3607.

[278] Lewis J A, Gratson G M. Direct writing in three dimensions. Mater. Today, 2004, 7(7): 32-39.

[279] Guo S Z, Gosselin F, Guerin N, Lanouette A M, Heuzey M C, Therriault D. Solvent-cast three-dimensional printing of multifunctional microsystems. Small, 2013, 9(24): 4118-4122.

[280] Passieux R, Guthrie L, Rad S H, Lévesque M, Therriault D, Gosselin F P. Instability-assisted direct writing of microstructured fibers featuring sacrificial bonds. Adv. Mater., 2015, 27(24): 3676-3680.

[281] Elbanna A E, Carlson J M. Dynamics of polymer molecules with sacrificial bond and hidden length systems: towards a physically-based mesoscopic constitutive law. PLOS One, 2013, 8(4): e56118.

[282] Lieou C K, Elbanna A E, Carlson J M. Sacrificial bonds and hidden length in biomaterials: A kinetic constitutive description of strength and toughness in bone. Phys. Rev. E, 2013, 88(1): 012703.

[283] Wang W, Elbanna A. Crack propagation in bone on the scale of mineralized collagen fibrils: role of polymers with sacrificial bonds and hidden length. Bone, 2014, 68, 20-31.

[284] Bell G I. Models for the specific adhesion of cells to cells. Science, 1978, 200(4342): 618-627.

[285] Rief M, Fernandez J M, Gaub H E. Elastically coupled two-level systems as a model for biopolymer extensibility. Phys. Rev. Lett., 1998, 81(21): 4764-4767.

[286] Long R, Hui C Y. Fracture toughness of hydrogels: measurement and interpretation. Soft Matter, 2016, 12(39): 8069-8086.

[287] Hui C Y, Long R. A constitutive model for the large deformation of a self-healing gel. Soft Matter, 2012, 8(31): 8209-8216.

[288] Long R, Mayumi K, Creton C, Narita T, Hui C Y. Time dependent behavior of a dual cross-link self-healing gel: Theory and experiments. Macromolecules, 2014, 47(20): 7243-7250.

[289] Guo J, Long R, Mayumi K, Hui C Y. Mechanics of a dual cross-link gel with dynamic bonds: steady state kinetics and large deformation effects. Macromolecules, 2016, 49(9): 3497-3507.

[290] Gong J P, Katsuyama Y, Kurokawa T, Osada Y. Double-network hydrogels with extremely high mechanical strength. Adv. Mater., 2003, 15(14): 1155-1158.

[291] Gong J P. Materials both tough and soft. Science, 2014, 344(6180): 161-162.

[292] Gong J P. Why are double network hydrogels so tough?. Soft Matter, 2010, 6(12): 2583-2590.

[293] Brown H R. A model of the fracture of double network gels. Macromolecules, 2007, 40(10): 3815-3818.

[294] Tanaka Y. A local damage model for anomalous high toughness of double-network gels. Europhys. Lett., 2007, 78(5): 56005.

[295] Lake G J, Thomas A G. The strength of highly elastic materials. Proc. R. Soc. London, Ser. A, 1967, 300(1460): 108-119.

[296] Chen Q, Zhu L, Zhao C, Wang Q, Zheng J. A robust, one-pot synthesis of highly mechanical and recoverable double network hydrogels using thermoreversible sol-gel polysaccharide. Adv. Mater., 2013, 25(30): 4171-4176.

[297] Luo F, Sun T L, Nakajima T, Kurokawa T, Zhao Y, Sato K, Ihsan A B, Li X, Guo H, Gong J P. Oppositely charged polyelectrolytes form tough, self-healing, and rebuildable hydrogels. Adv. Mater., 2015, 27(17): 2722-2727.

[298] Luo F, Sun T L, Nakajima T, Kurokawa T, Ihsan A B, Li X, Guo H, Gong J P. Free reprocessability of tough and self-healing hydrogels based on polyion complex. ACS Macro Lett., 2015, 4(9): 961-964.

[299] Luo F, Sun T L, Nakajima T, King D R, Kurokawa T, Zhao Y, Ihsan A B, Li X, Guo H, Gong J P. Strong and tough polyion-complex hydrogels from oppositely charged polyelectrolytes: a comparative study with polyampholyte hydrogels. Macromolecules, 2016, 49(7): 2750-2760.

[300] Sun T L, Kurokawa T, Kuroda S, Ihsan A B, Akasaki T, Sato K, Haque M A, Nakajima T, Gong J P. Physical hydrogels composed of polyampholytes demonstrate high toughness and viscoelasticity. Nat. Mater., 2013, 12(10): 932-937.

[301] Haque M A, Kurokawa T, Kamita G, Gong J P. Lamellar bilayers as reversible sacrificial bonds to toughen hydrogel: hysteresis, self-recovery, fatigue resistance, and crack blunting. Macromolecules, 2011, 44(22): 8916-8924.

[302] Haque M A, Kurokawa T, Gong J P. Anisotropic hydrogel based on bilayers: color, strength, toughness, and fatigue resistance. Soft Matter, 2012, 8(31): 8008-8016.

[303] Bai T, Zhang P, Han Y, Liu Y, Liu W, Zhao X, Lu W. Construction of an ultrahigh strength hydrogel with excellent fatigue resistance based on strong dipole–dipole interaction. Soft Matter, 2011, 7(6): 2825-2831.

[304] Zhao X, Huebsch N, Mooney D J, Suo Z. Stress-relaxation behavior in gels with ionic and covalent crosslinks. J. Appl. Phys., 2010, 107(6): 063509.

[305] Aizenberg J, Fratzl P. Biological and biomimetic materials. Adv. Mater., 2009, 21(4): 387-388.

[306] Wang J, Cheng Q, Tang Z. Layered nanocomposites inspired by the structure and mechanical properties of nacre. Chem. Soc. Rev., 2012, 41(3): 1111-1129.

[307] Peng F, Li G, Liu X, Wu S, Tong Z. Redox-responsive gel-sol/sol-gel transition in poly (acrylic acid) aqueous solution containing Fe (iii) ions switched by light. J. Am. Chem. Soc., 2008, 130(48): 16166-16167.

[308] Calvo-Marzal P, Delaney M P, Auletta J T, Pan T, Perri N M, Weiland L M, Waldeck D H, Clark W W, Meyer T Y. Manipulating mechanical properties with electricity: electroplastic elastomer hydrogels. ACS Macro Lett., 2011, 1(1): 204-208.

[309] Tang Z, Kotov N A, Magonov S, Ozturk B. Nanostructured artificial nacre. Nat. Mater., 2003, 2(6): 413-418.

[310] Decher G H, Hong J D, Schmitt J. Buildup of ultrathin multilayer films by a self-assembly process: III. Consecutively alternating adsorption of anionic and cationic polyelectrolytes on charged surfaces. Thin solid films, 1992, 210, 831-835.

[311] Decher G. Fuzzy nanoassemblies: toward layered polymeric multicomposites. Science, 1997, 277(5330): 1232-1237.

[312] Kovtyukhova N I, Ollivier P J, Martin B R, Mallouk T E, Chizhik S A, Buzaneva E V, Gorchinskiy A D. Layer-by-layer assembly of ultrathin composite films from micron-sized graphite oxide sheets and polycations. Chem. Mater., 1999, 11(3): 771-778.

[313] Das P, Walther A. Ionic supramolecular bonds preserve mechanical properties and enable synergetic performance at high humidity in water-borne, self-assembled nacre-mimetics. Nanoscale, 2013, 5(19): 9348-9356.

[314] Sheu S Y, Yang D Y, Selzle H L, Schlag E W. Energetics of hydrogen bonds in peptides. Proc. Natl. Acad. Sci. U. S. A., 2003, 100(22): 12683-12687.

[315] Houbenov N, Haataja J S, Iatrou H, Hadjichristidis N, Ruokolainen J, Faul C F, Ikkala O. Self-assembled polymeric supramolecular frameworks. Angew. Chem. Int. Ed., 2011, 50(11): 2516-2520.

[316] Sijbesma R P, Beijer F H, Brunsveld L, Folmer B J, Hirschberg J K, Lange R F, Lowe J K, Meijer E W. Reversible polymers formed from self-complementary monomers using quadruple hydrogen bonding. Science, 1997, 278(5343): 1601-1604.

[317] Martikainen L, Walther A, Seitsonen J, Berglund L, Ikkala O. Deoxyguanosine phosphate mediated sacrificial bonds promote synergistic mechanical properties in nacre-mimetic nanocomposites. Biomacromolecules, 2013, 14(8): 2531-2535.

[318] Beijer F H, Sijbesma R P, Kooijman H, Spek A L, Meijer E W. Strong dimerization of ureidopyrimidones via quadruple hydrogen bonding. J. Am. Chem. Soc., 1998, 120(27): 6761-6769.

[319] Folmer B J, Sijbesma R P, Kooijman H, Spek A L, Meijer E W. Cooperative dynamics in duplexes of stacked hydrogen-bonded moieties. J. Am. Chem. Soc., 1999, 121(39): 9001-9007.

[320] Söntjens S H, Sijbesma R P, van Genderen M H, Meijer E W. Stability and lifetime of quadruply hydrogen bonded 2-ureido-4[1 H]-pyrimidinone dimers. J. Am. Chem. Soc., 2000, 122(31): 7487-7493.

[321] Folmer B J, Sijbesma R P, Meijer E W. Unexpected entropy-driven ring-opening polymerization in a reversible supramolecular system. J. Am. Chem. Soc., 2001, 123(9): 2093-2094.

[322] Sherrington D C, Taskinen K A. Self-assembly in synthetic macromolecular systems via multiple hydrogen bonding interactions. Chem. Soc. Rev., 2001, 30(2): 83-93.

[323] Zhu B, Jasinski N, Benitez A, Noack M, Park D, Goldmann A S, Barner-Kowollik C, Walther A. Hierarchical nacre mimetics with synergistic mechanical properties by control of molecular interactions in self-healing polymers. Angew. Chem. Int. Ed., 2015, 54(30): 8653-8657.

[324] Zhu B, Noack M, Merindol R, Barner-Kowollik C, Walther A. Light-adaptive supramolecular nacre-mimetic nanocomposites. Nano Lett., 2016, 16(8): 5176-5182.

[325] McKee J R, Huokuna J, Martikainen L, Karesoja M, Nykänen A, Kontturi E, Tenhu H, Ruokolainen J, Ikkala O. Molecular engineering of fracture energy dissipating sacrificial bonds into cellulose nanocrystal nanocomposites. Angew. Chem. Int. Ed., 2014, 53(20): 5049-5053.

[326] Voit B I. Hyperbranched polymers: a chance and a challenge. C. R. Chimie, 2003, 6(8): 821-832.

[327] Voit B I, Lederer A. Hyperbranched and highly branched polymer architectures—synthetic strategies and major characterization aspects. Chem. Rev., 2009, 109(11): 5924-5973.

[328] Hu X, Xu Z, Gao C. Multifunctional, supramolecular, continuous artificial nacre fibres. Sci. Rep., 2012, 2: 767.

[329] Hao W, Ding S, Zhang L, Liu W, Yang W. Nacrelike nanocomposite films from fluorescent hyperbranched poly (amido amine) s and clay nanosheets. Chempluschem, 2014, 79(2): 211-216.

[330] Byette F, Laventure A, Marcotte I, Pellerin C. Metal–ligand interactions and salt bridges as sacrificial bonds in mussel byssus-derived materials. Biomacromolecules, 2016, 17(10): 3277-3286.

[331] Byette F, Pellerin C, Marcotte I. Self-assembled pH-responsive films prepared from mussel anchoring threads. J. Mater. Chem. B, 2014, 2(37): 6378-6386.

[332] Das P, Malho J M, Rahimi K, Schacher F H, Wang B, Demco D E, Walther A. Nacre-mimetics with synthetic nanoclays up to ultrahigh aspect ratios. Nat. Commun., 2015, 6: 5967.

[333] Hao W, Zhang L, Wang X, Wang J, Hu Z, Yang W. Tough and strong nacre-like composites from hyperbranched poly (amido amine) and clay nanosheets cross-linked by genipin. RSC Adv., 2016, 6(2): 1415-1421.

[334] Lin C, Gitsov I. Preparation and characterization of novel amphiphilic hydrogels with covalently attached drugs and fluorescent markers. Macromolecules, 2010, 43(23): 10017-10030.

[335] Vermonden T, Censi R, Hennink W E. Hydrogels for protein delivery. Chem. Rev., 2012, 112(5): 2853-2888.

[336] Lee K Y, Mooney D J. Hydrogels for tissue engineering. Chem. Rev., 2001, 101(7): 1869-1880.

[337] Söntjens S H, Nettles D L, Carnahan M A, Setton L A, Grinstaff M W. Biodendrimer-based hydrogel scaffolds for cartilage tissue repair. Biomacromolecules, 2006, 7(1): 310-316.

[338] Balakrishnan B, Banerjee R. Biopolymer-based hydrogels for cartilage tissue engineering. Chem. Rev., 2011, 111(8): 4453-4474.

[339] Peng G, Xu S, Peng Y, Wang J, Zheng L. A new amphoteric superabsorbent hydrogel based on sodium starch sulfate. Bioresour. Technol., 2008, 99(2): 444-447.

[340] Kabiri K, Omidian H, Zohuriaan-Mehr M J, Doroudiani S. Superabsorbent hydrogel composites and nanocomposites: a review. Polym. Compos., 2011, 32(2) : 277-289.

[341] Chang C, Duan B, Cai J, Zhang L. Superabsorbent hydrogels based on cellulose for smart swelling and controllable delivery. Eur. Polym. J., 2010, 46(1): 92-100.

[342] Spalding B P, Brooks S C, Watson D B. Hydrogel-Encapsulated Soil: A tool to measure contaminant attenuation in situ. Environ. Sci. Technol., 2010, 44(8): 3047-3051.

[343] Ozay O, Ekici S, Baran Y, Aktas N, Sahiner N. Removal of toxic metal ions with magnetic hydrogels. Water Res., 2009, 43(17): 4403-4411.

[344] Tan H, Chu C R, Payne K A, Marra K G. Injectable in situ forming biodegradable chitosan–hyaluronic acid based hydrogels for cartilage tissue engineering. Biomaterials, 2009, 30(13): 2499-2506.

[345] Hagiwara Y, Putra A, Kakugo A, Furukawa H, Gong J P. Ligament-like tough double-network hydrogel based on bacterial cellulose. Cellulose, 2010, 17(1): 93-101.

[346] Bassil M, Davenas J, Tahchi M E. Electrochemical properties and actuation mechanisms of polyacrylamide hydrogel for artificial muscle application. Sens. Actuators, B, 2008, 134(2): 496-501.

[347] Nakajima T, Sato H, Zhao Y, Kawahara S, Kurokawa T, Sugahara K, Gong J P. A universal molecular stent method to toughen any hydrogels based on double network concept. Adv. Funct. Mater., 2012, 22(21): 4426-4432.

[348] Hu J, Hiwatashi K, Kurokawa T, Liang S M, Wu Z L, Gong J P. Microgel-reinforced hydrogel films with high mechanical strength and their visible mesoscale fracture structure. Macromolecules, 2011, 44(19): 7775-7781.

[349] Hu J, Kurokawa T, Hiwatashi K, Nakajima T, Wu Z L, Liang S M, Gong J P. Structure optimization and mechanical model for microgel-reinforced hydrogels with high strength and toughness. Macromolecules, 2012, 45(12): 5218-5228.

[350] Hu J, Kurokawa T, Nakajima T, Sun T L, Suekama T, Wu Z L, Liang S M, Gong J P. High fracture efficiency and stress concentration phenomenon for microgel-reinforced hydrogels based on double-network principle. Macromolecules, 2012, 45(23): 9445-9451.

[351] Hu J, Kurokawa T, Nakajima T, Wu Z L, Liang S M, Gong J P. Fracture process of microgel-reinforced hydrogels under uniaxial tension. Macromolecules, 2014, 47(11): 3587-3594.

[352] Sun J Y, Zhao X, Illeperuma W R, Chaudhuri O, Oh K H, Mooney D J, Vlassak J J, Suo Z. Highly stretchable and tough hydrogels. Nature, 2012, 489(7414): 133-136.

[353] Yang C H, Wang M X, Haider H, Yang J H, Sun J Y, Chen Y M, Zhou J, Suo Z. Strengthening alginate/polyacrylamide hydrogels using various multivalent cations. ACS Appl. Mater. Interfaces, 2013, 5(21): 10418-10422.

[354] Lu X, Chan C Y, Lee K I, Ng P F, Fei B, Xin J H, Fu J. Super-tough and thermo-healable hydrogel–promising for shape-memory absorbent fiber. J. Mater. Chem. B, 2014, 2(43): 7631-7638.

[355] Stevens L, Calvert P, Wallace G G. Ionic-covalent entanglement hydrogels from gellan gum, carrageenan and an epoxy-amine. Soft Matter, 2013, 9(11): 3009-3012.

[356] Bakarich S E, Pidcock G C, Balding P, Stevens L, Calvert P. Recovery from applied strain in interpenetrating polymer network hydrogels with ionic and covalent cross-links. Soft Matter, 2012, 8(39): 9985-9988.

[357] Lin P, Ma S, Wang X, Zhou F. Molecularly engineered dual-crosslinked hydrogel with ultrahigh mechanical strength, toughness, and good self-recovery. Adv. Mater., 2015, 27(12): 2054-2059.

[358] Menyo M S, Hawker C J, Waite J H. Rate-dependent stiffness and recovery in interpenetrating network hydrogels through sacrificial metal coordination bonds. ACS Macro. Lett., 2015, 4(11): 1200-1204.

[359] Hu X, Vatankhah-Varnoosfaderani M, Zhou J, Li Q, Sheiko S S. Weak hydrogen bonding enables hard, strong, tough, and elastic hydrogels. Mater., 2015, 27(43): 6899-6905.

[360] Zhang Y, Li Y, Liu W. Dipole-dipole and H-bonding interactions significantly enhance the multifaceted mechanical properties of thermoresponsive shape memory hydrogels. Adv. Funct. Mater., 2015, 25(3): 471-480.

[361] Yang J, Ma M, Zhang X, Xu F. Elucidating dynamics of precoordinated ionic bridges as sacrificial bonds in interpenetrating network hydrogels. Macromolecules, 2016, 49(11): 4340-4348.

[362] Nicholls A, Sharp K A, Honig B. Protein folding and association: insights from the interfacial and thermodynamic properties of hydrocarbons. Proteins, 1991, 11(4): 281-296.

[363] Singer S J, Nicolson G L. The fluid mosaic model of the structure of cell membranes. Science, 1972, 175(4023): 720-731.

[364] Bao G, Suresh S. Cell and molecular mechanics of biological materials. Nat. Mater., 2003, 2(11): 715-725.

[365] Tsujii K, Hayakawa M, Onda T, Tanaka T. A novel hybrid material of polymer gels and bilayer membranes. Macromolecules, 1997, 30(24): 7397-7402.

[366] Haque M, Kamita G, Kurokawa T, Tsujii K, Gong J P. Unidirectional alignment of lamellar bilayer in hydrogel: One-dimensional swelling, anisotropic modulus, and stress/strain tunable structural color. Adv. Mater., 2010, 22(45): 5110-5114.

[367] Jiang G, Liu C, Liu X, Zhang G, Yang M, Liu F. Construction and properties of hydrophobic association hydrogels with high mechanical strength and reforming capability. Macromol. Mater. Eng., 2009, 294(12): 815-820.

[368] Geng Y, Lin X Y, Pan P, Shan G, Bao Y, Song Y, Wu Z L, Zheng Q. Hydrophobic association mediated physical hydrogels with high strength and healing ability. Polymer, 2016, 100: 60-68.

[369] Dong S, Zheng B, Wang F, Huang F. Supramolecular polymers constructed from macrocycle-based host-guest molecular recognition motifs. Acc. Chem. Res., 2014, 47(7): 1982-1994.

[370] Yu G, Jie K, Huang F. Supramolecular amphiphiles based on host-guest molecular recognition motifs. Chem. Rev., 2015, 115(15): 7240-7303.

[371] Schneider H J, Yatsimirsky A K. Selectivity in supramolecular host-guest complexes. Chem. Soc. Rev., 2008, 37(2): 263-277.

[372] Schmidt B V, Hetzer M, Ritter H, Barner-Kowollik C. Complex macromolecular architecture design via cyclodextrin host/guest complexes. Prog. Polym. Sci., 2014, 39(1): 235-249.

[373] McKee J R, Appel E A, Seitsonen J, Kontturi E, Scherman O A, Ikkala O. Healable, stable and stiff hydrogels: combining conflicting properties using dynamic and selective three-component recognition with reinforcing cellulose nanorods. Adv. Funct. Mater., 2014, 24(18): 2706-2713.

[374] Liu J, Tan C S, Yu Z, Lan Y, Abell C, Scherman O A. Biomimetic supramolecular polymer networks exhibiting both toughness and self-recovery. Adv. Mater., 2017, 29(10): 1604951.

[375] Nakahata M, Takashima Y, Harada A. Highly flexible, tough, and self-healing supramolecular polymeric materials using host-guest interaction. Macromol. Rapid Commun., 2016, 37(1): 86-92.

[376] Kakuta T, Takashima Y, Nakahata M, Otsubo M, Yamaguchi H, Harada A. Preorganized hydrogel: self-healing properties of supramolecular hydrogels formed by polymerization of host-guest-monomers that contain cyclodextrins and hydrophobic guest groups. Adv. Mater., 2013, 25(20): 2849-2853.

[377] Miyamae K, Nakahata M, Takashima Y, Harada A. Self-healing, expansion-contraction, and shape-memory properties of a preorganized supramolecular hydrogel through host-guest interactions. Angew. Chem. Int. Ed., 2015, 54(31): 8984-8987.

[378] Haraguchi K, Takehisa T. Nanocomposite hydrogels: a unique organic-inorganic network structure with extraordinary mechanical, optical, and swelling/de-swelling properties. Adv. Mater., 2002, 14(16): 1120.

[379] Ito K. Novel cross-linking concept of polymer network: synthesis, structure, and properties of slide-ring gels with freely movable junctions. Polym. J., 2007, 39(6): 489-499.

[380] Sakai T, Matsunaga T, Yamamoto Y, Ito C, Yoshida R, Suzuki S, Sasaki N, Shibayama M, Chung U I. Design and fabrication of a high-strength hydrogel with ideally homogeneous network structure from tetrahedron-like macromonomers. Macromolecules, 2008, 41(14): 5379-5384.

[381] Huang T, Xu H G, Jiao K X, Zhu L P, Brown H R, Wang H L. A novel hydrogel with high mechanical strength: a macromolecular microsphere composite hydrogel. Adv. Mater., 2007, 19(12): 1622-1626.

[382] Tanaka Y, Kuwabara R, Na Y H, Kurokawa T, Gong J P, Osada Y. Determination of fracture energy of high strength double network hydrogels. J. Phys. Chem. B, 2005, 109(23): 11559-11562.

[383] Haque M A, Kurokawa T, Gong J P. Super tough double network hydrogels and their application as biomaterials. Polymer, 2012, 53(9): 1805-1822.

[384] Yue Y F, Haque M A, Kurokawa T, Nakajima T, Gong J P. lamellar hydrogels with high toughness and ternary tunable photonic stop-band. Adv. Mater., 2013, 25(22): 3106-3110.

[385] Ducrot E, Chen Y, Bulters M, Sijbesma R P, Creton C. Toughening elastomers with sacrificial bonds and watching them break. Science, 2014, 344(6180): 186-189.

[386] Burnworth M, Tang L, Kumpfer J R, Duncan A J, Beyer F L, Fiore G L, Rowan S J, Weder C. Optically healable supramolecular polymers. Nature, 2011, 472(7343): 334-337.

[387] Bode S, Zedler L, Schacher F H, Dietzek B, Schmitt M, Popp J, Hager M D, Schubert U S. Self-healing polymer coatings based on crosslinked metallosupramolecular copolymers. Adv. Mater., 2013, 25(11): 1634-1638.

[388] Balkenende D W, Coulibaly S, Balog S, Simon Y C, Fiore G L, Weder C. Mechanochemistry with metallosupramolecular polymers. J. Am Chem. Soc., 2014, 136(29): 10493-10498.

[389] Sandmann B, Happ B, Kupfer S, Schacher F H, Hager M D, Schubert U S. The self-healing potential of triazole-pyridine-based metallopolymers. Macromol. Rapid Commun., 2015, 36(7): 604-609.

[390] Li C H, Wang C, Keplinger C, Zuo J L, Jin L, Sun Y, Zheng P, Cao Y, Lissel F, Linder C, You X Z. A highly stretchable autonomous self-healing elastomer. Nat. Chem., 2016, 8(6): 618-624.

[391] Zhang X, Tang Z, Guo B, Zhang L. Enabling design of advanced elastomer with bioinspired metal-oxygen coordination. ACS Appl. Mater. Interfaces, 2016, 8(47): 32520-32527.

[392] Huang J, Tang Z, Yang Z, Guo B. Bioinspired interface engineering in elastomer/graphene composites by constructing sacrificial metal-ligand bonds. Macromol. Rapid Commun., 2016, 37(13): 1040-1045.

[393] Kushner A M, Gabuchian V, Johnson E G, Guan Z. Biomimetic design of reversibly unfolding cross-linker to enhance mechanical properties of 3D network polymers. J. Am. Chem. Soc., 2007, 129(46): 14110-14111.

[394] Zhang H, Chen Y, Lin Y, Fang X, Xu Y, Ruan Y, Weng W. Spiropyran as a mechanochromic probe in dual cross-linked elastomers. Macromolecules, 2014, 47(19): 6783-6790.

[395] Gold B J, Hövelmann C H, Weiss C, Radulescu A, Allgaier J, Pyckhout-Hintzen W, Wischnewski A, Richter D. Sacrificial bonds enhance toughness of dual polybutadiene networks. Polymer, 2016, 87: 123-128.

[396] Huang J, Zhang L, Tang Z, Wu S, Ning N, Sun H, Guo B. Bioinspired design of a robust elastomer with adaptive recovery via triazolinedione click chemistry. Macromol. Rapid Commun., 2017, 38(7): 1600678.

[397] Liu J, Wang S, Tang Z, Huang J, Guo B, Huang G. Bioinspired engineering of two different types of sacrificial bonds into chemically cross-linked cis-1, 4-polyisoprene toward a high-performance Elastomer. Macromolecules, 2016, 49(22): 8593-8604.

[398] Chen Z, Lu H. Constructing sacrificial bonds and hidden lengths for ductile graphene/polyurethane elastomers with improved strength and toughness. J. Mater. Chem., 2012, 22(25): 12479-12490.

[399] Liu J, Tang Z, Huang J, Guo B, Huang G. Promoted strain-induced-crystallization in synthetic cis-1, 4-polyisoprene via constructing sacrificial bonds. Polymer, 2016, 97: 580-588.

[400] Chen Y, Spiering A J, Karthikeyan S, Peters G W, Meijer E W, Sijbesma R P. Mechanically induced chemiluminescence from polymers incorporating a 1, 2-dioxetane unit in the main chain. Nat. Chem., 2012, 4(7): 559-562.

Publication list

Publications in International Journals

[1] **Xinxin Zhou**, Baochun Guo, Liqun Zhang, and Guo-Hua Hu. Progress in bio-inspired sacrificial bonds in artificial polymeric materials. *Chemical Society Reviews*, 2017, 46(20), 6301-6329.

[2] **Xinxin Zhou**, Qinan Zhang, Runguo Wang, Baochun Guo, Yuri Lvov, Guo-Hua Hu, and Liqun Zhang. Preparation and performance of bio-based carboxylic elastomer/halloysite nanotubes nanocomposites with strong interfacial interaction. *Composites Part A: Applied Science and Manufacturing*, 2017, 102, 253-262.

[3] **Xinxin Zhou**, Lesi Cai, Weiwei Lei, He Qiao, Chaohao Liu, Xiuying Zhao, Jianfeng Chen, Runguo Wang, and Liqun Zhang. Preparation and intermolecular interaction of bio-based elastomer/hindered phenol hybrid with tunable damping properties. *Pure and Applied Chemistry*, 2015, 87(8), 767-777.

[4] **Xinxin Zhou**, Runguo Wang, Weiwei Lei, He Qiao, Haoling Ji, Liqun Zhang, Kuo-Chih, Hua, and Joseph Kulig. Design and synthesis by redox polymerization of a bio-based carboxylic elastomer for green tire. *Science China Chemistry*, 2015, 58(10), 1561-1569.

[5] Weiwei Lei†, **Xinxin Zhou**†, Thomas P. Russell, Kuo-Chih Hua, Xiaoping Yang, He Qiao, Wencai Wang, Fanzhu Li, Runguo Wang, and Liqun Zhang. High performance bio-based elastomers: energy efficient and sustainable materials for tires. *Journal of Materials Chemistry A*, 2016, 4(34), 13058-13062.

[6] **Xinxin Zhou**, Qinan, Zhang, Weiwei Lei, Runguo Wang, Guo-Hua Hu, and Liqun Zhang. A solvent-less green synthetic route toward sustainable bio-based elastomers: design, synthesis and characterization of poly(dibutyl itaconate-*co*-butadiene). *In preparation for Green Chemistry*.

Contributions to International Conferences

Xinxin Zhou and Liqun Zhang. Biobased and bioinspired elastomers with functional performance. *The 3rd International conference on Bioinspired and Biobased Chemistry & Materials*, October, 2016, Nice, France. (Invited lecture).

Xinxin Zhou, Runguo Wang, and Liqun Zhang. The structures and dynamic properties of bio-based elastomer/hindered phenol crosslinked composites. *The 23rd Annual International Conference on Composites/Nano Engineering (ICCE-23)*, July, 2015, Chengdu, China. (Oral presentation).

Synthesis, properties and applications of itaconate based engineering elastomers

Abstract

This thesis deals with the preparation and application of itaconate based engineering elastomers and their nanocomposites. The following elastomers or nanocomposites were prepared: (1) nanocomposites based on 3,9-bis[1,1-dim ethyl-2-{b-(3-tertbutyl-4-hydroxy-5-methylphenyl)propionyloxy}ethyl]-2,4,8,10-tetraoxaspiro-[5,5]-undecane (AO-80) and poly(diisoamyl itaconate-*co*-isoprene) (PDII), (2) a bio-based carboxylic elastomer, poly(dibutyl itaconate-*co*-isoprene-*co*-methacrylic acid) (PDIM), and nanocomposites based on it and silica or halloysite nanotubes, (3) a novel bio-based elastomer, poly(dibutyl itaconate-*co*-butadiene) (PDIB), and nanocomposites based on it and silica. Bio-based green tires were manufactured by using PDIB/silica nanocomposite in a tire tread formulation. In addition to the preparation of the above bio-based elastomers and their nanocomposites, this thesis also gives a review on the progresses on bio-inspired sacrificial bonds in polymeric materials. This review will serve as a guide to engineer sacrificial bonds into itaconate based elastomers with high strength and toughness.

Key words: Bio-based engineering elastomers, Preparation processes, Properties, Applications

Procédé de synthèse, propriétés et applications d'élastomères techniques à base d'itaconates

Résumé

Cette thèse traite la préparation et l'application d'élastomères bio-sourcés et leurs nanocomposites qui sont les suivants : (1) des nanocomposites basés sur le 3,9 - bis [ethyl-2-à 1,1 terne {b-(3-tertbutyle-4-hydroxy-5-méthylephényle) propionyloxy} éthyle]-2,4,8,10-tetraoxaspiro-[5,5]-undécane (AO-80) et le poly(itaconate de diisoamyle-co-isoprène) (PDII), (2) le poly(itaconate de dibutyle-*co*-isoprène-co-acide méthacrylique) (PDIM), un élastomère carboxylique bio-sourcé, et des nanocomposites basés sur cet élastomère et la silice ou les nanotubes de halloysite, (3) le poly(itaconate de dibutyle-*co*-butadiène) (PDIB), un nouvel élastomère bio-sourcé, et des nanocomposites basés sur cet élastomère et la silice. Des pneus verts bio ont été fabriqués en utilisant les nanocomposites PDIB/silice dans une formulation de bande de roulement de pneu. En plus de la préparation de ces dits élastomères bio et leurs nanocomposites, cette thèse donne aussi une revue sur les travaux sur des liaisons sacrificielles bio-inspirées qui sont introduites dans des matériaux polymères. Cette revue servira d'un guide pour incorporer des liaisons sacrificielles dans des élastomères à base d'itaconate ayant une grande rigidité et résistance.

Mots-clés : Bio-élastomères techniques, Procédés de synthèse, Propriétés, Applications